Molecular beam epitaxy of quantum dots on misoriented GaAs(111)B by droplet epitaxy

Dissertation

submitted to the Department of Physics
of the Universität Paderborn
for the award of the degree
'Doctor rerum naturalium'

submitted by

Alexander Trapp *né* Karlisch
from Paderborn

Paderborn, 28.02.2019

Doctoral committee

Prof. Dr. Wolf Gero Schmidt
Prof. Dr. Dirk Reuter
Prof. Dr. Artur Zrenner
Dr. Thomas Riedl

Kurzfassung

Die Tröpfchenepitaxie-Methode (DE) wurde auf fehlorientiertem GaAs(111)B angewandt, um selbstorganisierte GaAs Quantenpunkte (QDs) per Molekularstrahlepitaxie herzustellen.

In dem ersten Schritt wurde die glatte planare Abscheidung von (Al)GaAs auf dem Substrat optimiert. In dem nächsten Schritt wurden GaAs QDs mit Hilfe von DE auf $Al_{0.3}Ga_{0.7}As$ hergestellt. Jeder DE-Schritt wurde einzeln optimiert und mit Rasterkraftmikroskopie analysiert.

Eine Variation von Ga-Tröpfchenabscheidungstemperaturen wurde unter konstanter Abscheidungsmenge und -rate untersucht. Ein klarer Zusammenhang zur Tröpfchendichte wurde gefunden und mit einem Skalengesetz interpretiert. Tröpfchenform und -symmetrie wurden untersucht und ein Satz von Parametern, welcher die Dichte geeignet für strukturelle und optische Charakterisierungen hält, wurde identifiziert.

Der Kristallisationsvorgang von Tröpfchen zu QDs wurde in Temperatur und Zeit variiert. Für vollendete Kristallisation erwiesen sich extrem niedrige Temperaturen und lange Zeiten als notwendig. Verglichen mit Berichten von ähnlichen Experimenten auf (100)- und (111)A-Substraten musste auf (111)B eine stark verringerte Temperatur in beiden Schritten genutzt werden.

Nach Bedeckung und *ex-situ* Ausheilen waren die QDs optisch aktiv und zeigten Photolumineszenz. Ensemblemessungen der QDs mit breiten Emissionsspektra um 780 nm konnten bei 14 K erlangt werden. Einzelpunktlumineszenzmessungen ergaben exzitonische Linienbreiten von 0.2 meV.

Abstract

The droplet epitaxy (DE) method was applied to misoriented GaAs(111)B substrates to fabricate self-assembled GaAs quantum dots (QDs) by molecular beam epitaxy.

In the first step the planar deposition of GaAs and $Al_{0.3}Ga_{0.7}As$ on the substrate was optimized to yield smooth surfaces. The next step was to fabricate GaAs QDs on an $Al_{0.3}Ga_{0.7}As$ surface by DE. As DE is a multistage process, each step was optimized and analyzed individually using atomic force microscopy.

A variation of Ga droplet deposition temperatures was investigated while the amount and rate of deposited material were kept constant. A clear relation to the droplet density was found and interpreted using a scaling law approach. Droplet shape and symmetry were investigated and a set of parameters, which keeps a droplet density suitable for structural and optical characterization, was identified.

The crystallization process from droplets to QDs was varied in temperature and time. For complete crystallization extremely low temperatures and long times turned out to be necessary. When compared to reports of similar experiments on (100) and (111)A substrates, strongly decreased temperatures had to be used on (111)B to achieve similar results in both steps.

After capping and *ex-situ* annealing the QDs were optically active and showed photoluminescence. Ensemble measurements of the QDs with broad emission spectra around 780 nm could be acquired at 14 K. Single-dot luminescence revealed excitonic linewidths of 0.2 meV.

Contents

CHAPTER 1

Introduction

The steadily growing field of quantum technologies has advanced significantly in recent years so that its application in a large variety of fields such as communication, metrology and computation can be expected in the not-too-distant future [1–6]. Key components in this are the generation, manipulation, storage, transmission and probing of entangled particles. Entangled photons are likely an important particle type as they are naturally fast-moving qubits with strong resistance to decoherence [7]. As in classical computation the integration of several quantum components on a single chip promises very powerful devices, thus the development of solid-state components is highly desirable. Up to this point many solid-state single-photon emitter have been developed but none of them satisfies all requirements perfectly [8]. Especially semiconductor quantum dots (QDs) are a promising photon source as they make possible strongly integrated devices based on well-established semiconductor technology [9, 10]. In particular, self-assembled InGaAs QDs grown by molecular beam epitaxy (MBE) using the Stranski-Krastanov growth mode on GaAs(100) substrates can already be considered near-optimal single-photon sources [11]. They, however, struggle with generation of entangled photon-pairs: Theoretically the biexciton recombination cascade provides a viable scheme, but asymmetries in the basic substrate, which also affect the QDs, break entanglement by introducing an excitonic fine-structure splitting (FSS) in most QDs [12].

In QDs fabricated on GaAs(111)A/B substrates, on the other hand, a vanishing FSS due to the higher surface symmetry has been demonstrated theoretically [13]. The strain-driven Stranski-Krastanov growth mode cannot be employed on this surface as strain is instead relaxed by defect formation [14]. As an alternative method, droplet epitaxy (DE), which also allows fabrication of strain-free QDs, can be used on these substrates. As DE QDs are also self-organized they share the advantages of self-assembly as a nanofabrication technology [15]. Experimental validations for a vanishing FSS of GaAs/AlGaAs QDs fabricated by DE on GaAs(111)A substrates have already been reported [16–18]. On (111)A, however, extreme growth conditions have to be employed, enforcing low growth rates [19]. This complicates the future integration into larger heterostructures and, eventually, integrated chips massively. On misoriented GaAs(111)B substrates growth rates similar to those on the standard (100) substrates can be achieved [20]. As a result the fabrication of QDs on GaAs(111)B by DE is very desirable as a technological basis for an entangled photon pair generating device.

In this thesis the DE process is adapted to the fabrication of GaAs/AlGaAs QDs on misoriented GaAs(111)B substrates to the best of our knowledge for the first time. The QD samples are fabricated by MBE, an epitaxy method which is preferred in the scientific community due to its precise control over compositions and dimensions in nanostructure fabrication. Accordingly, MBE is the pivotal experimental method of this thesis. To present the results in a comprehensible manner the work was structured into the following parts:

The state of the art in single- and entangled photon generation is outlined in **chapter 1** elaborating the motivation for the thesis topic and providing an introduction.

Theoretical foundations necessary to comprehend the methods and results in this thesis are treated in **chapter 2**. The basic properties of the used material system and characteristics of QDs as well as the ways they can be fabricated from said material system are elaborated. In addition epitaxy, the basis of MBE, is outlined.

A rough sketch of the actual MBE system with emphasis on some key features vital for this thesis and additional devices to process and characterize the fabricated samples are described in **chapter 3**.

In **chapter 4** the intermediate results of all steps leading to optically active QDs are presented. This starts with parameters for smooth deposition of planar layers on misoriented GaAs(111)B substrates. This is a necessary step as these substrates are new to the system. Then individual, subsequent steps of the DE method are investigated and the impact of changing process parameters on structural properties such as QD density, size and symmetry are presented in detail. Atomic force microscopy measurements show the intermediate state of the forming QDs after each step. Finally, optically active QDs are fabricated and characterized in ensemble as well as individually by photoluminescence.

In the end, all results are summarized in **chapter 5** and an outlook of necessary next steps for further improvement of the achievements outlined in this thesis are given.

CHAPTER 2

Fundamentals

2.1 Semiconductors

Solids can be classified based on their electrical properties into metals, insulator and semiconductors [22]. Metals have partially filled energy bands while insulator only show completely filled and empty energy bands separated by the energy gap (or band gap energy) E_g. In a semiconductor both can be the case depending on the condition in which it is prepared. They can be insulators when cold but show conductivity at elevated temperatures below their melting point. This behavior was first observed by Faraday in 1833 [23]. Until the term 'semiconductor' was coined in today's sense of the word by Weiss, however, it took another 80 years and the work of several physicists [24]. Common examples of semiconductor materials can be found in group IV in the periodic table of elements, as III-V compounds and as II-VI compounds. The band structure for gallium arsenide (GaAs), a very well investigated semiconductor, is given in Figure 2.1. For this material E_g is the energy difference of valence and conduction band at the Γ-point, which is the case for most direct semiconductors. E_g of a semiconductor is typically below 3 eV [22]. While this is not a sharp distinction, materials with larger E_g are often called wide-bandgap semiconductors and then insulator. E_g is not a constant material property of a given semiconductor but depends on its current state and preparation. The temperature dependence, for example,

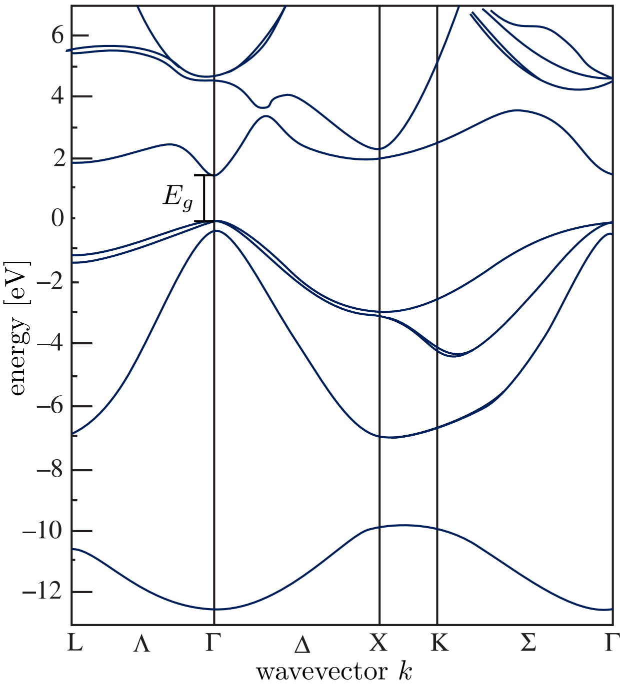

Figure 2.1: Electronic band structure of GaAs calculated by the pseudopotential technique. The plotted data was taken from [21].

can be described by the empirical Varshni formula [25]

$$E_g(T) = E_g(T=0) - \frac{\alpha_V T^2}{T+\beta_V} \quad , \tag{2.1}$$

where α_V and β_V are the Varshni parameters which are different for each semiconductor.

Semiconductor heterostructures are widely used for complex electrical devices [26] as diodes, transistors or optoelectronic devices [27] such as light emitting diodes [28], laser diodes [29] and charge-coupled devices [30]. These applications of semiconductor technology are nowadays used directly and indirectly by nearly every human and have greatly aided scientific endeavors in as well as outside of solid state physics [31, 32].

2.1.1 Group III - arsenides

The samples in this thesis are made of GaAs, indium arsenide (InAs), aluminum arsenide (AlAs) and their alloys, which are all typical examples of III-V compound semiconductors. These materials are commonly employed in basic research as well as in industry [35]. This is due to its technical maturity approaching that of the silicon industry and the fact that it is, in contrast to silicon, a direct semiconductor. Especially high-electron-mobility transistors [36] and laser diodes [37] are produced in industry based on this material system.

While E_g is paramount for the optoelectronic properties, the lattice constant a_0 of the crystal structure of the semiconductor is crucial for the fabrication of heterostructures [34]. The deposition of a semiconductor with high mismatch in a_0 to the substrate results in a strong degradation of crystal quality and general optoelectronic performance due to strain and defect formation. Group III - arsenides can be fabricated in the zincblende and, less commonly, in the wurtzite crystal structure. All samples in this thesis are of zincblende structure. Basic properties of these materials are given in Table 2.1.

Table 2.1: Basic properties of group III arsenides at 0 K. All calculations in this chapter are based on the given values. [33, 34]

property	AlAs	GaAs	InAs
direct energy gap at Γ-point E_g [eV]	3.099	1.519	0.417
Varshni parameter α_V [meV/K]	0.885	0.5405	0.276
Varshni parameter β_V [K]	530	204	93
zincblende lattice constant a_0 [Å]	5.6611	5.6426	6.0501
thermal expansion coefficient α [10^{-6} K^{-1}]	5.2	5.7	4.5
electron effective mass at Γ-point $m^*_{e,\Gamma}$ [m_e]	0.15	0.067	0.026

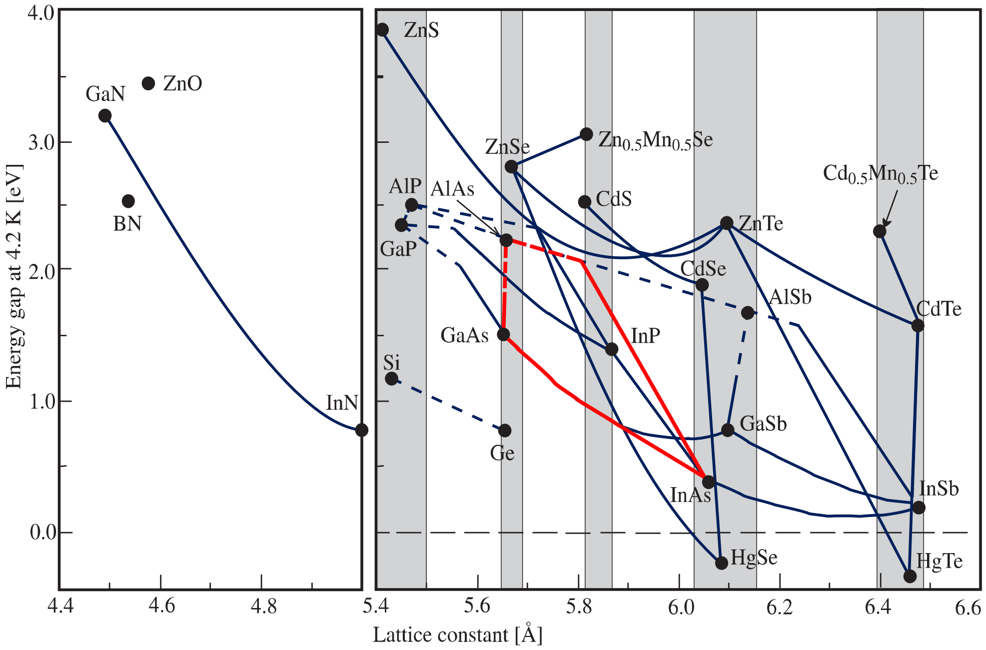

Figure 2.2: Low-temperature E_g versus a_0 of diamond and zincblende semiconductors and their alloys. The shaded regions highlight several families of semiconductors with similar lattice constants. Solid lines denote direct band gaps and dashed lines indirect ones. Arsenides, which are the subject of this thesis, are highlighted. Plot adopted from [38] including updated values given in 4th edition.

The lattice constant of a crystalline alloy A_xB_{1-x} can be linearly interpolated from the values of the pure crystals A and B according to Vegard's law [39]

$$a_{0,A_xB_{1-x}} = xa_{0,A} + (1-x)\, a_{0,B}$$

with molar fraction x of A in A_xB_{1-x}. This is not necessarily the case for E_g which typically requires a parabolic approximation

$$E_{g,A_xB_{1-x}} = x \cdot E_{g,A} + (1-x) \cdot E_{g,B} - b_{AB} \cdot x(1-x)$$

with bowing parameter b. For $Al_xGa_{1-x}As$ and $In_xGa_{1-x}As$ the respective bowing parameter values at the Γ-point are given as $b_{Al_xGa_{1-x}As} = -0.127 + 1.310x$ and $b_{In_xGa_{1-x}As} = 0.477$ [33]. AlGaAs is an example of rather exotic alloys where the parabolic approximation is considered not sufficient.

In Figure 2.2 values for E_g and a_0 which result from the given formulas are shown for various diamond and zincblende semiconductors and their alloys. One should especially note that the lattice constant of GaAs and AlAs are nearly identical with a misfit of 0.33 % at 0 K and 0.23 % at 900 K, which is typically the maximum temperature heterostructures are exposed to during fabrication by molecular beam epitaxy. When compared with the misfit of InAs on GaAs of 6.74 % (independent of temperature in this range), nanostructures based on AlGaAs can be described as strain-free.

It can be seen that AlAs and its Al-rich alloys are indirect semiconductors. AlGaAs becomes indirect with an Al molar fraction of more than 0.38 [33]. As only molar fractions of up to 0.33 are relevant for in this thesis, the theory of indirect semiconductors is not relevant to this work.

2.1.2 The GaAs(111) surface

Zincblende GaAs can be grown in many different orientations. The most commonly used wafer surface of GaAs is (100) and growth on this surface has been characterized exhaustively [41]. Growth on higher-index surfaces such as (111)A/B has also been investigated, although to a lesser amount [42, 43], and further investigations are still actively performed [19, 40, 44]. This is due to the narrower window of smooth layer growth on these surfaces (see Figure 2.3) and the related stricter demands on parameter control. In this section the structural difference between the (100) and (111) surfaces, which make growth on this surface attractive despite the difficulty, will be elaborated.

A sketch of the GaAs unit cell including these planes is shown in Figure 2.4. The (111)A and (111)B surfaces, also called (111) and $(\bar{1}\bar{1}\bar{1})$, only differ structurally by the atomic species which terminate the surface. (111)A surfaces are terminated by Ga atoms and (111)B by As atoms. Therefore the

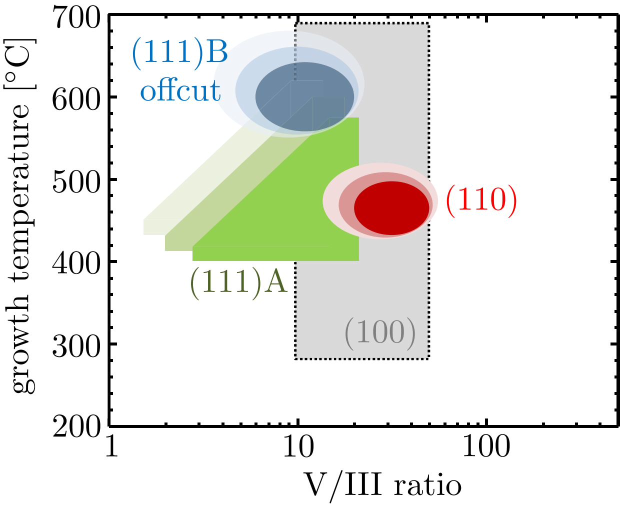

Figure 2.3: Growth parameter windows for molecular beam epitaxy of smooth GaAs layers on GaAs substrates of different orientations. Contours of increasing intensity show how growth conditions improve surface roughness. This plot was adopted from [40].

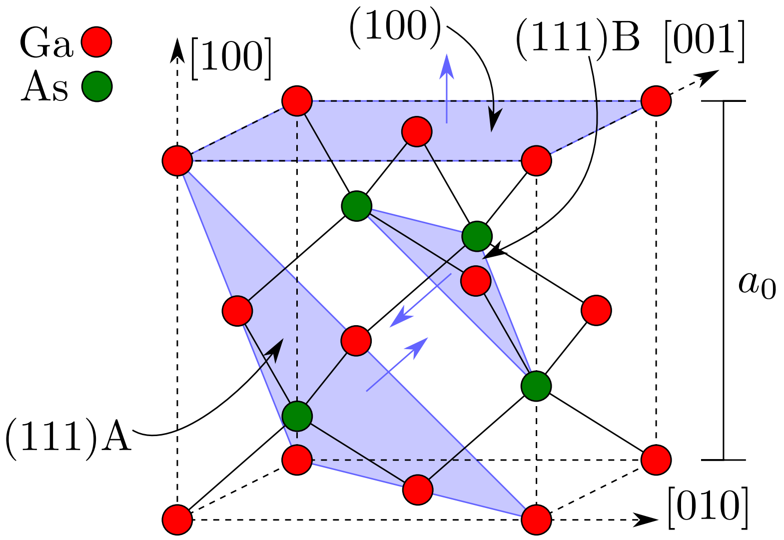

Figure 2.4: GaAs unit cell with highlighted (100), (111)A and (111)B surfaces. The blue normal vectors on the planes signify the direction where no crystal would be present if they were surface planes. The atoms in the blue planes would then be surface atoms.

chemical behavior of both planes is, for example during growth and etching, not the same [45]. In the shown unit cell two monolayers (ML) of GaAs can be seen in [100] direction and a total of three ML lies in between diametrically opposed edge Ga atoms in [111]. Therefore one can easily calculate that the ML thickness in [100] is

$$a_0 = 2\,\mathrm{ML} \quad \Leftrightarrow \quad 1\,\mathrm{ML} = \frac{a_0}{2} \approx 2.8\,\text{Å}$$

and in [111] is

$$\sqrt{3a_0^2} = 3\,\mathrm{ML}_{(111)} \quad \Leftrightarrow \quad 1\,\mathrm{ML}_{(111)} = \frac{a_0}{\sqrt{3}} \approx 3.3\,\text{Å} \quad .$$

As the 3D density of atoms in a crystal is independent on its surface one can see that the (111) surfaces must have a higher 2D atom density with a ratio of $2/\sqrt{3}$ to the 2D density on (100) which is $6.26 \times 10^{14}\,\mathrm{cm}^{-2}$. Obviously this also impacts growth and etching mechanisms on these surfaces.

ML values are convenient units to denote layer thickness. Deposition rates and fluxes are often given in units of ML/s where for instance a Ga deposition rate of 1 ML/s is equivalent to the flux of Ga atoms which is necessary for the growth of 1 ML GaAs per second. For a unity sticking coefficient this is $1\,\mathrm{ML/s} = 6.26 \times 10^{14}\,\mathrm{cm}^{-2}\,\mathrm{s}^{-1}$.

For better visualization of the (111)A/B surfaces the crystal is projected onto the $(1\bar{1}0)$ plane in Figure 2.5. One can see how the cleaving planes through the crystal are chosen so that only one bond in the bulk crystal is broken. Any alternative, where three bonds per atoms would be severed, is unstable [46]. Therefore exactly these two variants can be observed as (111) surfaces. This is also the reason why the backside of a monocrystalline substrate with a (111)A surface is always expected to be a (111)B surface.

When the (100) and (111)B surfaces are viewed from top (Figure 2.6) it is apparent that the (100) surface exhibits a 180° rotational symmetry as well as two mirror symmetry axes (also called C_{2v}). The (111) surface

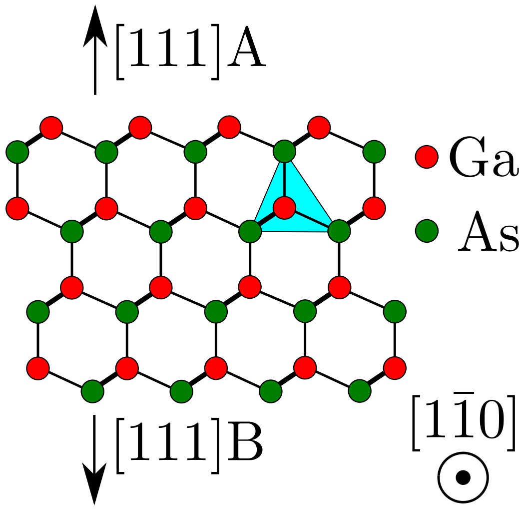

Figure 2.5: Projection of GaAs crystal on $(1\bar{1}0)$ plane. Thicker connection lines signify a bond to another As atom which then completes the highlighted, tetragonal primitive unit cell.

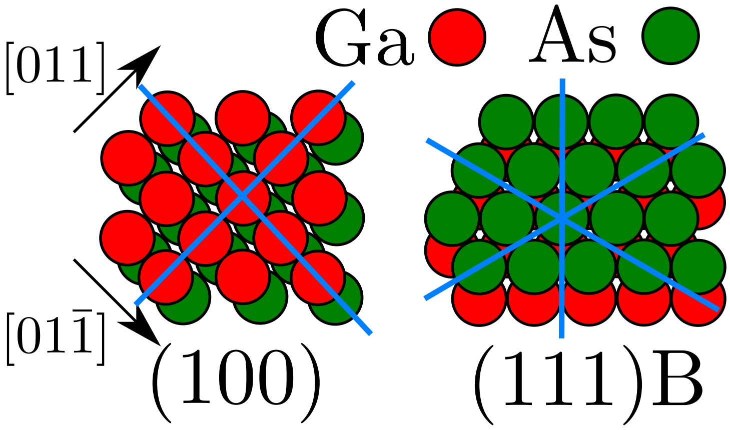

Figure 2.6: (100) and (111)B surface MLs of GaAs viewed from normal direction. Note the higher rotational symmetry and the additionally highlighted mirror symmetry plane of the (111)B surface.

exhibits a 120° rotational symmetry and three mirror symmetry axes, which conforms to the C_{3v} symmetry group [47]. Especially the asymmetry on the (100) surface along the [011] and $[01\bar{1}]$ directions results in an anisotropic diffusion constant for adatoms during epitaxial growth on this surface. In the real system this is, of course, not directly due to diffusion on the shown unreconstructed surfaces but on surface reconstructions which obey the 2D group symmetries shown here [48, 49].

In addition to an anisotropic growth process, unwanted anisotropy in heterostructures grown on a GaAs(100) substrate are incentives to develop the fabrication of nanostructures on GaAs(111) substrates. Properties which show a higher symmetry on GaAs(111) include piezoelectric fields [13] and electron-hole exchange interaction [50]. In section 2.3.3 the implications of substrate symmetry will be further discussed for the specific case of semiconductor QDs.

2.2 Epitaxy

Epitaxy is the growth of a crystalline layer on a crystalline substrate where the crystal structures of the layer are oriented with respect to the substrate [52]. The thermodynamic driving force of crystallization is the chemical potential between the source phase (gaseous or liquid) and the crystallized phase. It depends on a multitude of growth parameters such as ambient temperature, pressure and different material properties. Due to the special properties of semiconductors expounded in section 2.1 the field of semiconductor epitaxy is of special interest in general and in this thesis in particular. Commonly applied semiconductor epitaxy techniques are liquid-phase epitaxy [53], metalorganic vapor-phase epitaxy (MOVPE) [54] and molecular beam epitaxy (MBE) [41]. In this thesis only MBE was applied and its general working principle will be detailed in section 2.2.3.

Epitaxy can be modeled using thermodynamics and atomistic-kinetic models. A thermodynamical approach is presented in the next section to categorize epitaxial growth modes. In the following an abridged kinetic model will be described. A more sophisticated approach can be found in the review paper by Levi and Kotrla [55] or in the book by Pimpinelli and Villain [56].

During epitaxy atoms from the source phase reach the substrate and are

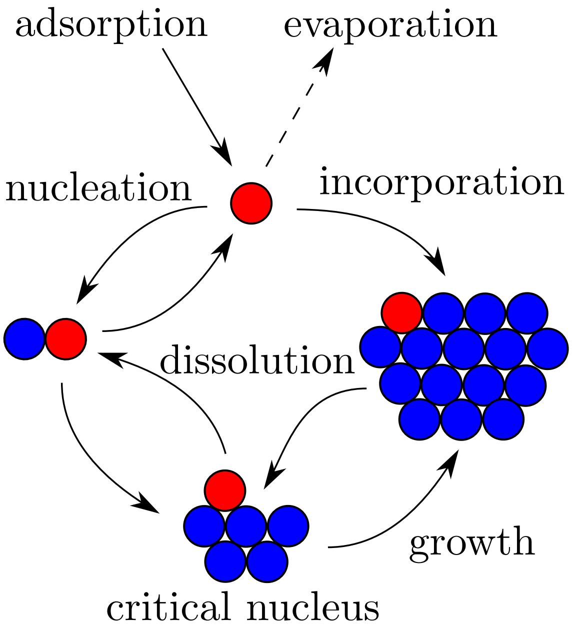

Figure 2.7: Competing atomistic processes of an adatom during epitaxial growth. Sketch reproduced after [34, 51].

adsorbed without forming a chemical bond. Figure 2.7 shows competing atomistic processes these adatoms can be subjected to. The adsorption rate is controlled by the surrounding source material (such as the flux of a vapor phase or concentration in a liquid phase) while the probabilities for nucleation of a 2D nucleus, re-evaporation, incorporation and dissolution are subject to a variety of parameters. These include the substrate temperature, density of adatoms and material properties such as the adatom surface diffusion (which again depends on a variety of parameters). The probability of thermally activated processes (diffusion, re-evaporation, dissolution ...) can typically be described by an Arrhenius equation

$$P_i = P_{i,0} \exp\left(-\frac{\mathit{\Delta} E_i}{k_B T}\right) \quad , \tag{2.2}$$

where P_i is the probability of process i, $P_{i,0}$ its probability constant, $\mathit{\Delta} E_i$ the activation energy of the process, k_B Boltzmann constant and T the temperature. In the specific case of the surface diffusion of an adatom the diffusion constant D follows the same equation

$$D = \nu \exp\left(-\frac{E_d}{k_B T}\right)$$

with the surface diffusion activation energy E_d and the vibrational frequency [57]

$$\nu = \frac{2k_B T}{h} \quad , \tag{2.3}$$

where h is the Planck constant. The diffusion length l can then be calculated via Einstein's formula

$$l = \sqrt{D\tau} \quad , \tag{2.4}$$

where τ is the mean time of surface diffusion until an adatom reevaporates, nucleates or is incorporated. l is a decisive variable during epitaxy in general and the formation of self-assembled 3D nanostructures in particular as it is very closely related to their surface density [58]. With rising l the distance between forming nanostructures can also rise which decreases the surface density.

The described system and its rate equations are already quite complex, although these considerations neglect the important contributions of surface reconstructions, dislocations, interdiffusion and more complex chemical reactions. Accordingly the inclusion of these effects in the model is beyond this thesis. The presented considerations can nonetheless be employed for the interpretation of epitaxial growth processes [59] by acknowledging e.g. that a higher T generally results in increased diffusion if no change in reconstruction (or chemical reactions or ...) is involved.

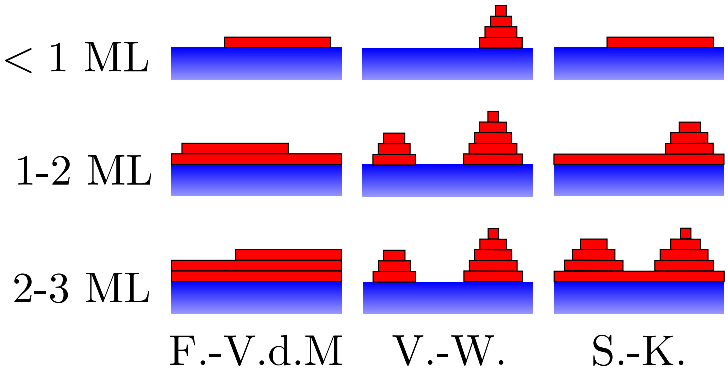

Figure 2.8: Illustration of the three epitaxial growth modes with different coverages in units of ML. The blue colored material is the substrate and the nucleating, deposited crystal is colored in red.

2.2.1 Epitaxial growth modes

The initial stage of layer deposition during heteroepitaxy on smooth substrates can be categorized into three different growth modes due to thermodynamic considerations [34]. The modes are schematically shown in Figure 2.8. Which of these modes actually manifests depends on the ambient-substrate surface tension γ_{as}, nucleus-substrate surface tension γ_{ns} and ambient-nucleus surface tension γ_{an}. If

$$\gamma_{as} \geq \gamma_{ns} + \gamma_{an}$$

two-dimensional nuclei will form on the substrate and coalesce to complete layers. The crystal is deposited in a layer-by-layer manner which is called the Frank-Van der Merve (F.-V.d.M.) growth mode [60]. This growth mode is typically desired in epitaxy as it provides smooth planar growth. If

$$\gamma_{ns} \geq \gamma_{as} + \gamma_{an}$$

the nucleus does not wet the substrate and disjunct islands form on the surface in the Volmer-Weber (V.-W.) growth mode [61]. Ultimately these islands can also coalesce but typically form a severe dislocation network in the process. This growth mode is employed to fabricate self-assembled 3D nanostructures which are completely disconnected from each other. One example of this is the droplet epitaxy method further detailed in section 2.3.2. The intermediate Stranski-Krastanov (S.-K.) [62] growth mode describes the case when the criterium for F.-V.d.M. is valid for a critical thickness of a few ML of deposited material and then becomes invalid in favor of the V.-W. criterium. A typical trigger for such a change would be the accumulation of strain energy during the pseudomorphic growth of a layer with a nonzero misfit to the substrate. This layer-plus-island growth is widely used to fabricate self-assembled 3D nanostructures, especially InAs QDs on GaAs(100).

2.2.2 Misoriented substrates and step-flow growth mode

When the substrate surface is not perfectly aligned with a low-index crystal plane (abc) but misoriented by a small angle φ towards another plane (xyz) ML steps emerge on the surface. This introduces additional kinks and thus massively increases the possible sites where adatoms can be incorporated into the crystal. If the diffusion length l of the adatoms on the terraces is large compared to the terrace width between steps w, 2D nucleation is suppressed and the crystal grows only by adatom incorporation at the step sites. This is called step-flow growth mode. The growth mode is schematically shown in Figure 2.9. Misoriented substrates and the step-flow growth mode are used to extend the parameter window of smooth growth by circumventing any problems involving 2D nucleation of new layers. Further applications include the fabrication of low-dimensional nanostructures such as magnetic and atomic wires suitable for transport at the steps [63] but will not be discussed here. There are three mayor disadvantages: An additional roughness introduced by the steps. The introduction of a new surface anisotropy between the direction of misorientation [xyz] and perpendicular to it. Emerging instabilities of the step-flow growth mode itself.

The new surface anisotropy arises from an energy barrier which hinders

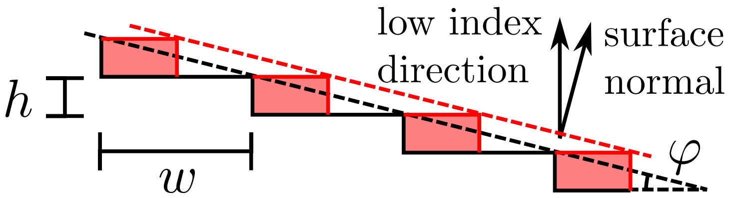

Figure 2.9: Illustration of the step-flow growth process on a substrate with a misorientation of φ. The movement of steps due to the deposition of material equivalent to $h/2$ planar deposition is indicated in red.

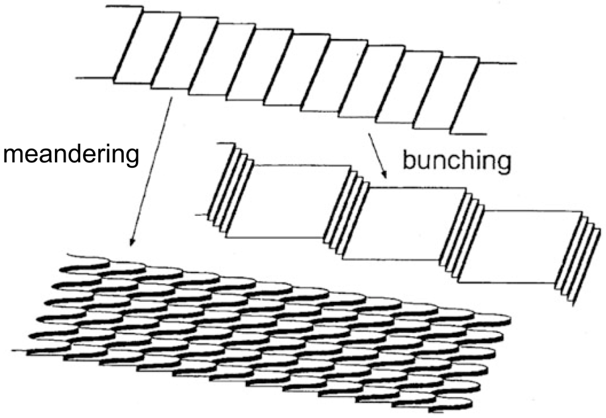

Figure 2.10: Illustration of the different instabilities of the step-flow growth mode (taken from [59]).

diffusion between terraces over steps (along [xyz]) and a potential sink which promotes it along the steps (perpendicular to [xyz]). These properties of vicinal surfaces are known as Ehrlich-Schwöbel barrier (and the related step-Ehrlich-Schwöbel effect) [64, 65] and kink-Ehrlich-Schwöbel effect [66], respectively.

Instabilities of the step-flow growth mode

In Figure 2.10 the results of two instabilities of the step-flow growth mode are shown.

The step bunching instability reinforces small fluctuations in terrace widths and creates regions of high step density which are separated by large terraces. The instability results from a negligible Ehrlich-Schwöbel barrier as will be motivated in the following. When a strong barrier is present the rate of step advancement r_{step} is proportional to the width of its lower terrace w_{lower} as adatoms from the upper terrace, with width w_{upper}, can not diffuse down and contribute to its growth. Consequently smaller fluctuations of the terrace width are removed because a step with a smaller lower terrace will move slower until all terraces are equidistant again. When no barrier is present $r_{\text{step}} \propto (w_{\text{upper}} + w_{\text{lower}})$ is valid so that the speed of a step will not change if it randomly lags behind slightly. This situation is unstable because the next lower step will accelerate and the upper step will decelerate which amplifies the random fluctuation and forms step bunching.

The Bales-Zangwill instability [67], also called step meandering, results from small fluctuations in the step curvature which are strengthened further to form long-range periodically curved steps. The mechanism which leads to the instability is shown schematically in Figure 2.11. If a strong Ehrlich-Schwöbel barrier exists so that only the lower terrace contributes to the movement of a step, segments of the step which are curved into the upper surface have a smaller effective adatom collection area and thus advance more slowly. The opposite is true for segments curved into the lower terrace. The strength of this effect increases with increasing curvature. The periodic modulation of r_{step} propagates through surrounding straight steps so that the step curvatures align to each other and form one periodic, aligned pattern. A negligible Ehrlich-Schwöbel barrier would restore the symmetry of the system so that upper and lower terraces equally contribute to step advancement and the mentioned instability vanishes. This instability is suppressed if the curvature periodicity is small compared to the 1D diffusion length along the steps which is increased by the Kink-Ehrlich-Schwöbel effect.

The properties of misoriented substrates and the related step-flow growth mode, which are addressed in this section, show that the slight misorientation of a substrate, on which the deposition of smooth layers is very unlikely on-axis, can enlarge the viable growth parameter window. Doing this, however, introduces new effects and instabilities during growth which have to be

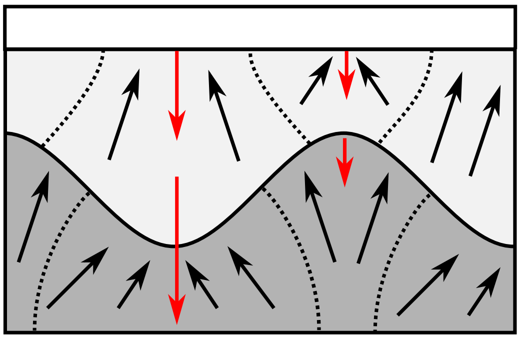

Figure 2.11: Schematic of the Bales-Zangwill instability where the steps are moving from top to bottom. The effective areas which contribute to the advancement of step parts with different curvatures are marked. Black arrows signify the adatom flow and red arrows the magnitude of r_{step}. Note that the curvy as well as the straight step show the same modulations in r_{step}. This leads to long-range alignment of the curvature.

scrutinized. Of special concern in this thesis is the introduced asymmetry along and parallel to the steps.

2.2.3 Molecular beam epitaxy

MBE is an epitaxy technique far from thermodynamic equilibrium which is preferred to other techniques when atomically sharp interfaces and a high control of growth rates, compositions and material purity is desired. It was developed by Arthur [68], LePore [69] and Cho [70] for III/V semiconductors in late 1960. MBE revolutionized the semiconductor field, particularly in the scientific area, by allowing the fabrication of tunnel barriers, quantum wells, resonant tunneling devices and superlattices with high precision for the first time [71]. The major disadvantage of MBE compared to other techniques is a slow growth rate in the order of $1\,\mathrm{\mu m\,h^{-1}}$ [72]. The molecular beams, this technique is named after, are generated by thermal heating of source material in effusion cells. Within these beams molecules travel towards the sample without any interaction. To maintain these beam characteristics, the pressure of atoms in the beam, as well as the base pressure in the system, have to be well in the high vacuum regime ($\leq 1 \times 10^{-4}\,\mathrm{mbar}$) [72]. The base

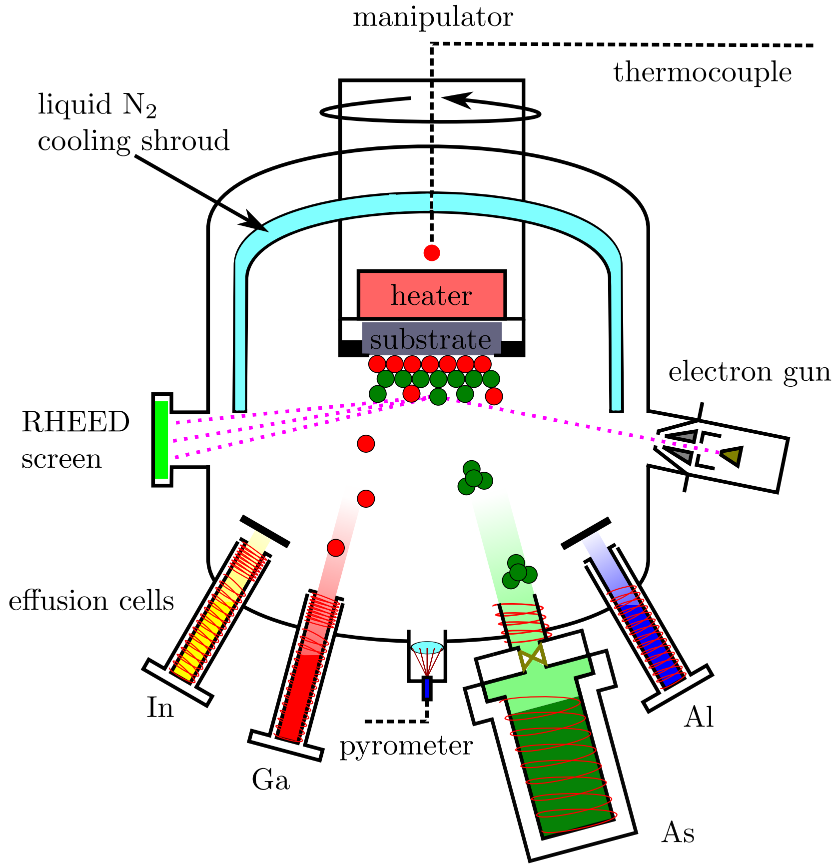

Figure 2.12: Sketch of a vertical MBE growth chamber for group III arsenides during deposition of GaAs.

pressure of the system has to even be in the ultra high vacuum (UHV) range ($<1 \times 10^{-9}$ mbar) to prevent severe contamination of the grown structures with foreign atoms. For critical contaminants like carbon-containing molecules $<1 \times 10^{-11}$ mbar partial pressure is required [41]. This is directly due to the low growth rates and especially critical during long pauses in material deposition where unintentional δ-doping can occur. To achieve and maintain UHV in the growth chamber a multitude of vacuum pumps as well as cooling shrouds have to be employed. Greatest possible care is required when opening the chamber to ambient air during maintenance and when introducing new substrates and material to the system.

During the MBE process, a single or multiple beams deposit adatoms which react with each other and the substrate surface to form an epitaxial layer according to the mechanisms explained in the previous section 2.2. In Figure 2.12 an arsenide MBE growth chamber is schematically shown during GaAs deposition. There are different designs to heat the substrate and measure the temperature. A radiative heater with a thermocouple in close vicinity and a pyrometer, as shown in the sketch, are common combinations. This varies with varying substrate materials depending on their light absorption behavior. The UHV environment allows the use of electron-beam based diagnostic tools such as reflection high-energy electron diffraction (RHEED), low-energy electron diffraction or Auger electron spectroscopy. Especially the highly surface sensitive RHEED system is an important tool to characterize the sample surface during epitaxy and regulate growth parameters accordingly. Therefore almost every MBE system includes RHEED.

Parts such as a substrate shutter in front of the sample holder or a beam flux measurement device, which are included in every MBE system but are not necessary for the basic working principle, are not shown in the sketch. These and other specifics of the MBE system, which has been used to fabricate the samples investigated in this thesis, are presented in section 3.1.

2.3 Quantum dots

Due to quantum mechanics the confinement of a particles movements leads to quantization of its motion. This can be qualitatively motivated by the Heisenberg uncertainty principle. An example for such a system is an electron located in the conduction band of a semiconductor which is surrounded by another semiconductor with higher conduction band energies (or an insulator). If the heterojunction between both semiconductors is of type 1, an electron in the conduction band as well as a hole in the valence band can be confined in their motion. In this case one speaks of a semiconductor quantum well (QW), quantum wire or quantum dot (QD) for 1D, 2D and 3D confinement,

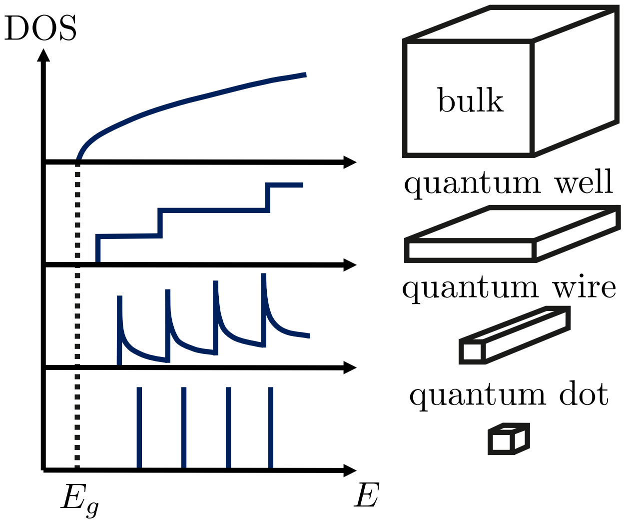

Figure 2.13: Density of states of an electron gas confined in zero to three dimensions and the respective nanostructures. Note that with increasing confinement the energy of the lowest state differs increasingly from E_g by the zero-point energy.

respectively. The density of states for confined electrons is schematically shown in Figure 2.13 for each case. The quasi-zero-dimensional QDs are of special interest because of their energetically completely discretized electronic states similar to the states of an atom. They are thus also frequently called artificial atoms [73]. An important difference to natural atoms is the possibility to control the energy levels of QDs by choosing the semiconductor material composition, size and morphology. Theoretically this allows the realization of different confinement potentials, e.g. simple rectangular or parabolic, with a specific emission/absorption energy range on demand.

For the quantization effect to be relevant, the zero-point energy (or confinement energy) has to exceed the thermal energy associated to motion in the confinement direction. The charges thus have to at least be confined to a region in the range of the De Broglie wavelength for thermal motion

$\lambda_{\text{de Broglie}}$ of the relevant charge carriers

$$\lambda_{\text{de Broglie}} = \frac{h}{\sqrt{3m^* k_B T}}$$

with Planck constant h, the effective mass m^*, Boltzmann constant k_B and temperature T [74]. For GaAs this would be 24 nm at room temperature (300 K), 47 nm at the temperature of boiling nitrogen (77 K) and 203 nm at the temperature of boiling helium (4.2 K) with the values from Table 2.1. Due to these typical length scales, semiconductors with quantized energy levels, especially QDs, are in the domain of nanostructures. They could only be realized with advances in nanotechnology as will be detailed in the next section.

2.3.1 Fabrication techniques

QDs can be fabricated by a multitude of different techniques. The first QDs, which had demonstrably discretized energy levels, were produced in the 1980s by electron-beam lithography of a MBE-grown InGaAs quantum well and had a lateral size of 100-250 nm [75, 76]. Further refinements in this approach lead to GaAs QDs with laterals sizes around 50 nm [77]. In a closely related technique, the same base structures (MBE-grown QWs) can be processed to QDs by only performing lithography on metallic contacts on the sample surface and not etching the optically active semiconductor itself [78]. The in-plane confinement of the carriers is in this case not affected by another confining material but by the modulated electric potential due to the patterned contacts. A third method to fabricate QDs with a lateral size down to 300 nm from QWs employs laser-induced local interdiffusion of the QW material with the surrounding matrix material [79]. As the energy levels in treated parts of the QW are higher, untreated QW regions become QDs. QDs manufactured by these methods are of higher optical quality due to the absence of etching-related defects in the optically active region. The expounded techniques are called top-down processes because the already-grown structures are post-processed introducing the full 3D confinement. Advantages of top-down processes are that QDs can be positioned on demand and with high control. The main disadvantage is that QDs have to be fabricated one-by-one making the production of higher QD numbers very inefficient and expensive.

Bottom-up approaches, on the other hand, grow confined nanocrystals directly on prepatterned substrates [80] or use self-organization in a multitude of systems. Especially the self-organized growth techniques allow the fabrication of many QDs simultaneously without individual preparation and are thus of vast interest for scientific and technological applications [81]. An early experiment in the fabrication of self-assembled QDs involved silicate glass with about 1 % semiconductor material dissolved during its synthesis [82]. During long annealing of these silicate samples, cadmium sulfide crystals with sizes down to 1.2 nm could be fabricated. Even earlier the synthesis of similar QDs (in that time called microcrystals) via colloidal chemical techniques from a solution was performed [83]. These QDs, which are not surrounded by another semiconductor on a substrate, are nowadays very attractive fluorescents because of their narrow emission spectra, stability against photobleaching and the possibility to tune their emission wavelength by changing their size [84] and are used in biology [85], display technology and lighting [86]. Note that the mentioned fabrication techniques do not employ a substrate and thus do not use epitaxy.

Examples of epitaxial self-assembled QD growth techniques include the growth of a very thin QW where the ML thickness fluctuations provide a 3D confinement so that thicker parts of the QW are QDs [87]. Also cleaved edge overgrowth [88] where multiple MBE growth runs are combined with *in situ* cleaving of a multilayer sample is used to generate QDs.

A highly successful technique is the fabrication of coherently strained InAs QDs on GaAs(100) in the Stranski-Krastanov growth mode (see section 2.2.1) pioneered in 1994 [89–91]. This strain-driven technique allows the fabrication of high-quality QDs with densities in the range of 10^8-$10^{11}\,\mathrm{cm}^{-2}$ depending on the growth parameters only by deposition InAs on GaAs without any pre- or post-processing. Due to the S-K growth mode the QDs are, however, not completely enclosed by the substrate and overgrowth material but all QDs are connected by a thin QW which is called wetting layer. The technique can be extended to $\mathrm{In}_x\mathrm{Ga}_{1-x}\mathrm{As}$ QDs with down to $x = 0.44$ [92] and other material combinations such as silicon-germanium on silicon or gallium nitride on silicon carbide [93]. This technique is well established in our group and recent results can be viewed in the thesis of Nand Lal Sharma [94].

As the generation of QDs by this method is strain-driven it can generally not be employed to fabricate strain-free QDs or to produce QDs on surfaces which feature strain relaxation processes that inhibit the strain-energy build-up characteristic for S-K growth. An example for such a behavior is the deposition of InAs on the GaAs(111)A/B surface, where an increased intermixing, promoted by the surface reconstruction, and formation of dislocations relax strain [14, 95]. An alternative technique which is not subjected to these inhibitions is droplet epitaxy (DE). This technique is used for QD fabrication in this thesis and will thus be explained in detail in the following section.

Based on DE the local droplet etching (LDE) technology was developed by Wang in 2006 [96]. LDE utilizes the etching of group III droplets into III-V substrates at high temperatures to fabricate self-assembled nanoholes. In contrast to DE, the droplet deposition is not performed in the regime of complete condensation but with considerable re-evaporation. The nanoholes are subsequently filled with a lower band gap material to fabricate QDs. This technology has been employed successfully in the recent past [97] and, even though not used in this thesis, it is being used in our group [98].

In an example for selective area epitaxy [99], where a substrate is partially masked during epitaxy to enable site-control, DE through a shadow mask is also employed as an ongoing research endeavor in our group [100, 101].

2.3.2 Droplet epitaxy

In contrast to Stranski-Krastanov QD fabrication, DE grows QDs in a Volmer-Weber-like growth mode [102]. Both methods share the advantage of using the formation of nanostructures by the atomic rearrangement of homogeneously deposited material without any need for nanopatterning before or after. In DE this is achieved by first depositing a group III element which forms droplets due to surface tension and subsequently crystallizing these droplets by a group V element flux. The driving force for self-organization in DE is thus not strain but the minimization of surface energy. As a result this technique is applicable to strain-free material systems and systems where strain is relaxed through mechanisms different from S-K. Due to its basic working principle DE is limited to III-V semiconductors and MBE or MOCVD [103].

The application of this method was first published by Koguchi and Ishige in 1993 [104] but it required a sulfur-termination process detrimental to the optical quality of resulting QDs. In 2000 the modified droplet epitaxy method, which does not require the sulfur-termination anymore, was published by Watanabe, Koguchi and Gotoh [105]. This technique has largely replaced the prior DE method so that modern literature often omits the "modified". In this thesis only modified droplet epitaxy is detailed as well as used and will for the sake of simplicity be just called DE. Despite the early development this method has only recently received worldwide attention [106]. This delay is due to the simultaneously developed S-K QD fabrication on which many resources of the scientific community were focused.

A detailed, theoretical description of the droplet epitaxy process based on kinetic Monte Carlo simulations with subsequent experimental validation was reported by Reyes *et al.* [107].

In Figure 2.14 the DE process is illustrated with the fabrication of GaAs QDs in an AlGaAs matrix as an example for better legibility instead of a general group III - group V. This is interchangeable with different combi-

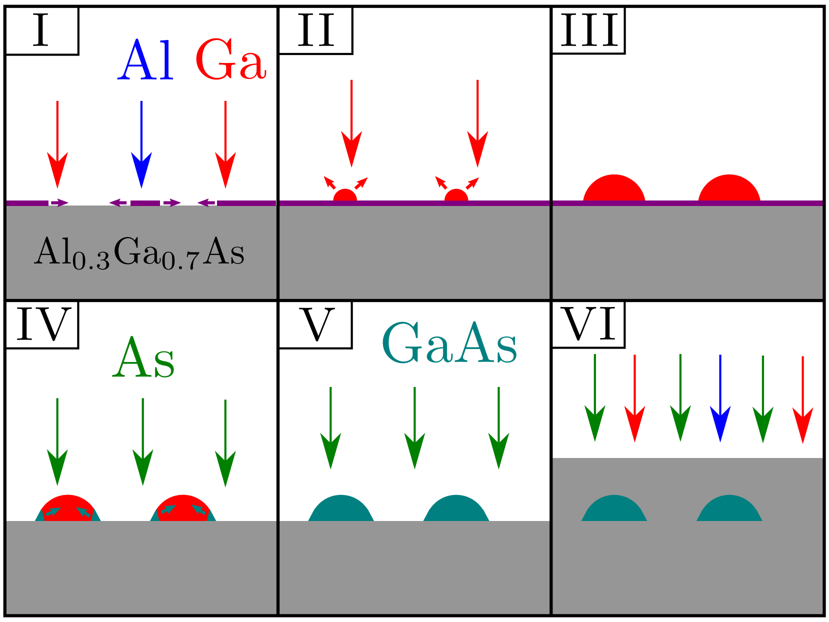

Figure 2.14: Illustration of the droplet epitaxy process and its different steps. As an exemplary material system the fabrication of GaAs QDs in an AlGaAs matrix, which is also performed in this thesis, is shown. The purple line signifies a group-III-rich surface of the AlGaAs whereas an absence of this line signifies a group-V-rich surface.

nations of III-V compounds including nitrides [108], phosphides [109] and antimonides [110]. The process can be divided into six different steps:

I. Deposition of a small amount of AlGa with the same composition as the substrate material (without As) at droplet deposition temperature T_{dep}. This step is important when the sample has been prepared in an As-rich environment and thus features a reconstruction with excess As. When pure group III material is then deposited, the first small amount immediately crystallizes as a thin homogeneous layer. This would form a quantum well similar to the wetting layer in S-K QD fabrication if Ga was deposited. This is typically not desired.

II. Deposition of a specific amount d of Ga with rate r_{Ga} at T_{dep} which forms liquid droplets on the sample surface. During this step the areal

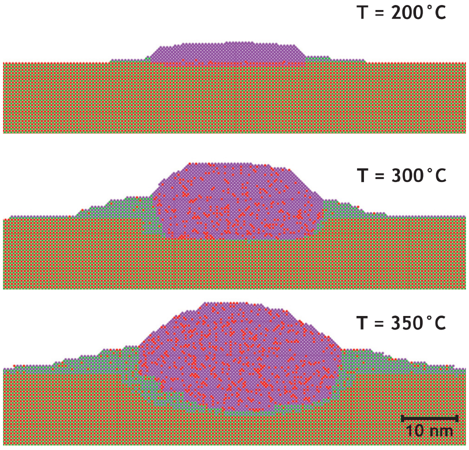

Figure 2.15: Simulation results of Ga droplet deposition on GaAs(100) with $r_{\mathrm{Ga}} = 0.1$ ML/s and $d = 4.0$ ML at different T_{dep} without previous surface saturation step (taken from [107]). Material initially belonging to the substrate is colored red (Ga) and green (As), Ga deposited during the step is colored purple. It can be seen that with rising T_{dep} the droplets become bigger and etch deeper into the substrate. The size increase of the droplets is due to a lower droplet density at higher T_{dep} and material conservation. The etching is, again, a thermally activated process which obeys Arrhenius law.

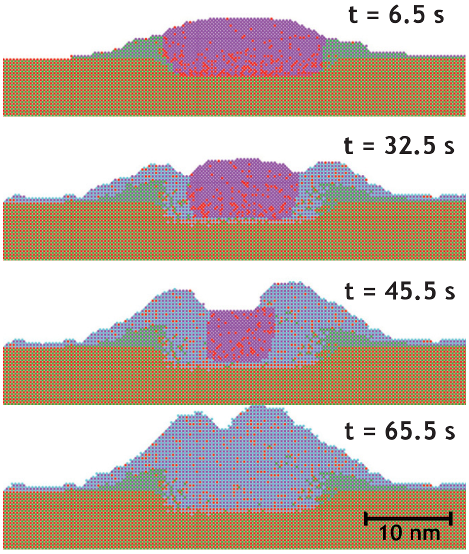

Figure 2.16: Simulation results of Ga droplet crystallization on GaAs(100) with $T_{\mathrm{As}} = 275\,°\mathrm{C}$ and arsenic flux corresponding to a GaAs growth with 0.06 ML/s at different times t (taken from [107]). Material initially belonging to the substrate is colored red (Ga) and green (As), when deposited during the DE process is colored purple (Ga) and blue (As). It is easily visible that crystallization starts at the droplet edges and proceeds to its center. The small amount of droplet material covering the substrate around the nanostructure is due to a wicking effect of the As covered substrate.

droplet density n is decided. The parameter with the highest impact on n is T_{dep} because a higher value, on the one hand, decreases the probability of formation of a stable droplet nucleus by promoting its dissolution and, on the other hand, increases the Ga adatom diffusion constant according to Arrhenius law. The influence of r_{Ga} on n is due to a higher Ga adatom density at faster r_{Ga} which promotes nucleation and thus increases the surface density. d, in conjunction with n, decides the size of the droplets. As an additional effect, temperature-dependent intermixing of the droplet material with the crystalline substrate due to droplet etching, as shown in Figure 2.15, can occur at higher T_{dep} during this step.

From classical nucleation theory [51] the density of stable 3D nuclei can be calculated as

$$n \propto r_{\mathrm{Ga}}^{p_n} \exp\left(\frac{E_n}{k_B T_{\mathrm{dep}}}\right) \quad . \tag{2.5}$$

Note that this is not a thermally activated process which obeys Arrhenius law as the exponent is positive: A rising E_n leads to a larger n and a lower T_{dep} leads to more nuclei. For complete condensation, which is the case when no material is desorbed after adsorption (typically the case during DE), the nucleation parameters p_n and E_n are

$$p_n = \frac{i}{i + 2.5} \quad ; \quad E_n = \frac{E_i + iE_d}{i + 2.5} \quad ,$$

where i is the number of atoms in a stable nucleus and E_i its energy. DE typically takes place in the regime of complete condensation. At higher T_{dep} Ostwald ripening further decreases the droplet density. In this case also the deposition time $t_{\mathrm{dep}} = \frac{d}{r_{\mathrm{Ga}}}$ becomes relevant as ripening time. Heyn et. al. [111] proposed an extended scaling law based on classical nucleation theory which also includes Oswald ripening to calculate n as

$$\begin{aligned} n &\propto r_{\mathrm{Ga}}^{p_n}\left[\nu^{-1}\exp\left(\frac{E_n}{k_B T_{\mathrm{dep}}}\right)^{-1} + t_{\mathrm{dep}}\exp\left(\frac{E_n+E_r}{k_B T_{\mathrm{dep}}}\right)^{-1}\right]^{-1} \\ &= r_{\mathrm{Ga}}^{p_n}\left[\frac{h}{2k_B}\frac{1}{T_{\mathrm{dep}}}\exp\left(\frac{E_n}{k_B T_{\mathrm{dep}}}\right)^{-1} + t_{\mathrm{dep}}\exp\left(\frac{E_n+E_r}{k_B T_{\mathrm{dep}}}\right)^{-1}\right]^{-1} \end{aligned} \tag{2.6}$$

with Ostwald ripening energy E_r. This is basically the weighted harmonic mean of the classical nucleation scaling law (equation 2.5) with an additional Ostwald ripening scaling law, where the weights are t_{dep} in the order of seconds and $\nu^{-1} \approx 80\,\mathrm{fs}$ at room temperature. Please note that the relevant ripening time is actually the deposition time disregarding any pauses as has been explicitly stated by Heyn et al.

III. Lowering of the sample temperature from T_{dep} to the crystallization temperature T_{As}. During this step density and size of the droplets stay largely constant. In case of a high T_{dep} or a very slow cooling non-negligible Ostwald ripening can occur.

IV. Droplet crystallization at T_{As} for a time t_{As} under a specific As flux r_{As}. In this step the shape of the individual nanostructure is decided. Figure 2.16 shows the time-evolution of a droplet which is then fully crystallized to a nanostructure. This would be a QD if it were not the same material as the substrate in this simulation. If one modulates the As flux during this step a multitude of nanostructures different from QDs, such as concentric multi-rings can be fabricated [112]. This is due to the fact that the epitaxial crystallization starts at the droplet edges and proceeds to the center so that an interruption leaves a crystallized outer ring with a smaller liquid droplet in the center. Because the surrounding substrate is no longer group III terminated, as it is after step I, liquid droplet material is wicked to the substrate and crystallizes there in a wide, thin layer around the nanostructure. This also happens without an interruption and, for e.g. QD fabrication, needs to be suppressed by a fast crystallization (higher As flux) or by suppressing diffusion (low temperature). If crystallization is promoted too strongly polycrystalline GaAs can nucleate on top of the droplet without connection to the substrate and thus enclose a liquid Ga core in crystallized GaAs. It is also possible that the crystallizing side walls enclose liquid Ga epitaxially. This is known in the theory of solidification of dilute binary alloys as Mullins-Sekerka instability [113]. During this step the density of nanostructures does not change as all droplets of remotely similar size perform the same transformation [111].

V. Heating the sample to annealing temperature T_{an} and holding it for annealing time t_{an} without interrupting As flux. This step is important to improve the crystalline and optical quality of the QDs which have been crystallized at low temperatures [114]. During this step liquid inclusions can crystallize due to increased diffusion of As through the crystalline shell or its intermediate dissolution. For higher T_{an} the QD morphology can change due to diffusion of GaAs on the QD to a thermodynamically preferential spot on the surrounding surface.

VI. Capping of GaAs QDs by AlGaAs. A thin layer of a AlGaAs is deposited at T_{an} to protect the QDs from disassociation once the substrate temperature is increased to standard growth temperature. After this step the DE process is complete and the remaining structure of the sample can be grown.

In contrast to the single-step S-K QD fabrication the multi-step DE process with its higher number of parameters is more complex to employ but allows the independent control of QD density, size, aspect ratio and faceting on a wider range of III-V material systems [115]. Particularly, the QD density can be controlled easily over a wide range in DE while the fabrication of S-K QDs in low densities homogeneously over a wafer is quite challenging [116].

A severe disadvantage of DE is the low crystallization temperature and the resulting bad crystal quality of the QD [117]. In addition to the annealing step directly after crystallization (step V) post-growth annealing *in situ* [118] as well as *ex situ* are commonly employed to counteract this [114]. Although advances improving the crystal quality have been achieved it is still judged as far from satisfactory and requires further efforts [106].

DE has already been employed successfully on the arsenide material system on (100)-, (112)- and (111)A-oriented GaAs substrates [16, 119]. On the (111)B surface, however, reports of DE are quite scarce so that the first accounting of strain-free GaAs/AlGaAs QDs on (111)B was published by the author [120]. Experimental results for the DE steps I-III will be reported in section 4.2, for steps IV-V in section 4.3 and for step VI in section 4.4.

2.3.3 Electronic structure and luminescence

The simplest model to describe the energetic states of an electron in a QD is the particle in a box model. The energies of allowed states of an electron, which is trapped in a rectangular box with edge lengths $L_{x/y/z}$ by an infinite potential, are known from basic quantum mechanics as

$$E_{n_x,n_y,n_z} = \frac{\hbar^2\pi^2}{2m^*}\left(\frac{n_x^2}{L_x^2}+\frac{n_y^2}{L_y^2}+\frac{n_z^2}{L_x^2}\right) \quad ,$$

where m^* is the effective mass and the quantum numbers $n_{x/y/z}$ are positive integers [121]. Although this is a primitive model for semiconductor QDs it qualitatively describes important properties such as discretized energy states, a nonzero energy of the lowest state due to confinement and an increase of the energy of all states when $L_{x/y/z}$ is reduced. It is also apparent that the smallest confinement length and the corresponding quantum number have the strongest impact on total energy.

While rectangular QDs can be fabricated (although with only finite potential barriers), self-assembled semiconductor QDs by S-K growth or DE are typically lens-shaped, pyramidal or truncated pyramidal [122]. The QD

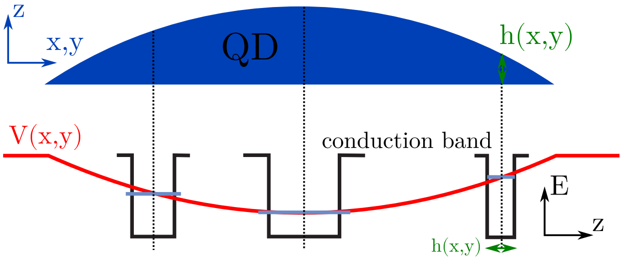

Figure 2.17: Illustration of parabolic confinement potential on in-plane wave function of a QD due to its lens-shape. In the shown case the separated confinement in z is strong enough to ensure that only the ground state is occupied in this direction.

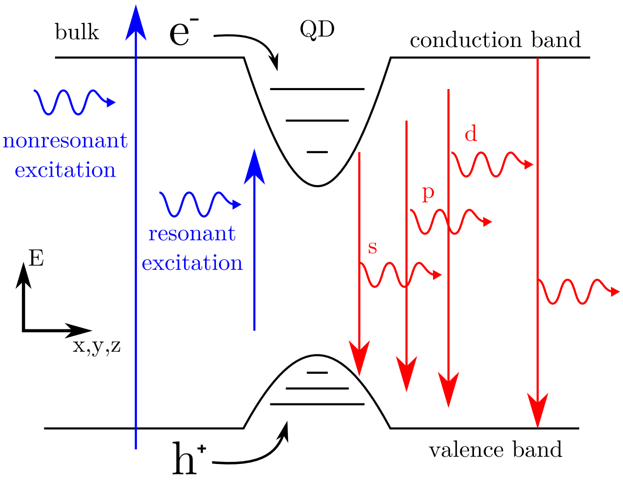

Figure 2.18: Schematic representation of processes during photoluminescence in a QD sample. Alternative decay paths e.g. via defects are omitted.

base width is typically a multitude of its height [123]. Realistic energy levels, including e.g. strain, have to be calculated numerically by using for example the $\mathbf{k} \cdot \mathbf{p}$ perturbation theory [124]. It has, however, been shown that the electronic wave function of a lens-shaped QD can be accurately described without numerics by a QD with parabolic confinement in-plane and an infinite potential in growth direction [125]. Figure 2.17 shows an illustration of the adiabatic approximation which allows the separated handling of in-plane and growth direction wave functions. Due to the high aspect ratio and the resulting strong confinement in z only the ground energy level in this direction is typically a bound state. The resulting discrete energy values in a lens-shape QD are thus those of the Fock-Darwin states of a 2D harmonic oscillator with an offset E_z

$$E_{n,l} = \hbar\omega_0(2n + |l| + 1) + E_z \quad ,$$

with radial and angular momentum quantum numbers n and l [126].

The processes in a QD with the elaborated electronic structure during a luminescence experiment are shown in Figure 2.18. Electrons and holes are created nonresonantly in the bulk material or resonantly in the QD itself. If created nonresonantly they thermalize to the respective band edges, diffuse along the sample and recombine either directly over the band gap or after capture by a defect or QD. In the QD they each relax to the lowest unoccupied state under phonon emission and recombine with emission of a photon with energy determined by the QD states. With lower probability recombination can also occur directly from higher-energy states. Selection rules resulting from angular momentum conservation allow the shown decay routes which are, analogous to atomic physics, indexed as s-, p-, d-, ... like. While at low excitation rates mostly s-like emission can be observed the higher-energy decay paths emerge for stronger excitation. This is a direct result from Fermi's Golden Rule, which (among other things) states that state transitions with smaller energy changes have a higher probability than those with larger energy changes [127]. As a result most electrons decay to the lowest unoccupied state in the conduction band before crossing it to the highest unoccupied state in the valence band. When the excitation rate is significantly higher than the decay rate of the ground state, this state becomes generally occupied and due to the Pauli exclusion principle the next-highest state becomes the lowest reachable one. Filling the QD states successively by a growing excitation rate, thus increasing the amount of electrons which recombine over the band gap from higher states, is called shell filling.

In single-dot experiments narrow emission lines with a Lorentzian line shape due to homogeneous broadening are expected instead of perfect lines as suggested by the discrete states in a QD. In ensemble measurements of multiple QDs simultaneously, variations in dot sizes (and thus confinement potentials) introduce an additional much larger inhomogeneous broadening. This is typically described with a Gaussian line shape if no better information on QD size distribution is available [128].

Fine-structure splitting of excitonic complexes

As electrons and holes are electrostatically charged they not only interact by recombination but also by Coulomb interaction. As a result an electron and hole may form a neutral exciton in which they are bound analogue to an electron and proton in a hydrogen atom. At low temperature the exciton emission replaces the free electron-hole recombination of the bulk semiconductor reducing the peak energy by the exciton binding energy of 4-40 meV for typical semiconductors [38]. In QDs the exciton binding energy strongly depends on the geometry and can be positive, negative and zero [129]. Similarly charged excitons with unequal numbers of electrons and holes as well as neutral biexcitons with two electrons and holes in one complex show a nonzero binding energy each. These excitonic complexes can be traced in luminescence experiments as split-offs from the basic s-shell emission.

Excitons which obey the mentioned selection rules for radiative recombination, called bright excitons, have a total angular momentum of 1. This can be realized by combining an electron with spin $\mp\frac{1}{2}$ with a heavy hole with angular momentum $\pm\frac{3}{2}$ to form excitons denoted with $|\pm1\rangle$. According to the previously calculated electronic structure, bright excitons share the same recombination energy (are degenerate) and emit left- and right-handed circularly polarized photons (σ_+ and σ_-), respectively. The biexciton recombination cascade, as illustrated in Figure 2.19, thus emits first a photon with less energy (assuming positive biexciton binding energy) when decaying from the biexciton XX to one of the bright exciton X states. The exciton

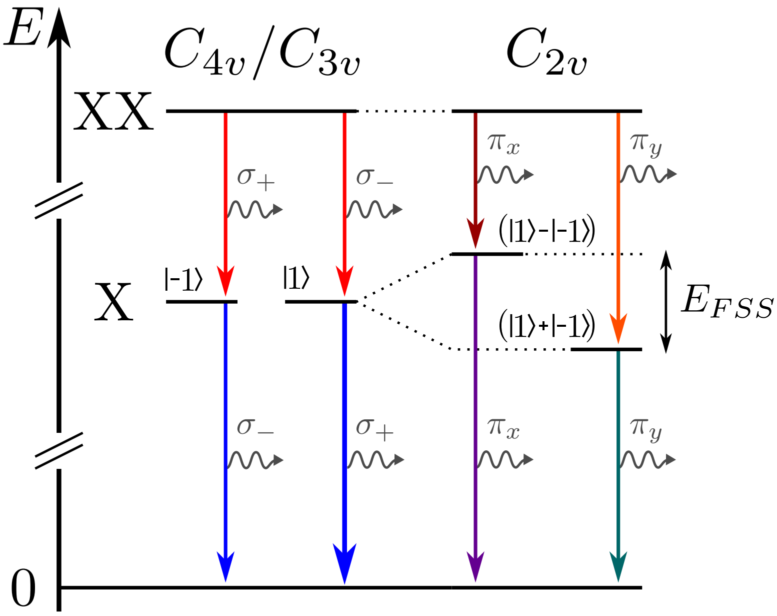

Figure 2.19: Energy scheme representation of the biexciton recombination cascade in a QD without and with FSS due to different confinement potential symmetries.

then recombines and emits a photon of higher energy. Depending on the decay path the photons have different polarizations which can not be determined by measuring their energy and are thus polarization-entangled but indistinguishable in energy.

When the confinement potential is, however, lowered to C_{2v} the bright states mix and nondegenerate bright doublet states $(|1\rangle \pm |-1\rangle)$ emerge. Upon recombination these exciton states emit photons $\pi_{x/y}$ linearly polarized along each of the remaining mirror symmetry planes of the QD x and y. The biexciton is not split as it has a spin of 0 and the splitting is symmetric. The energy by which the doublet states are separated is called exciton fine-structure splitting (FSS).

The FSS of photons from In(Ga)As QDs on (Al)GaAs(100), which are typically polarized in $x = [011]$ and $y = [01\bar{1}]$, can be anything between 0 and 1000 µeV [130]. It has been shown that FSS not only emerges due to the morphological asymmetry of QDs on (100), which arise from an asymmetric diffusion constant, but also from strain-induced, asymmetric piezoelectric fields [131]. As a result even perfectly symmetric In(Ga)As QDs on (100) are expected to show a finite FSS [132]. Even strain-free GaAs/AlGaAs QDs on (100) with a symmetric shape showed a generally nonzero FSS [133]. As has been repeatedly stated, this is not the case for QDs on (111)A/B.

CHAPTER 3

Experimental techniques

3.1 Molecular beam epitaxy system

While the basic working principle of MBE was already detailed in section 2.2.3 the actual system with which the samples in this thesis were fabricated is presented in this section. In Figure 3.1 a sketch of our solid-source III-V MBE system is shown. A total of 15 effusion cells allow the generation of molecular beams of Al, Ga, In, As_2, As_4, Sb_n, Sb_2, Si and C. For the samples in this thesis only the group III elements, As_4 (from now on only As) and Si were used. Unlike the other cells, the group V cells are equipped with valves which allow very fast flux changes without ramping the source material temperature. The effusion cells and the sample manipulator each have a mechanical shutter to block molecular beams on demand. They, as well as all temperatures and valves, are typically remotely controlled by a dedicated computer which also allows automatic operation using previously written growth recipes. In the software the opening and closing time of shutters can be controlled with 0.1 s accuracy which is expected to be slightly increased due to hardware delays such as the shutter transient. Molecular fluxes are controlled via a beam flux monitor which measures the beam equivalent pressure (BEP) in front of the sample and by recording RHEED oscillations which allow the direct measurement of the deposition rate.

During growth the samples are typically rotated in the manipulator at 10 RPM to achieve deposition homogeneity. For short deposition times (e.g.

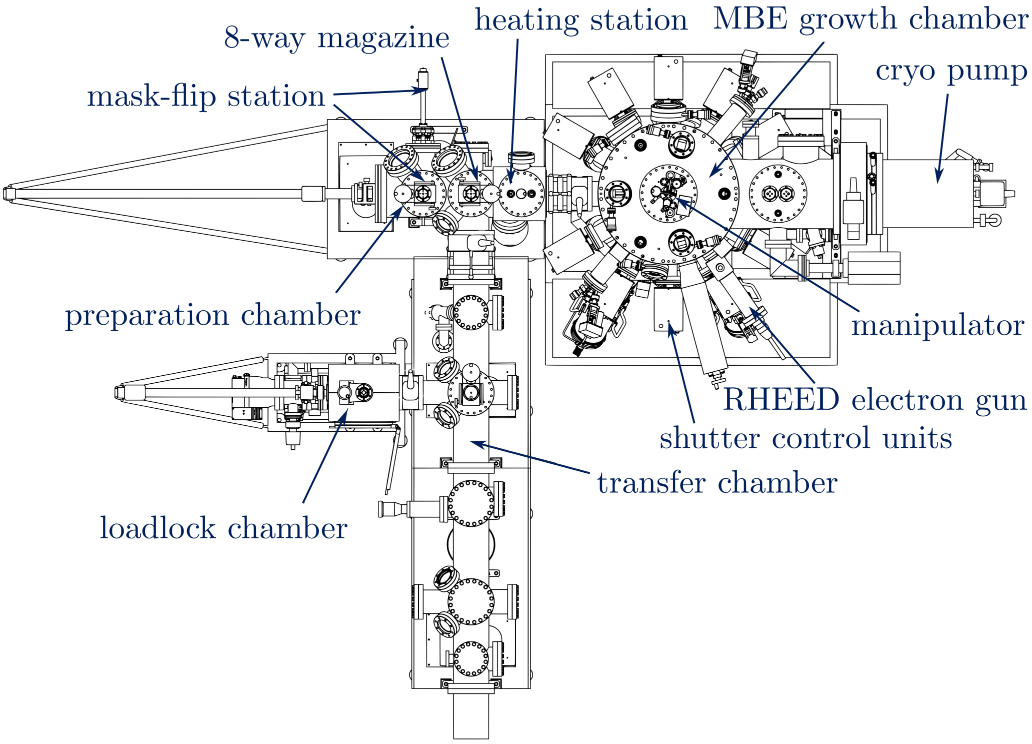

Figure 3.1: Top-view sketch of the MBE system employed in this thesis. This sketch was provided by MBE Komponenten upon system delivery.

droplet deposition) this was ensured by adjusting this frequency to achieve an integer number of rotations.

A typical figure of merit for MBE performance is the electron mobility in a two-dimensional electron gas in AlGaAs/GaAs heterostructures [134]. During growth campaigns this quantity is routinely determined and a steady increase is expected due to maturing effects of an MBE system. As such the highest value up to 2018 could be measured with $2.48 \times 10^6\,\mathrm{cm^2\,V^{-1}\,s^{-1}}$ at $4.2\,\mathrm{K}$ without illumination on sample A0849. This shows that the system was in good condition during the last growth campaign where the optically active samples shown in the thesis were fabricated.

3.1.1 Substrate preparation

In this thesis the substrates used are semi-insulating GaAs wafers with a GaAs(111)B surface misoriented by 1° to the (211) direction. This substrate orientation combines the higher surface symmetry of the (111) face (as detailed in section 2.1.2) with the characteristics of the step-flow growth mode (see section 2.2.2). It was chosen due to reports of the comparably high growth rates possible on this substrate orientation [20].

First growth experiments on misoriented GaAs(111)B were performed on $\frac{1}{2}$ 2 inch wafers from WAFER TECHNOLOGY LTD. which were cut from ingot WV23231/Un (datasheet in Figure A.2). These wafers were mounted alongside different $\frac{1}{2}$ 2 inch wafers in a wafer holder designed for a full 2 inch wafer in first experiments to compare different miscut directions. These different miscut directions were not chosen for further experiments as their performance was inferior and are thus also not featured in this thesis. Further experiments, including everything related to the DE process, were performed on $\frac{1}{6}$ 3 inch wafers from MATECK GMBH cut from ingots 615291, 614330 and 17030816 with identical datasheet (Figure A.1) and performance. The main difference between the two wafer sizes was an increased pyrometer signal in the 2 inch-wafer case due to a small slit between the wafer halves through which light from the heater could be seen. Also the relation of thermocouple temperature T_{TC} and pyrometer temperature T_{pyro} was different as will be generally discussed in the following section. To trace which wafer was used for which sample, the growth reports of all samples which are used during this thesis are appended in chapter B.

As the used wafers are bought epi-ready, no further chemical processing is necessary. After cleaving of the whole substrate wafers the pieces are placed individually on a molybdenum sample holder upside down. The holder features a central recess slightly larger than the cleaved substrate but matching its shape and a small, thin ledge which keeps the substrate from falling completely through the hole. The substrate is held only by gravity and no clamps or indium bonding is necessary. Every substrate and its holder then runs through the following steps:

1. First degassing: The substrate is introduced into the vented loadlock chamber, which is then evacuated and upon reaching a better pressure than 1×10^{-6} mbar the chamber heats to 120 °C for 8 h to remove introduced contaminants, especially water.
2. After the loadlock chamber was cooled down and a pressure below 1×10^{-7} mbar is reached the substrate is transferred through the transfer chamber to the preparation chamber.
3. Second degassing: In the preparation chamber the substrate is loaded to the heating station which is already at 200 °C to further remove contaminants. It is degassed for 1 h or until the degassing pressure spike abated significantly.
4. When preparation chamber and growth chamber pressures are both below 5×10^{-9} mbar the substrate is transferred to the growth chamber and assigned a sample number. During this step the As flux in the growth chamber is zero and the growth chamber manipulator temperature is not higher than 300 °C.
5. Deoxidation and annealing: After providing an As flux to the sample it is heated to $T_{pyro} = 620\,°\mathrm{C}$ (well above the deoxidation temperature around 595 °C) to reduce the oxidized surface to GaAs, annealed there for 10 min to smoothen the surface and then cooled to growth temperature.
6. After manual deposition of GaAs at the optimum growth conditions to further smoothen the surface, RHEED and temperature measurements with thermocouple and pyrometer are performed to determine necessary parameter adjustments.

After these steps and once the growth recipe was updated to the recent measurements, fabrication of the desired sample structure can begin.

3.1.2 Substrate temperature control

Controlling the substrate temperature during growth is crucial as well as difficult due to the vacuum and the related absence of a direct thermal contact. In our MBE the sample backside is heated radiatively by a tantalum heating filament behind a pyrolytic boron nitride diffuser plate optimized for temperature homogeneity. A type C thermocouple situated behind the heating filament and a pyrometer directed non-normal to the sample surface, mounted at the chamber bottom, are used to measure the sample temperature. The central wavelength of the pyrometer is $(0.94 \pm 0.05)\,\mu\mathrm{m}$. The fundamental absorption edge of GaAs, which is positioned at E_g, passes the central wavelength at $T = 243\,^\circ\mathrm{C}$ (see Varshni formula Eq. 2.1). This assures that the pyrometer will not detect the heater light at substrate temperatures well above $T = 375\,^\circ\mathrm{C}$, which corresponds to the upper limit of the pyrometer detection wavelength at $0.99\,\mu\mathrm{m}$.

To demonstrate the different temperature measurement methods the pyrometer was used during the ramp-up portion of a deoxidation step of a $\frac{1}{6}$ 3 inch and a full 3 inch wafer. The measured values are shown in Figure 3.2. It is immediately apparent that the different wafer sizes/shapes impact the temperature measurements. At low T_{TC} the full wafer shows a massively higher T_{pyro}. This is suspected to be due to the (very bright) heater light which is partially transmitted through the sample and reaches the pyrometer. The abrupt T_{pyro} increase at the immediate start of the ramping procedure, when the heater power is increased abruptly, as well as the negative slope when the GaAs becomes slowly opaque to the pyrometer wavelength range when heating, points to this explanation. While a partial blocking of this due to the much smaller hole in the $\frac{1}{6}$ 3 inch molybdenum holder can be expected it is not clear why it appears to be blocked out completely for the smaller wafer. At higher temperatures this effect vanishes so that an approximately constant temperature offset separates the wafer shapes. The observation that larger exposed GaAs substrate areas in the MBE need higher T_{TC} to reach

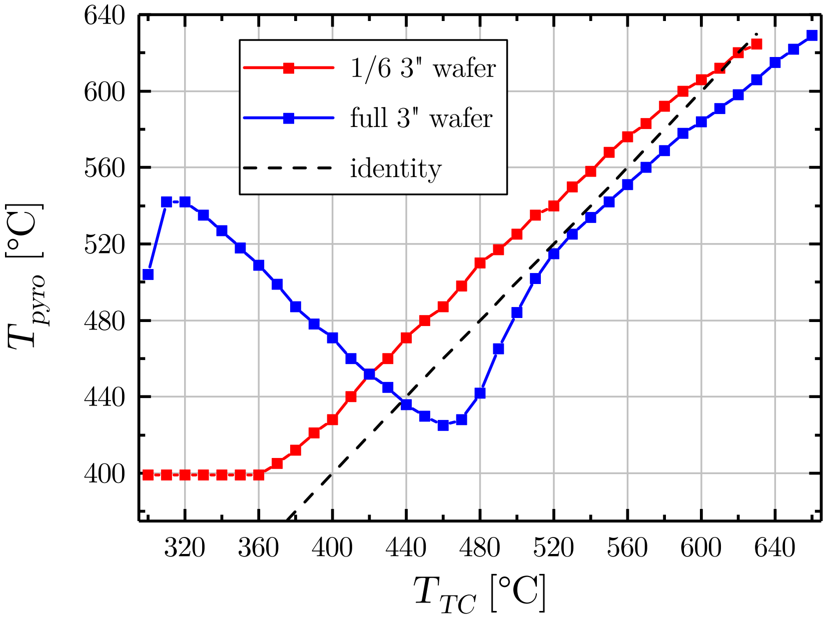

Figure 3.2: T_{pyro} in dependence on PID-controlled T_{TC} during the ramping part of the deoxidation step of a 1/6 3" and a full 3" wafer. The T_{TC} set-point was increased linearly in time with 20 K min^{-1} starting at T_{TC} = 300 °C. 400 °C is the lowest temperature the pyrometer can show, it is also displayed when the pyrometer shutter is closed.

the same T_{pyro} is true for all tried wafer shapes around the 600 °C range. One can conclude that the pyrometer is reliable for temperatures above 500 °C but not necessarily below. Consequently all substrate temperature values noted in this thesis above this value were measured by pyrometer and below by thermocouple if not explicitly stated otherwise.

The shown relation between both temperature measurement techniques are also not perfectly stable for the same wafer shapes. The cleaved wafer pieces can vary by a few 100 µm, can have different or no flats, and can be positioned differently in the substrate holder recess influencing the thermal coupling from sample to holder so that T_{pyro} can vary by ±10 K for the same T_{TC}. Due to thin film interference the pyrometer would measure false values for an arbitrary layered sample and can only be used reliably before growth. Because of this the MBE control program regulates only T_{TC} during a recipe. This necessitates the measurement of new T_{TC} values for specific T_{pyro} values (such as typical growth temperatures around 600 °C) for every individual sample as part of the last substrate preparation step. These values are then used to update the growth recipe.

At very low temperatures (below 100 °C), where exchange of warmth due to radiation becomes very weak, the temperature control with the thermocouple is judged to be insufficient. To remedy this a band-edge thermometry system, which does not exhibit such limitations, is currently put into operation on our MBE system so that it will be possible to measure the sample temperature with higher accuracy over an extended range.

3.1.3 Reflection high-energy electron diffraction

As already mentioned, RHEED is used in almost every MBE system to analyze the atomic structure of the crystal surface *in situ* due to its ease of use, versatility and analytic power. Figure 3.3 shows a schematic diagram of RHEED: A finely collimated electron beam is directed onto the sample at grazing incidence and the forward scattered diffraction patterns are monitored on a fluorescence screen. Due to the small grazing angle the electron beam only interacts with the topmost monolayers of the sample and is thus very surface-sensitive [136]. The grazing angle due to our chamber geometry is 4 ° but can be adjusted by beam deflection in the electron gun. At specific azimuth angles, where the electron beam is aligned to crystal directions with low Miller indices, the emerging diffraction pattern allows the determination of surface periodicity and structure including its reconstruction. An in-depth introduction to RHEED and a plethora of possible applications is given by Ichimiya and Cohen in their book of the same name [137].

Direct applications assisting the growth of high-quality structures in MBE specifically are:

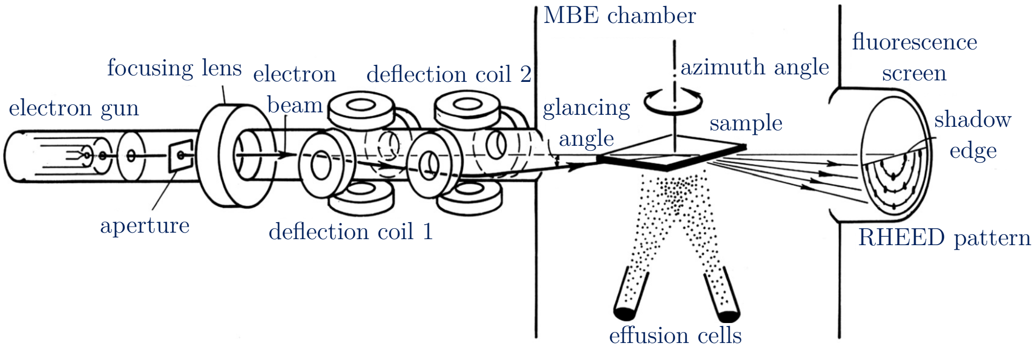

Figure 3.3: Sketch of the RHEED apparatus in operation during sample fabrication by MBE. (adopted from [135])

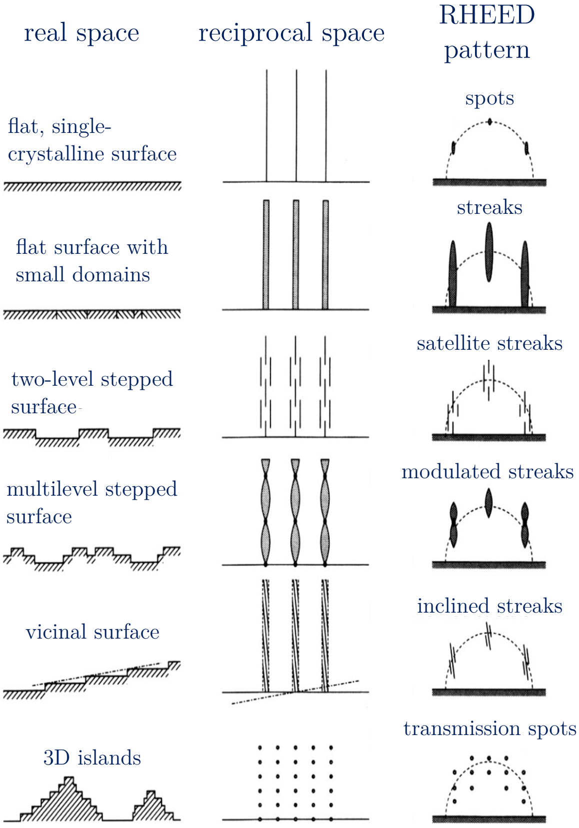

Figure 3.4: Schematics of various kinds of realistic surfaces in real space morphology, reciprocal space and with their respective RHEED patterns. (adopted from [135])

- Reconstructions can be used to describe the specific state of a sample during growth mostly system-independent. Parameters specific to each MBE system (like temperatures and pressures which depend on geometry and measurement technique) can not so easily be translated to other systems.
- Intensity oscillations of individual diffraction maxima during planar growth can be used to measure the growth rate [138].
- Imperfect samples change the RHEED pattern qualitatively depending on which kind of deviation from the perfectly flat, monocrystalline case is present as is illustrated in Figure 3.4. This allows a fast diagnosis of a faulty growth process if the domain size of the unwanted, emerging structure is smaller than the electron beam coherence length. For a standard electron gun with 10 keV, as used in this work, acceleration this is $100 - 200$ nm in longitudinal and $30 - 80$ nm in transversal direction [135].

3.2 Atomic force microscopy

Atomic force microscopy (AFM) is a type of scanning probe microscopy which allows the imaging of surfaces with subnanometer resolution. This exceeds the capabilities of optical microscopy by far. Its development by Binning, Quate and Gerber in 1986 [139] has provided a sophisticated tool for imaging, measurement of material properties as well as manipulation on the nanoscale. A schematic representation of the working principle is shown in Figure 3.5: A cantilever with a small tip is moved over the sample surface while the distance between cantilever and sample is controlled by a piezoelectric motor. Depending on the displacement of the cantilever, whose spring constant is known, a laser is reflected by the mirrored backside and detected by a photodiode. From the position of the laser spot on the photodiode the force which acts on tip and cantilever can be calculated.

In this thesis the Nanosurf Mobile S AFM system was employed. The

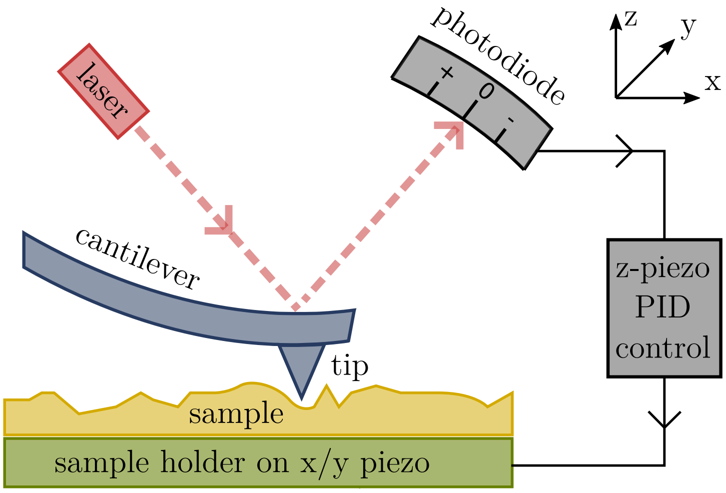

Figure 3.5: Illustration of an AFM measurement setup.

system supports various measurement modes such as

- static mode (or contact mode), where on every measured point of the sample the cantilever is adjusted to yield a constant force or height and the other quantity is recorded to map the sample.
- dynamic mode (or tapping mode), in which the cantilever oscillates at high frequency at or close to resonance. Then amplitude, frequency and/or phase of the cantilever oscillation depend on the distance to the sample and other local properties and can thus be used to characterize the sample surface.
- electrical AFM mode, where a voltage or current is applied to the tip during static or dynamic mode to also investigate electric properties on the sample.

The micrographs shown in this thesis were measured in the static mode with a constant force of 18 nN without tip voltage. The used PID constants were $(10000, 1500, 0)$ and the standard resolution is 256×256. The measured area varies from $(0.5\,\mu\mathrm{m})^2$ to $(9.81\,\mu\mathrm{m})^2$. The measurement time per every scanned line was chosen as 1 s as a compromise between higher noise levels at faster tip movement and noticeable in-plane drift of the sample when longer measurement times are used. Standard contact mode AFM probes PPP-CONTR from Nanosensors with highly doped, pyramidal Si tips with $< 7\,\mathrm{nm}$ tip radius, $30\,\mathrm{nm}$ thick Al reflection coating on the detector side and a low spring constant of $0.2\,\mathrm{N\,m^{-1}}$ were employed.

A key quantity to describe sample quality after MBE growth is the root mean square roughness of the surface which is defined as

$$\sigma_q = \sqrt{\frac{1}{N}\sum_{i=1}^{N}(z_i - \bar{z})^2} \quad ,$$

where N is the total number of pixels, z_i the measured height at pixel i, and $\bar{z}$ the sample mean height. σ_q, however, depends on the fitting algorithm which is applied to the measured data to make it usable. The result of different algorithms provided by the AFM manufacturer are shown in Figure 3.6. It is obvious that a constant z-drift makes the unprocessed data unusable for sample characterization. While a line fit in x, which sets $\bar{z}$ for each horizontal line to zero, removes this problem and is thus the basis of every fitting algorithm, it introduces a "shadow" along lines which include uncommonly high z values (e.g. when droplets or QDs are present). The mean fit algorithm, which additionally performs fitting in y, decreases this line-fitting artifact but is not able to remove it completely. Higher-order fitting algorithms such as the shown parabola fit are even more susceptible to single high-z regions and create artifact hills on top of trenches. As a result all shown AFM images which include droplets or QDs were subjected to the mean fit algorithm and all the other ones to the line fit algorithm. A fitting in x and y for which areas occupied by QDs were manually excluded during base-line calculation was only performed once for Figure 4.23 & 4.24.

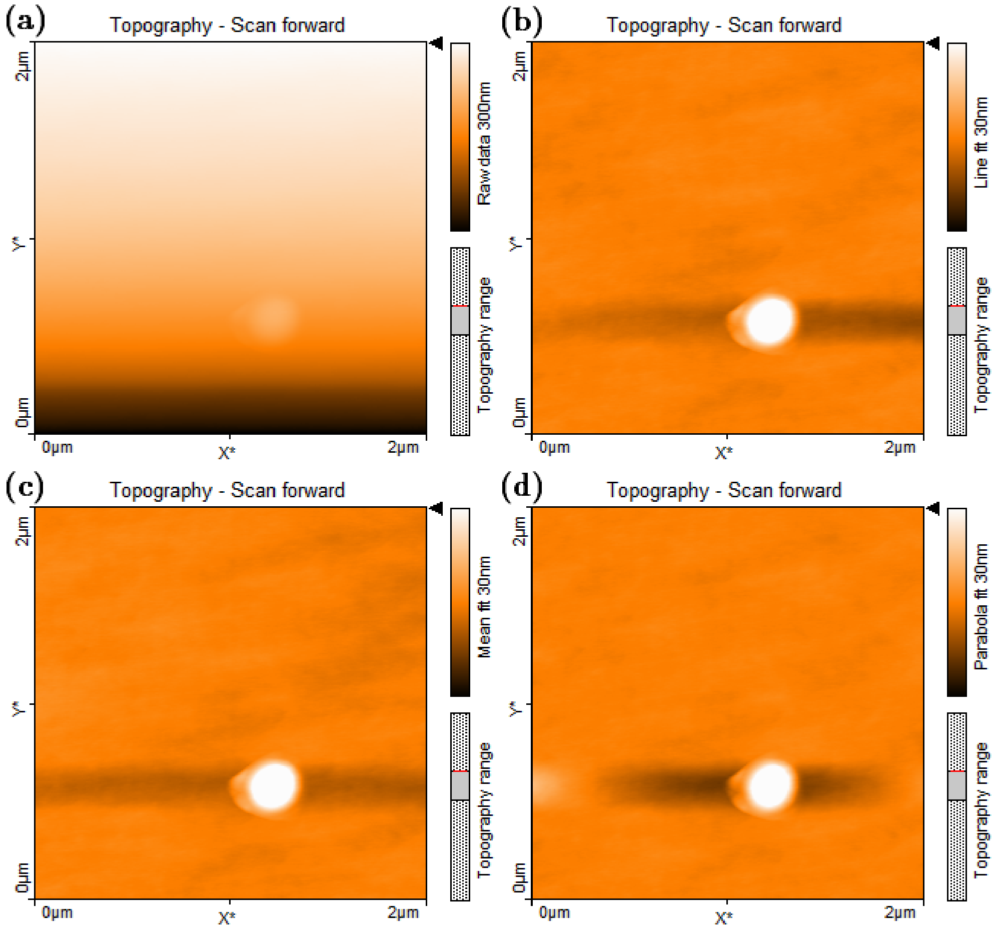

Figure 3.6: Results of different data processing modes available in NANOSURF MOBILE S SOFTWARE v 1.3.0.2 as they are displayed in the software itself. The raw, unprocessed data (a), line fit (b), mean fit (c) and parabola fit (d) are all based on an identical set of measured height values acquired on sample A0352. They yield different roughnesses of 320 nm, 2.6 nm, 2.7 nm and 2.4 nm, respectively.

3.3 Rapid thermal annealing

Post-growth rapid thermal annealing (RTA) is a common technique in the field of semiconductor technology in which a sample is basically just heated, annealed and cooled for a short time. It is generally used to effect strong

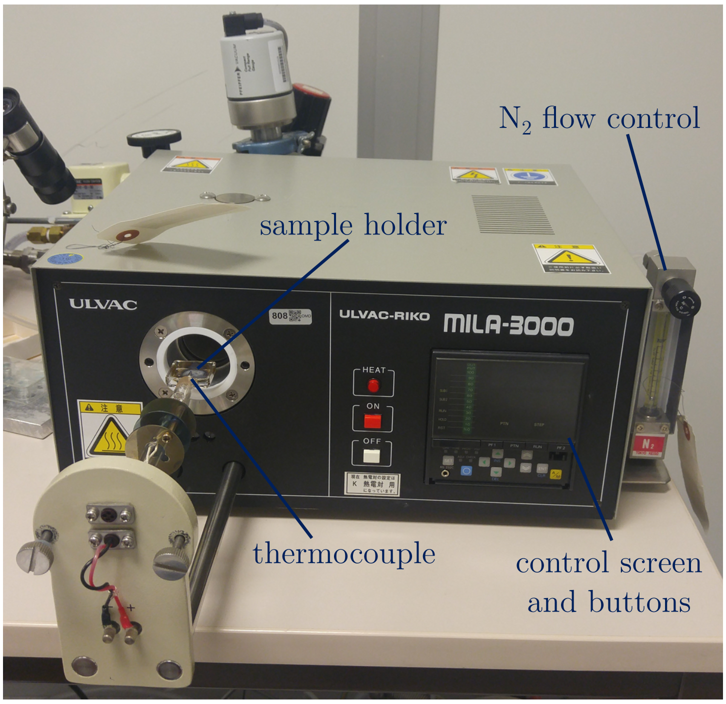

Figure 3.7: Picture of RTA system with annotations on important components.

diffusion in a sample to promote the decay of crystal defects [140] or interdiffusion of heterostructure layers [141]. The short times allow to use temperatures which would normally destroy the semiconductor completely. GaAs, for example, typically decomposes for $T > 400\,°\mathrm{C}$ when no As atmosphere is present but this effect is contained to the sample surface in RTA. An additional measure to reduce degradation, which is used here, is to place a slightly larger piece of GaAs substrate on top of the to-annealed sample upside down so that a protective As atmosphere can form in the small space between both samples during annealing. This technique is called proximity capping [142].

Figure 3.7 shows the used RTA oven. The samples were cleaved in equilateral triangles or trapezoids with side lengths of around 4.5 mm so that $<\bar{1}10>$ facets emerge as this is where GaAs(111)B substrates naturally frac-

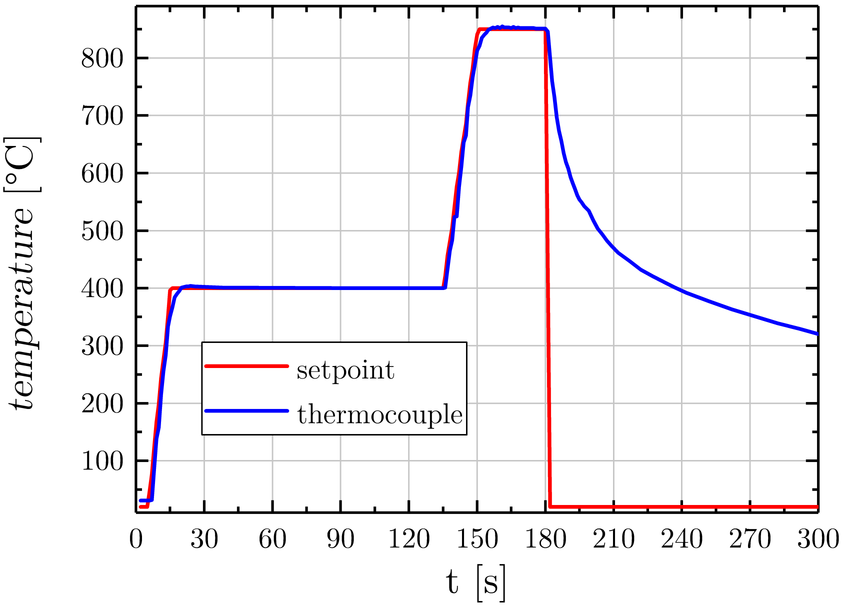

Figure 3.8: Set-point and thermocouple temperature of the RTA oven during a typical annealing process with 850 °C held for 30 s. The sample is held at 400 °C for 120 s before annealing for better thermal stability. The subsequent fast ramp to 850 °C takes 14 s.

ture with minimum applied force. The sample holder area is approximately 1 cm^2. They were then placed into the sample holder close to the thermocouple and proximity capped. After carefully shoving the sample holder into the oven, the glass tube surrounding it is evacuated and flushed with N_2 to atmospheric pressure to remove any traces of oxygen, water and other atmospheric contaminants. Under a steady N_2 flow, the annealing process is then started and the sample is radiatively heated by halogen lamps. The set-point and thermocouple temperatures during a typical annealing process where the sample is subjected to 850 °C for 30 s are shown in Figure 3.8. It can be seen that the PID parameters which control the heating power are well chosen and no strong temperature deviations or oscillations are present.

All optically active samples shown in this thesis were annealed with the stated parameters.

The annealing temperature, time and capping type were optimized by Martin Eppinger during his bachelor's thesis [143] which contains information regarding variations of the mentioned parameters.

3.4 Photoluminescence spectroscopy

Photoluminescence (PL) spectroscopy is widely used to characterize the optical response of semiconductor samples. It is non-destructive, requires minimal sample preparation and allows investigation of a plethora of semiconductor properties. As the QDs in this thesis are fabricated specifically for their optical properties, QD characterization is the main application for PL here. To this end the sample is illuminated by a high-energy laser to excite charge carriers which then, upon decay via a radiative channel, emit lower-energy light specific to the channel. This resulting light spectrum is then analyzed and conclusions concerning the decay channels, and with this general properties of the sample, can be drawn.

The experimental setup used in this thesis is displayed in Figure 3.9. A 532 nm continuous wave laser with 2.33 eV photon energy (larger than E_g of both GaAs and $\mathrm{Al_{0.3}Ga_{0.7}As}$) and 4.5 mW power is employed. The reflective microscope objective LMM-15X-P01 by ThorLabs with 0.30 numerical aperture can be moved perpendicular to the sample surface for focusing. A lamp and camera can be coupled into the beam path by a movable beamsplitter to aid focusing or to characterize specifically marked sample regions. The sample is glued on a copper sample holder in the cryostat with Marabu Fixogum. The cryostat MicrostatHe by Oxford Instruments is movable in-plane by micrometer screw gauges and can be cooled by a continuous flow of liquid gases such as nitrogen and helium. The temperatures of the samples when cooled in this setup are 89 K and 14 K, respectively. At the sample position an excitation power of 130 µW

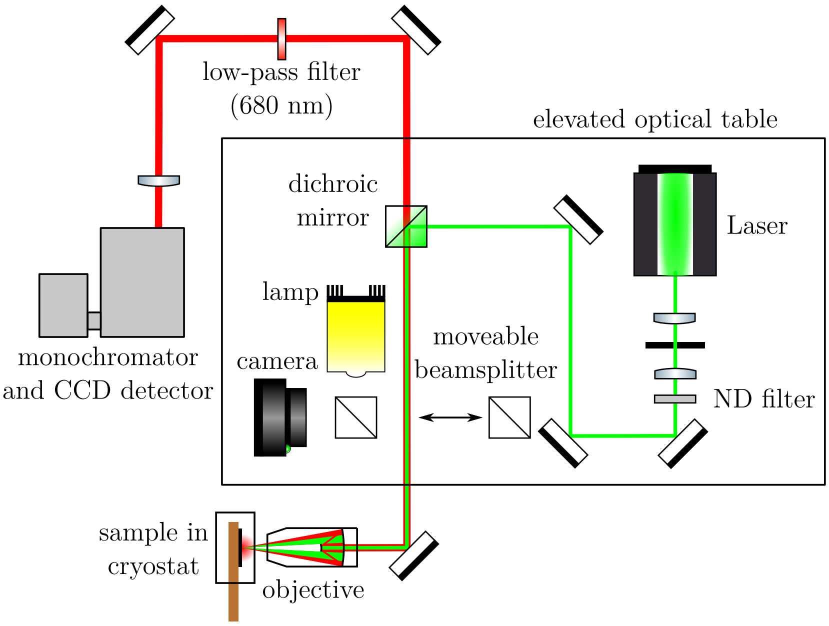

Figure 3.9: Sketch of the confocal PL setup used in this thesis.

was measured without an ND filter. The monochromator Acton SP2150 by Princeton Instruments with a focal length of 0.150 m and a 600 mm^{-1} grating has a nominal resolution of 0.8 nm which is, however, increased as the entrance slit width was enlarged to 100 µm. The Andor iDus DU490A-1.7 InGaAs line detector is operated at −60 °C. As it is optimized for wavelengths around 1.7 µm the detector quantum efficiency is below 20 % for $\lambda < 800$ nm, which is the region of interest in this thesis. Due to the low detector sensitivity and the low-pass filter the band-to-band transition of He-cooled $\mathrm{Al_{0.3}Ga_{0.7}As}$ at 640 nm can not be observed in this setup. An additional edge-pass filter, which is usually (for S-K InGaAs QDs) employed to reduce the measured laser signal, was removed as a strong decrease in intensities below 850 nm was detected.

All shown spectra in section 4.5.1 were measured under He cooling at nominally 14 K, without ND filter and with 200 s integration time.

A very detailed description of the PL setup and especially the sample holder and cryostat is given in the bachelor's thesis of Christian Kiessler, where the last major modification of the setup is documented [144].

CHAPTER 4

Results and discussion

4.1 Planar growth on misoriented GaAs(111)B

A plane surface is a vital prerequisite for QD fabrication by self-assembly both by DE and S-K growth. Any hills and mounds on the surface can serve as nucleation site and impact QD fabrication in undesirable ways changing QD morphology and creating an inhomogeneous QD density distribution. As already stated in chapter 2 the fabrication of smooth planar layers on GaAs(111)B requires a careful selection of growth parameters. These parameters include the growth rate r, the substrate temperature T_{sub} and the As flux r_{As} or BEP p_{As}. Note that the MBE growth of planar GaAs is typically performed in the As-rich regime where As that does not contribute to the growth of GaAs is reevaporated from the sample surface. As a result the total growth rate in As-rich conditions depends completely on the rate of group III material. Below 640 °C the sticking coefficients of Ga and Al have been reported as unity [145] so that the growth rate can be easily converted to the flux of these materials. The substrate temperatures used in this thesis are below 640 °C so that the redundant group III fluxes are omitted and only the total growth rates are stated. For In at $T_{\mathrm{sub}} > 500\,^{\circ}\mathrm{C}$ on the other hand, a nonvanishing, strongly temperature-dependent reevaporation can be measured [146], which introduces a considerable error.

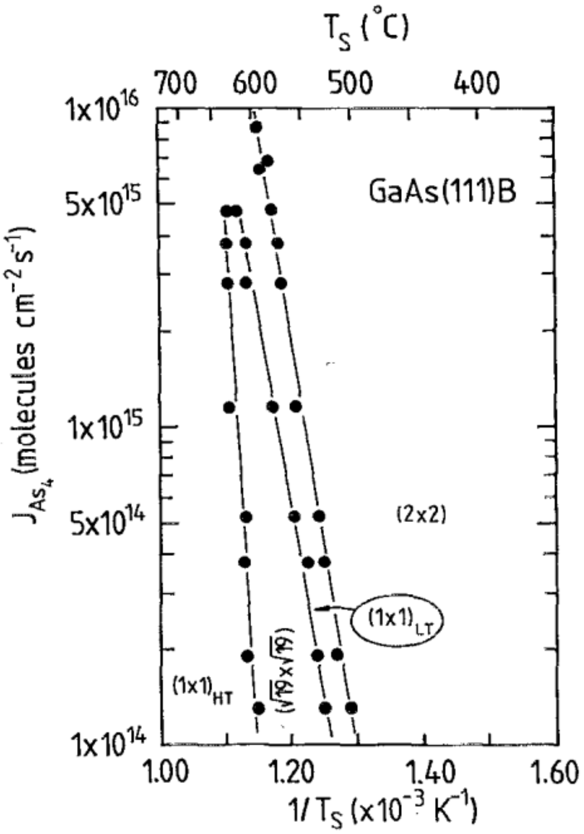

Figure 4.1: Static phase map of GaAs(111)B with different substrate temperatures $T_S = T_{\mathrm{sub}}$ and As fluxes J_{As_4} (taken from [42]). Note how the $(\sqrt{19} \times \sqrt{19})R \pm 23.4^\circ$ reconstruction only occurs at a narrow temperature interval and is quenched completely for high As fluxes.

4.1.1 Reconstructions of GaAs(111)B

Monitoring the surface phase of the growing semiconductor by surface-sensitive methods such as RHEED (see section 3.1.3) provides valuable information about the actual state of the sample surface. For GaAs(111)B it is known that planar, homoepitaxial growth of GaAs occurs on the $(\sqrt{19} \times \sqrt{19})R \pm 23.4^\circ$ reconstruction [43]. Figure 4.1 shows the static phase map of GaAs(111)B, which describes which reconstructions is present under varying parameters without deposition. These reconstructions could

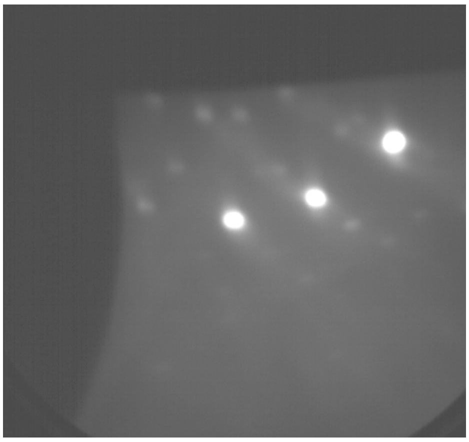

Figure 4.2: Typical RHEED signal of a $(\sqrt{19} \times \sqrt{19})R \pm 23.4°$ reconstruction on miscut GaAs(111)B. The picture was taken at $T_{\text{sub}} = 590\,°\text{C}$ and $p_{\text{As}} = 1.5 \times 10^{-5}\,\text{mbar}$ without deposition. With carefully chosen parameters this reconstruction can also be seen during deposition.

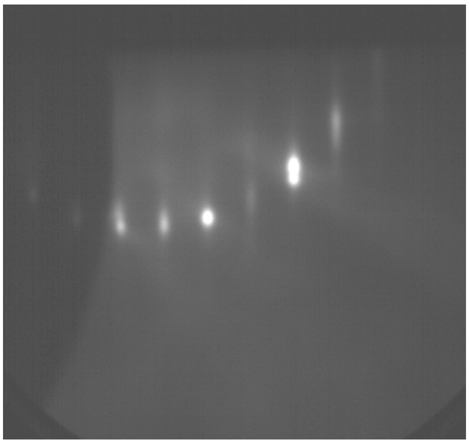

Figure 4.3: Typical RHEED signal of a (2×2) reconstruction of a smoothly grown AlGaAs layer deposited on misoriented GaAs(111)B. The picture was taken at $T = 200\,°\text{C}$ and in absence of an As flux without deposition. A pure GaAs surface results in a very similar signal at these parameters.

also be identified in our system and RHEED screenshots of the Ga-rich $(\sqrt{19} \times \sqrt{19})R \pm 23.4°$ and the As-rich (2×2) reconstructions [147] are shown in Figures 4.2 & 4.3 exemplary. To generate the reconstructions with the shown clarity, samples have to be prepared according to the scheme reported in section 3.1.1.

The precise atomic structure of the reconstructions of GaAs(111)B is not relevant in this thesis but can be viewed in this paper by Biegelsen *et al.* [49] when desired.

4.1.2 $\text{Al}_x\text{Ga}_{1-x}\text{As}$

In this section the 2D deposition of strain-free $\text{Al}_x\text{Ga}_{1-x}\text{As}$ in the step-flow growth mode with its growth parameters and error modes is presented. For the deposition of GaAs and $\text{Al}_{0.3}\text{Ga}_{0.7}\text{As}$ the following growth parameters

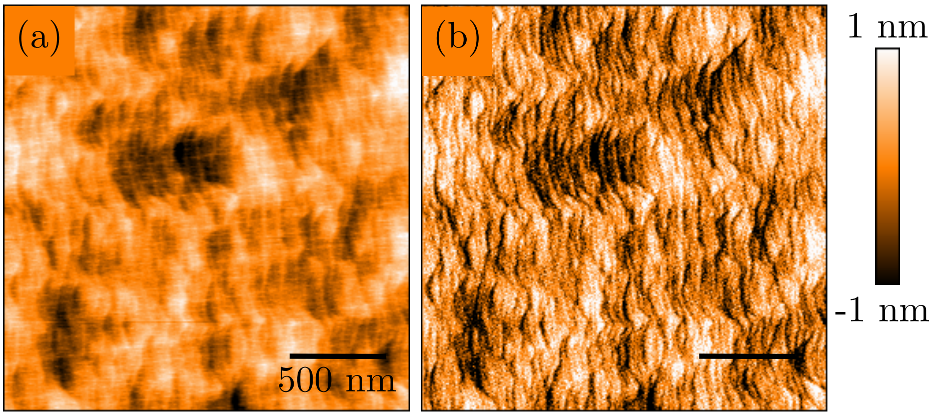

Figure 4.4: AFM measurement of sample A0288 with 100 nm $Al_{0.3}Ga_{0.7}As$ grown on a 200 nm GaAs buffer layer and capped with 5 nm GaAs to prevent oxidation. The standard growth parameters were employed. The roughness of this area is $\sigma_q = 0.33\,\mathrm{nm}$. Meandering steps which signify a weak Bales-Zangwill instability can be seen. While (a) shows the background-subtracted height profile (b) shows a contrast-enhanced "shaded map" generated by the AFM software where the steps are more pronounced but the color scale does not represent the height anymore.

lead to planar growth:

$$\begin{aligned} T_{\mathrm{sub}} &= 590\,^{\circ}\mathrm{C} \\ p_{\mathrm{As}} &= 1.5 \times 10^{-5}\,\mathrm{mbar} \\ r_{\mathrm{Ga}} &= 0.35\,\mathrm{ML/s} \approx 0.1\,\mathrm{nm\,s^{-1}} \\ r_{\mathrm{Al}} &= 0.175\,\mathrm{ML/s} \approx 0.05\,\mathrm{nm\,s^{-1}} \end{aligned}$$

These standard growth parameters have been used for all planar $Al_xGa_{1-x}As$ growth in this thesis when not stated differently and leads to surfaces as shown in Figure 4.4. Note the visible, curvy steps which signify a weak Bales-Zangwill instability and the low roughness of $\sigma_q = 0.33\,\mathrm{nm} \approx 1\,\mathrm{ML}_{(111)}$. The error of this roughness measurement can be estimated around 0.1 nm. A line-scan of a higher-resolution AFM measurement of a smoothly deposited layer is shown in Figure 4.5. The measured step height suggests that ac-

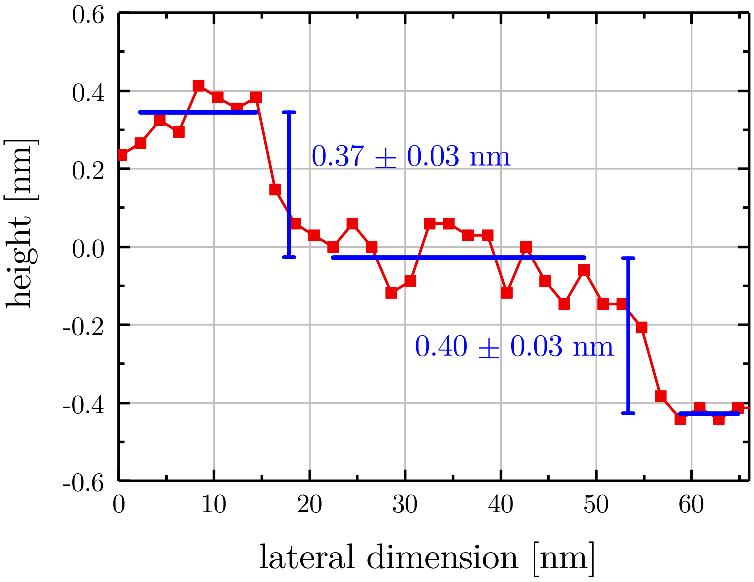

Figure 4.5: Line-scan of a higher-resolution AFM measurement of the same sample as shown in Figure 4.4. Steps and terraces are clearly visible and step-heights close to the monolayer thickness of 0.33 nm were calculated.

tual monolayers instead of bilayers are present on the surface so that step bunching can be ruled out. The terrace widths w deviate strongly from the geometrically expected $\bar{w} = \frac{1\,\mathrm{ML}_{(111)}}{\tan 1^\circ} \approx 19\,\mathrm{nm}$ due to the Bales-Zangwill instability.

Deviations from these growth parameters and their effects on the surface roughness are shown in Figures 4.6 & 4.7. The growth process is very sensible on T_{sub} so that 3D structures already form with small temperature deviations. While for small changes in As pressure the planar growth is still largely intact the emergence of holes and elongated hillocks would prevent successful fabrication of QDs by DE on these surfaces. Note that all of these samples formed the $(\sqrt{19} \times \sqrt{19})R \pm 23.4^\circ$ reconstruction directly before growth. This shows that the preparation of this reconstruction is necessary but not sufficient to ascertain smooth growth.

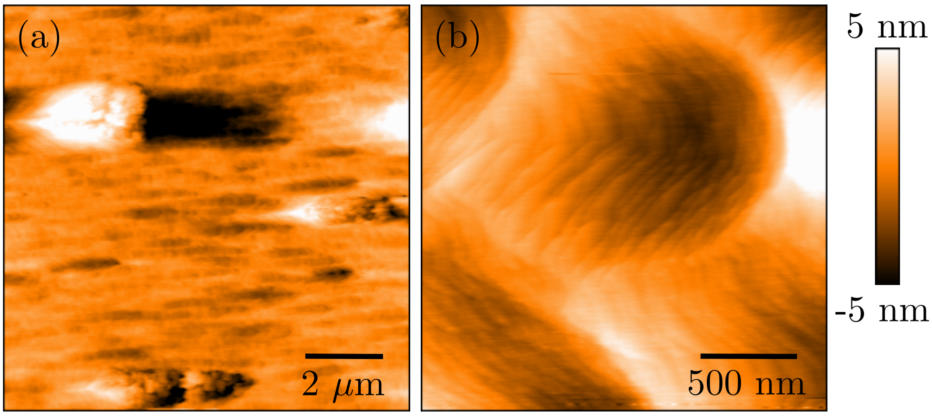

Figure 4.6: AFM measurements of the same sample structure as grown for Figure 4.4 but with T_{sub} changed by 20 °C down (a, A0289) or up (b, A0255) from the standard value of 590 °C. The roughnesses are $\sigma_q = 1.7$ nm and 1.9 nm, respectively. The emergence of hillocks and mounds clearly prevents planar growth.

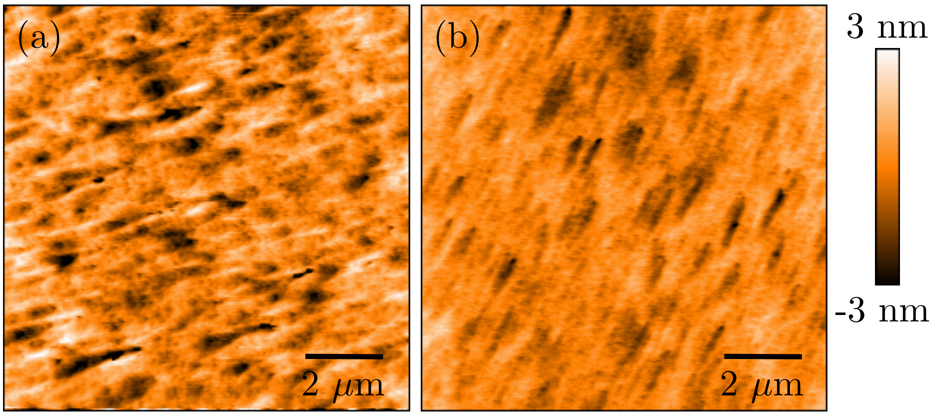

Figure 4.7: AFM measurements of the same sample structure as grown for Figure 4.4 but with $p_{\text{As}} = 2.1 \times 10^{-5}$ mbar (a, A0330) and 1.2×10^{-5} mbar (b, A0324) instead of 1.5×10^{-5} mbar. The roughness are $\sigma_q = 1.0$ nm and 0.66 nm, respectively. The emergence of hillocks (in (a)) and holes (in both) of a smaller scale than shown in Fig. 4.6 are still not acceptable since they would strongly influence the DE process.

The standard growth parameters also allow n-doping by Si and p-doping by C without detrimental effect on the surface roughness. While the successful n-doping was only shortly verified by Hall measurements, C doping was

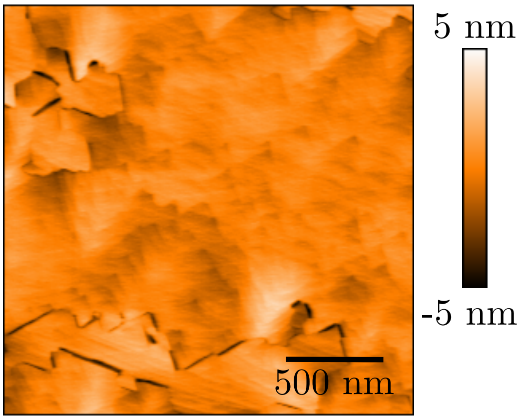

Figure 4.8: AFM measurement of sample A0597 with 100 nm AlAs grown on a GaAs buffer layer and capped with 10 nm GaAs to prevent oxidation. The standard growth parameters were employed. The roughness of this area is $\sigma_q = 0.88\,\mathrm{nm}$.

characterized in-depth in our group by Henksmeier *et al.* [148, 149].

The deposition of pure AlAs with the given growth parameters, however, does not lead to smooth samples. As shown in Figure 4.8 there are up to $1\,\mu\mathrm{m}^2$ big, smooth areas with $\sigma_q < 0.5\,\mathrm{nm}$ which are interrupted by deep gouges which follow the trigonal symmetry of the surface. While not a catastrophic result this suggests that slightly different growth parameters need to be chosen for pure AlAs deposition.

In conclusion, the growth parameters of smooth $\mathrm{Al}_x\mathrm{Ga}_{1-x}\mathrm{As}$ with $x \leq 0.3$ on misoriented GaAs(111)B were explored and a suitable set of parameters was identified. Higher Al contents seem to require a different set of parameters so that the deposition of pure AlAs/GaAs heterostructures, such as Bragg mirrors, with unchanging, stable growth parameters, as possible on GaAs(100), does not seem feasible on GaAs(111)B.

4.1.3 $\mathrm{In}_x\mathrm{Ga}_{1-x}\mathrm{As}$

In contrast to GaAs(100), where the lattice mismatch of InAs to GaAs results in S-K growth, the fabrication of 2D $\mathrm{In}_x\mathrm{Ga}_{1-x}\mathrm{As}$ with a high In content was reported on GaAs(111)A [150] and GaAs(111)B [14]. In the context of this thesis planar In-rich buffer layers are attractive as matrix material for InAs QDs to reduce strain and have an additional parameter for emission tuning. This is, however, only a tangent to the main objective of fabricating strain-free GaAs QDs in AlGaAs by DE and will only be presented shortly in this section as a few first experiments.

Two different approaches were tried: The direct growth of $\mathrm{In_{0.6}Ga_{0.4}As}$ on GaAs and the growth of $\mathrm{In_{0.6}Ga_{0.4}As}$ after a thin pure InAs layer for faster strain relaxation.

Figure 4.9 shows the result of the deposition of 5 nm of $\mathrm{In_{0.6}Ga_{0.4}As}$ on a buffer layer of 100 nm of GaAs. The GaAs was deposited at standard parameters and the $\mathrm{In_{0.6}Ga_{0.4}As}$ with

$$\begin{aligned} T_{\mathrm{sub}} &= 540\,^{\circ}\mathrm{C} \\ p_{\mathrm{As}} &= 0.8 \times 10^{-5}\,\mathrm{mbar} \\ r_{\mathrm{Ga}} &= 0.175\,\mathrm{ML/s} \approx 0.050\,\mathrm{nm\,s^{-1}} \\ r_{\mathrm{In}} &= 0.26\,\mathrm{ML/s} \approx 0.075\,\mathrm{nm\,s^{-1}} \end{aligned}$$

The surface shows very wide and rather smooth terraces with up to $8\,\mathrm{ML}_{(111)}$ high steps. This is an obvious result of step bunching and suggests that the Ehrlich-Schwöbel barrier is smaller for In rich arsenides at these temperatures. Note that at this T_{sub} already a substantial fraction of In is expected to reevaporate so that the actual InAs content of the alloy is significantly below 60 %. This surface is the best result of a wide parameter sweep. For lower T_{sub} strong 3D island growth was observed and higher T_{sub} would most likely improve the sample surface. $T_{\mathrm{sub}} = 540\,^{\circ}\mathrm{C}$ is, however, already known as upper limit for InAs deposition in our system from experiments on GaAs(100).

When more material is deposited with these parameters (see Figure 4.10) the 3D island growth already known for lower T_{sub}, which is not shown, also manifests here. One can conclude that the inset of a Volmer-Weber-like growth is postponed to thicker layers by a higher T_{sub} but not prevented.

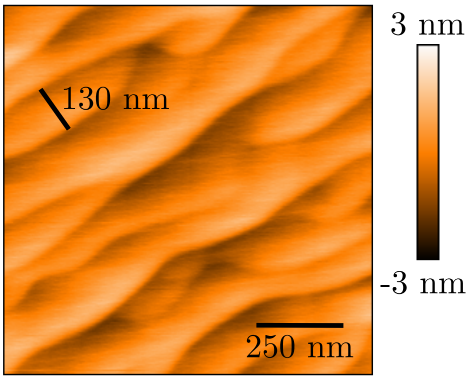

Figure 4.9: AFM measurement of sample A0496 with 5 nm $In_{0.6}Ga_{0.4}As$ grown on a 100 nm GaAs buffer layer. The roughness of this area is 0.91 nm.

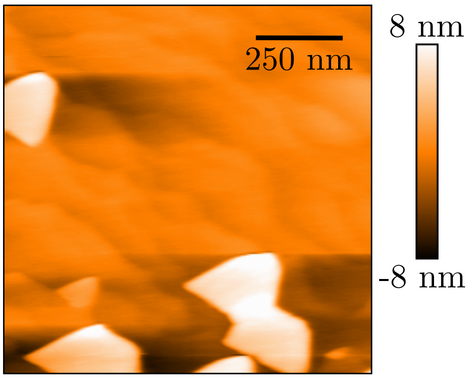

Figure 4.10: AFM measurement of sample A0466 with 15 nm $In_{0.6}Ga_{0.4}As$ grown on a 100 nm GaAs buffer layer. The roughness of this area is 2.6 nm and approximately 0.6 nm between the islands. The triangular islands have a height of around 10 nm.

Whether this is solely due to a decreasing In content of the layer with higher T_{sub} is uncertain. This suggests that for successful deposition one would have to increase T_{sub} to temperatures where all InAs would reevaporate.

Since it is likely that the strain due to the lattice mismatch of InAs and GaAs or the strain relaxation mechanisms (dislocation formation, step bunching) contribute to the surface roughening, an additional thin pure InAs layer before the InGaAs is introduced. Insertion of a thin InAs layer for metamorphic InGaAs growth on GaAs is a known technique in the literature [151]. In theory, a misfit-dislocation network is formed in the early stages of InAs deposition which relaxes strain and increases the lattice constant of the growing surface to better accommodate InGaAs growth. In the following

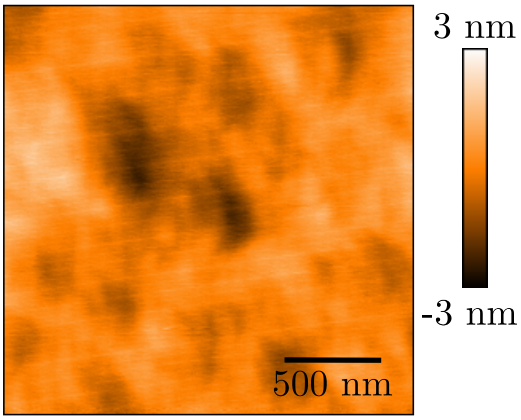

Figure 4.11: AFM measurement of sample A0514 with 1.5 nm InAs grown on a 100 nm GaAs buffer layer. The roughness of this area is $\sigma_q = 0.61\,\mathrm{nm}$.

experiments an InAs layer of 1.5 nm is deposited with

$$\begin{aligned} T_{\mathrm{sub}} &= 500\,^{\circ}\mathrm{C} \\ p_{\mathrm{As}} &= 0.8 \times 10^{-5}\,\mathrm{mbar} \\ r_{\mathrm{In}} &= 0.26\,\mathrm{ML/s} \approx 0.075\,\mathrm{nm\,s^{-1}} \end{aligned}$$

Note that T_{sub} was decreased substantially to allow a sticking coefficient of ≈ 1. An AFM measurement of the bare InAs layer is shown in Figure 4.11. While the surface does not show optimal roughness it is considered sufficient as a basis for the growth of InGaAs.

Figure 4.12 shows the results of 10 nm of $\mathrm{In_{0.5}Ga_{0.5}As}$ deposited with varying growth parameters on the InAs layer prepared as above. The parameters used for (c) are most suitable for planar growth since the terraces have at most a step height of $5\,\mathrm{ML_{(111)}}$ and no big islands are visible. While this surface with high steps and holes is still not suitable for heterostructure fabrication a definitive improvement over the other cases can be found. Especially the possibility to grow InGaAs surfaces with σ_q in the order of 1 nm, at T_{sub} which allows a sticking coefficient of one, is an improvement which is to be attributed to the introduced InAs layer.

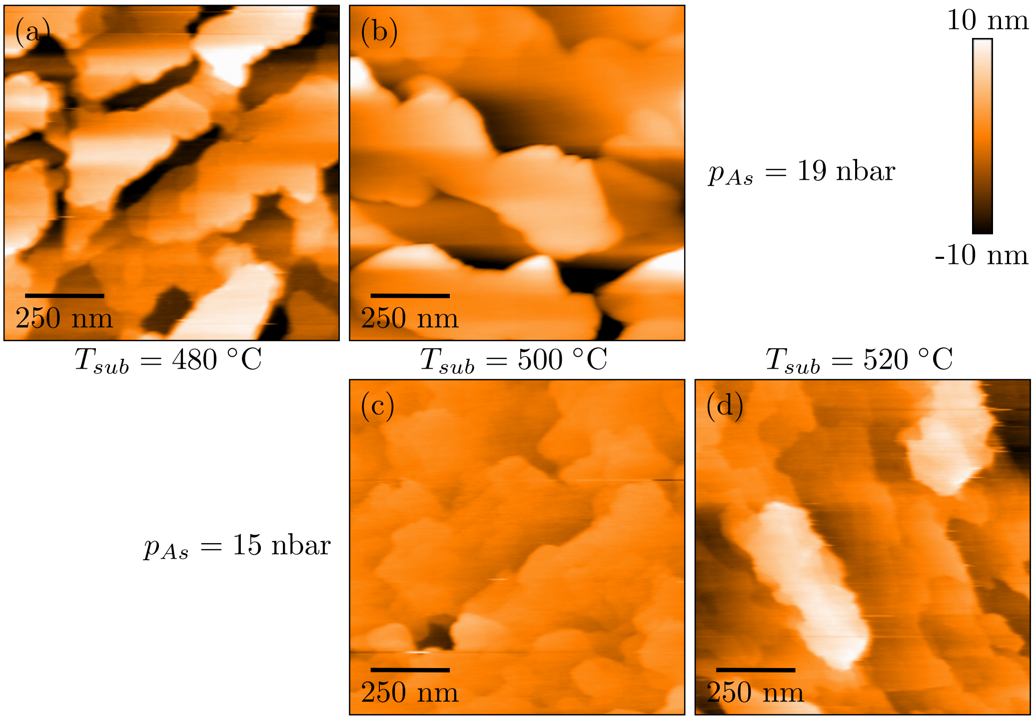

Figure 4.12: AFM measurements of samples with 10 nm of $In_{0.5}Ga_{0.5}As$ deposited on 1.5 nm InAs as prepared for Figure 4.11. The measurements have been arranged so that columns share the same T_{sub} and rows the same p_{As}. The roughnesses for (a)-(d) are $\sigma_q = 4.8$ nm, 3.5 nm, 1.1 nm and 3.6 nm, respectively. The samples are designated as A0536, A0546, A0518 and A0537.

In conclusion, the parameter window of smooth InGaAs growth on misoriented GaAs(111)B seems to be very narrow. Advancements in the deposition process were achieved but results are still not satisfactory and ready to proceed to the fabrication of functional structures on these layers. Further refinements of the growth process are still necessary.

4.2 Droplet deposition

In this section the results of the first steps of the droplet epitaxy process (steps I and II as described in section 2.3.2) on misoriented GaAs(111)B substrates are presented. After the deposition of a 200 nm GaAs buffer

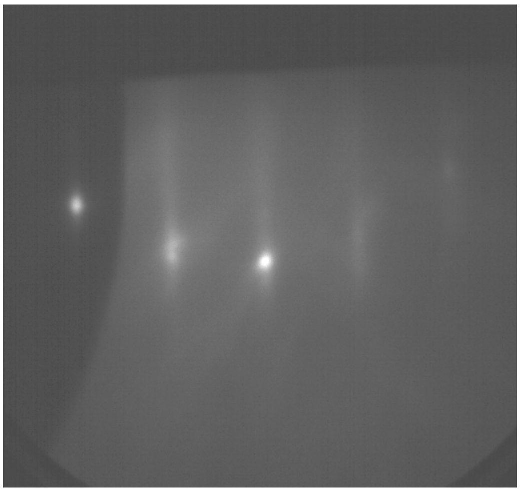

Figure 4.13: RHEED signal of the (1×1) surface phase immediately after the deposition of Ga droplets on $Al_{0.3}Ga_{0.7}As$. The picture was taken at $T = 200\,°C$. The RHEED signal of the same sample before droplet deposition is shown in Figure 4.3.

layer and a 100 nm $Al_{0.3}Ga_{0.7}As$ buffer layer (in case of Ga droplets) T_{sub} is lowered to T_{dep} and the As flux is stopped. After a 2 min break to stabilize the temperature and remove residual As from the chamber, group III droplets are deposited. A RHEED measurement of the still As rich (2×2) reconstruction at this moment during the process can be seen in Figure 4.3. In step I $d_{\mathrm{sat}} = 1.5\,\mathrm{ML}$ of the current surface group III composition (so Ga or AlGa) is deposited to saturate the surface with metal. This amount was reported to be sufficient for the (2×2) reconstruction [119, 147]. After a 30 s pause, the droplet material is deposited in step II. After another 30 s pause the sample is cooled down or immediately taken to the preparation chamber if $T_{\mathrm{dep}} \leq 200\,°C$. The samples were then taken out of the MBE system through the loadlock chamber and characterized with the AFM. A RHEED measurement of the sample during the last pause is shown in Figure 4.13. The (2×2) reconstruction was visibly replaced by a (1×1) phase signifying that the surface is indeed no longer As terminated. There is, however, no spotty patter which can be related to a 2D-3D growth transition. This is not surprising since the droplets are still liquid at this stage.

Since the density of QDs and droplets n is typically decided by this step a strong emphasis is placed on the control of n in this section. The possible emergence of asymmetries in the droplets and their general morphology is also investigated.

4.2.1 Ga droplets on $\mathrm{Al_{0.3}Ga_{0.7}As(111)B}$

In this section the first step towards the main objective of this thesis, the fabrication of strain-free GaAs QDs, is shown. As this type of QDs have been mainly fabricated on (100) and (111)A substrates up till now, the shown results are compared to the published literature of GaAs QDs fabricated by DE on these surfaces.

In all samples the deposition rates of Ga and Al were not changed from the rates for planar growth

$$\begin{aligned} r_{\mathrm{Ga}} &= 0.35\,\mathrm{ML/s} \approx 0.1\,\mathrm{nm\,s^{-1}} \\ r_{\mathrm{Al}} &= 0.175\,\mathrm{ML/s} \approx 0.05\,\mathrm{nm\,s^{-1}} \end{aligned}$$

This is advantageous since the effusion cell temperatures do not have to be changed during the recipes and a higher growth rate stability is achieved. During this thesis T_{dep} was varied in a range of 100 °C and 300 °C. The amount of droplet material d, which was deposited after $d_{\mathrm{sat}} = 1.5\,\mathrm{ML}$ $\mathrm{Al_{0.3}Ga_{0.7}}$, was varied from 1.25 ML to 2.5 ML.

Droplet density

Surface micrographs of the limit temperatures and an intermediate case of $T_{\mathrm{dep}} = 200\,°\mathrm{C}$ are shown in Figure 4.14 with $d = 2.0\,\mathrm{ML}$ in $t_{\mathrm{dep}} = 5.7\,\mathrm{s}$. As our AFM can only measure a maximum of $(9.81\,\mu\mathrm{m})^2$ in one shot, the low n of the sample grown with $T_{\mathrm{dep}} = 300\,°\mathrm{C}$ necessitates the use of an optical microscope in the differential interference contrast color mode to be able to obtain proper droplet ensemble. Measurements on multiple different

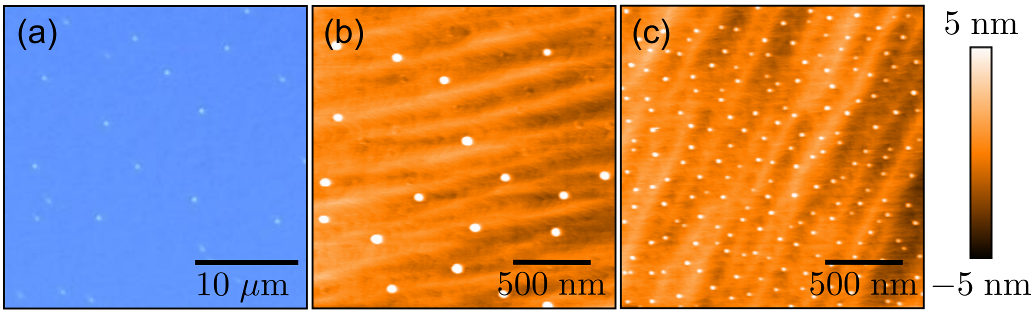

Figure 4.14: Optical microscopy and AFM images of Ga droplets deposited at $T_{\mathrm{dep}} = 300\,°\mathrm{C}$ (a, A0352), $200\,°\mathrm{C}$ (b, A0359) and $100\,°\mathrm{C}$ (c, A0356). The surface densities of the droplets are $n = 2.7 \times 10^6\,\mathrm{cm}^{-2}$, $5.0 \times 10^8\,\mathrm{cm}^{-2}$ and $4.9 \times 10^9\,\mathrm{cm}^{-2}$, respectively.

spots of the samples shown in this thesis confirm that the displayed areas are indeed typical. No gradient in density or size of the droplets could be detected in any sample direction so that it can be concluded that the samples are homogeneous in the center with a distance of approximately 5 mm from the growth borders where the substrate is covered by the sample holder during epitaxy. Throughout this thesis n is always calculated from multiple micrographs so that at least a few hundred droplets/QDs and their respective areas are considered and the statistical error is kept low.

Note how n increases strongly with decreasing T_{dep} and the size of the droplets decreases, as is expected from theory. This behavior can be observed for all samples with surface Ga droplets or GaAs QDs. The measured droplet/QD densities n of every fabricated sample with surface Ga droplets and GaAs QDs in dependence on T_{dep} are shown in Figure 4.15. The shown fit to the data points with $d = 2.0\,\mathrm{ML}$, and thus $t_{\mathrm{dep}} = 5.7\,\mathrm{s}$, corresponds to the scaling law equation 2.6

$$n = C \left[\frac{h}{2k_B} \frac{1}{T_{\mathrm{dep}}} \exp\left(\frac{E_n}{k_B T_{\mathrm{dep}}} \right)^{-1} + t_{\mathrm{dep}} \exp\left(\frac{E_n + E_r}{k_B T_{\mathrm{dep}}} \right)^{-1} \right]^{-1} .$$

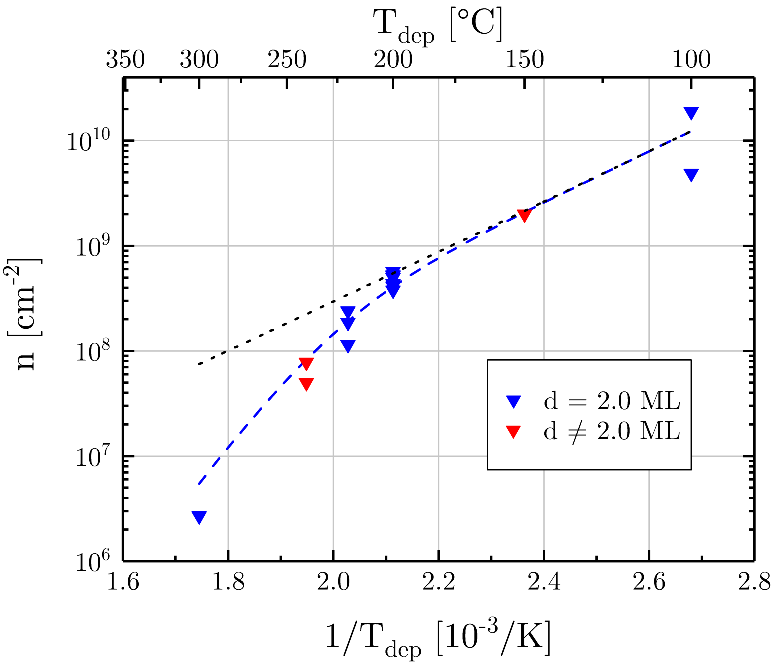

Figure 4.15: Plot of droplet/QD density n over deposition temperature T_{dep} for every fabricated sample with uncapped Ga droplets or GaAs QDs. The scaling law equation 2.6 was fitted to the data with $d = 2.0\,\text{ML}$. The dotted line represents the classical nucleation part of the fit without ripening. The high difference in n of the samples grown at 100 °C is due to poor temperature control at these low temperatures for which the MBE system is not optimized. All samples which contribute to this plot are named in appendix B.

This fit, with fitting parameters

$$\begin{aligned} \text{proportionality constant } C &= 10^{-4}\,\text{s}\,\text{cm}^{-2} \quad , \\ \text{nucleation energy } E_n &= (0.51 \pm 0.10)\,\text{eV} \quad , \\ \text{Ostwald ripening energy } E_r &= (0.80 \pm 0.08)\,\text{eV} \quad , \end{aligned}$$

agrees very well with the experimental behavior. Even the samples with slightly deviating d and t_{dep}, which did not contribute to the fit, show good agreement. Especially the fact that the data points obviously do not lay on a straight line show that the inclusion of Ostwald ripening into the model is necessary. Unfortunately $E_n = \frac{E_i + iE_d}{i+2.5}$ cannot be separated to the constituent Ga adatom diffusion activation energies E_d and critical nucleus formation energy E_i since the critical nucleus size i is not known. Calculating i is possible by using the fact that $C \propto r_{\mathrm{Ga}}^{p_n}$. Further experiments with varying deposition rates r_{Ga} and a constant T_{dep} (preferably low to make Ostwald ripening negligible and decrease the influence of a changing t_{dep}) are necessary to use this relation. Due to the advantages of constant rates as noted above, such experiments would only complicate the growth procedure by introducing additional error sources and are thus not part of this thesis. The additional insights in the nucleation process would not directly aid the fabrication of QDs and thus currently do not justify dedicated experiments/samples.

Compared to results which have been reported for Ga droplet deposition on GaAs(100) and GaAs(111)A substrates T_{dep} has to be chosen much lower on GaAs(111)B to achieve comparable droplet densities. In case of n in mid-range $10^8\,\mathrm{cm}^2$ with similar other growth parameters $n = 8.5 \times 10^8\,\mathrm{cm}^{-2}$ was reported for $T_{\mathrm{dep}} = 400\,°\mathrm{C}$ on (111)A [16] and $n = 6 \times 10^8\,\mathrm{cm}^{-2}$ for $T_{\mathrm{dep}} = 350\,°\mathrm{C}$ on (100) [115]. These temperatures are 200 K and 150 K above the values we found. This general difference between the surface orientations is true for the whole range of T_{dep}: The extended scaling law model was applied on Ga droplet deposition on $\mathrm{Al_{0.3}Ga_{0.7}As}$(100) by Heyn *et al.* [111] and on GaAs(100) and GaAs(111)A by Ohtake *et al.* [147]. The reported values for E_n on (100) (0.225 eV for GaAs and 0.32 eV for $\mathrm{Al_{0.3}Ga_{0.7}As}$) and GaAs(111)A (0.13 eV) are significantly smaller than the 0.51 eV measured on $\mathrm{Al_{0.3}Ga_{0.7}As}$(111)B here.

From the scaling law itself one would expect an increased n for higher E_n (check section 2.3.2) but the opposite is observed here as well as in the literature. A strong change in C over multiple orders of magnitude for changing surface orientations is necessary for this behavior. Unfortunately the values of C are not given in both papers. To clarify this, the influence of the different surfaces on the proportionality factor C has to be scrutinized more deeply in the future. E_r, on the other hand, follows the expected trend with $E_r = 1.5\,\mathrm{eV}$ for (100), $1.67\,\mathrm{eV}$ for (111)A and $0.80\,\mathrm{eV}$ for (111)B. This means that the potential barrier to remove one nucleus by Ostwald ripening is the lowest for (111)B. This is also again consistent with the reported diffusion lengths l of Ga on these surfaces which obey $l_{\mathrm{GaAs}(111)B} \gg l_{\mathrm{GaAs}(100)} \gg l_{\mathrm{GaAs}(111)A}$ with at least an order of magnitude between each value at equal T_{sub} [58].

It has to be concluded that the diffusion of Ga atoms on the (111)B surface is enhanced which leads to generally lower droplet densities. This enhancement is, however, not necessarily due to a lower diffusion barrier E_d but can also be due to a higher diffusion time τ. It has actually been reported that Ga atoms on a GaAs(111)B surface, in the absence of As, exhibit a slightly higher $E_{d,(111)B} = (345 \pm 11)\,\mathrm{meV}$ than on GaAs(111)A ($E_{d,(111)A} = (315 \pm 5)\,\mathrm{meV}$) and GaAs(100) ($E_{d,(100)} = (293 \pm 16)\,\mathrm{meV}$) at temperatures typical for droplet deposition and still show the highest l [58]. The strongly different τ are mainly explained by different stable nucleus sizes i which are reported as $i = 1$ for a GaAs(111)A surface and $i = 5$ for GaAs(100) [147]. It is thus reasonable to expect an even higher i in our case but, as mentioned above, no corresponding experiments were performed as the constant r_{Ga} would have to be changed during the recipe.

Droplet morphology

Higher-resolution AFM pictures of single Ga droplets are shown in Figure 4.16. The samples are the same as shown in Figure 4.14. Note that monolayer steps are visible which signifies that the surface is still smooth after droplet deposition. The droplets are larger than the monolayer terraces and cover multiple steps. No trace of alignment to the steps can be seen. While the droplets deposited at lower T_{dep} appear circular, the droplet with $T_{\mathrm{dep}} = 300\,^{\circ}\mathrm{C}$ shows a non-circular base. To illustrate the size difference of the droplets and their symmetry, line-scans along the horizontal (x) and vertical (y) direction were performed and are seen in Figure 4.17. In this representation the massively different sizes of the droplets can be better

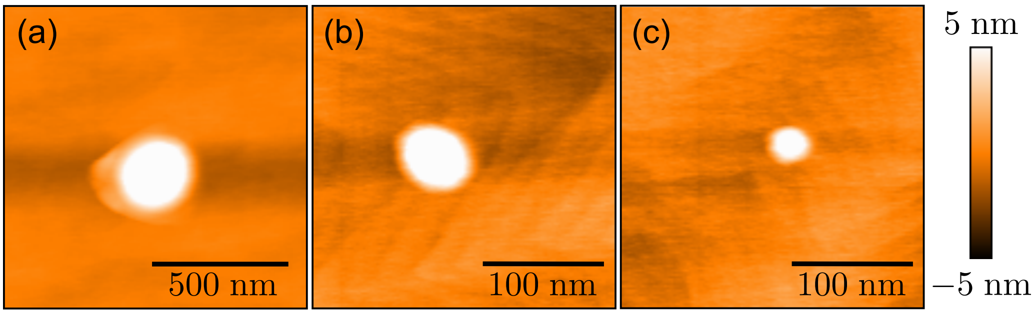

Figure 4.16: AFM images of typical, randomly picked, single Ga droplets deposited at $T_{\text{dep}} = 300\,°\text{C}$ (a), 200 °C (b) and 100 °C (c) corresponding to the ensemble measurements shown in Figure. 4.14. The color scale in (a) is in the range of [−15 nm; 15 nm].

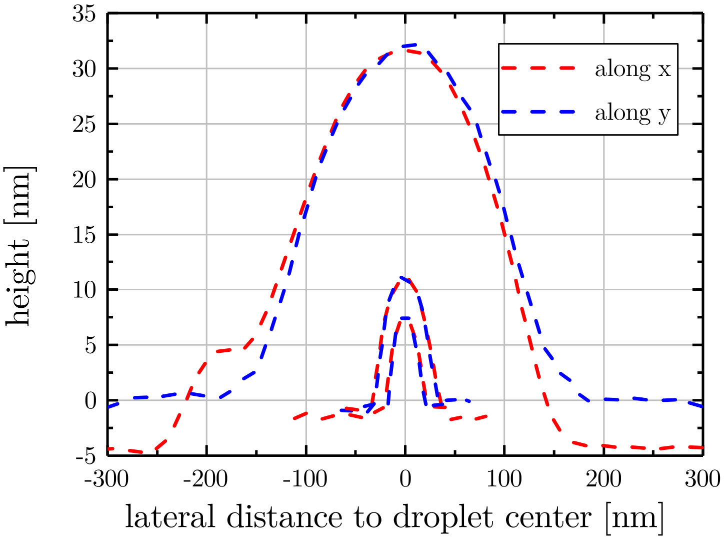

Figure 4.17: Horizontal line-scan of a higher-resolution AFM measurement of the droplets shown in Figure 4.16 along perpendicular directions. The small, intermediate and large droplet was deposited at 100 °C, 200 °C and 300 °C, respectively. The base-line deviation, especially of the biggest droplet, along y is an artifact of the line-fitting algorithm, which also creates the horizontal "shadows" in Figure 4.16. The origin of this artifact is further detailed in section 3.2.

appreciated. The smaller droplets are symmetric within the measurement accuracy and no influence by the anisotropy introduced by the misorientation can be seen.

For a more statistical analysis multiple droplet line-scans were performed on the three samples to acquire their height h_d and base diameter d_b. The resulting mean values are shown in Table 4.1. The broad size distributions with standard deviations between 14 % and 17 % for h_d are typical for the DE process. The volume of each droplet V_d was calculated by assuming a spherical-cap shape with

$$V_d = \frac{\pi}{6} h_d \left(\frac{3}{4} d_b^2 + h_d^2 \right) \quad . \tag{4.1}$$

The strong change in size with changing T_{dep} already seen for the single droplets is obviously a collective behavior of the whole ensemble. A decrease of size with increasing n is, of course, expected due to material conservation which should hold because no reevaporation is present. This can, however, be checked by calculating the number of Ga atoms per droplet N_d using the

Table 4.1: Average structural properties of single Ga droplets on samples shown in Figure 4.14. 20-30 single droplets were characterized by AFM for each ensemble to calculate the arithmetic mean and its standard deviation. Densities were calculated from low-resolution ensemble droplet AFM and optical microscope measurements.

T_{dep} [°C]	300	200	100
n [cm^{-2}]	2.7×10^6	5.0×10^8	4.9×10^9
h_d [nm]	37 ± 5	12 ± 2	6.5 ± 0.9
d_b [nm]	480 ± 30	85 ± 10	38 ± 3
V_d [10^3 nm^3]	3400 ± 700	36 ± 12	3.9 ± 0.9
N_d [10^5]	1700 ± 400	19 ± 6	2.0 ± 0.5
η_{Ga} [%]	38 ± 8	74 ± 24	78 ± 18
sample	A0352	A0359	A0356

atomic volume of Ga $\bar{V}_{\mathrm{Ga}} = 11.803\,\mathrm{cm}^3\,\mathrm{mol}^{-1}$ [152]. Multiplying the result with n and comparing the product with the areal density of deposited Ga atoms $r_{\mathrm{Ga}} \cdot t_{\mathrm{dep}}$ yields the fraction of deposited Ga in droplets η_{Ga}. The result in the last row of the table shows that for all T_{dep} the amount of Ga in the droplets is below the expected 100 %. While the amount of Ga which contributes to droplet formation is, especially when considering the error, close to this at low T_{dep}, for $T_{\mathrm{dep}} = 300\,°\mathrm{C}$ a large discrepancy is apparent. A likely explanation is etching of the droplet into the substrate, as detailed in section 2.3.2, which submerges the droplet partially and decreases the height measurable by AFM. Other possible explanations, which are independent of T_{dep}, include the possibility that the surface saturation during step I is incomplete or that residual As in the chamber slowly crystallizes the surface between the droplets which is then resaturated by droplet material. Crystallization due to residual As is, however, very unlikely because crystallized QDs, which underwent much longer pauses in metallic form, show a very similar deficit as will be shown in section 4.3.1.

In conclusion, it was demonstrated that the Ga droplets deposited with

$$\begin{aligned} T_{\mathrm{dep}} &= 200\,°\mathrm{C} \\ d &= 2.0\,\mathrm{ML} \end{aligned}$$

on misoriented GaAa(111)B substrates are proper candidates for the fabrication of GaAs QDs. This is on the one hand due to the density in the order of $10^8\,\mathrm{cm}^{-2}$, which is suitable for optical characterization of single QDs as well as for ensemble characterizations by AFM. On the other hand the droplets show a good size well below the De Broglie wavelength at low temperatures, to ensure quantization, but above the average terrace width. This decreases the likelihood of crystallization conforming to the steps and introducing the asymmetry of the misoriented substrate to the QDs. Crystallization of these droplets will be presented in section 4.3.1.

4.2.2 In droplets on GaAs(111)B

The fabrication of InAs QDs is generally interesting due to their potential emission in the telecommunication wavelengths 1.3 µm and 1.55 µm. While InAs is not strain-free on GaAs(111)B the direction of piezoelectric fields is expected to point into the growth direction. As a result the in-plane symmetry should not be broken and a significantly lowered FSS in comparison to (100) is expected. Because of the suppression of the S-K growth mode on (111)B, droplet epitaxy is a promising candidate for self-assembled QD fabrication for InAs QDs too.

In droplets were deposited with the same rate as the previous Ga droplets $r_{\mathrm{In}} = 0.35\,\mathrm{ML/s} \approx 0.1\,\mathrm{nm\,s^{-1}}$ and the same amount $d = 2.0\,\mathrm{ML}$ after saturation of the surface with 1.5 ML Ga on a GaAs buffer layer. The most promising result with $T_{\mathrm{dep}} = 50\,°\mathrm{C}$ is shown in Figure 4.18. There is no indication that the T_{dep} below the melting point of In at 156.6 °C inhibits the adatom diffusion. This is consistent with reports that the In melting point can be lowered by more than 100 K in case of In nanostructures [153]. Compared to the deposition of Ga droplets the density $n = 7.7 \times 10^{8}\,\mathrm{cm^{-2}}$ measured at this temperature is very low. This was the highest achievable density as T_{dep} is already at the lower limit of our MBE system and beyond the limit of reliable temperature control. r_{In} is also already exceptionally high when compared to the usual use cases. Due to this no reliable quantitative analysis of In droplet nucleation, as shown in the previous chapter, can be performed. Plausible reasons are a strongly enhanced In adatom diffusion and maybe increased size of the critical In nucleus compared to the Ga case. The average droplet height $h_d = 3.2\,\mathrm{nm}$ and base diameter $d_b = 50\,\mathrm{nm}$ are quite small for this density so that the indium in the droplet accounts for only 10 % of deposited In. The origin of this deficit could not be discovered. Nonetheless the crystallization of these droplets is presented in section 4.3.2.

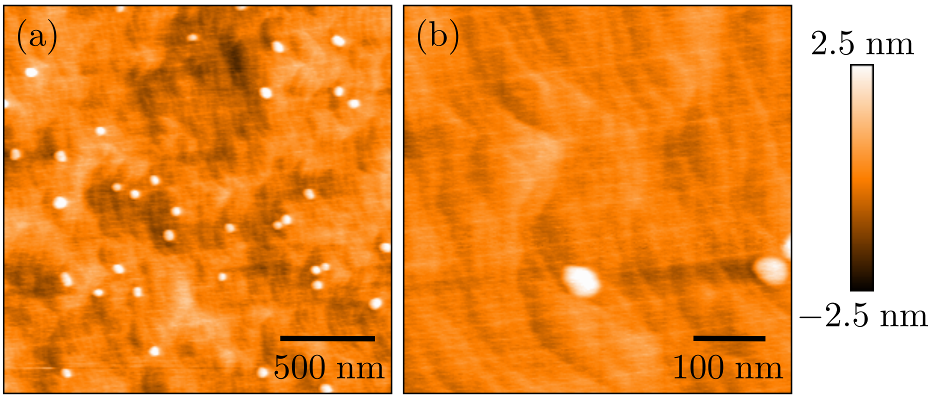

Figure 4.18: Low (a) and high (b) resolution AFM measurements of sample A0603 with In droplets deposited at 50 °C on a GaAs(111)B buffer layer.

4.3 Droplet crystallization and annealing

In this section the results of the crystallization and subsequent annealing (steps III-V in section 2.3.2) of metallic droplets on misoriented GaAs(111)B are presented. As the annealing step is an important way to assure a proper crystallization step they are shown here together.

After droplet deposition, T_{sub} is lowered to the crystallization temperature T_{As} in an up to 60 min long ramp. During this time the substrate shutter is closed to prevent residual As and other contaminants from reaching the sample surface. The lowest $T_{\mathrm{As}} = 35\,°\mathrm{C}$ is achieved by switching the substrate heater completely off at $T_{\mathrm{sub}} = 100\,°\mathrm{C}$ and waiting for 30 min. To wait for an additional 30 min decreases the measured temperature only to $T_{\mathrm{sub}} = 18\,°\mathrm{C}$. The droplets are then crystallized by opening the substrate shutter and As valve to achieve approximately $p_{\mathrm{As}} = 2.2 \times 10^{-5}$ mbar. At this point the (1×1) RHEED pattern vanishes. During this stage T_{sub} is kept constant or, in case of $T_{\mathrm{As}} = 35\,°\mathrm{C}$, the heater is kept off. After the crystallization time t_{As} the sample is heated to the annealing temperature T_{an} with a ramp of $10\,\mathrm{K\,min^{-1}}$ under constant As flux. At T_{an} the QDs are annealed for the annealing time t_{an} and then cooled down to $T_{\mathrm{sub}} = 200\,°\mathrm{C}$ fast and taken out of the MBE system for AFM measurements. The slowly reemerging

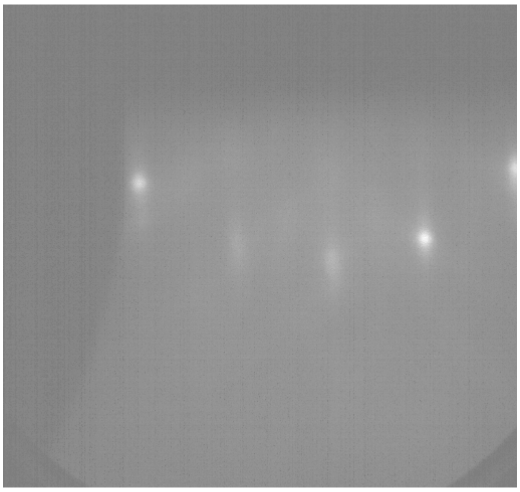

Figure 4.19: RHEED signal of the (1×1) surface phase during annealing of GaAs QDs on $\mathrm{Al_{0.3}Ga_{0.7}As}$ at $T_{\mathrm{an}} = 350\,°\mathrm{C}$ during the fabrication of sample A0399. The electron beam intensity had to be strongly increased to make the shown pattern visible. This also scaled up the background brightness.

RHEED signal during the annealing is shown in Figure. 4.19. While the (1×1) diffraction pattern is clearly visible, the expected multiple spots due to the 3D-nature of the QDs (as predicted in section 3.1.3) can only be seen very weakly and appear as slight background modulation. This is explained by the low QD density $n \approx 5 \times 10^8\,\mathrm{cm^{-2}}$ which provides for large, smooth areas between QDs well above the coherence length of the RHEED electrons.

4.3.1 GaAs quantum dots

In this section the crystallization and annealing of strain-free surface GaAs QDs is presented. Figure 4.20 shows the results of different crystallization attempts of Ga droplets with $t_{\mathrm{As}} = 3\,\mathrm{min}$ without annealing. They were prepared identically to the ones characterized in section 4.2.1 with

$$\begin{aligned} T_{\mathrm{dep}} &= 200\,°\mathrm{C} & t_{\mathrm{dep}} &= 5.7\,\mathrm{s} \\ r_{\mathrm{Ga}} &= 0.35\,\mathrm{ML/s} & r_{\mathrm{Al}} &= 0.175\,\mathrm{ML/s} \\ d &= 2.0\,\mathrm{ML} & d_{\mathrm{sat}} &= 1.5\,\mathrm{ML} \end{aligned}$$

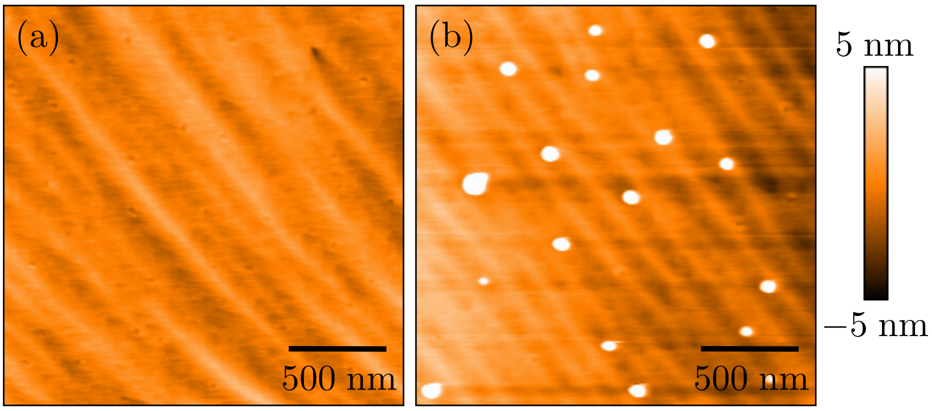

Figure 4.20: AFM images of DE samples after the crystallization step but before annealing. The crystallization parameters are $t_{\mathrm{As}} = 3\,\mathrm{min}$ and $T_{\mathrm{As}} = 100\,°\mathrm{C}$ for (a, A0364) and $T_{\mathrm{As}} = 35\,°\mathrm{C}$ for (b, A0375).

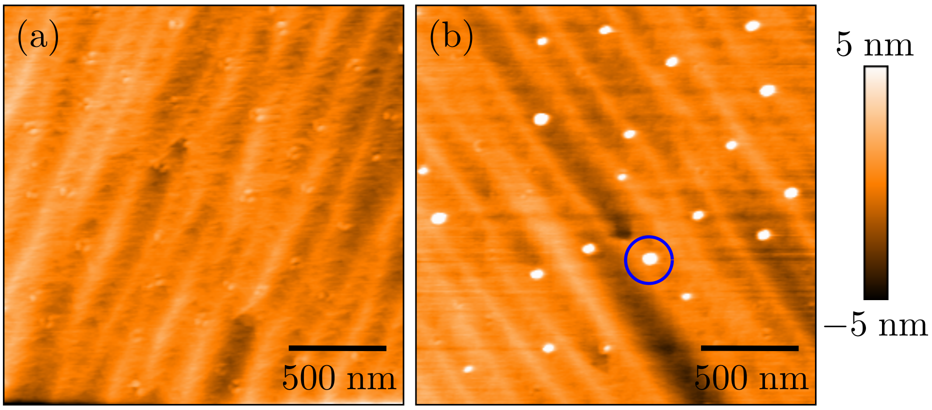

Figure 4.21: AFM images of DE samples after the crystallization and annealing step. The annealing parameters are $t_{\mathrm{an}} = 5\,\mathrm{min}$ and $T_{\mathrm{an}} = 350\,°\mathrm{C}$. The crystallization parameters are $T_{\mathrm{As}} = 35\,°\mathrm{C}$ and $t_{\mathrm{As}} = 3\,\mathrm{min}$ (a, A0382) and $t_{\mathrm{As}} = 30\,\mathrm{min}$ for (b, A0393). The QD marked by a blue circle is shown with higher resolution in Figures 4.23 & 4.24.

It is obvious that the crystallization at $T_{\mathrm{As}} = 100\,°\mathrm{C}$ did not yield QDs but a mostly smooth surface with $\sigma_q = 0.67\,\mathrm{nm}$. When scrutinized closely, small ring-hole nanostructures with a $n \approx 6 \times 10^8\,\mathrm{cm}^{-2}$ are visible on the surface. As this is close to the expected droplet density, it is probable that each hole-ring nanostructure is the result of a crystallized droplet. The crystallization at $T_{\mathrm{As}} = 35\,°\mathrm{C}$ on the other hand does yield compact nanostructures. These are, however, not QDs but GaAs shells with a liquid Ga core. This can be proven by applying the annealing step to an identically prepared sample with $t_{\mathrm{an}} = 5\,\mathrm{min}$ at $T_{\mathrm{an}} = 350\,°\mathrm{C}$ as shown in Figure 4.21(a). The surface again shows only ring-hole nanostructures. But this time each ring is separated into three segments which form a triangle around the hole and are slightly higher and thus better visible in the AFM measurement. When increasing T_{sub} the Ga core starts to etch the thin GaAs shell and afterwards spreads onto the surrounding surface which is kept As rich by the high As flux. Increasing t_{As} to 30 min results in completely crystallized GaAs QDs, which are largely stable against annealing at this temperature, as shown in Figure 4.21(b).

Whether the GaAs shells, which form for low T_{As}, result from polycrystalline heterogeneous nucleation or the Mullins-Sekerka instability is unknown. As the former can be recrystallized into epitaxial GaAs QDs during annealing [107], even the presence of luminescence from properly crystallized QDs cannot decide which shell formation mechanism is present here. The visibly worse surface roughness in the shown crystallized samples can be explained by the low T_{As} which is several 100 K below the optimum growth temperatures of $T_{\mathrm{sub}} = 590\,°\mathrm{C}$ so that proper step-flow growth cannot be expected.

The height distribution of QDs fabricated this way is shown in Figure 4.22. The height is obviously not distributed normally but, as is indicated by the smoothed line, can be described as a strongly overlapping, rather broad bimodal distribution.

In the shown AFM measurements the QDs exhibit a notable horizontal elongation. To investigate this possible asymmetry a higher-resolution AFM scan with $(4\,\mathrm{nm})^2$ pixel size of the QD marked in Figure 4.21(b) is performed. This QD was chosen because it is rather large and shows a well pronounced elongation. As measurements with one very high feature and otherwise flat surface are very susceptible to the line-fitting artifact, manual line- and mean-fits were performed to remove it here. The horizontal direction, along which the AFM needle performs single line-scans, is x. The direction along which

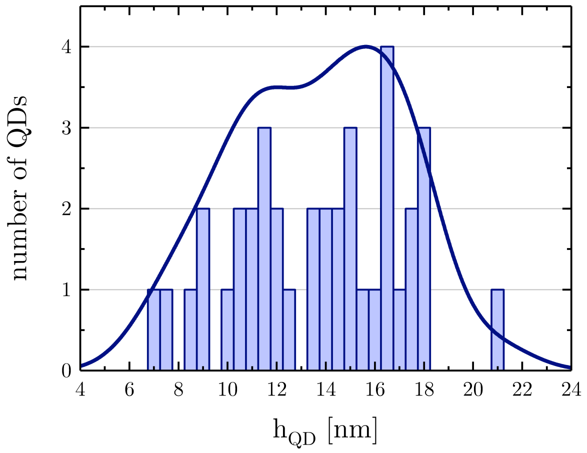

Figure 4.22: Histogram of QD heights for $T_{\text{an}} = 350\,°\text{C}$ measured on sample A0393. The kernel-smoothed histogram data (blue line) suggests a bimodal height distribution with strong overlap.

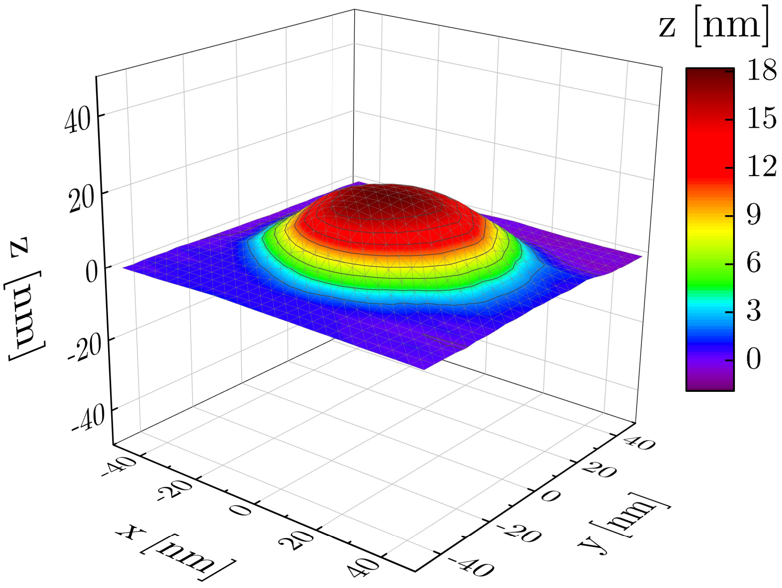

Figure 4.23: Isometric AFM image of the QD marked in Figure 4.21(b). The spherical-cap or lens shape is apparent.

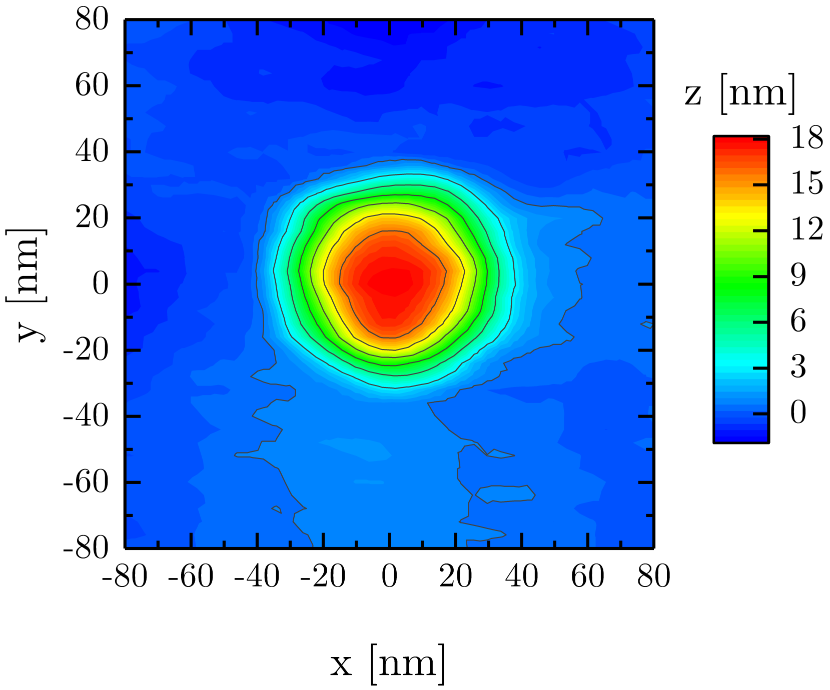

Figure 4.24: Isometric AFM contour plot of the QD marked in Figure 4.21(b) with the same data as used in Figure 4.23.

the line-scans are stacked to form the picture is y, the measured height is z. The resulting isometric 3D plot of the QD is shown in Figure 4.23. It is visible that the QD has a broad plateau on top which validates the spherical-cap approximation instead of 2D Gaussian function or similar. While it appears rotationally symmetric in this representation, the contour plot of the same data shown in Figure 4.24 again shows a very slight horizontal elongation. To quantify this, the full width at half maximum (FWHM) values of the QD along x and y through its center are calculated as

$$\begin{aligned} FWHM_x &= 53.1\,\mathrm{nm} \\ FWHM_y &= 49.1\,\mathrm{nm} \quad . \end{aligned}$$

The difference is precisely the width of one pixel in the measurement. As it turns out this holds true for all resolutions and surface positions (16 measurements total) so that the asymmetry goes down with increasing magnification. It can thus be concluded that the slight apparent elongation in x is an artifact which might be due to not perfectly chosen PID parameters. It can thus be stated that the QD morphology has rotational symmetry in the growth plane within the measurement accuracy.

In the following the influence of higher T_{an} on successfully fabricated GaAs QDs with

$$\begin{aligned} T_{\mathrm{As}} &= 35\,^{\circ}\mathrm{C} \\ t_{\mathrm{As}} &= 30\,\mathrm{min} \\ t_{\mathrm{an}} &= 5\,\mathrm{min} \end{aligned}$$

is presented. Figure 4.25 shows QDs annealed at different T_{an}. At $T_{\mathrm{an}} = 450\,^{\circ}\mathrm{C}$, 100 K above what was used before, some QDs changed from the circular shape to a slightly triangular shape. In the shown color scale the QD size seems unchanged which signifies that the base width is constant with T_{an}. At $T_{\mathrm{an}} = 500\,^{\circ}\mathrm{C}$ the triangular shape is very pronounced and a decreasing height becomes visible alongside a larger base area. The visible QDs range from a height of 4 nm to nearly vanished QDs with heights below 1 nm. At $T_{\mathrm{an}} = 550\,^{\circ}\mathrm{C}$, which is only 40 K below optimal planar growth temperatures, the QDs vanished completely leaving a smooth surface with $\sigma_q = 0.34\,\mathrm{nm}$.

As the flat surface is thermodynamically preferential a stronger diffusion due to the higher T_{an} is consistent with these findings. The triangle as intermediate shape between spherical cap and flat surface can be explained by a higher stability of the $[01\bar{1}]$, $[1\bar{1}0]$ and $[10\bar{1}]$ facets. Note that the C_{3v} symmetry is not broken by a flat island with an equilateral triangle as base and the named facets as side walls.

Horizontal line scans of randomly chosen QDs with different T_{an} and an exemplary droplet, from which the QDs were fabricated, are shown in Figure 4.26. This illustrates the size evolution from the Ga droplet to the

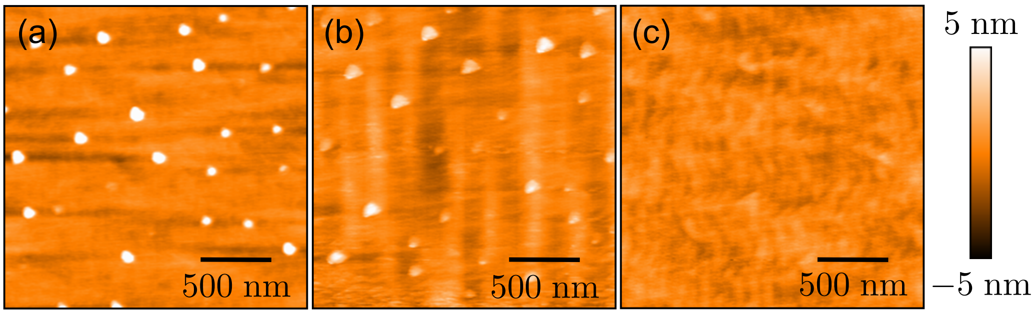

Figure 4.25: AFM images of identically prepared GaAs QDs annealed with $T_{\mathrm{an}} = 450\,^{\circ}\mathrm{C}$ (a, A0427), $500\,^{\circ}\mathrm{C}$ (b, A0435) and $550\,^{\circ}\mathrm{C}$ (c, A0431) for $t_{\mathrm{an}} = 5\,\mathrm{min}$. n stays generally constant if there are QDs at all. This, again, validates the prediction that n is controlled by the droplet deposition step.

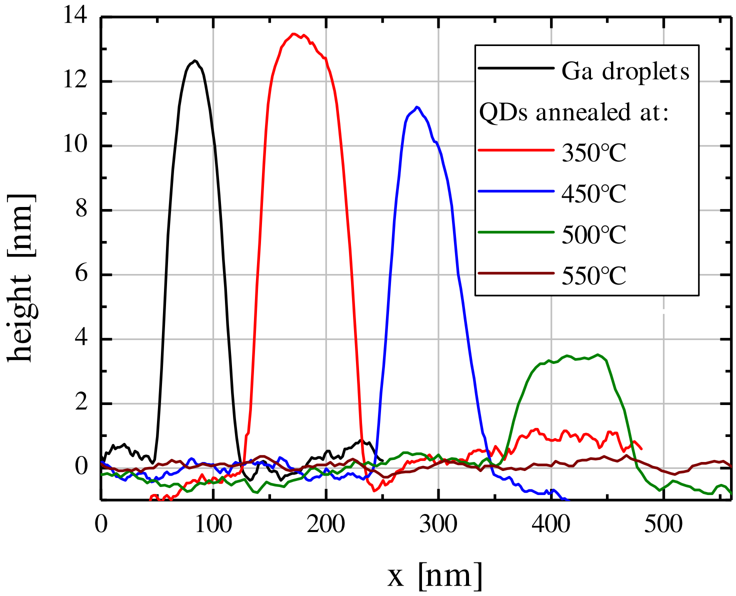

Figure 4.26: AFM line scans of a Ga droplet fabricated at $T_{\mathrm{dep}} = 200\,^{\circ}\mathrm{C}$ and randomly chosen QDs crystallized from corresponding droplets and annealed for $t_{\mathrm{an}} = 5\,\mathrm{min}$ at different T_{an}.

GaAs QDs annealed at different temperatures. The increase of size during crystallization is expected because additional As atoms are incorporated.

For $T_{\mathrm{an}} = 450\,°\mathrm{C}$ deviation of the symmetric case due to faceting is visible. While the base width d_{QD} stays largely constant the QD height h_{QD} is decreased. A nudge at the top of the QD shows that the QD material is removed mostly from the top by the thermally activated mass transport process during annealing. This is also shown to a stronger extend for the QD with $T_{\mathrm{an}} = 500\,°\mathrm{C}$ with its flat plateau as top. As a result this QD resembles a truncated pyramid more closely than a lens. Note that this mass transport during annealing may form a thin, interconnecting GaAs layer between the QDs, similar to the wetting layer in S-K grown QDs.

Analogue to the statistic analysis of the droplet morphology in Table 4.1, an ensemble of annealed QDs is characterized by line scans and the structural properties are shown in Table 4.2. The single-QD volumes V_{QD} are also calculated by approximating them as spherical caps with equation 4.1. This, of course, introduces an error due to the faceting at higher T_{an}. Consequently only the QDs annealed at 350 °C and 450 °C are included in the table. The average number of GaAs monomers per QD N_{QD} was calculated using the

Table 4.2: Average structural properties of annealed GaAs QDs measured by AFM. 20-30 single QDs were characterized for each ensemble to calculate the arithmetic mean and its standard deviation. Densities were calculated from low-resolution ensemble droplet AFM measurements. The QDs were fabricated from droplets deposited at $T_{\mathrm{dep}} = 200\,°\mathrm{C}$ with corresponding structural properties shown in Table 4.1.

T_{an} [°C]	350	450
n [cm^{-2}]	5.3×10^8	5.2×10^8
h_{QD} [nm]	15 ± 3	9 ± 3
d_{QD} [nm]	113 ± 13	104 ± 11
V_{QD} [$10^3\,\mathrm{nm}^3$]	81 ± 27	44 ± 21
N_{QD} [10^5]	18 ± 6	10 ± 5
η_{QD} [%]	76 ± 26	40 ± 20
sample	A0393	A0427

molecular volume of GaAs $\bar{V}_{\mathrm{GaAs}} = 27.201\,\mathrm{cm}^3\,\mathrm{mol}^{-1}$ [45].

For the QDs annealed at 350 °C the relative standard deviations of all quantities are the same as they were for the corresponding droplets. Also the number of Ga atoms in each nanostructure changes only slightly by 0.7×10^5 ($-4\,\%$), which is basically negligible when considering the standard deviation of 6×10^5. The same is also signified by a constant fraction of deposited Ga in droplets and QDs η_{QD}. From this, one can conclude that each droplet was crystallized and annealed without diffusion of Ga or GaAs to the surrounding surface as far as can be measured by AFM. It can thus be stated that the QDs are thermally stable at 350 °C and actually free from an interconnecting GaAs layer.

In contrast to this, for $T_{\mathrm{an}} = 450\,°\mathrm{C}$ the relative standard deviations were strongly enlarged. For the height, as an example, it increased from 17 % to 33 %. This suggests that annealing at this temperature acts differently on QDs of different sizes with the effect that smaller QDs shrink faster than bigger ones. Since the diffusion mass transport acts on the QD surface this can be explained by the higher surface-to-volume ratio of smaller QDs.

When again compared to DE of GaAs QDs on the more common (100) and (111)A substrates the trend to lower T_{sub} on (111)B for similar results continues. Crystallization of Ga droplets which result in narrow hole-rings as shown in Figure 4.20(a) with $T_{\mathrm{As}} = 100\,°\mathrm{C}$ are only known for $T_{\mathrm{As}} > 300\,°\mathrm{C}$ and very low As fluxes on (100) [107]. A typical value reported for (111)A is 200 °C [16]. This can, however, again be explained by the strongly enhanced Ga surface diffusion on (111)B which needs to be suppressed by, in our case, a low T_{As}. Incomplete droplet crystallization, as shown in Figure 4.25(a), is reported for (100) only when $t_{\mathrm{As}} < 80\,\mathrm{s}$ and low As flux are used [154]. The necessity of a longer crystallization step can be explained by the low T_{As} which slows down As diffusion into the droplet and the whole crystallization process. In contrast to this the fully crystallized GaAs QDs show the same thermal stability to uncapped annealing as GaAs QDs on (100) but, importantly, not the reported elongation in $[01\bar{1}]$ [115].

In conclusion, the successful crystallization and annealing of GaAs QDs with $n \approx 5 \times 10^8\,\mathrm{cm}^{-2}$ on AlGaAs(111)B is demonstrated. Although the very low temperatures involved are at the limit of our MBE system, the DE process could be adapted to the miscut GaAs(111)B substrate and a reproducible growth recipe could be developed. No morphological breaking of the high C_{3v} symmetry of the substrate could be detected. The response of GaAs QDs to annealing was investigated and a way to fabricate triangular QDs, which are the epitome of C_{3v} symmetry, was discovered.

4.3.2 InAs quantum dots

In this section the crystallization of In droplets, whose deposition was shown in section 4.2.2, is presented. The parameters for droplet deposition and crystallization are

$$\begin{aligned} T_\mathrm{dep} &= 50\,^\circ\mathrm{C} & t_\mathrm{dep} &= 5.7\,\mathrm{s} \\ r_\mathrm{In} &= 0.35\,\mathrm{ML/s} & r_\mathrm{Ga} &= 0.35\,\mathrm{ML/s} \\ d &= 2.0\,\mathrm{ML} & d_\mathrm{sat} &= 1.5\,\mathrm{ML} \\ T_\mathrm{As} &= 35\,^\circ\mathrm{C} & t_\mathrm{As} &= 30\,\mathrm{min} \end{aligned}$$

T_As is, in contrast to before, not reached by switching the heater off at 100 °C but at $T_\mathrm{dep} = 50\,^\circ\mathrm{C}$. The waiting time to reach T_As is consequently decreased so that crystallization was started manually when the desired temperature was reached. The result of this process without the annealing step is shown in Figure 4.27. The emerging structures are obviously of considerably lower density then the droplets in Figure 4.18 with $n = 7.7 \times 10^8\,\mathrm{cm}^{-2}$, and also much bigger. The size inhomogeneity is even larger as the one seen on GaAs QDs. The hills appear to each have a triangular base, which are still in formation, with identical facets. This, again, can be explained by the high stability of the $< \bar{1}10 >$ facets. An emergence of similar hills has already been seen in section 4.1.3 for the deposition of In-rich $\mathrm{In}_x\mathrm{Ga}_{1-x}\mathrm{As}$ layers. This suggests that the very high In adatom diffusion on GaAs(111)B is still

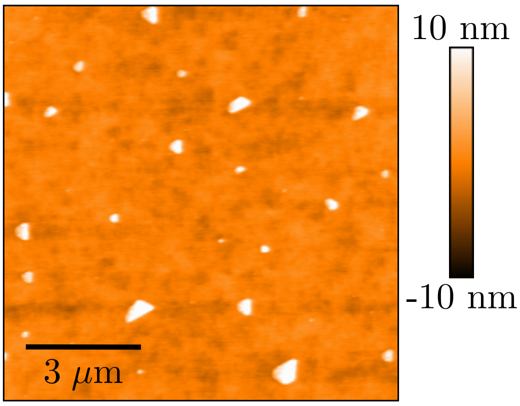

Figure 4.27: AFM measurement of crystallized In droplets on sample A0617. The density of hills is $n = 0.24 \times 10^8\,\mathrm{cm}^{-2}$.

not sufficiently quenched at this low temperatures. With edge lengths of up to 800 nm the structures cannot be expected to show fully quantized states and can thus not be called QDs. To fabricate InAs QDs by DE one would need to suppress the In adatom diffusion by different means since T_{As} cannot really be decreased further and p_{As} is already close to the maximum without risking to damage the As effusion cell in our system.

4.3.3 $\mathrm{In_{0.2}Ga_{0.8}As}$ quantum dots

As pure InAs QDs could not be fabricated, the possibility of $\mathrm{In_{0.2}Ga_{0.8}As}$ QDs is explored shortly in this section. The most promising parameters, with an acceptable T_{dep} and which result in the desired n, are

$$\begin{aligned} T_{\mathrm{dep}} &= 100\,^{\circ}\mathrm{C} & t_{\mathrm{dep}} &= 3.4\,\mathrm{s} \\ r_{\mathrm{In}} &= 0.0875\,\mathrm{ML/s} & r_{\mathrm{Ga}} &= 0.35\,\mathrm{ML/s} \\ d &= 1.5\,\mathrm{ML} & d_{\mathrm{sat}} &= 1.5\,\mathrm{ML} \\ T_{\mathrm{As}} &= 35\,^{\circ}\mathrm{C} & t_{\mathrm{As}} &= 30\,\mathrm{min} \\ T_{\mathrm{an}} &= 350\,^{\circ}\mathrm{C} & t_{\mathrm{an}} &= 5\,\mathrm{min} \end{aligned}$$

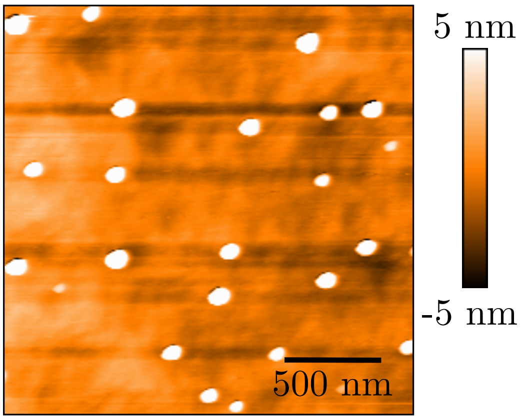

Figure 4.28: AFM measurement of $In_{0.2}Ga_{0.8}As$ QDs fabricated by DE on sample A0845. The QD density is $n = 5.3 \times 10^8\,\mathrm{cm}^{-2}$.

The resulting InGaAs QDs are shown in Figure 4.28. The QD morphology is comparable to what was found for GaAs annealed at the same temperature. While the QDs need a low T_{dep} for formation in the desired density, they are still stable to annealing at the same T_{an} as was observed for pure GaAs QDs. It can be assumed that the liquid droplets prior crystallization are homogeneous [155]. An indiscriminate crystallization of GaAs and InAs from the liquid phase is, however, not given. This might lead to a composition gradient within the QDs but was not investigated.

It is thus shown that the fabrication of In-containing QDs by DE on GaAs(111)B is possible despite the difficulties with pure InAs QDs. The optical characterization of these QDs is beyond this thesis due to the emphasis placed on unstrained GaAs QDs.

4.4 GaAs quantum dot capping and ex-situ annealing

In this section the results of capping (step VI in section 2.3.2) and ex-situ annealing of the GaAs QDs fabricated on $Al_{0.3}Ga_{0.7}As(111)B$ are presented.

After the droplets were annealed at T_{An} the As pressure is decreased to $p_{\mathrm{As}} = 1.5 \times 10^{-5}$ mbar, the standard for planar growth, and an $Al_{0.3}Ga_{0.7}As$ layer with thickness $d_{\mathrm{cap,low}}$ is deposited at this temperature. Subsequently

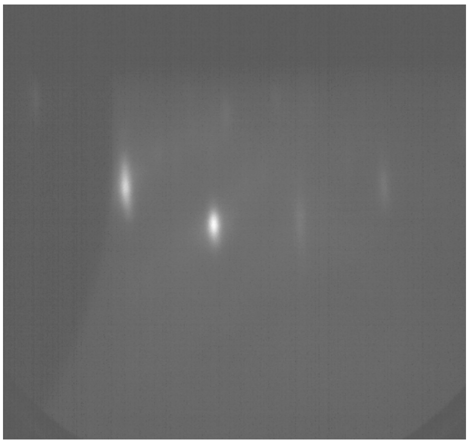

Figure 4.29: RHEED signal of sample A0399 after the complete capping process but before cooling down. A weak $(\sqrt{19} \times \sqrt{19})R \pm 23.4^\circ$ reconstruction is visible.

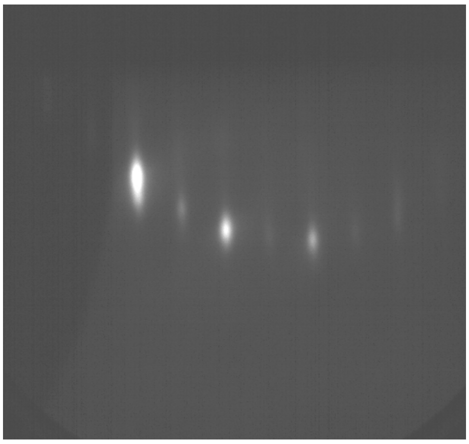

Figure 4.30: RHEED signal of sample A0399 after the complete capping process and cooling down directly before the sample is taken out of the chamber. The (2×2) reconstruction is clearly visible.

T_{sub} is increased to 590 °C so that the standard growth parameters for planar growth, as detailed in section 4.1.2, are restored. At these parameters the remaining $Al_{0.3}Ga_{0.7}As$ capping layer with thickness $d_{\text{cap,high}}$ is deposited. After the deposition of a thin GaAs layer, which prevents oxidation of the AlGaAs *ex-situ*, the samples are cooled down and taken out of the MBE chamber. In some cases an AlAs blocking layer was added below the GaAs oxidation protection layer to prevent charge carrier diffusion to and their recombination on the surface. This measure enhances the QD PL signal. RHEED measurements of a sample with capped GaAs QDs directly after growth and after cooling down are shown in Figures 4.29 & 4.30, respectively. The presence of reconstructions signifies that a GaAs(111)B surface is still present. When compared to the RHEED measurements prior DE, as shown in section 4.1.1, the spots exhibit a notable vertical elongation. This suggests that a multilevel stepped surface instead of a flat one is present.

The typical surfaces of capped samples are shown in Figure 4.31. In both cases the QDs were fabricated according to the process detailed in section 4.3.1

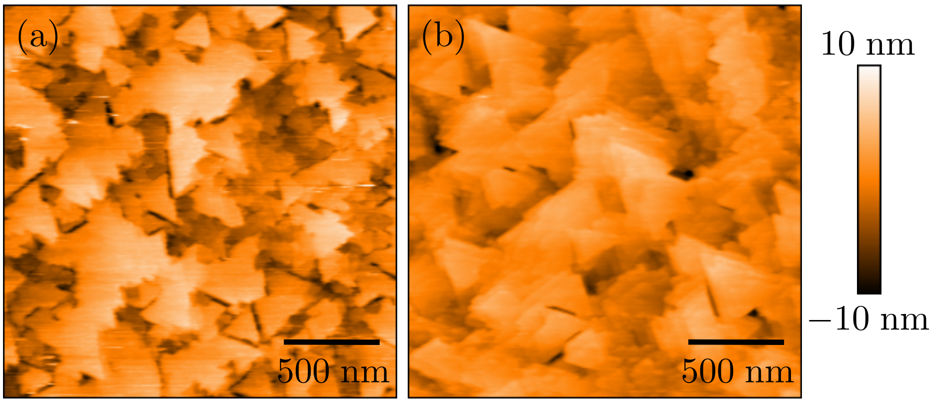

Figure 4.31: AFM measurement of capped but not annealed GaAs QDs in sample A0399 (a) and A0448 (b). The surface roughness is $\sigma_q = 2.9\,\mathrm{nm}$ and $2.0\,\mathrm{nm}$, respectively. The only difference in sample preparation is that $T_{\mathrm{an}} = 350\,°\mathrm{C}$ for (a) and $T_{\mathrm{an}} = 500\,°\mathrm{C}$ for (b).

with capping layer consisting of $d_{\mathrm{cap,low}} = 20\,\mathrm{nm}$ and $d_{\mathrm{cap,low}} = 60\,\mathrm{nm}$ with 5 nm GaAs on top. Obviously capping at the given parameters does not yield a smooth layer-by-layer growth as was achieved before. The emerging triangular structures again reflect the basic symmetry of the surface. Possible reasons for this are the not ideal growth of the capping layer at T_{an} and the disruption of the step-flow growth mode by the QDs. If the latter is the case one would expect that each QD would form a hill, mound or general artifact so that the emerging structure shows feature density comparable to the QD density. This is, however, not true as the expected $n \approx 5 \times 10^8\,\mathrm{cm}^{-2}$ would result in only 20 features in the shown area and the actual density of plateaus is considerably higher. If, on the other hand, the low T_{sub} is the main problem, the surface of the sample with higher T_{an} should be considerably smoother. While this is the case, the difference is rather small which might be due to the fact that T_{an} is still 90 K below the optimum temperature of the quite small growth window. The difference may also be due to the smaller height of the strongly annealed QDs so that no definitive decision about which effect dominates can be made. Samples with larger capping, such as A0779 with 280 nm total capping and $\sigma_q = 4.3\,\mathrm{nm}$, show larger, interconnected plateaus and deeper trenches which results in the higher roughness values. This suggests that the rough surface will not revert to the smooth surface before DE by just increasing the capping layer thickness. Despite the rough surfaces, the now buried QDs are optically active as shown in the next section. It is, however, clear that the surface quality will have to be improved before heterostructures such as Bragg mirrors can be added. Possible techniques such as migration enhanced epitaxy (MEE) [156], which is commonly employed for DE QD capping [114, 157], or additional annealing steps may lead to drastic improvement but are not part of this thesis.

After characterization by AFM, the samples are treated in the RTA oven as detailed in section 3.3. Without this process step no luminescence could be measured in our PL setup. This step is typical for DE-fabricated nanostructures in general to improve luminescence drastically [140]. Due to the extremely low T_{As} used in this thesis, a high defect density is expected in and around the QDs. The necessity of a RTA step to decrease these defects is thus even stronger. As shown by Martin Eppinger [143] the surface roughness is increased slightly by RTA with the used parameters due to the generation of a few Ga droplets on the surface by non-stoichiometric evaporation.

4.5 Optical properties of GaAs QDs

In this section the luminescence of GaAs QDs, which were fabricated on misoriented GaAs(111)B substrates by DE in the course of this thesis as detailed above, is investigated. The PL setup introduced in section 3.4 is used to characterize larger QD ensembles and a µPL setup, which belongs to the AG Zrenner[1], is used to measure the PL of individual QDs in section 4.5.2.

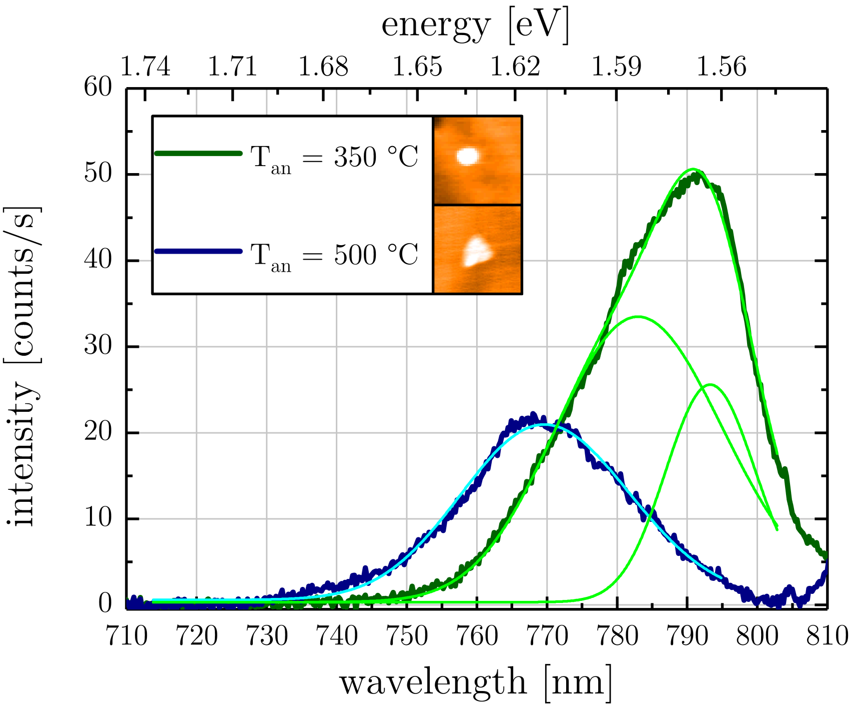

Figure 4.32: Ensemble PL spectra of otherwise equally prepared GaAs QDs with different T_{an} measured at 14 K. The small insets show the typical shape of uncapped QDs annealed at the respective temperatures. The shown fits are Gaussian on the energy scale. The characterized samples are A0399 and A0448 whose pre-annealed surfaces are shown in Figure 4.31.

4.5.1 Ensemble measurements

PL measurements of capped and annealed QDs with $n \approx 5 \times 10^8\,\mathrm{cm}^{-2}$ and different T_{an} are shown in Figure 4.32. The luminescence demonstrates that the fabricated QDs are optically active. This shows that high crystal quality was achieved, including stoichiometry very close to the ideal 1:1 case despite the very low T_{As}. Equally prepared, different pieces of the same sample show very similar results when chosen with at least 5 mm distance from the

---

[1] Nanostructure optoelectronics group at the University of Paderborn, headed by Prof. Dr. Artur Zrenner; `https://physik.uni-paderborn.de/en/zrenner/`

growth boarder, which again shows that DE fabricates a homogeneous layer of QDs over the whole sample. The strong GaAs bulk emission at higher wavelength was deliberately not measured as it saturates the detector with the used measurement parameters. No emission which can be associated with the formation of a GaAs QW could be detected. The emission of QDs annealed at 500 °C exhibit a significant blue-shift when compared to the ones annealed at 350 °C. This is consistent with their strongly decreased height from around 15 nm to below 4 nm observed in section 4.3.1 which leads to higher confinement energy in the smaller QDs. While the luminescence of the more strongly annealed QD ensemble can be well described by a Gaussian in the energy scale, the QDs annealed at lower temperatures have an asymmetric spectrum which requires a combination of not less than two Gaussians. The peak energys (and related photon wavelengths) and FWHMs of each fit are

$$\begin{aligned}
E_{\text{low } T_{\text{An}},1} &= (1.563 \pm 0.001)\,\text{eV} \mathrel{\widehat{=}} 793\,\text{nm} \quad ,\\
FWHM_{\text{low } T_{\text{An}},1} &= (30 \pm 2)\,\text{meV} \quad ,\\
E_{\text{low } T_{\text{An}},2} &= (1.584 \pm 0.002)\,\text{eV} \mathrel{\widehat{=}} 783\,\text{nm} \quad ,\\
FWHM_{\text{low } T_{\text{An}},1} &= (57 \pm 2)\,\text{meV} \quad ,\\
E_{\text{high } T_{\text{An}}} &= (1.6112 \pm 0.0002)\,\text{eV} \mathrel{\widehat{=}} 770\,\text{nm} \quad ,\\
FWHM_{\text{high } T_{\text{An}}} &= (59.2 \pm 0.4)\,\text{meV} \quad .
\end{aligned}$$

The peak shapes are independent on excitation power so that shell filling as explanation for the asymmetric peak can be excluded. In contrast to S-K QDs, which usually show Gaussian s-shell emission on ensemble measurements, QDs fabricated by DE have often been reported to show more complex ensemble emissions due to multi-modal size distributions [158]. The existence of two strongly overlapping Gaussians in the spectra is, in fact, consistent with the measured bimodal distribution of QD heights shown in Figure 4.22 since QD height, as smallest dimension of the QD, is the decisive quantity when determining the confinement energy. It is, however, contradictory that peak 2 (around 783 nm) in the PL spectrum suggests a higher number of QDs in the part of the height distribution with smaller values, which is not the case. A possible explanation would be that bigger QDs are on average less optically active since they have an increased probability to include a non-radiative defect (if these are distributed isotropically over the QD-containing layer). Annealing at high temperature, and its size-sensitive effect on smaller and larger QDs, seems to transform the QD ensemble into a normal size distribution.

The emission of QDs annealed at $T_{\mathrm{an}} = 350\,^{\circ}\mathrm{C}$ is slightly red-shifted to GaAs QDs of equal h_{QD} in $\mathrm{Al_{0.3}Ga_{0.7}As}$ reported for GaAs(100) substrates with an emission around 1.67 eV and FWHM of approximately 150 meV [159]. The same holds for the QDs annealed at higher T_{an}: GaAs QDs emitting around wavelengths as high as $770 - 780$ nm with $h_{\mathrm{QD}} = 4$ nm could only recently be realized on (111)A substrates by decreasing the Al content of the surrounding barrier to 15 % and thus decreasing the confinement potential [18]. This general shift to higher wavelengths with respect to reported GaAs QD emissions in the literature can possibly be explained by weaker intermixing of QD material with the substrate during crystallization due to the very low T_{As}.

Si-doping related emission

To be able to electrically tune the QDs a Si-doped n-$\mathrm{Al_{0.3}Ga_{0.7}As}$ back contact with $n_{\mathrm{Si}} \approx 1 \times 10^{18}\,\mathrm{cm^{-3}}$ and a i-$\mathrm{Al_{0.3}Ga_{0.7}As}$ tunnel barrier were introduced below the QDs. Ensemble PL measurements of samples with Si doping show an additional very broad luminescence signal between 800 nm and 1200 nm with a strong, narrower peak around 920 nm and a smaller shoulder around 860 nm instead of a bulk GaAs emission as can be seen in Figure 4.33. The same luminescence also manifests when an undoped sample is not annealed with proximity capping in the RTA but instead capped by $\mathrm{SiO_2}$. A subsequent removal of the capping does not remove the luminescence, which suggests that the $\mathrm{SiO_2}$ deposition is not perfect and leaves enough atomic Si on the

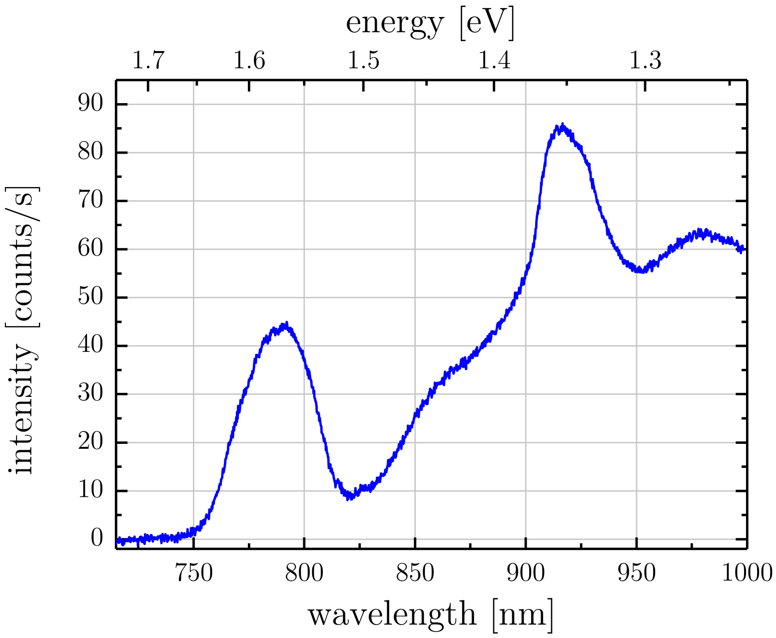

Figure 4.33: Ensemble PL spectra of GaAs QDs in sample A0779 measured at 14 K. The back contact is 300 nm thick with a tunneling barrier of 30 nm to the QDs. Due to a strong second order signal of the laser around 1050 nm the remaining (featureless) part of the broad luminescence was not measured with this integration time.

semiconductor surface which then diffuses into the sample and dopes it. One can conclude that the signal results from the interaction of Si with AlGaAs. This is backed by the observation of similar peaks reported for Si-doped, annealed $Al_{0.3}Ga_{0.7}As$ layers grown on (100) substrates by Pavesi *et al.* [160]. A peak at the energy 1.47 eV is there attributed to a complex consisting of a Ga atom on a As lattice point (Ga_{As} antisite defect) and a Si_{Ga} donor defect. A peak at 1.355 eV is attributed to a complex of a Ga vacancy with Si_{Ga}. In this publication also the diffusion of Si into the semiconductor is investigated by PL and consistent with the observation that the signal is similar to the corresponding semiconductor which is intentionally doped during growth. In conclusion, the doped $Al_{0.3}Ga_{0.7}As$ shows additional defect luminescence in the PL spectrum which suggests a lower crystal quality and demands further optimization of the growth parameters in the future. The stronger vulnerability of a pure GaAs PL signal (without defect luminescence) to Si doping on the (111)A/B surfaces in contrast to GaAs grown on (100) has also been reported by Yaremenko *et al.* [161].

4.5.2 Single-dot measurements

For single-dot measurements the QD samples were optimized by further reducing the density to $n \approx 0.5 \times 10^{8}\,\mathrm{cm}^{-2}$ to massively increase the probability of only one QD contributing to each measured spectrum. To achieve this, while keeping the QD size approximately constant, the droplet deposition parameters were changed to

$$T_{\mathrm{dep}} = 240\,^{\circ}\mathrm{C} \qquad d = 1.25\,\mathrm{ML}$$

from the values employed in section 4.3.1 (200 °C and 2.0 ML) with all other parameters kept constant. For first characterizations the samples with $T_{\mathrm{an}} = 350\,^{\circ}\mathrm{C}$ and $T_{\mathrm{an}} = 520\,^{\circ}\mathrm{C}$ have been identified as most interesting due to their different morphology. AFM measurements of uncapped QDs which correspond to each are shown in Figure 4.34. The circular and triangular QD bases at low and high T_{an}, as seen previously, are still present with the changed parameters. Samples with such a low n did not show a discernible QD peak in ensemble PL measurements.

After RTA the capped QD samples (sample structure in Figure 4.35) were processed so that an ohmic connection to the back contact and a Schottky contact on the surface allow to apply a bias to the QDs. A microscope image of the contacted samples is shown in Figure 4.36. The sequence of the contacting process is

1. Place small In pieces to the sample edges and alloy under forming gas for 5 min at 395 °C.
2. Deposit a 40 nm Au layer in regular squares. Here photolithography including oxide plasma ashing of remaining photoresist is employed.

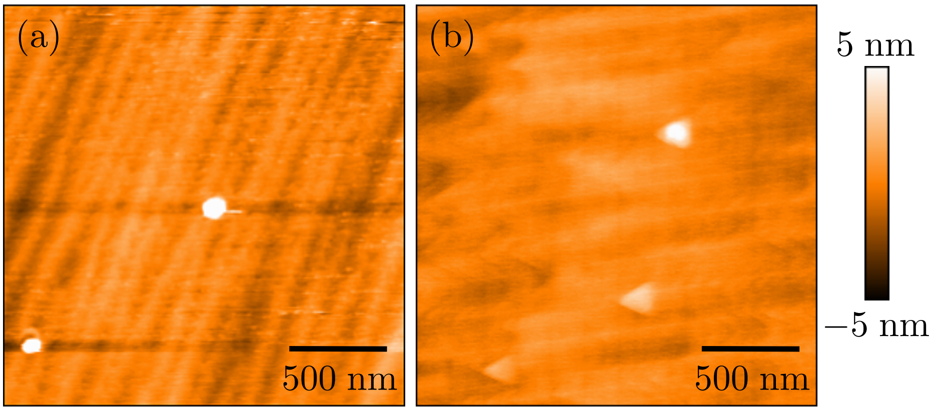

Figure 4.34: AFM measurement of sample A0811 (a) and A0828 (b) with uncapped GaAs QDs annealed at $T_{\text{an}} = 350\,^\circ\text{C}$ and $520\,^\circ\text{C}$, respectively.

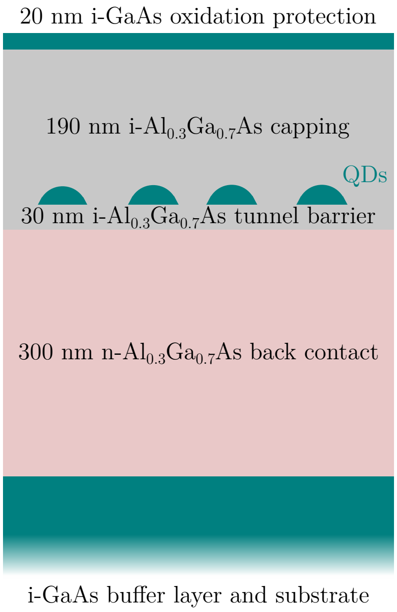

Figure 4.35: Schematic structure of samples characterized by µPL in this section.

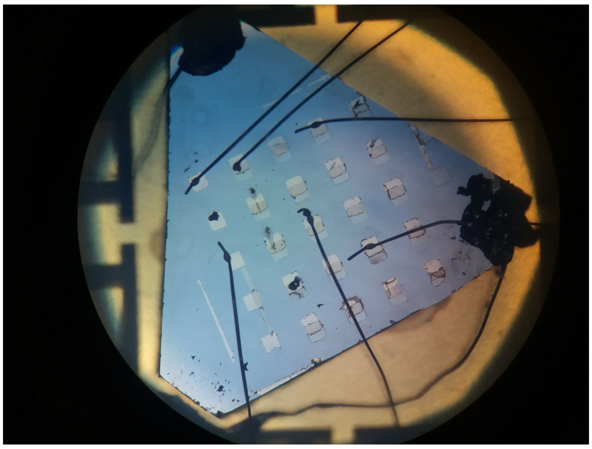

Figure 4.36: Microscope image of a piece of sample A0816 after contacting. The two edges are covered by In which provides an ohmic contact to the n-$Al_{0.3}Ga_{0.7}As$ back contact. The small squares each represent a Schottky contact.

3. Deposit a 10 nm to 20 nm semitransparent Ti layer in regular squares shifted by half an square edge using the same process.
4. Bond Au wire to the Au/In pads and connect to chip contacts.

The resulting structure allows the voltage-dependent characterization of QDs which are only covered by Ti but not by opaque Au pads and wires.

To characterize individual GaAs QDs, measurements were performed by Björn Jonas of AG Zrenner in their µPL setup. As the measurements were not performed by the author personally, a detailed description of the used setup is omitted in this thesis. For more details the PhD theses of Simon Gordon in German [162] and Ashish Kumar Rai in English [163] are recommended. The excitation source is, again, a laser emitting at 532 nm. The most prominent difference to the setup used for ensemble measurements is a generally higher performance of multiple parts in the relevant wavelength range:

- aspheric objective with numerical aperture of 0.6
- higher-resolution monochromator with 1200 mm^{-1} grid and Blaze angle of 750 nm
- Si-CCD-camera with high sensitivity between 450 nm and 950 nm
- complete submersion of sample holder in liquid He to reach temperatures below 10 K
- remote XYZ nanopositioning

A sample piece was processed for each T_{an} and characterized by µPl. The integration time for every spectrum shown here is 1 s. Unfortunately the processed piece of sample A0815 with $T_{\mathrm{an}} = 350\,°\mathrm{C}$ only had one working Schottky contact with a diode-like I-V curve under which no QD emission could be found. A QD spectrum next to a bond pad without external bias is shown in Figure 4.37 for different excitation powers. Several intensity peaks and their evolution with varying excitation power are visible. At 5 µW the FWHM of the neutral exciton can be calculated as 0.3 meV and that of the

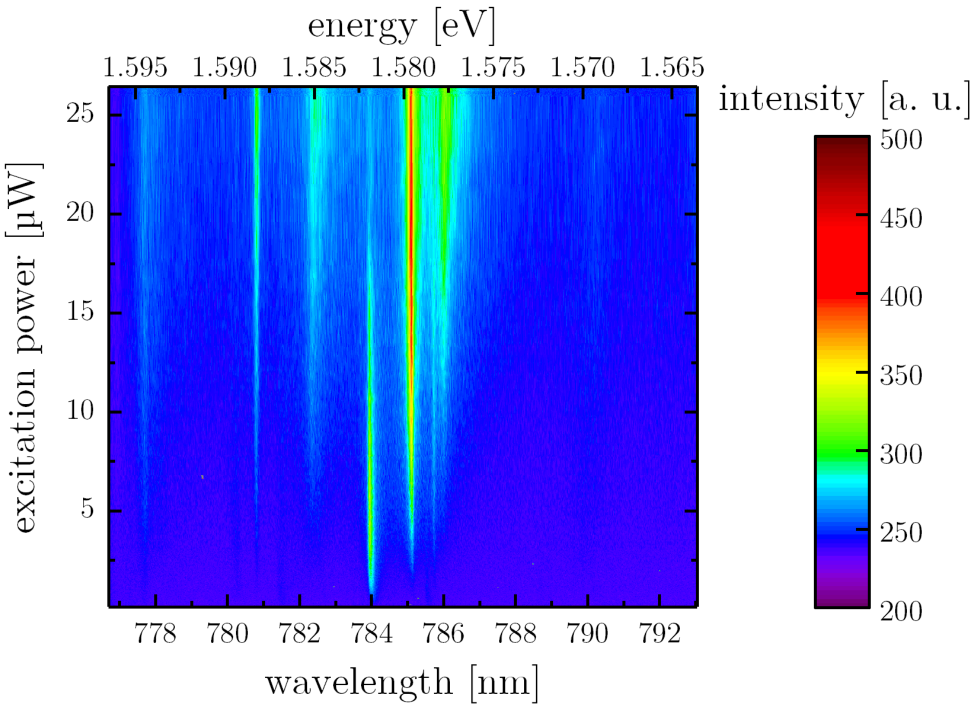

Figure 4.37: Excitation-power-dependent, single-dot PL spectra of a GaAs QD in sample A0815 without bias. The emissions at 783.97 nm and 785.10 nm are attributed to the neutral exciton and biexciton recombination, respectively.

biexciton as 0.2 meV. Note that the emission wavelength of this randomly chosen QD is very close to the 780 nm resonance with the ^{87}Rb D_2 transition [164].

On sample A0816 on the other hand, characterization of a QD under different voltages was possible. Its emission for a constant bias and changing excitation power and vice versa are shown in Figures 4.38 & 4.39. The Stark effect which changes the QDs emission wavelength is apparent. At 0.5 V and 5 µW the emissions at 751.04 nm and 752.16 nm are identified as signals of the neutral exciton and biexciton recombination. The FWHM of the Lorentz-fitted peaks is 0.2 meV each. The peaks are separated by a biexciton binding energy of 2.47 meV which is loosely consistent with measurements and simulations of GaAs QDs by DE on other substrate orientations [129].

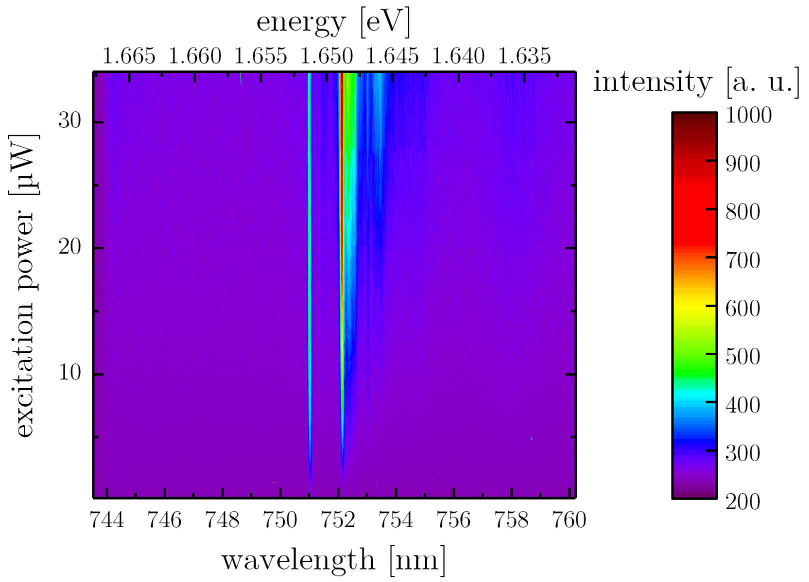

Figure 4.38: Excitation-power-dependent, single-dot PL spectra of a GaAs QD in sample A0816 with bias of 0.5 V.

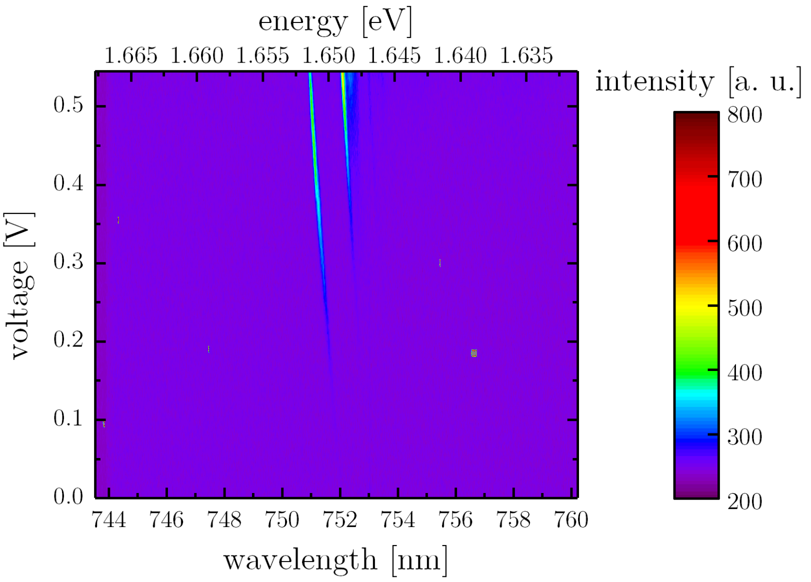

Figure 4.39: Voltage-dependent, single-dot PL spectra of a GaAs QD in sample A0816 with 6.8 µW excitation power.

The fact that nearly no emission can be measured in the absence of external bias suggests that the sample structure, especially doping and tunnel barrier thickness, has to be reviewed.

In conclusion, optically active GaAs QDs in AlGaAs fabricated by DE on (111)B were characterized individually. The measured FWHM-linewidths are much larger than the expected lifetime limit of 3 µeV for GaAs QDs in AlGaAs [18]. This is in itself insufficient for the intended quantum entanglement application but also prevents a precise FSS measurement when the FSS is below the linewidth, as is desired. Linewidths in the order of magnitude of 100 µeV and above have, however, been commonly reported for GaAs QDs fabricated by the DE processes when it has not yet been especially optimized for narrow linewidths [158, 165]. So this result is within expectations.

This broadening is typically explained by charging and discharging of trap defects in the surrounding of a QD which imparts a changing electromagnetic field on the QD and as a result changes its emission wavelength faster than the integration time during µPL. This phenomenon is referred to as spectral diffusion, wandering or charge noise in the literature [166, 167]. It can be expected that the very low T_{As} and the overgrowth below normal growth temperatures result in a high density of defects around the QDs in our samples. Additionally, the with $> 100\,\mathrm{nm}$ rather large QD base size increases the Stark coefficients and makes the QDs susceptible to charge noise [159].

Possible countermeasures to charge noise could be an increase of crystal quality by increasing T_{As} simultaneously with the As flux (currently not possible in our MBE), employing MEE during capping, decreasing the QD size or changing the measurement setup to resonant excitation. Unfortunately a laser for resonant excitation in the relevant wavelength range is currently being procured and not yet available. As a result FSS- and complementary photocurrent measurements on the shown QDs have to be postponed to a later date.

CHAPTER 5

Summary and outlook

In this thesis the DE process was applied to GaAs(111)B substrates to fabricate GaAs QDs for the first time. To this end the planar deposition of GaAs and $Al_{0.3}Ga_{0.7}As$ on misoriented GaAs(111)B substrates was successfully introduced to our MBE system. Smooth deposition of layers with higher Al or In contents, however, require further optimization. Subsequently, the different steps of DE were individually analyzed and optimized:

Ga droplets were deposited on $Al_{0.3}Ga_{0.7}As(111)B$ with different deposition temperatures T_{dep} and a clear relation between droplet density n and T_{dep} in the form of a scaling law could be determined. Individual Ga droplets were analyzed morphologically for different T_{dep}. The height, base diameter and symmetry of Ga droplets were evaluated statistically and a set of parameters which yields $n \approx 5 \times 10^{8}\,\mathrm{cm}^{-3}$ and shows no morphological break in symmetry due to e.g. the misorientation was identified.

The Ga droplets could only be crystallized to GaAs QDs at very low crystallization temperature $T_{\mathrm{As}} \approx 35\,^{\circ}\mathrm{C}$ close to the limit of our system and very long crystallization times $t_{\mathrm{As}} \approx 30\,\mathrm{min}$. The QD morphology was investigated and, again, no reduction of the substrates symmetry could be detected. Statistical evaluation of multiple individually measured QD sizes suggests that droplet crystallization was complete without the formation of an interconnecting GaAs layer.

Upon uncapped annealing the QDs transition from a spherical shape to triangular based plateaus and at last to a flat surface with increasing temperature T_{an}. As the triangles all form $< 0\bar{1}1 >$ facets, the C_{3v} symmetry is not violated.

The results of all steps were compared to reports of GaAs QD DE in the literature on other substrate orientations. A higher diffusion length of Ga adatoms on metal-rich AlGaAs(111)B compared to the cases on (100) and (111)A could be identified as a common source of differences encountered during the DE process. For In on GaAs(111)B an even stronger diffusivity prevented the fabrication of InAs QDs by DE. InGaAs QDs, however, could be fabricated although their optical activity was not verified.

Capped GaAs QDs fabricated by the developed process are optically active. Ensemble measurements of the lens-shaped QDs consistent with the QD size distribution and broad emission spectra around 790 nm could be acquired at 14 K. The smaller triangular QDs have an ensemble emission blue-shifted from the lens-shaped ones with peak intensity at 770 nm. Both have quite an overlap with the ^{87}Rb D_2 transition which allows the use of an atomic-based optical slow medium for storage of a polarization qubit photon. Experiments involving Rb gas and the here fabricated QDs could be interesting in the future. For GaAs QDs on (111)A it was reported that QD shape and barrier material had to be significantly changed to match this wavelength [18].

First voltage- and power-dependent single-dot spectra show clear exciton-lines with FWHM-linewidths around 200 µeV.

These results promise a low or vanishing fine structure splitting and eventually a functional application of this kind of QDs as solid-state polarization-entangled photon source. This, however, requires additional efforts to massively reduce the exciton linewidths. As a secondary objective the capping process has to be improved to yield a lower surface roughness in order to be able to embed the active QDs in more complex heterostructures.

Bibliography

1. N. Gisin, G. Ribordy, W. Tittel, and H. Zbinden: 'Quantum cryptography'. *Rev. Mod. Phys.* Vol. **74**: 145–195 (2002).
2. M. A. Nielsen and I. Chuang: *Quantum computation and quantum information.* Cambridge university press, 2010.
3. N. Gisin and R. Thew: 'Quantum communication'. *Nature photonics*, vol. **1**: 165 (2007).
4. J. I. Cirac and P. Zoller: 'Goals and opportunities in quantum simulation'. *Nature Physics*, vol. **8**: 264–266 (2012).
5. C. L. Degen, F. Reinhard, and P. Cappellaro: 'Quantum sensing'. *Reviews of Modern Physics*, vol. **89**: 1–39 (2017).
6. A. W. Harrow and A. Montanaro: 'Quantum computational supremacy'. *Nature*, vol. **549**: 203–209 (2017).
7. A. Orieux, M. A. Versteegh, K. D. Jöns, and S. Ducci: 'Semiconductor devices for entangled photon pair generation: a review'. *Reports on Progress in Physics*, vol. **80**: 076001 (2017).
8. I. Aharonovich, D. Englund, and M. Toth: 'Solid-state single-photon emitters'. *Nature Photonics*, vol. **10**: 631–641 (2016).
9. P. Senellart, G. Solomon, and A. White: 'High-performance semiconductor quantum-dot single-photon sources'. *Nature Nanotechnology*, vol. **12**: 1026–1039 (2017).

10. S. Buckley, K. Rivoire, and J. Vučković: 'Engineered quantum dot single-photon sources'. *Reports on Progress in Physics*, vol. **75** (2012).
11. N. Somaschi et al.: 'Near-optimal single-photon sources in the solid state'. *Nature Photonics*, vol. **10**: 340–345 (2016).
12. M. Bayer, G. Ortner, O. Stern, A. Kuther, A. A. Gorbunov, A. Forchel, P. Hawrylak, S. Fafard, K. Hinzer, T. L. Reinecke, S. N. Walck, J. P. Reithmaier, F. Klopf, and F. Schäfer: 'Fine structure of neutral and charged excitons in self-assembled In(Ga)As/(Al)GaAs quantum dots'. *Physical Review B - Condensed Matter and Materials Physics*, vol. **65**: 195315 (2002).
13. A. Schliwa, M. Winkelnkemper, A. Lochmann, E. Stock, and D. Bimberg: 'In(Ga)As/GaAs quantum dots grown on a (111) surface as ideal sources of entangled photon pairs'. *Physical Review B - Condensed Matter and Materials Physics*, vol. **80**: 161307(R) (2009).
14. H. Wen, Z. M. Wang, J. L. Shultz, B. L. Liang, and G. J. Salamo: 'Growth and characterization of InAs epitaxial layer on GaAs(111)B'. *Physical Review B - Condensed Matter and Materials Physics*, vol. **70**: 205307 (2004).
15. B. A. Parviz, D. Ryan, and G. M. Whitesides: 'Using Self-Assembly for the Fabrication of Nano-Scale Electronic and Photonic Devices'. *IEEE Transactions on Advanced Packaging*, vol. **26**: 233–241 (2003).
16. T. Mano, M. Abbarchi, T. Kuroda, B. Mcskimming, A. Ohtake, K. Mitsuishi, and K. Sakoda: 'Self-assembly of symmetric GaAs quantum dots on (111)A substrates: Suppression of fine-structure splitting'. *Applied Physics Express*, vol. **3**: 065203 (2010).

17. T. Kuroda, T. Mano, N. Ha, H. Nakajima, H. Kumano, B. Urbaszek, M. Jo, M. Abbarchi, Y. Sakuma, K. Sakoda, I. Suemune, X. Marie, and T. Amand: ‘Symmetric quantum dots as efficient sources of highly entangled photons: Violation of Bell’s inequality without spectral and temporal filtering’. *Physical Review B - Condensed Matter and Materials Physics*, vol. **88**: 3–7 (2013).

18. F. Basso Basset, S. Bietti, M. Reindl, L. Esposito, A. Fedorov, D. Huber, A. Rastelli, E. Bonera, R. Trotta, and S. Sanguinetti: ‘High-Yield Fabrication of Entangled Photon Emitters for Hybrid Quantum Networking Using High-Temperature Droplet Epitaxy’. *Nano Letters*, vol. **18**: 505–512 (2018).

19. L. Esposito, S. Bietti, A. Fedorov, R. Noetzel, and S. Sanguinetti: ‘Ehrlich-Schwoebel Effect on the Growth Dynamics of GaAs(111)A surfaces’. *Physical Review Materials*, vol. **1**: 024602 (2017).

20. F. Herzog, M. Bichler, G. Koblmüller, S. Prabhu-Gaunkar, W. Zhou, and M. Grayson: ‘Optimization of AlAs/AlGaAs quantum well heterostructures on on-axis and misoriented GaAs (111) B’. *Applied Physics Letters*, vol. **100**: 192106 (2012).

21. M. L. Cohen and J. R. Chelikowsky: *Electronic structure and optical properties of semiconductors*. Vol. 75. Springer, 1989.

22. N. Ashcroft and N. Mermin: *Solid State Physics*. Brooks/Cole, 1976.

23. M. Faraday: ‘Experimental Researches in Electricity. Fourth Series’. *Philosophical Transactions of the Royal Society of London*, vol. **123**: 507–522 (1833).

24. G. Busch: ‘Early history of the physics and chemistry of semiconductors-from doubts to fact in a hundred years’. *European Journal of Physics*, vol. **10**: 254–264 (1989).

25. Y. Varshni: ‘Temperature dependence of the energy gap in semiconductors’. *Physica*, vol. **34**: 149–154 (1967).
26. S. M. Sze and K. K. Ng: *Physics of semiconductor devices.* John Wiley & Sons, 2006.
27. J. Singh: *Optoelectronics: An introduction to materials and devices.* McGraw-Hill College, 1996.
28. E. F. Schubert: *Light-Emitting Diodes.* Cambridge University Press, 2006.
29. G. P. Agrawal and N. K. Dutta: *Semiconductor lasers.* Springer Science & Business Media, 2013.
30. W. S. Boyle and G. E. Smith: ‘Charge coupled semiconductor devices’. *Bell System Technical Journal*, vol. **49**: 587–593 (1970).
31. G. E. Smith: ‘The invention and early history of the CCD’. *Nuclear Instruments and Methods in Physics Research, Section A: Accelerators, Spectrometers, Detectors and Associated Equipment*, vol. **607**: 1–6 (2009).
32. S. Nakamura: ‘Background Story of the Invention of Efficient InGaN Blue-Light-Emitting Diodes (Nobel Lecture)’. *Angewandte Chemie - International Edition*, vol. **54**: 7770–7788 (2015).
33. I. Vurgaftman, J. R. Meyer, and L. R. Ram-Mohan: ‘Band parameters for III-V compound semiconductors and their alloys’. *Journal of Applied Physics*, vol. **89**: 5815–5875 (2001).
34. U. W. Pohl: *Epitaxy of Semiconductors: Introduction to Physical Principles.* Springer, 2013.
35. R. Szweda: *Gallium Arsenide, Electronics Materials and Devices. A Strategic Study of Markets, Technologies and Companies Worldwide 1999-2004.* Elsevier, 2000.

36. T. Mimura, S. Hiyamizu, T. Fujii, and K. Nanbu: ‘A new field-effect transistor with selectively doped GaAs/n-AlxGa1-xAs heterojunctions’. *Japanese Journal of Applied Physics*, vol. **19**: L225–L227 (1980).

37. L. A. Coldren, S. W. Corzine, and M. L. Mashanovitch: *Diode lasers and photonic integrated circuits.* second edition. John Wiley & Sons, 2012.

38. P. Y. Yu and M. Cardona: *Fundamentals of semiconductors: physics and materials properties.* Springer Science & Business Media, 2010.

39. L. Vegard: ‘Die Konstitution der Mischkristalle und die Raumfüllung der Atome’. *Zeitschrift für Physik*, vol. **5**: 17–26 (1921).

40. C. D. Yerino, B. Liang, D. L. Huffaker, P. J. Simmonds, and M. L. Lee: ‘Review Article: Molecular beam epitaxy of lattice-matched InAlAs and InGaAs layers on InP (111)A, (111)B, and (110)’. *Journal of Vacuum Science & Technology B, Nanotechnology and Microelectronics: Materials, Processing, Measurement, and Phenomena*, vol. **35**: 010801 (2017).

41. R. F. Farrow: *Molecular beam epitaxy: applications to key materials.* Elsevier, 1995.

42. D. A. Woolf, D. I. Westwood, and R. H. Williams: ‘Surface reconstructions of GaAs(111)A and (111)B: A static surface phase study by reflection high-energy electron diffraction’. *Applied Physics Letters*, vol. **62**: 1370–1372 (1993).

43. P. Chen, K. C. Rajkumar, and A. Madhukar: ‘Growth control of GaAs epilayers with specular surface free of pyramids and twins on nonmisoriented (111)B substrates’. *Applied Physics Letters*, vol. **58**: 1771–1773 (1991).

44. J. Ritzmann, R. Schott, K. Gross, D. Reuter, A. Ludwig, and A. D. Wieck: ‘Overcoming Ehrlich-Schwöbel barrier in (1 1 1)A GaAs molecular beam epitaxy’. *Journal of Crystal Growth*, vol. **481**: 7–10 (2018).

45. J. S. Blakemore: ‘Semiconducting and other major properties of gallium arsenide’. *Journal of Applied Physics*, vol. **53**: R123 (1982).

46. D. J. Stirland and B. W. Straughan: ‘A review of etching and defect characterisation of gallium arsenide substrate material’. *Thin Solid Films*, vol. **31**: 139–170 (1976).

47. R. McWeeny: *Symmetry: An introduction to group theory and its applications*. Courier Corporation, 2002.

48. D. Biegelsen, R. D. Bringans, J. E. Northrup, and L.-E. Swartz: ‘Surface reconstructions of GaAs(100) observed by scanning tunneing microscopy’. *Physical Review B - Condensed Matter and Materials Physics*, vol. **41**: 5701–5706 (1990).

49. D. K. Biegelsen, R. D. Bringans, J. E. Northrup, and L.-E. Swartz: ‘Reconstructions of GaAs (1 1 1) surfaces observed by scanning tunneling microscopy’. *Physical Review Letters*, vol. **65**: 452 (1990).

50. K. F. Karlsson, M. A. Dupertuis, D. Y. Oberli, E. Pelucchi, A. Rudra, P. O. Holtz, and E. Kapon: ‘Fine structure of exciton complexes in high-symmetry quantum dots: Effects of symmetry breaking and symmetry elevation’. *Physical Review B - Condensed Matter and Materials Physics*, vol. **81**: 161307(R) (2010).

51. J. Venables, G. D. T. Splitter, and M. Hanbrücken: ‘Nucleation and growth of thin films’. *Reports on Progress in Physics*, vol. **47**: 399–459 (1984).

52. M. A. Herman, W. Richter, and H. Sitter: *Epitaxy: physical principles and technical implementation*. Springer, 2004.

53. P. Capper and M. Mauk: *Liquid phase epitaxy of electronic, optical and optoelectronic materials*. Vol. 21. John Wiley & Sons, 2007.

54. G. B. Stringfellow: *Organometallic vapor-phase epitaxy: theory and practice*. Elsevier, 1999.

55. A. C. Levi and M. Kotrla: 'Theory and simulation of crystal growth'. *Journal of Physics: Condensed Matter*, vol. **9**: 299 (1997).

56. A. Pimpinelli and J. Villain: *Physics of crystal growth*. Vol. 19. Cambridge University Press, 1998.

57. S. Clarke and D. D. Vvedensky: 'Origin of reflection high-energy electron-diffraction intensity oscillations during molecular-beam epitaxy: A computational modeling approach'. *Physical Review Letters*, vol. **58**: 2235 (1987).

58. J. S. Kim: 'Ga-migration on a Ga-rich and As-stabilized surfaces: Ga-droplet and GaAs- nanostructure formation'. *Materials Science in Semiconductor Processing*, vol. **57**: 70–76 (2017).

59. T. Michely and J. Krug: *Islands, mounds and atoms*. Springer, 2004.

60. F. Frank and J. H. van der Merwe: 'One-dimensional dislocations. I. Static theory'. *Proceedings of the Royal Society of London A: Mathematical, Physical and Engineering Sciences*, vol. **198**: 205–216 (1949).

61. M. Volmer and A. Weber: 'Keimbildung in übersättigten Gebilden'. *Zeitschrift für physikalische Chemie*, vol. **119**: 277–301 (1926).

62. I. N. Stranski and L. Krastanow: 'Zur Theorie der orientierten Ausscheidung von Ionenkristallen aufeinander'. *Monatshefte für Chemie und verwandte Teile anderer Wissenschaften*, vol. **71**: 351–364 (1937).

63. C. Tegenkamp: 'Vicinal surfaces for functional nanostructures'. *Journal of Physics: Condensed Matter*, vol. **21**: 013002 (2009).

64. G. Ehrlich and F. G. Hudda: ‘Atomic view of surface self-diffusion: Tungsten on tungsten’. *The Journal of Chemical Physics*, vol. **44**: 1039–1049 (1966).

65. R. L. Schwoebel and E. J. Shipsey: ‘Step motion on crystal surfaces’. *Journal of Applied Physics*, vol. **37**: 3682–3686 (1966).

66. O. Pierre-Louis, M. R. D’ Orsogna, and T. L. Einstein: ‘Edge diffusion during growth: The kink ehrlich-schwoebel effect and resulting instabilities’. *Physical Review Letters*, vol. **82**: 3661–3664 (1999).

67. G. Bales and A. Zangwill: ‘Morphological instability of a terrace edge during step-flow growth’. *Physical Review B - Condensed Matter and Materials Physics*, vol. **41**: 5500 (1990).

68. J. R. Arthur: ‘Interaction of Ga and As2 Molecular Beams with GaAs Surfaces’. *Journal of Applied Physics*, vol. **39**: 4032–4034 (1968).

69. J. R. Arthur and J. J. LePore: ‘GaAs, GaP, and GaAsxP1-x Epitaxial Films Grown by Molecular Beam Deposition’. *Journal of Vacuum Science and Technology*, vol. **6**: 545–548 (1969).

70. A. Cho: ‘Morphology of epitaxial growth of GaAs by a molecular beam method: The observation of surface structures’. *Journal of Applied Physics*, vol. **41**: 2780–2786 (1970).

71. L. L. Chang and K. Ploog: *Molecular beam epitaxy and heterostructures.* Vol. 87. Springer Science & Business Media, 2012.

72. M. Henini: *Molecular beam epitaxy: from research to mass production.* Elsevier, 2013.

73. L. Jacak, P. Hawrylak, and A. Wójs: *Quantum dots.* Springer, 1998.

74. D. Bimberg, M. Grundmann, and N. N. Ledentsov: *Quantum dot heterostructures.* John Wiley & Sons, 1999.

75. M. Reed, R. Bate, K. Bradshaw, W. Duncan, W. Frensley, J. Lee, and H. Shih: ‘Spatial quantization in GaAs–AlGaAs multiple quantum dots’. *Journal of Vacuum Science & Technology B: Microelectronics Processing and Phenomena*, vol. **4**: 358–360 (1986).

76. M. Reed, J. Randall, R. Aggarwal, R. Matyi, T. Moore, and A. Wetsel: ‘Observation of discrete electronic states in a zero-dimensional semiconductor nanostructure’. *Physical Review Letters*, vol. **60**: 535 (1988).

77. J. Cibert, P. M. Petroff, G. J. Dolan, S. J. Pearton, A. C. Gossard, and J. H. English: ‘Optically detected carrier confinement to one and zero dimension in GaAs quantum well wires and boxes’. *Applied Physics Letters*, vol. **49**: 1275–1277 (1986).

78. R. C. Ashoori, H. L. Stormer, J. S. Weiner, L. N. Pfeiffer, S. J. Pearton, K. W. Baldwin, and K. W. West: ‘Single-electron capacitance spectroscopy of discrete quantum levels’. *Physical Review Letters*, vol. **68**: 3088–3091 (1992).

79. K. Brunner, U. Bockelmann, G. Abstreiter, M. Walther, G. Böhm, G. Tränkle, and G. Weimann: ‘Photoluminescence from a single GaAs/AlGaAs quantum dot’. *Physical Review Letters*, vol. **69**: 3216–3219 (1992).

80. T. Fukui, S. Ando, Y. Tokura, and T. Toriyama: ‘GaAs tetrahedral quantum dot structures fabricated using selective area metalorganic chemical vapor deposition’. *Applied Physics Letters*, vol. **58**: 2018–2020 (1991).

81. Z. M. Wang: *Self-assembled quantum dots*. Vol. 1. Springer Science & Business Media, 2008.

82. A. I. Ekimov, A. L. Efros, and A. A. Onushchenko: ‘Quantum size effect in semiconductor microcrystals’. *Solid State Communications*, vol. **56**: 921–924 (1985).

83. R. Rossetti, J. L. Ellison, J. M. Gibson, and L. E. Brus: ‘Size effects in the excited electronic states of small colloidal CdS crystallites’. *The Journal of Chemical Physics*, vol. **80**: 4464–4469 (1984).

84. W. C. Chan, D. J. Maxwell, X. Gao, R. E. Bailey, M. Han, and S. Nie: ‘Luminescent quantum dots for multiplexed biological detection and imaging’. *Current Opinion in Biotechnology*, vol. **13**: 40–46 (2002).

85. I. L. Medintz, H. T. Uyeda, E. R. Goldman, and H. Mattoussi: ‘Quantum dot bioconjugates for imaging, labelling and sensing’. *Nature Materials*, vol. **4**: 435 (2005).

86. Y. Shirasaki, G. J. Supran, M. G. Bawendi, and V. Bulović: ‘Emergence of colloidal quantum-dot light-emitting technologies’. *Nature Photonics*, vol. **7**: 13–23 (2013).

87. K. Brunner, G. Abstreiter, G. Böhm, G. Tränkle, and G. Weimann: ‘Sharp-Line Photoluminescence and Two-Photon Absorption of Zero-Dimensional Biexcitons in a GaAs/AlGaAs Structure’. *Physical Review Letters*, vol. **73**: 1138–1141 (1994).

88. W. Wegscheider, G. Schedelbeck, G. Abstreiter, M. Rother, and M. Bichler: ‘Atomically Precise GaAs/AlGaAs Quantum Dots Fabricated by Twofold Cleaved Edge Overgrowth’. *Physical Review Letters*, vol. **79**: 1917–1920 (1997).

89. J. M. Moison, F. Houzay, F. Barthe, L. Leprince, E. André, and O. Vatel: ‘Self-organized growth of regular nanometer-scale InAs dots on GaAs’. *Applied Physics Letters*, vol. **64**: 196–198 (1994).

90. A. Madhukar, Q. Xie, P. Chen, and A. Konkar: ‘Nature of strained InAs three-dimensional island formation and distribution on GaAs(100)’. *Applied Physics Letters*, vol. **64**: 2727–2729 (1994).

91. D. Leonard, M. Krishnamurthy, C. Reaves, S. P. DenBaars, and P. M. Petroff: ‘Direct formation of quantum-sized dots from uniform coherent islands of InGaAs on GaAs surfaces’. *Applied Physics Letters*, vol. **63**: 3203–3205 (1993).

92. C. Heyn: ‘Critical coverage for strain-induced formation of InAs quantum dots’. *Physical Review B - Condensed Matter and Materials Physics*, vol. **64**: 165306 (2001).

93. J. Stangl, V. Holỳ, and G. Bauer: ‘Structural properties of self-organized semiconductor nanostructures’. *Reviews of Modern Physics*, vol. **76**: 725 (2004).

94. N. L. Sharma: ‘Molecular beam epitaxy of tailored (In,Ga)As/GaAs quantum dot heterostructures’. PhD thesis. 2017.

95. H. Yamaguchi, J. Belk, X. Zhang, J. Sudijono, M. Fahy, T. Jones, D. Pashley, and B. Joyce: ‘Atomic-scale imaging of strain relaxation via misfit dislocations in highly mismatched semiconductor heteroepitaxy: InAs/GaAs(111)A’. *Physical Review B - Condensed Matter and Materials Physics*, vol. **55**: 1337–1340 (1997).

96. Z. M. Wang, B. L. Liang, K. A. Sablon, and G. J. Salamo: ‘Nanoholes fabricated by self-assembled gallium nanodrill on GaAs(100)’. *Applied Physics Letters*, vol. **90**: 2005–2008 (2007).

97. C. Heyn: ‘Kinetic model of local droplet etching’. *Physical Review B - Condensed Matter and Materials Physics*, vol. **83**: 165302 (2011).

98. C. Kiessler: ‘Metamorphic InGaAs buffer layers on GaAs(100) as templates for nanostructure formation’. Master’s Thesis. University of Paderborn, 2018.

99. S. Ohkouchi, Y. Nakamura, N. Ikeda, Y. Sugimoto, and K. Asakawa: ‘In situ mask designed for selective growth of InAs quantum dots in narrow regions developed for molecular beam epitaxy system’. *Review of Scientific Instruments*, vol. **78**: 073908 (2007).

100. V. Zolatanosha and D. Reuter: ‘Robust Si3N4masks for 100 nm selective area epitaxy of GaAs-based nanostructures’. *Microelectronic Engineering*, vol. **180**: 35–39 (2017).

101. V. Zolatanosha and D. Reuter: ‘Site-controlled droplet epitaxy of GaAs quantum dots by deposition through shadow masks’. *Journal of Vacuum Science & Technology B, Nanotechnology and Microelectronics: Materials, Processing, Measurement, and Phenomena*, vol. **36**: 02D105 (2018).

102. D. Heitmann: *Quantum Materials*. Springer, 2010.

103. M. A. Surnina, R. K. Akchurin, A. A. Marmalyuk, T. A. Bagaev, and A. L. Sizov: ‘Growing InAs/GaAs quantum dots by droplet epitaxy under MOVPE conditions’. *Technical Physics Letters*, vol. **42**: 747–749 (2016).

104. N. Koguchi and K. Ishige: ‘Growth of GaAs epitaxial microcrystals on an S-terminated GaAs substrate by successive irradiation of Ga and As molecular beams’. *Japanese Journal of Applied Physics*, vol. **32**: 2052 (1993).

105. K. Watanabe, N. Koguchi, and Y. Gotoh: ‘Fabrication of GaAs quantum dots by modified droplet epitaxy’. *Japanese Journal of Applied Physics*, vol. **39**: L79 (2000).

106. J. Wu and Z. M. Wang: ‘Droplet epitaxy for advanced optoelectronic materials and devices’. *Journal of Physics D: Applied Physics*, vol. **47**: 173001 (2014).

107. K. Reyes, P. Smereka, D. Nothern, J. M. Millunchick, S. Bietti, C. Somaschini, S. Sanguinetti, and C. Frigeri: ‘Unified model of droplet epitaxy for compound semiconductor nanostructures: Experiments and theory’. *Physical Review B - Condensed Matter and Materials Physics*, vol. **87**: 165406 (2013).

108. T. Maruyama, H. Otsubo, T. Kondo, Y. Yamamoto, and S. Naritsuka: ‘Fabrication of GaN dot structure by droplet epitaxy using NH3’. *Journal of Crystal Growth*, vol. **301-302**: 486–489 (2007).

109. W. Jevasuwan, P. Boonpeng, S. Panyakeow, and S. Ratanathammaphan: ‘Influence of crystallization temperature on InP ring-shaped quantum-dot molecules grown by droplet epitaxy’. *Microelectronic Engineering*, vol. **87**: 1416–1419 (2010).

110. B. Liang, A. Lin, N. Pavarelli, C. Reyner, J. Tatebayashi, K. Nunna, J. He, T. J. Ochalski, G. Huyet, and D. L. Huffaker: ‘GaSb/GaAs type-II quantum dots grown by droplet epitaxy’. *Nanotechnology*, vol. **20**: 455604 (2009).

111. C. Heyn, A. Stemmann, A. Schramm, H. Welsch, W. Hansen, and Á. Nemcsics: ‘Regimes of GaAs quantum dot self-assembly by droplet epitaxy’. *Physical Review B - Condensed Matter and Materials Physics*, vol. **76**: 075317 (2007).

112. T. Mano, T. Kuroda, S. Sanguinetti, T. Ochiai, T. Tateno, J. Kim, T. Noda, M. Kawabe, K. Sakoda, G. Kido, and N. Koguchi: ‘Self-assembly of concentric quantum double rings’. *Nano Letters*, vol. **5**: 425–428 (2005).

113. W. W. Mullins and R. F. Sekerka: ‘Stability of a planar interface during solidification of a dilute binary alloy’. In: *Dynamics of Curved Fronts*, pp. 345-352. Elsevier, 1988.

114. T. Mano, M. Abbarchi, T. Kuroda, C. A. Mastrandrea, A. Vinattieri, S. Sanguinetti, K. Sakoda, and M. Gurioli: ‘Ultranarrow emission from single GaAs self-assembled quantum dots grown by droplet epitaxy’. *Nanotechnology*, vol. **20**: 395601 (2009).

115. S. Bietti, J. Bocquel, S. Adorno, T. Mano, J. G. Keizer, P. M. Koenraad, and S. Sanguinetti: ‘Precise shape engineering

of epitaxial quantum dots by growth kinetics'. *Physical Review B - Condensed Matter and Materials Physics*, vol. **92**: 075425 (2015).

116. H. Song, T. Usuki, Y. Nakata, N. Yokoyama, H. Sasakura, and S. Muto: 'Formation of In As/ Ga As quantum dots from a subcritical InAs wetting layer: A reflection high-energy electron diffraction and theoretical study'. *Physical Review B*, vol. **73**: 115327 (2006).

117. V. Mantovani, S. Sanguinetti, M. Guzzi, E. Grilli, M. Gurioli, K. Watanabe, and N. Koguchi: 'Low density GaAs/ AlGaAs quantum dots grown by modified droplet epitaxy'. *Journal of applied physics*, vol. **96**: 4416–4420 (2004).

118. K. Watanabe, S. Tsukamoto, Y. Gotoh, and N. Koguchi: 'Photoluminescence studies of GaAs quantum dots grown by droplet epitaxy'. *Journal of Crystal Growth*, vol. **227-228**: 1073–1077 (2001).

119. J. Treu, C. Schneider, A. Huggenberger, T. Braun, S. Reitzenstein, S. Höfling, and M. Kamp: 'Substrate orientation dependent fine structure splitting of symmetric In(Ga)As/GaAs quantum dots'. *Applied Physics Letters*, vol. **101**: 022102 (2012).

120. A. Trapp and D. Reuter: 'Formation of self-assembled GaAs quantum dots via droplet epitaxy on misoriented GaAs(111)B substrates'. *Journal of Vacuum Science & Technology B, Nanotechnology and Microelectronics: Materials, Processing, Measurement, and Phenomena*, vol. **36**: 02D106 (2018).

121. J. H. Davies: *The physics of low-dimensional semiconductors: an introduction.* Cambridge university press, 1998.

122. W. Sheng and J. P. Leburton: 'Electron-hole alignment in InAs/-GaAs self-assembled quantum dots: Effects of chemical composition and dot shape'. *Physical Review B - Condensed Matter and Materials Physics*, vol. **63**: 1–4 (2001).

123. R. Leon, S. Fafard, D. Leonard, J. L. Merz, and P. M. Petroff: ‘Visible luminescence from semiconductor quantum dots in large ensembles’. *Applied Physics Letters*, vol. **67**: 521 (1995).

124. A. Schliwa, M. Winkelnkemper, and D. Bimberg: ‘Impact of size, shape, and composition on piezoelectric effects and electronic properties of In (Ga) AsGaAs quantum dots’. *Physical Review B - Condensed Matter and Materials Physics*, vol. **76**: 1–17 (2007).

125. A. Wojs, L. Jacak, P. Hawrylak, and S. Fafard: ‘Electronic structure and magneto-optics of self-assembled quantum dots’. *Physical Review B - Condensed Matter and Materials Physics*, vol. **54**: 5604–5608 (1996).

126. R. Ashoori: ‘Electrons in artificial atoms’. *Nature*, vol. **379**: 413 (1996).

127. E. Merzbacher: *Quantum Mechanics.* John Wiley & Sons, 1998.

128. L. Bányai and S. W. Koch: *Semiconductor Quantum Dots.* World Scientific Publishing, 1993.

129. M. Abbarchi, T. Kuroda, T. Mano, K. Sakoda, C. A. Mastrandrea, A. Vinattieri, M. Gurioli, and T. Tsuchiya: ‘Energy renormalization of exciton complexes in GaAs quantum dots’. *Physical Review B - Condensed Matter and Materials Physics*, vol. **82**: 201301(R) (2010).

130. R. Seguin, A. Schliwa, S. Rodt, K. Potschke, U. W. Pohl, and D. Bimberg: ‘Size-dependent fine-structure splitting in self-organized InAs/GaAs quantum dots’. *Physical Review Letters*, vol. **95**: 257402 (2005).

131. G. Bester, A. Zunger, X. Wu, and D. Vanderbilt: ‘Effects of linear and nonlinear piezoelectricity on the electronic properties of InAsGaAs quantum dots’. *Physical Review B - Condensed Matter and Materials Physics*, vol. **74**: 3–6 (2006).

132. G. Bester, S. Nair, and A. Zunger: 'Pseudopotential calculation of the excitonic fine structure of million-atom self-assembled In1-xGaxAs/GaAs quantum dots'. *Physical Review B*, vol. **67**: 161306 (2003).

133. M. Abbarchi, C. A. Mastrandrea, T. Kuroda, T. Mano, K. Sakoda, N. Koguchi, S. Sanguinetti, A. Vinattieri, and M. Gurioli: 'Exciton fine structure in strain-free GaAs/Al0.3Ga0.7As quantum dots: Extrinsic effects'. *Physical Review B*, vol. **78**: 125321 (2008).

134. G. C. Gardner, S. Fallahi, J. D. Watson, and M. J. Manfra: 'Modified MBE hardware and techniques and role of gallium purity for attainment of two dimensional electron gas mobility >35×10^6 cm^2/Vs in AlGaAs/GaAs quantum wells grown by MBE'. *Journal of Crystal Growth*, vol. **441**: 71–77 (2016).

135. S. Hasegawa: 'Reflection High-Energy Electron Diffraction'. *Characterization of Materials.* American Cancer Society, 2012: pp. 1–14.

136. W. Braun: *Applied RHEED: reflection high-energy electron diffraction during crystal growth.* Vol. 154. Springer Science & Business Media, 1999.

137. A. Ichimiya, P. I. Cohen, and P. I. Cohen: *Reflection high-energy electron diffraction.* Cambridge University Press, 2004.

138. J. H. Neave, B. A. Joyce, P. J. Dobson, and N. Norton: 'Dynamics of film growth of GaAs by MBE from Rheed observations'. *Applied Physics A*, vol. **31**: 1–8 (1983).

139. G. Binnig, C. F. Quate, and C. Gerber: 'Atomic force microscope'. *Physical review letters*, vol. **56**: 930 (1986).

140. S. Sanguinetti, T. Mano, A. Gerosa, C. Somaschini, S. Bietti, N. Koguchi, E. Grilli, M. Guzzi, M. Gurioli, and M. Abbarchi: 'Rapid thermal annealing effects on self-assembled quantum dot and quantum ring structures'. *Journal of Applied Physics*, vol. **104**: 113519 (2008).

141. S. Malik, C. Roberts, R. Murray, and M. Pate: 'Tuning self-assembled InAs quantum dots by rapid thermal annealing'. *Applied Physics Letters*, vol. **71**: 1987 (1997).

142. A. Babiński, J. Jasiński, R. Bozek, A. Szepielow, and J. M. Baranowski: 'Rapid thermal annealing of InAs/GaAs quantum dots under a GaAs proximity cap'. *Applied Physics Letters*, vol. **79**: 2576–2578 (2001).

143. M. Eppinger: 'Untersuchung des Einflusses von Temperschritten auf die strukturellen und optischen Eigenschaften von Tröpfchen-Epitaxie-Nanostrukturen'. Bachelors's Thesis. University of Paderborn, 2018.

144. C. Kiessler: 'Aufbau und Inbetriebnahme eines Tieftemperaturelektrolumineszenzmessplatzes'. Bachelors's Thesis. University of Paderborn, 2016.

145. R. Fischer, J. Klem, T. J. Drummond, R. E. Thorne, W. Kopp, H. Morkoç, and A. Y. Cho: 'Incorporation rates of gallium and aluminum on GaAs during molecular beam epitaxy at high substrate temperatures'. *Journal of Applied Physics*, vol. **54**: 2508–2510 (1983).

146. C. Heyn: 'Stability of InAs quantum dots'. *Physical Review B - Condensed Matter and Materials Physics*, vol. **66**: 075307 (2002).

147. A. Ohtake, N. Ha, and T. Mano: 'Extremely high- and low-density of Ga droplets on GaAs{111}A,B: Surface-polarity dependence'. *Crystal Growth and Design*, vol. **15**: 485–488 (2015).

148. T. Henksmeier: 'Electrical and optical investigation of III-V heterostructures'. Master's Thesis. University of Paderborn, 2018.

149. T. Henksmeier, S. Shvarkov, A. Trapp, and D. Reuter: 'Molecular beam epitaxy growth and temperature-dependent electrical characterization of carbon-doped GaAs on GaAs(1 1 1)B'. *Journal of Crystal Growth*, vol. **512**: 164–168 (2019).

150. H. Yamaguchi, M. R. Fahy, and B. A. Joyce: 'Inhibitions of three dimensional island formation in InAs films grown on GaAs (111)A surface by molecular beam epitaxy'. *Applied Physics Letters*, vol. **69**: 776–778 (1996).

151. T. Mano, K. Mitsuishi, N. Ha, A. Ohtake, A. Castellano, S. Sanguinetti, T. Noda, Y. Sakuma, T. Kuroda, and K. Sakoda: 'Growth of metamorphic InGaAs on GaAs (111)A: Counteracting lattice mismatch by inserting a thin InAs interlayer'. *Crystal Growth and Design*, vol. **16**: 5412–5417 (2016).

152. C. N. Singman: 'Atomic volume and allotropy of the elements'. *Journal of Chemical Education*, vol. **61**: 137 (1984).

153. M. Zhang, M. Y. Efremov, F. Schiettekatte, E. A. Olson, A. T. Kwan, S. L. Lai, T. Wisleder, J. E. Greene, and L. H. Allen: 'Size-dependent melting point depression of nanostructures: Nanocalorimetric measurements'. *Physical Review B - Condensed Matter and Materials Physics*, vol. **62**: 10548–10557 (2000).

154. S. Bietti, C. Somaschini, and S. Sanguinetti: 'Crystallization kinetics of Ga metallic nano-droplets under As flux.' *Nanotechnology*, vol. **24**: 205603 (2013).

155. T. J. Anderson and I. Ansara: 'The Ga-In (Gallium-Indium) System'. *Journal of Phase Equilibria*, vol. **12**: 64–72 (1991).

156. Y. Horikoshi, M. Kawashima, and H. Yamaguchi: 'Migration-enhanced epitaxy of GaAs and AlGaAs'. *Japanese Journal of Applied Physics*, vol. **27**: 169–179 (1988).

157. A. Scaccabarozzi, S. Adorno, S. Bietti, M. Acciarri, and S. Sanguinetti: ‘Evidence of two-photon absorption in strain-free quantum dot GaAs/AlGaAs solar cells’. *Physica Status Solidi - Rapid Research Letters*, vol. **7**: 173–176 (2013).

158. S. Sanguinetti, E. Poliani, M. Bonfanti, M. Guzzi, E. Grilli, M. Gurioli, and N. Koguchi: ‘Electron-phonon interaction in individual strain-free GaAs/Al0.3 Ga0.7 As quantum dots’. *Physical Review B - Condensed Matter and Materials Physics*, vol. **73**: 125342 (2006).

159. N. Ha, T. Mano, Y. L. Chou, Y. N. Wu, S. J. Cheng, J. Bocquel, P. M. Koenraad, A. Ohtake, Y. Sakuma, K. Sakoda, and T. Kuroda: ‘Size-dependent line broadening in the emission spectra of single GaAs quantum dots: Impact of surface charge on spectral diffusion’. *Physical Review B - Condensed Matter and Materials Physics*, vol. **92**: 075306 (2015).

160. L. Pavesi, N. H. Ky, J. D. Ganière, F. K. Reinhart, N. Baba-Ali, I. Harrison, B. Tuck, and M. Henini: ‘Role of point defects in the silicon diffusion in GaAs and Al0.3Ga0.7As and in the related superlattice disordering’. *Journal of Applied Physics*, vol. **71**: 2225–2237 (1992).

161. N. G. Yaremenko, M. V. Karachevtseva, V. A. Strakhov, G. B. Galiev, and V. G. Mokerov: ‘Photoluminescence of Si-Doped GaAs Epitaxial Layers’. *Semiconductors*, vol. **42**: 1480–1486 (2008).

162. S. Gordon: ‘Einzelne Quantenpunkte in elektrisch abstimmbaren Diodenstrukturen: Photolumineszenz und kohärente Photostromspektroskopie’. PhD thesis. 2017.

163. A. K. Rai: ‘Optically pumped and electrically triggered single photon emission from a single quantum dot’. PhD thesis. 2017.

164. D. A. Steck: ‘Rubidium 87 D Line Data’. http://steck.us/alkalidata. 2015.

165. K. Kuroda, T. Kuroda, K. Watanabe, T. Mano, G. Kido, N. Koguchi, and K. Sakoda: ‘Distribution of exciton emission linewidth observed for GaAs quantum dots grown by droplet epitaxy’. *Journal of Luminescence*, vol. **130**: 2390–2393 (2010).

166. M. Abbarchi, F. Troiani, C. Mastrandrea, G. Goldoni, T. Kuroda, T. Mano, K. Sakoda, N. Koguchi, S. Sanguinetti, A. Vinattieri, and M. Gurioli: ‘Spectral diffusion and line broadening in single self-assembled GaAs/AlGaAs quantum dot photoluminescence’. *Applied Physics Letters*, vol. **93**: 162101 (2008).

167. A. V. Kuhlmann, J. Houel, A. Ludwig, L. Greuter, D. Reuter, A. D. Wieck, M. Poggio, and R. J. Warburton: ‘Charge noise and spin noise in a semiconductor quantum device’. *Nature Physics*, vol. **9**: 570–575 (2013).

APPENDIX A

Wafer datasheets

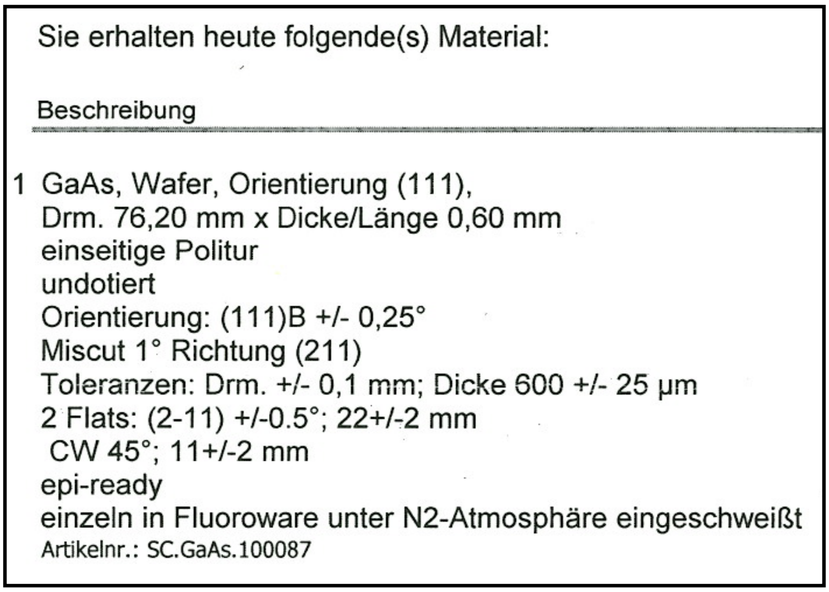

Sie erhalten heute folgende(s) Material:

Beschreibung

1 GaAs, Wafer, Orientierung (111),
Drm. 76,20 mm x Dicke/Länge 0,60 mm
einseitige Politur
undotiert
Orientierung: (111)B +/- 0,25°
Miscut 1° Richtung (211)
Toleranzen: Drm. +/- 0,1 mm; Dicke 600 +/- 25 µm
2 Flats: (2-11) +/-0.5°; 22+/-2 mm
CW 45°; 11+/-2 mm
epi-ready
einzeln in Fluoroware unter N2-Atmosphäre eingeschweißt
Artikelnr.: SC.GaAs.100087

Figure A.1: Datasheet of wafers supplied by MaTeck. Note the typographical error in the major flat direction. Since a flat is always perpendicular to the wafer surface it should obviously be $(2\bar{1}\bar{1})$.

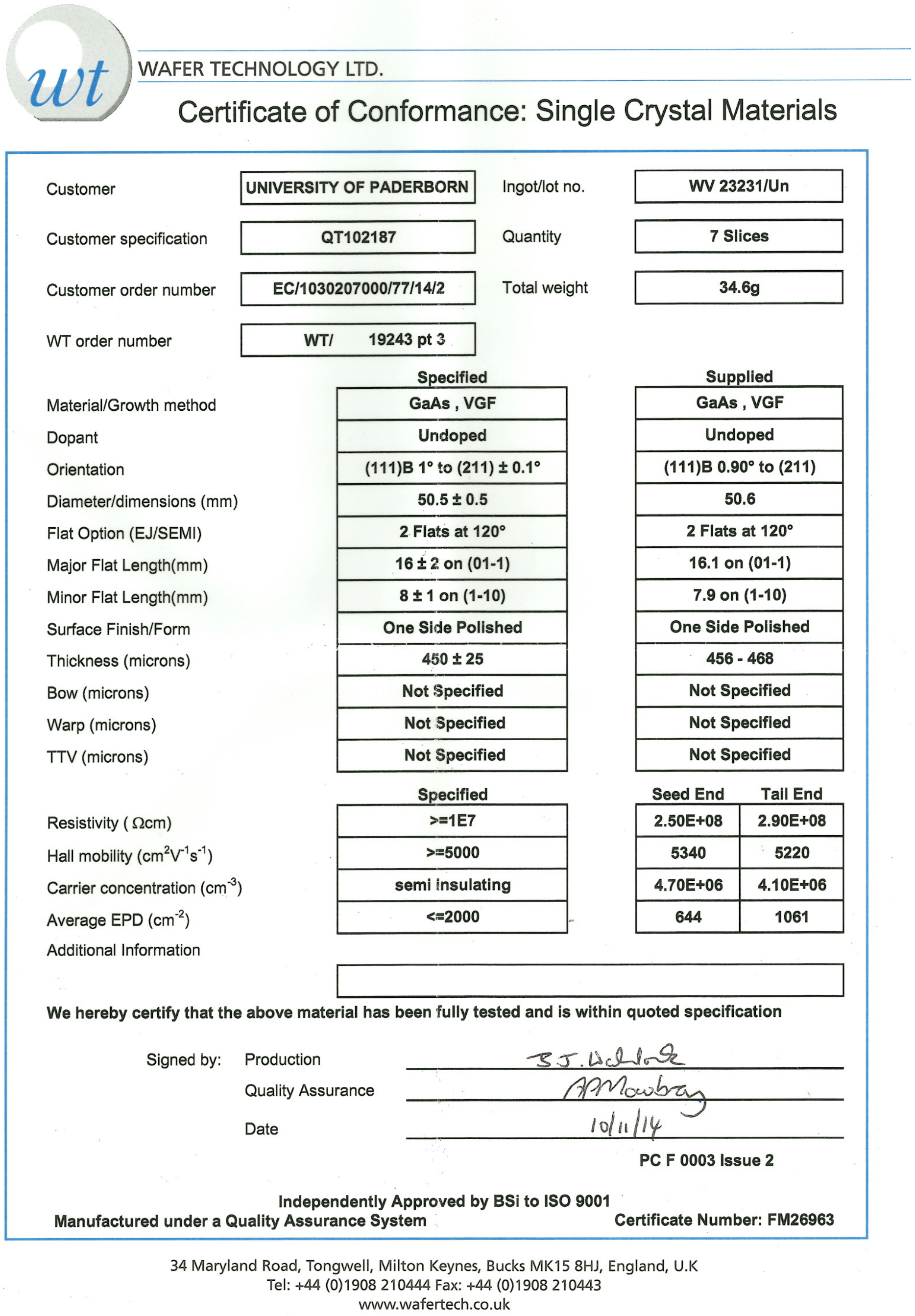

WAFER TECHNOLOGY LTD.

Certificate of Conformance: Single Crystal Materials

Customer	UNIVERSITY OF PADERBORN	Ingot/lot no.	WV 23231/Un
Customer specification	QT102187	Quantity	7 Slices
Customer order number	EC/1030207000/77/14/2	Total weight	34.6g
WT order number	WT/ 19243 pt 3		

	Specified	Supplied
Material/Growth method	GaAs , VGF	GaAs , VGF
Dopant	Undoped	Undoped
Orientation	(111)B 1° to (211) ± 0.1°	(111)B 0.90° to (211)
Diameter/dimensions (mm)	50.5 ± 0.5	50.6
Flat Option (EJ/SEMI)	2 Flats at 120°	2 Flats at 120°
Major Flat Length(mm)	16 ± 2 on (01-1)	16.1 on (01-1)
Minor Flat Length(mm)	8 ± 1 on (1-10)	7.9 on (1-10)
Surface Finish/Form	One Side Polished	One Side Polished
Thickness (microns)	450 ± 25	456 - 468
Bow (microns)	Not Specified	Not Specified
Warp (microns)	Not Specified	Not Specified
TTV (microns)	Not Specified	Not Specified

	Specified	Seed End	Tail End
Resistivity (Ωcm)	>=1E7	2.50E+08	2.90E+08
Hall mobility ($cm^2V^{-1}s^{-1}$)	>=5000	5340	5220
Carrier concentration (cm^{-3})	semi insulating	4.70E+06	4.10E+06
Average EPD (cm^{-2})	<=2000	644	1061

Additional Information

We hereby certify that the above material has been fully tested and is within quoted specification

Signed by: Production

Quality Assurance AMowbray

Date 10/11/14

PC F 0003 Issue 2

Independently Approved by BSi to ISO 9001

Manufactured under a Quality Assurance System **Certificate Number: FM26963**

34 Maryland Road, Tongwell, Milton Keynes, Bucks MK15 8HJ, England, U.K
Tel: +44 (0)1908 210444 Fax: +44 (0)1908 210443
www.wafertech.co.uk

Figure A.2: Datasheet of wafers supplied by Wafer Technologies.

APPENDIX B

Growth reports

In this chapter the growth reports of all samples described in this thesis are shown. The reports are generated semi-automatically and only feature steps in the recipe in which material is deposited. Substrate and cell temperature changes as well as growth pauses and rotation speed changes are omitted. Important parameters for the DE process have been manually added to the "Comment" box.

During MBE maintenance in 2016 the substrate manipulator was expanded by additional shielding which strongly changed the relationship of thermocouple and pyrometer temperatures. Nearly all samples in this thesis were generated after this change. All temperature values stated in this thesis are given for the new system state after the changes. This is noted here to prevent confusion when reviewing the growth sheets of the earliest samples where the temperatures are not consistent with the chronologically later ones.

During 2017 a flake fell into the pyrometer viewport and was only removed in November of that year. During this time the pyrometer was not operational and only T_{TC} could be measured. This is noted here to explain the absence of T_{pyro} values on growth sheets in that time.

The data points in Figure 4.15 also include samples which are not mentioned otherwise in this thesis. Especially capped and uncapped QDs deposited at $T_{\mathrm{dep}} = 200\,^{\circ}\mathrm{C}$ were repeatedly fabricated (typically after maintenance cycles) to ascertain constant ambient parameters during the last two years. For better legibility the contributing samples are named (and linked) here instead of the figure caption: A0352, A0356, A0357, A0359, A0375, A0393, A0427, A0516, A0612, A0695, A0703, A0748, A0781, A0798, A0799, A0811, A0819, A0828.

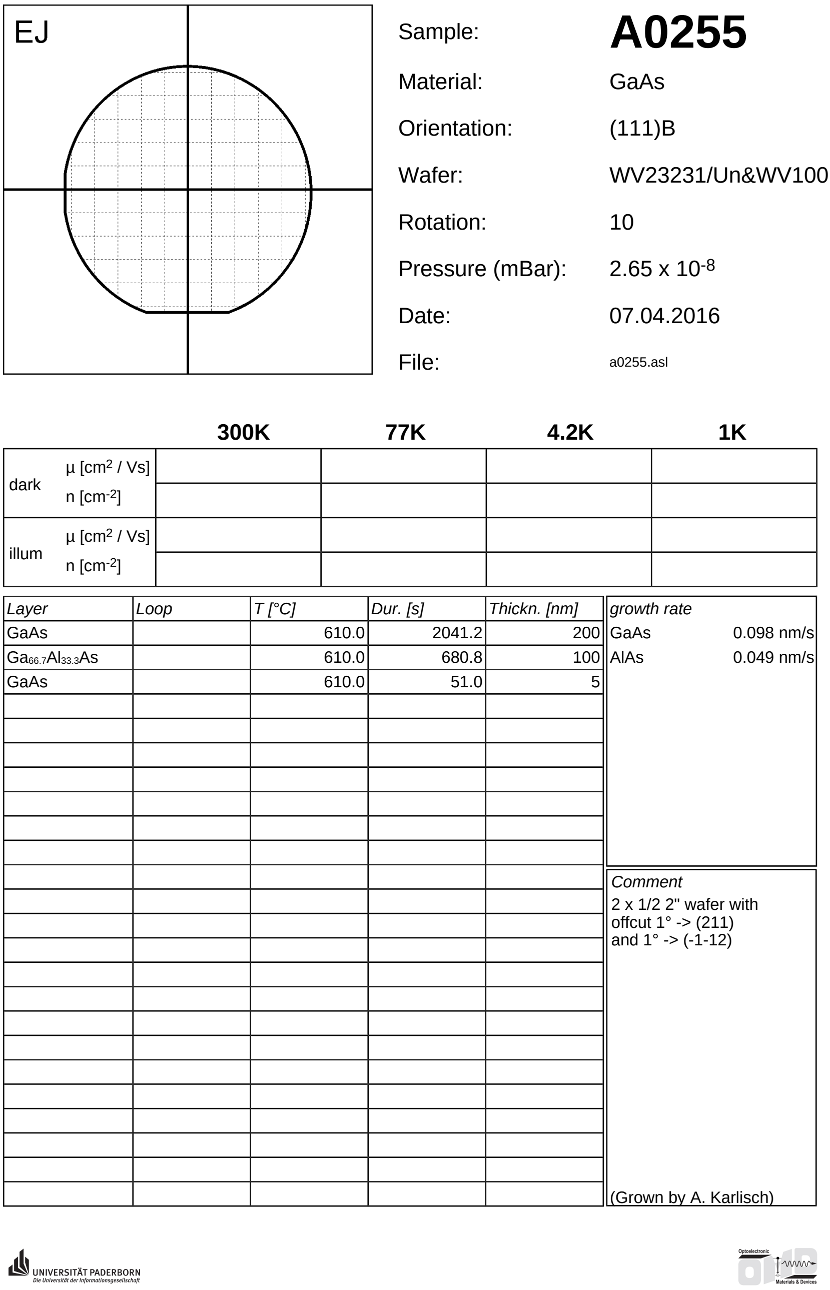

Sample: **A0255**
Material: GaAs
Orientation: (111)B
Wafer: WV23231/Un&WV10013/Un
Rotation: 10
Pressure (mBar): 2.65×10^{-8}
Date: 07.04.2016
File: a0255.asl

		300K	**77K**	**4.2K**	**1K**
dark	μ [cm^2 / Vs]				
	n [cm^{-2}]				
illum	μ [cm^2 / Vs]				
	n [cm^{-2}]				

Layer	*Loop*	*T [°C]*	*Dur. [s]*	*Thickn. [nm]*
GaAs		610.0	2041.2	200
$Ga_{66.7}Al_{33.3}As$		610.0	680.8	100
GaAs		610.0	51.0	5

growth rate	
GaAs	0.098 nm/s
AlAs	0.049 nm/s

Comment
2 x 1/2 2" wafer with
offcut 1° -> (211)
and 1° -> (-1-12)

(Grown by A. Karlisch)

UNIVERSITÄT PADERBORN
Die Universität der Informationsgesellschaft

Optoelectronic Materials & Devices

Figure B.1: Growth report of sample A0255.

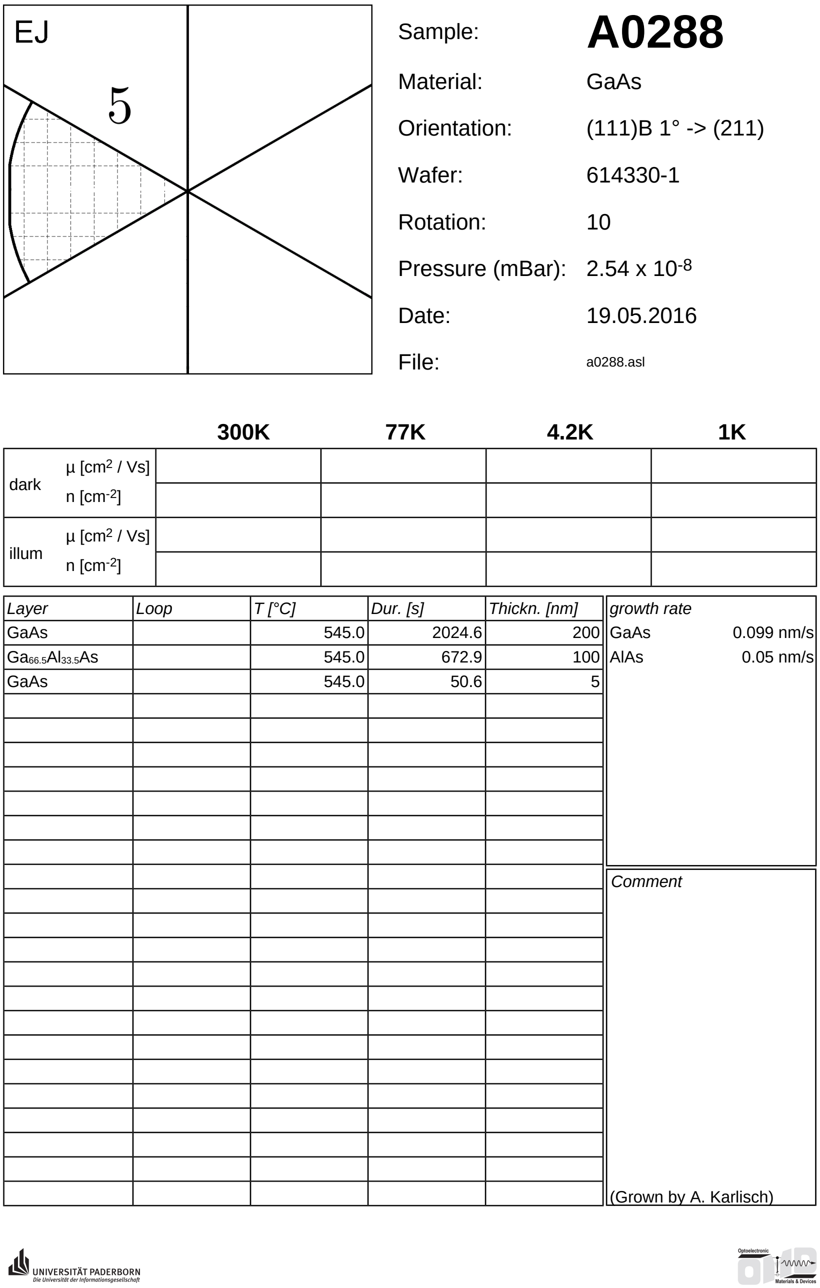

EJ

5

Sample: **A0288**

Material: GaAs

Orientation: (111)B 1° -> (211)

Wafer: 614330-1

Rotation: 10

Pressure (mBar): 2.54 x 10^{-8}

Date: 19.05.2016

File: a0288.asl

		300K	**77K**	**4.2K**	**1K**
dark	μ [cm^2 / Vs]				
	n [cm^{-2}]				
illum	μ [cm^2 / Vs]				
	n [cm^{-2}]				

Layer	*Loop*	*T [°C]*	*Dur. [s]*	*Thickn. [nm]*
GaAs		545.0	2024.6	200
$Ga_{66.5}Al_{33.5}As$		545.0	672.9	100
GaAs		545.0	50.6	5

growth rate	
GaAs	0.099 nm/s
AlAs	0.05 nm/s

Comment

(Grown by A. Karlisch)

UNIVERSITÄT PADERBORN
Die Universität der Informationsgesellschaft

Optoelectronic Materials & Devices

Figure B.2: Growth report of sample A0288.

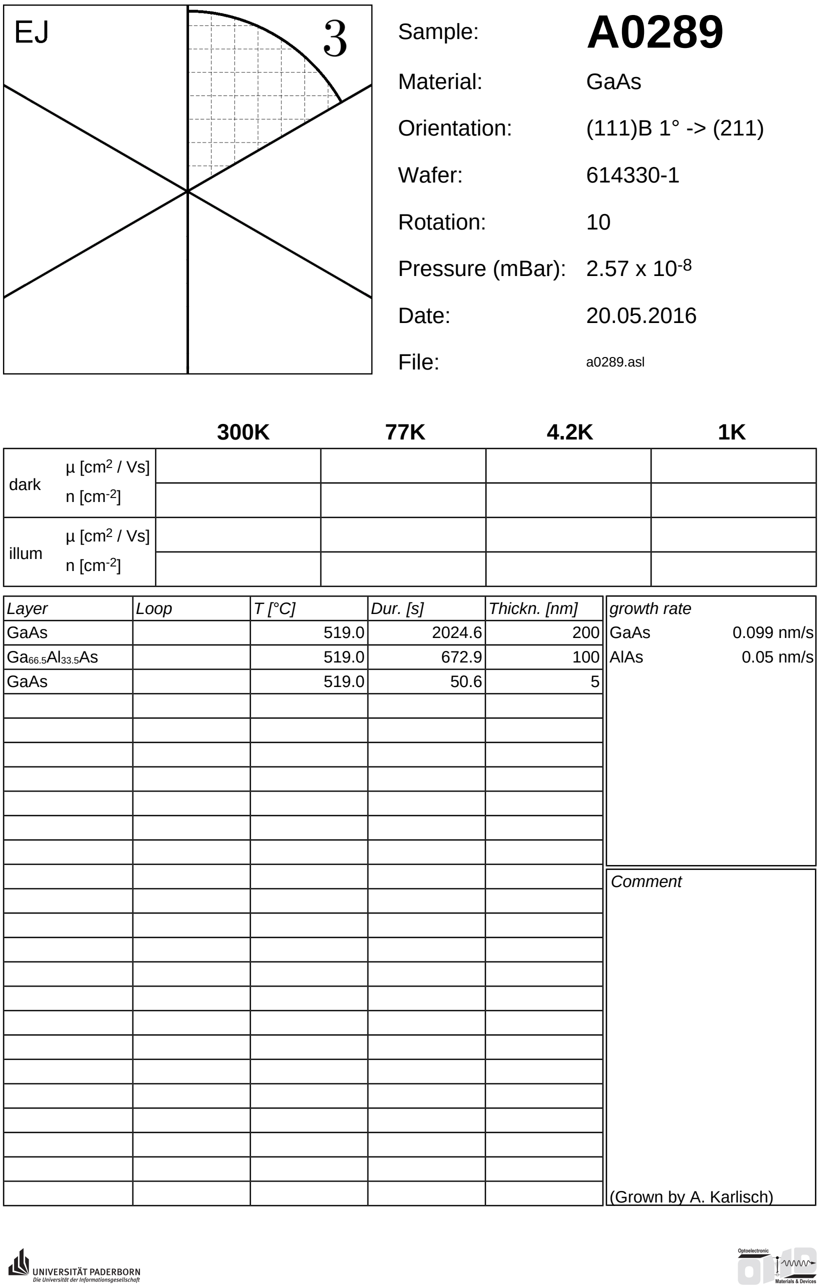

Sample: **A0289**

Material: GaAs

Orientation: (111)B 1° -> (211)

Wafer: 614330-1

Rotation: 10

Pressure (mBar): 2.57×10^{-8}

Date: 20.05.2016

File: a0289.asl

		300K	77K	4.2K	1K
dark	μ [cm^2 / Vs]				
	n [cm^{-2}]				
illum	μ [cm^2 / Vs]				
	n [cm^{-2}]				

Layer	*Loop*	*T [°C]*	*Dur. [s]*	*Thickn. [nm]*
GaAs		519.0	2024.6	200
$Ga_{66.5}Al_{33.5}As$		519.0	672.9	100
GaAs		519.0	50.6	5

growth rate	
GaAs	0.099 nm/s
AlAs	0.05 nm/s

Comment

(Grown by A. Karlisch)

UNIVERSITÄT PADERBORN
Die Universität der Informationsgesellschaft

Optoelectronic Materials & Devices

Figure B.3: Growth report of sample A0289.

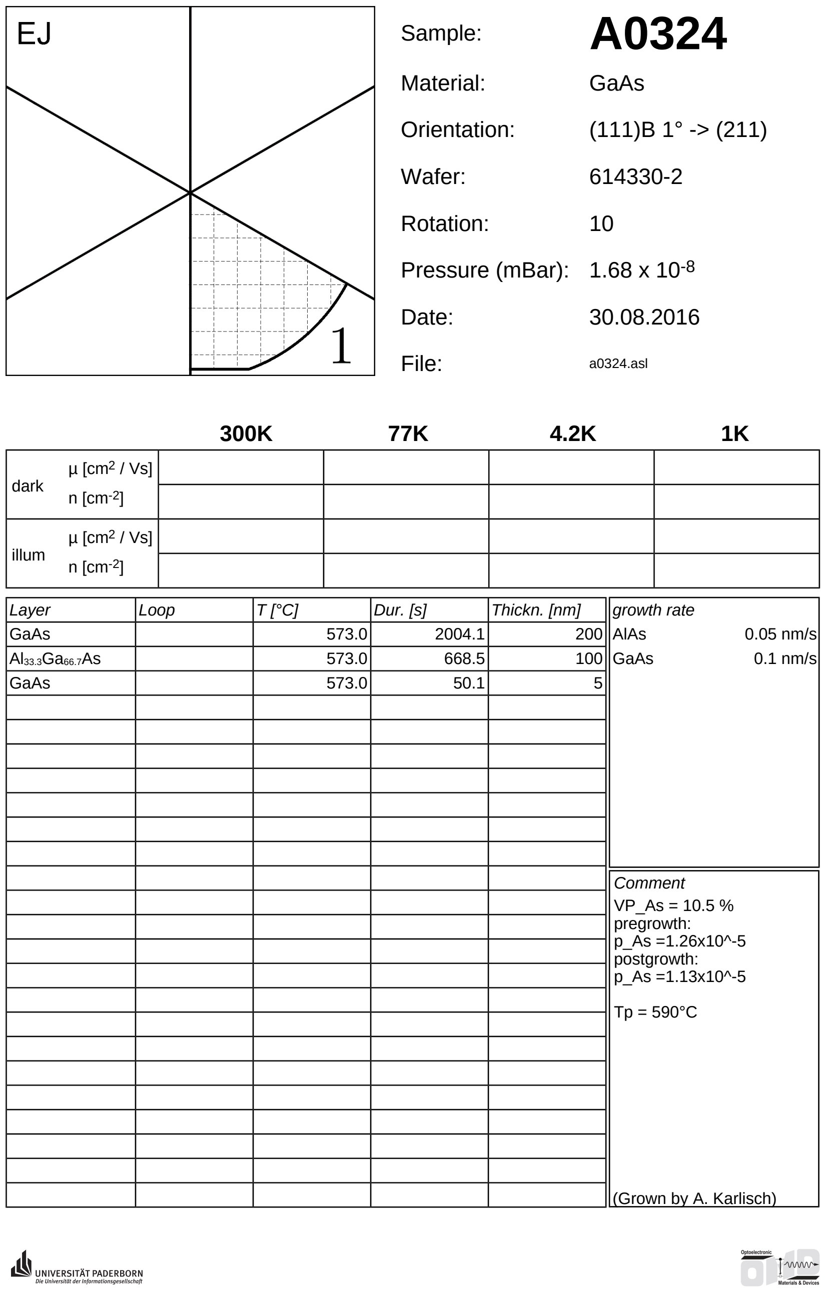

EJ

1

Sample: **A0324**

Material: GaAs

Orientation: (111)B 1° -> (211)

Wafer: 614330-2

Rotation: 10

Pressure (mBar): 1.68 x 10^{-8}

Date: 30.08.2016

File: a0324.asl

		300K	77K	4.2K	1K
dark	μ [cm^2 / Vs]				
	n [cm^{-2}]				
illum	μ [cm^2 / Vs]				
	n [cm^{-2}]				

Layer	*Loop*	*T [°C]*	*Dur. [s]*	*Thickn. [nm]*
GaAs		573.0	2004.1	200
$Al_{33.3}Ga_{66.7}As$		573.0	668.5	100
GaAs		573.0	50.1	5

growth rate	
AlAs	0.05 nm/s
GaAs	0.1 nm/s

Comment

VP_As = 10.5 %
pregrowth:
p_As =1.26x10^-5
postgrowth:
p_As =1.13x10^-5

Tp = 590°C

(Grown by A. Karlisch)

UNIVERSITÄT PADERBORN
Die Universität der Informationsgesellschaft

Optoelectronic Materials & Devices

Figure B.4: Growth report of sample A0324.

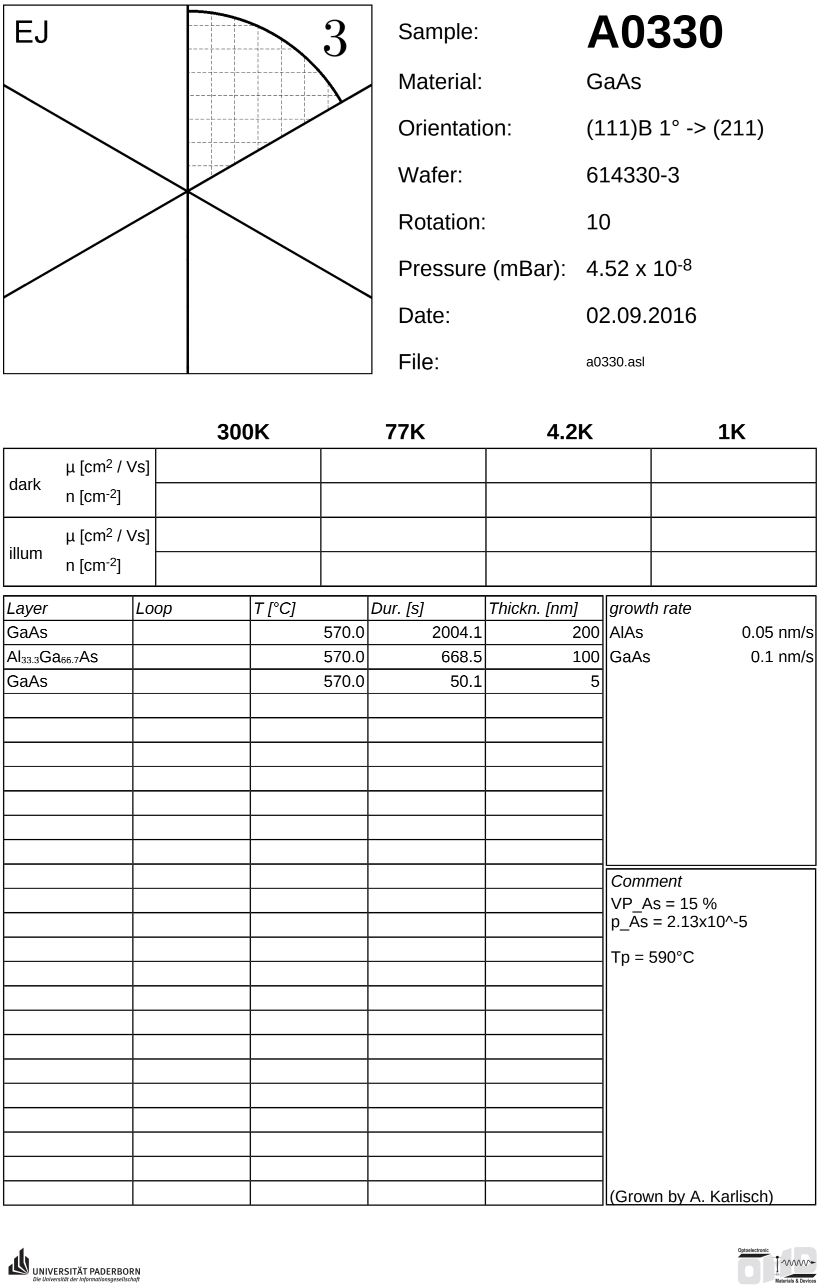

Sample: **A0330**
Material: GaAs
Orientation: (111)B 1° -> (211)
Wafer: 614330-3
Rotation: 10
Pressure (mBar): 4.52×10^{-8}
Date: 02.09.2016
File: a0330.asl

		300K	**77K**	**4.2K**	**1K**
dark	μ [cm^2 / Vs]				
	n [cm^{-2}]				
illum	μ [cm^2 / Vs]				
	n [cm^{-2}]				

Layer	*Loop*	*T [°C]*	*Dur. [s]*	*Thickn. [nm]*
GaAs		570.0	2004.1	200
$Al_{33.3}Ga_{66.7}As$		570.0	668.5	100
GaAs		570.0	50.1	5

growth rate	
AlAs	0.05 nm/s
GaAs	0.1 nm/s

Comment
VP_As = 15 %
p_As = 2.13x10^-5

Tp = 590°C

(Grown by A. Karlisch)

UNIVERSITÄT PADERBORN
Die Universität der Informationsgesellschaft

Optoelectronic Materials & Devices

Figure B.5: Growth report of sample A0330.

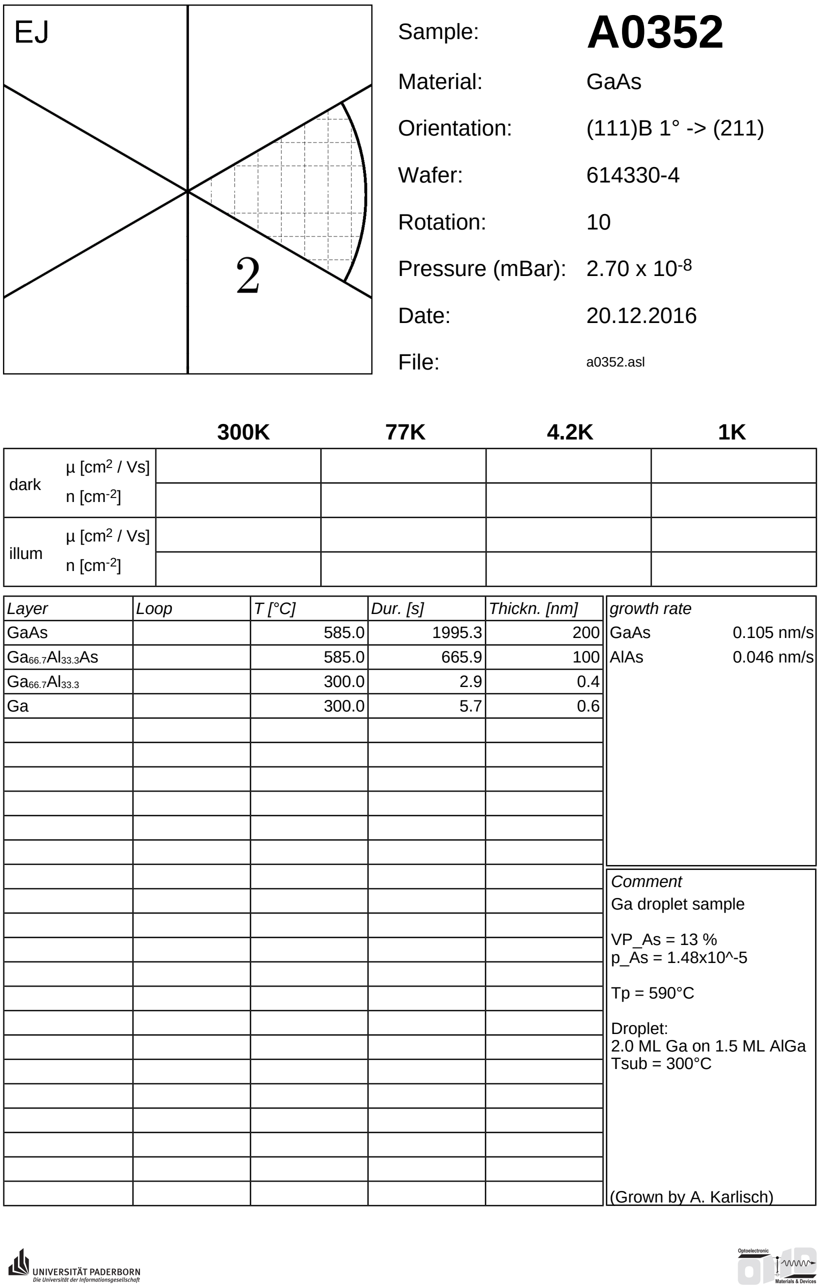

Sample: **A0352**
Material: GaAs
Orientation: (111)B 1° -> (211)
Wafer: 614330-4
Rotation: 10
Pressure (mBar): 2.70×10^{-8}
Date: 20.12.2016
File: a0352.asl

		300K	77K	4.2K	1K
dark	μ [cm^2 / Vs]				
	n [cm^{-2}]				
illum	μ [cm^2 / Vs]				
	n [cm^{-2}]				

Layer	*Loop*	*T [°C]*	*Dur. [s]*	*Thickn. [nm]*
GaAs		585.0	1995.3	200
$Ga_{66.7}Al_{33.3}As$		585.0	665.9	100
$Ga_{66.7}Al_{33.3}$		300.0	2.9	0.4
Ga		300.0	5.7	0.6

growth rate	
GaAs	0.105 nm/s
AlAs	0.046 nm/s

Comment
Ga droplet sample

VP_As = 13 %
p_As = 1.48x10^-5

Tp = 590°C

Droplet:
2.0 ML Ga on 1.5 ML AlGa
Tsub = 300°C

(Grown by A. Karlisch)

UNIVERSITÄT PADERBORN
Die Universität der Informationsgesellschaft

Optoelectronic Materials & Devices

Figure B.6: Growth report of sample A0352.

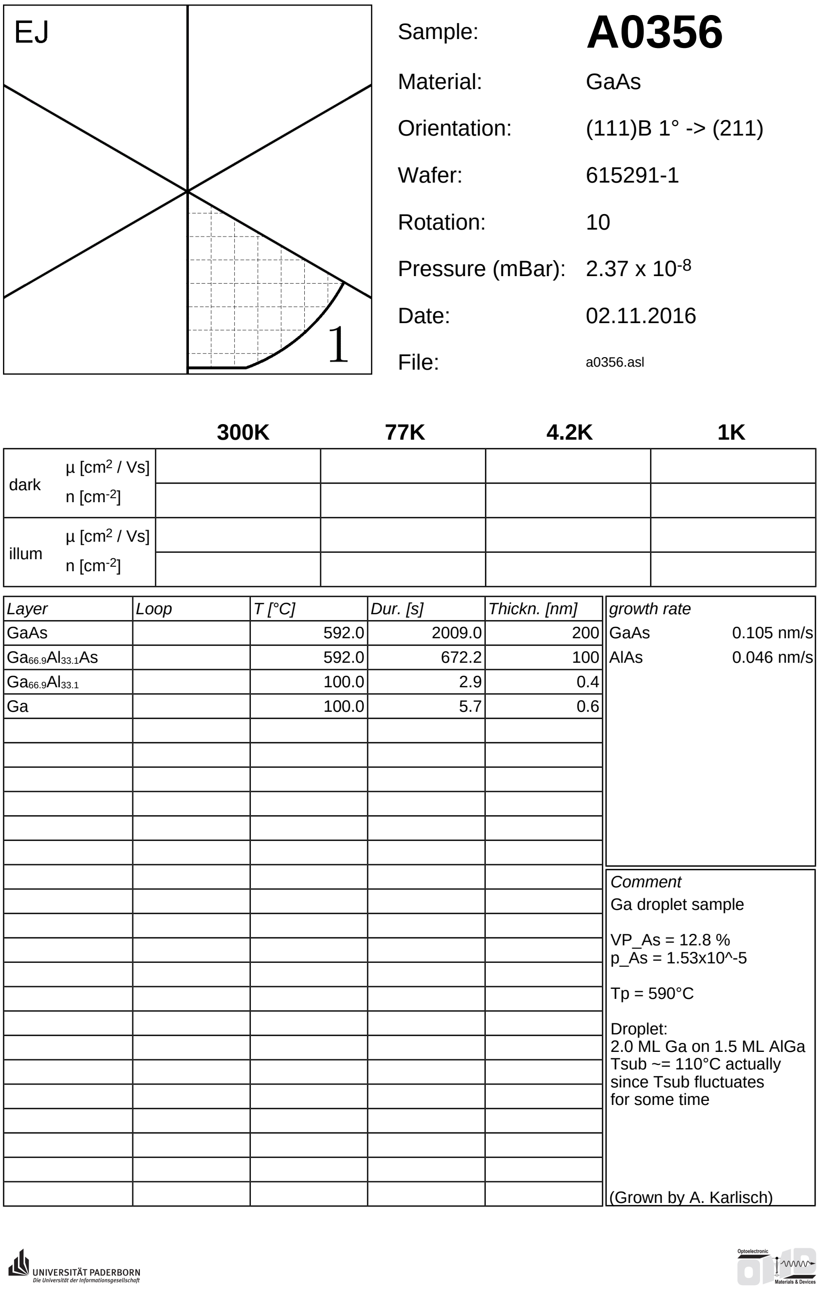

Sample: **A0356**

Material: GaAs

Orientation: (111)B 1° -> (211)

Wafer: 615291-1

Rotation: 10

Pressure (mBar): 2.37 x 10^{-8}

Date: 02.11.2016

File: a0356.asl

		300K	**77K**	**4.2K**	**1K**
dark	µ [cm^2 / Vs]				
	n [cm^{-2}]				
illum	µ [cm^2 / Vs]				
	n [cm^{-2}]				

Layer	*Loop*	*T [°C]*	*Dur. [s]*	*Thickn. [nm]*
GaAs		592.0	2009.0	200
Ga$_{66.9}$Al$_{33.1}$As		592.0	672.2	100
Ga$_{66.9}$Al$_{33.1}$		100.0	2.9	0.4
Ga		100.0	5.7	0.6

growth rate	
GaAs	0.105 nm/s
AlAs	0.046 nm/s

Comment

Ga droplet sample

VP_As = 12.8 %
p_As = 1.53x10^-5

Tp = 590°C

Droplet:
2.0 ML Ga on 1.5 ML AlGa
Tsub ~= 110°C actually
since Tsub fluctuates
for some time

(Grown by A. Karlisch)

Figure B.7: Growth report of sample A0356.

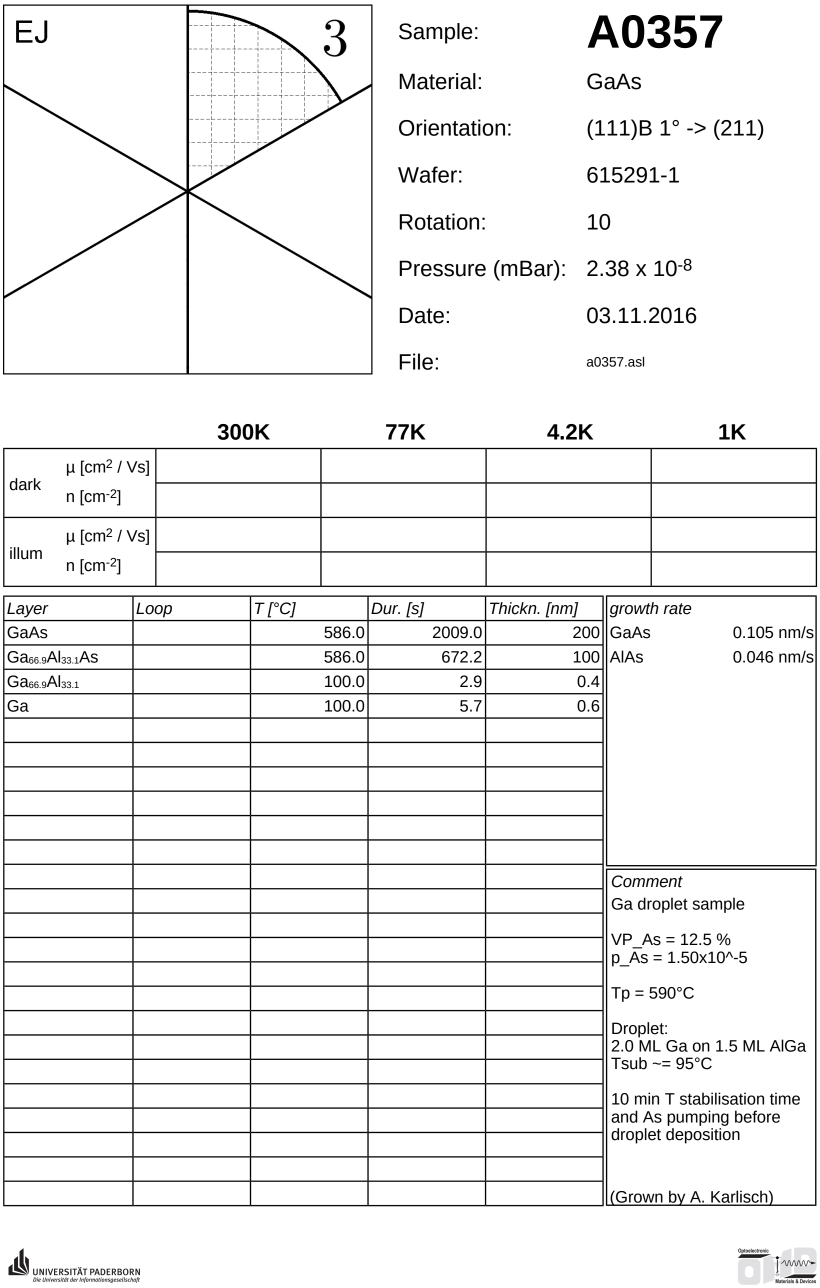

Sample: **A0357**
Material: GaAs
Orientation: (111)B 1° -> (211)
Wafer: 615291-1
Rotation: 10
Pressure (mBar): 2.38×10^{-8}
Date: 03.11.2016
File: a0357.asl

		300K	77K	4.2K	1K
dark	μ [cm^2 / Vs]				
	n [cm^{-2}]				
illum	μ [cm^2 / Vs]				
	n [cm^{-2}]				

Layer	*Loop*	*T [°C]*	*Dur. [s]*	*Thickn. [nm]*
GaAs		586.0	2009.0	200
$Ga_{66.9}Al_{33.1}As$		586.0	672.2	100
$Ga_{66.9}Al_{33.1}$		100.0	2.9	0.4
Ga		100.0	5.7	0.6

growth rate	
GaAs	0.105 nm/s
AlAs	0.046 nm/s

Comment
Ga droplet sample

VP_As = 12.5 %
p_As = 1.50x10^-5

Tp = 590°C

Droplet:
2.0 ML Ga on 1.5 ML AlGa
Tsub ~= 95°C

10 min T stabilisation time
and As pumping before
droplet deposition

(Grown by A. Karlisch)

UNIVERSITÄT PADERBORN
Die Universität der Informationsgesellschaft

Optoelectronic
Materials & Devices

Figure B.8: Growth report of sample A0357.

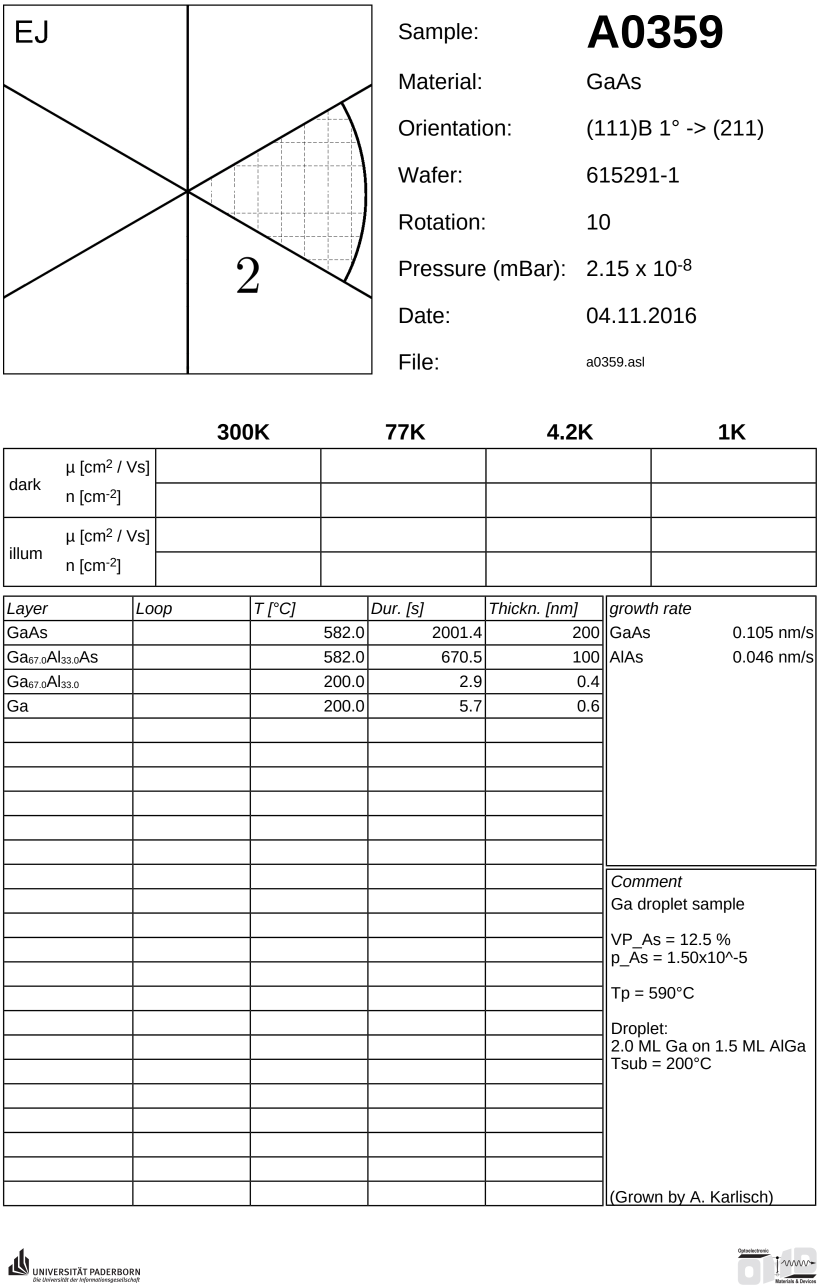

EJ

2

Sample: **A0359**
Material: GaAs
Orientation: (111)B 1° -> (211)
Wafer: 615291-1
Rotation: 10
Pressure (mBar): 2.15×10^{-8}
Date: 04.11.2016
File: a0359.asl

		300K	**77K**	**4.2K**	**1K**
dark	μ [cm^2 / Vs]				
	n [cm^{-2}]				
illum	μ [cm^2 / Vs]				
	n [cm^{-2}]				

Layer	*Loop*	*T [°C]*	*Dur. [s]*	*Thickn. [nm]*
GaAs		582.0	2001.4	200
Ga$_{67.0}$Al$_{33.0}$As		582.0	670.5	100
Ga$_{67.0}$Al$_{33.0}$		200.0	2.9	0.4
Ga		200.0	5.7	0.6

growth rate	
GaAs	0.105 nm/s
AlAs	0.046 nm/s

Comment
Ga droplet sample

VP_As = 12.5 %
p_As = 1.50x10^-5

Tp = 590°C

Droplet:
2.0 ML Ga on 1.5 ML AlGa
Tsub = 200°C

(Grown by A. Karlisch)

UNIVERSITÄT PADERBORN
Die Universität der Informationsgesellschaft

Optoelectronic
Materials & Devices

Figure B.9: Growth report of sample A0359.

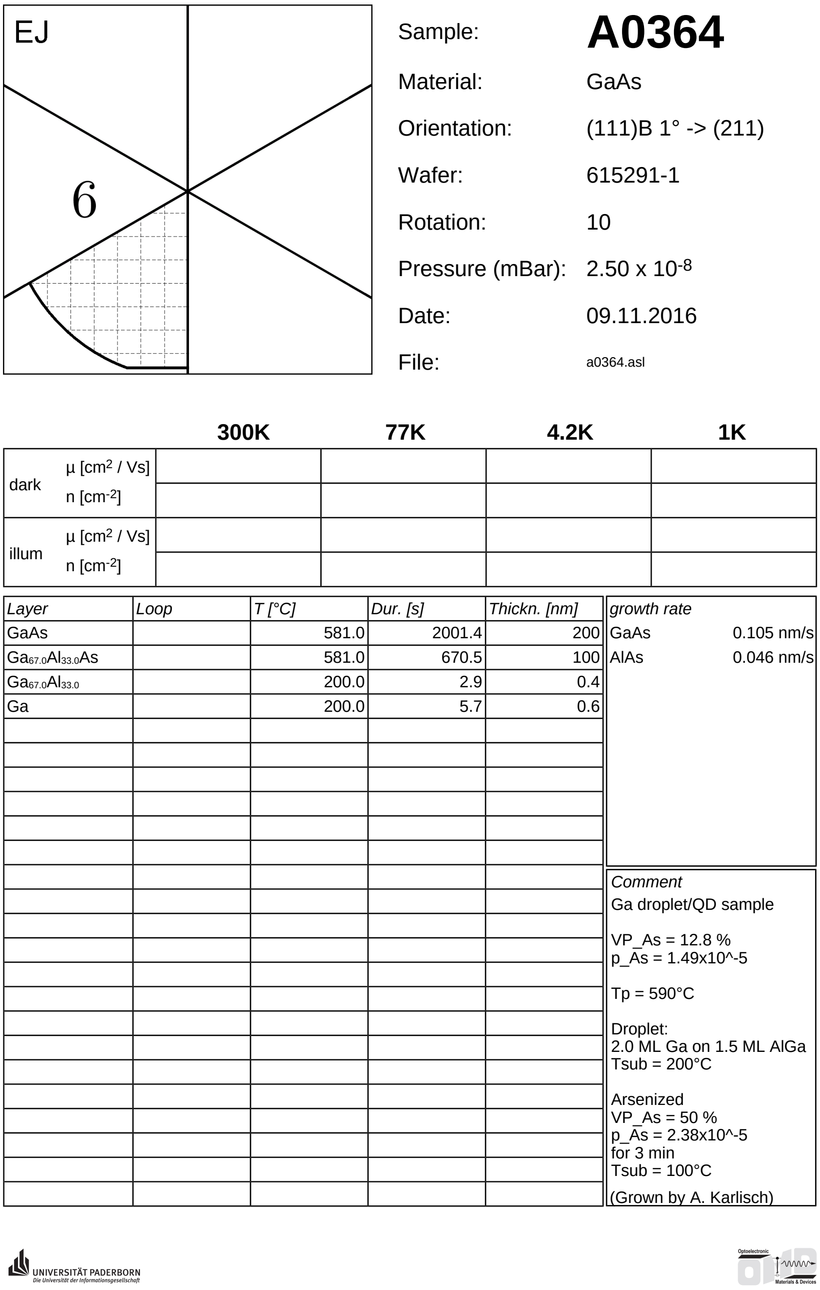

Sample: **A0364**
Material: GaAs
Orientation: (111)B 1° -> (211)
Wafer: 615291-1
Rotation: 10
Pressure (mBar): 2.50 x 10^{-8}
Date: 09.11.2016
File: a0364.asl

		300K	77K	4.2K	1K
dark	μ [cm^2 / Vs]				
	n [cm^{-2}]				
illum	μ [cm^2 / Vs]				
	n [cm^{-2}]				

Layer	*Loop*	*T [°C]*	*Dur. [s]*	*Thickn. [nm]*
GaAs		581.0	2001.4	200
$Ga_{67.0}Al_{33.0}As$		581.0	670.5	100
$Ga_{67.0}Al_{33.0}$		200.0	2.9	0.4
Ga		200.0	5.7	0.6

growth rate	
GaAs	0.105 nm/s
AlAs	0.046 nm/s

Comment

Ga droplet/QD sample

VP_As = 12.8 %
p_As = 1.49x10^-5

Tp = 590°C

Droplet:
2.0 ML Ga on 1.5 ML AlGa
Tsub = 200°C

Arsenized
VP_As = 50 %
p_As = 2.38x10^-5
for 3 min
Tsub = 100°C

(Grown by A. Karlisch)

Figure B.10: Growth report of sample A0364.

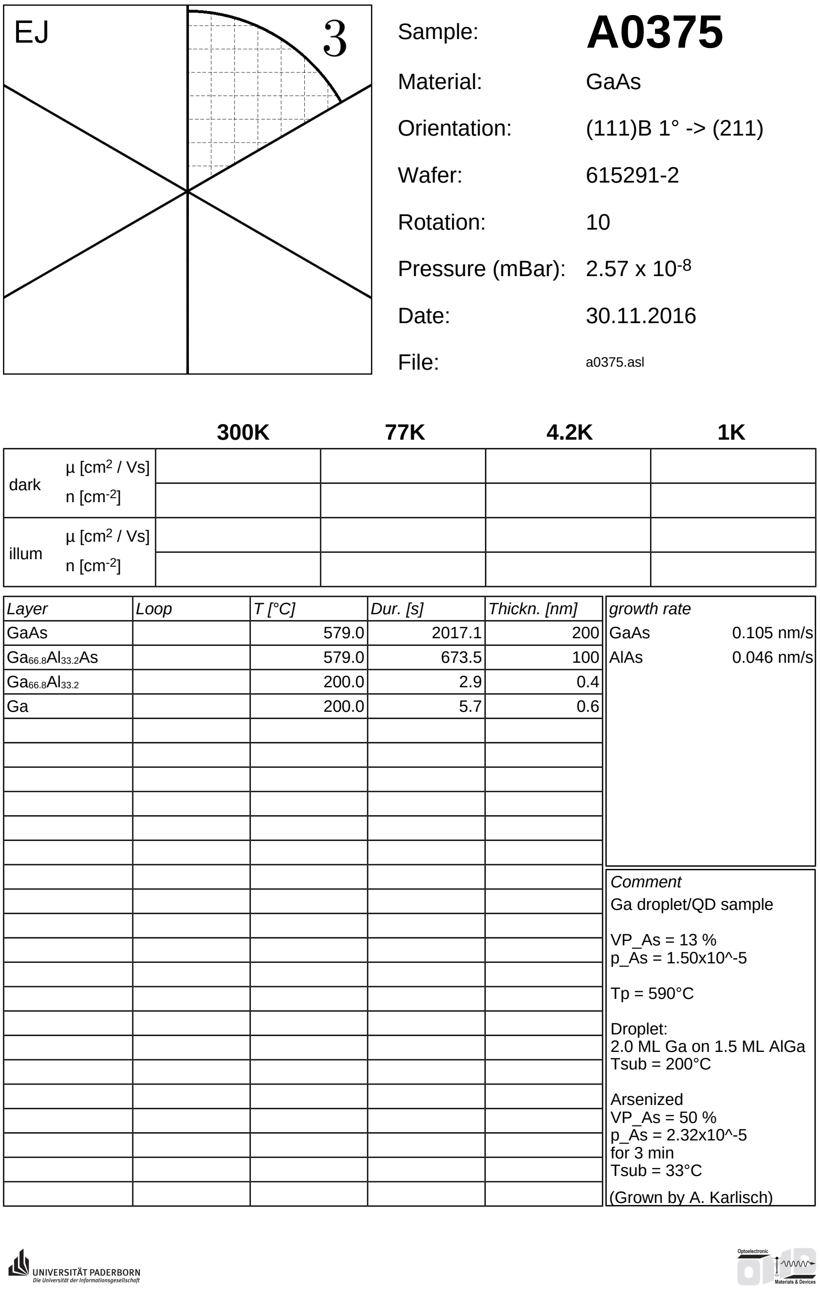

Sample: **A0375**

Material: GaAs

Orientation: (111)B 1° -> (211)

Wafer: 615291-2

Rotation: 10

Pressure (mBar): 2.57×10^{-8}

Date: 30.11.2016

File: a0375.asl

		300K	77K	4.2K	1K
dark	μ [cm^2 / Vs]				
	n [cm^{-2}]				
illum	μ [cm^2 / Vs]				
	n [cm^{-2}]				

Layer	*Loop*	*T [°C]*	*Dur. [s]*	*Thickn. [nm]*
GaAs		579.0	2017.1	200
Ga$_{66.8}$Al$_{33.2}$As		579.0	673.5	100
Ga$_{66.8}$Al$_{33.2}$		200.0	2.9	0.4
Ga		200.0	5.7	0.6

growth rate	
GaAs	0.105 nm/s
AlAs	0.046 nm/s

Comment

Ga droplet/QD sample

VP_As = 13 %
p_As = 1.50x10^-5

Tp = 590°C

Droplet:
2.0 ML Ga on 1.5 ML AlGa
Tsub = 200°C

Arsenized
VP_As = 50 %
p_As = 2.32x10^-5
for 3 min
Tsub = 33°C

(Grown by A. Karlisch)

UNIVERSITÄT PADERBORN
Die Universität der Informationsgesellschaft

Optoelectronic Materials & Devices

Figure B.11: Growth report of sample A0375.

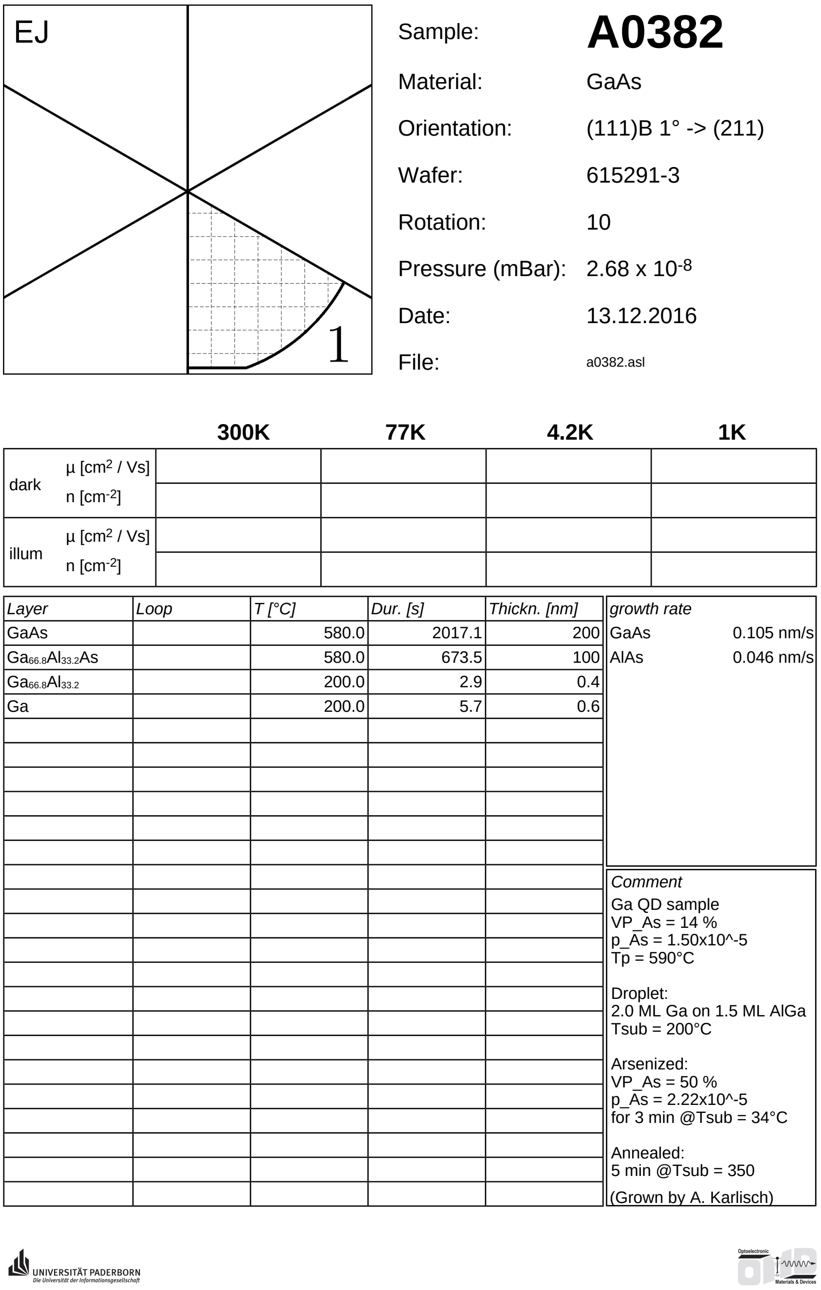

Sample: **A0382**
Material: GaAs
Orientation: (111)B 1° -> (211)
Wafer: 615291-3
Rotation: 10
Pressure (mBar): 2.68 x 10^{-8}
Date: 13.12.2016
File: a0382.asl

		300K	**77K**	**4.2K**	**1K**
dark	μ [cm^2 / Vs]				
	n [cm^{-2}]				
illum	μ [cm^2 / Vs]				
	n [cm^{-2}]				

Layer	*Loop*	*T [°C]*	*Dur. [s]*	*Thickn. [nm]*
GaAs		580.0	2017.1	200
$Ga_{66.8}Al_{33.2}As$		580.0	673.5	100
$Ga_{66.8}Al_{33.2}$		200.0	2.9	0.4
Ga		200.0	5.7	0.6

growth rate	
GaAs	0.105 nm/s
AlAs	0.046 nm/s

Comment
Ga QD sample
VP_As = 14 %
p_As = 1.50x10^-5
Tp = 590°C

Droplet:
2.0 ML Ga on 1.5 ML AlGa
Tsub = 200°C

Arsenized:
VP_As = 50 %
p_As = 2.22x10^-5
for 3 min @Tsub = 34°C

Annealed:
5 min @Tsub = 350

(Grown by A. Karlisch)

UNIVERSITÄT PADERBORN
Die Universität der Informationsgesellschaft

Figure B.12: Growth report of sample A0382.

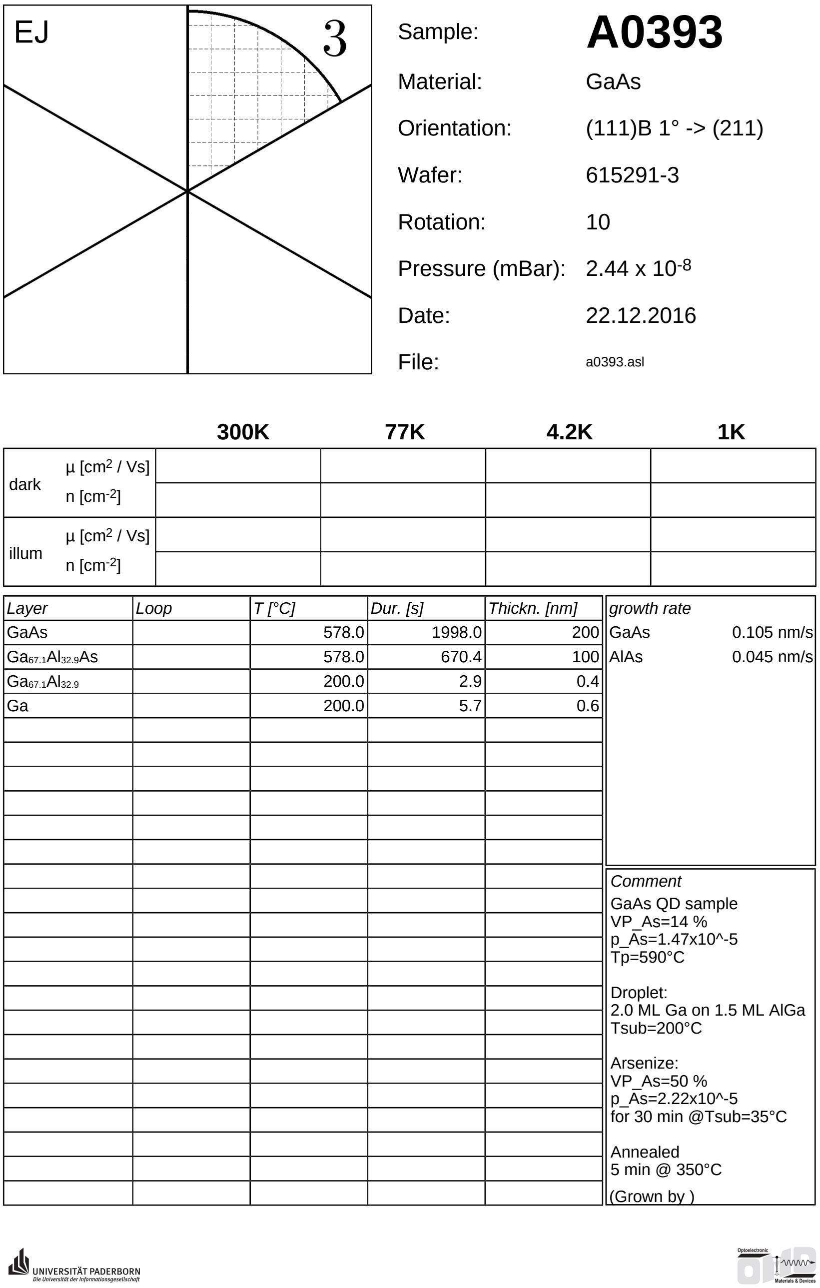

Sample: **A0393**
Material: GaAs
Orientation: (111)B 1° -> (211)
Wafer: 615291-3
Rotation: 10
Pressure (mBar): 2.44×10^{-8}
Date: 22.12.2016
File: a0393.asl

		300K	77K	4.2K	1K
dark	μ [cm^2 / Vs]				
	n [cm^{-2}]				
illum	μ [cm^2 / Vs]				
	n [cm^{-2}]				

Layer	*Loop*	*T [°C]*	*Dur. [s]*	*Thickn. [nm]*
GaAs		578.0	1998.0	200
$\mathrm{Ga}_{67.1}\mathrm{Al}_{32.9}\mathrm{As}$		578.0	670.4	100
$\mathrm{Ga}_{67.1}\mathrm{Al}_{32.9}$		200.0	2.9	0.4
Ga		200.0	5.7	0.6

growth rate	
GaAs	0.105 nm/s
AlAs	0.045 nm/s

Comment
GaAs QD sample
VP_As=14 %
p_As=1.47x10^-5
Tp=590°C

Droplet:
2.0 ML Ga on 1.5 ML AlGa
Tsub=200°C

Arsenize:
VP_As=50 %
p_As=2.22x10^-5
for 30 min @Tsub=35°C

Annealed
5 min @ 350°C
(Grown by)

UNIVERSITÄT PADERBORN
Die Universität der Informationsgesellschaft

Optoelectronic Materials & Devices

Figure B.13: Growth report of sample A0393.

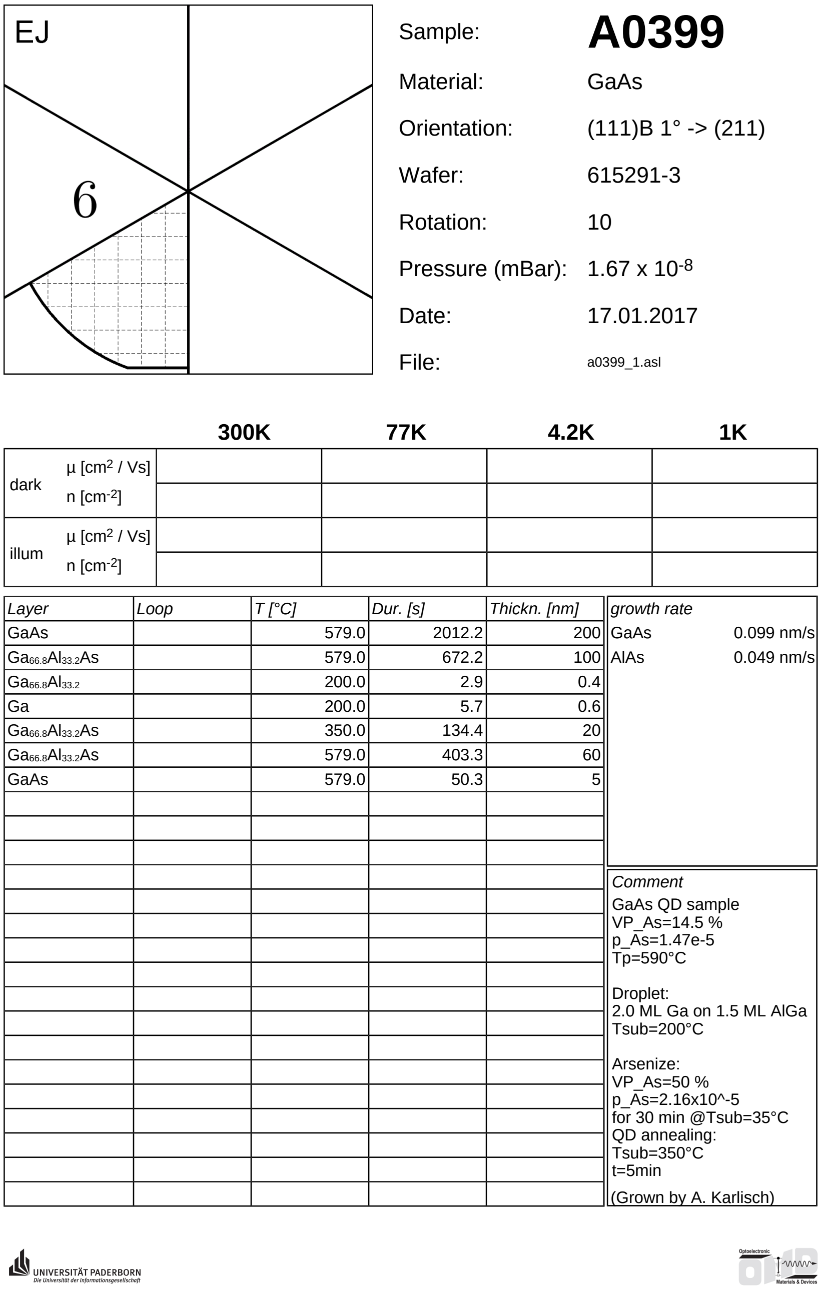

Sample:	**A0399**
Material:	GaAs
Orientation:	(111)B 1° -> (211)
Wafer:	615291-3
Rotation:	10
Pressure (mBar):	1.67 x 10^{-8}
Date:	17.01.2017
File:	a0399_1.asl

		300K	**77K**	**4.2K**	**1K**
dark	µ [cm^2 / Vs]				
	n [cm^{-2}]				
illum	µ [cm^2 / Vs]				
	n [cm^{-2}]				

Layer	*Loop*	*T [°C]*	*Dur. [s]*	*Thickn. [nm]*
GaAs		579.0	2012.2	200
$Ga_{66.8}Al_{33.2}As$		579.0	672.2	100
$Ga_{66.8}Al_{33.2}$		200.0	2.9	0.4
Ga		200.0	5.7	0.6
$Ga_{66.8}Al_{33.2}As$		350.0	134.4	20
$Ga_{66.8}Al_{33.2}As$		579.0	403.3	60
GaAs		579.0	50.3	5

growth rate	
GaAs	0.099 nm/s
AlAs	0.049 nm/s

Comment
GaAs QD sample
VP_As=14.5 %
p_As=1.47e-5
Tp=590°C

Droplet:
2.0 ML Ga on 1.5 ML AlGa
Tsub=200°C

Arsenize:
VP_As=50 %
p_As=2.16x10^-5
for 30 min @Tsub=35°C
QD annealing:
Tsub=350°C
t=5min

(Grown by A. Karlisch)

UNIVERSITÄT PADERBORN
Die Universität der Informationsgesellschaft

Optoelectronic Materials & Devices

Figure B.14: Growth report of sample A0399.

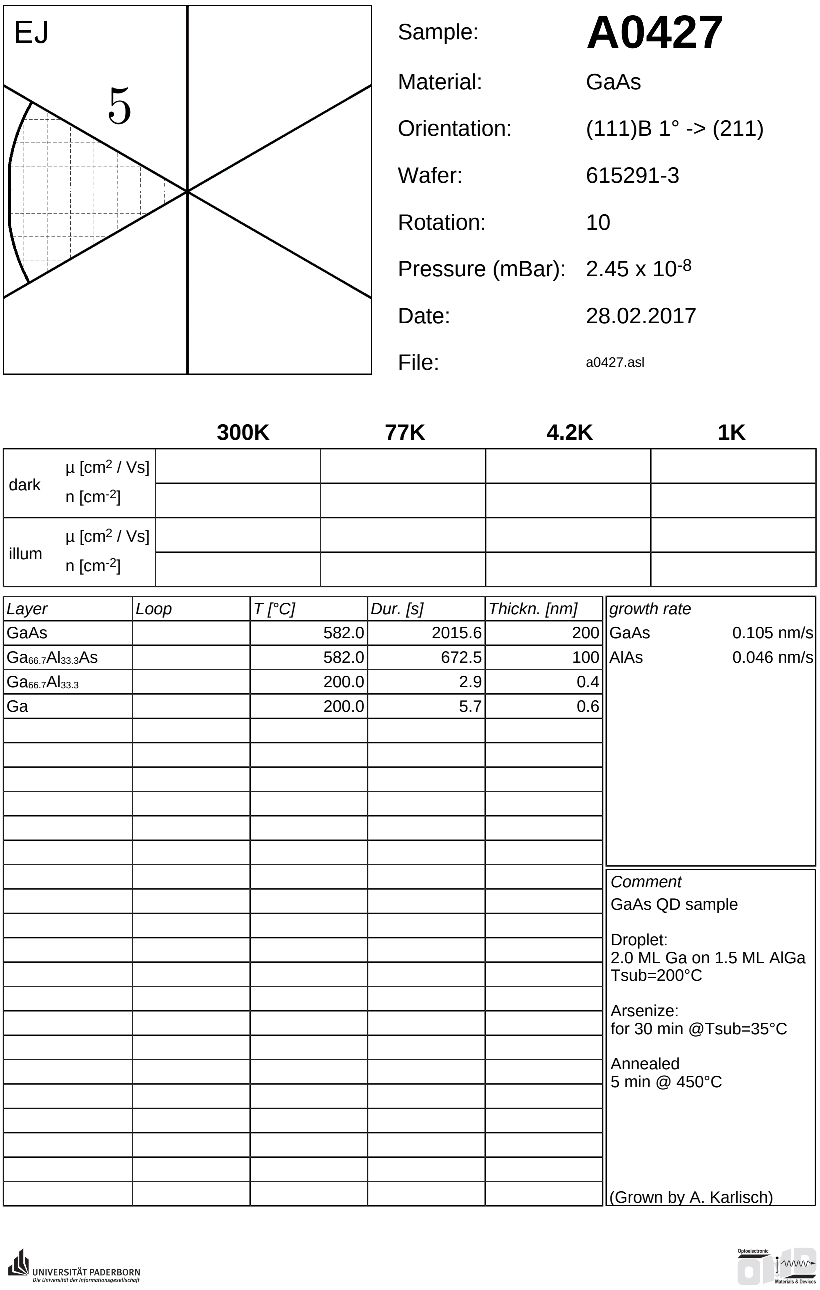

EJ

5

Sample:	**A0427**
Material:	GaAs
Orientation:	(111)B 1° -> (211)
Wafer:	615291-3
Rotation:	10
Pressure (mBar):	2.45×10^{-8}
Date:	28.02.2017
File:	a0427.asl

		300K	**77K**	**4.2K**	**1K**
dark	μ [cm^2 / Vs]				
	n [cm^{-2}]				
illum	μ [cm^2 / Vs]				
	n [cm^{-2}]				

Layer	*Loop*	*T [°C]*	*Dur. [s]*	*Thickn. [nm]*
GaAs		582.0	2015.6	200
$Ga_{66.7}Al_{33.3}As$		582.0	672.5	100
$Ga_{66.7}Al_{33.3}$		200.0	2.9	0.4
Ga		200.0	5.7	0.6

growth rate	
GaAs	0.105 nm/s
AlAs	0.046 nm/s

Comment

GaAs QD sample

Droplet:
2.0 ML Ga on 1.5 ML AlGa
Tsub=200°C

Arsenize:
for 30 min @Tsub=35°C

Annealed
5 min @ 450°C

(Grown by A. Karlisch)

UNIVERSITÄT PADERBORN
Die Universität der Informationsgesellschaft

Optoelectronic
Materials & Devices

Figure B.15: Growth report of sample A0427.

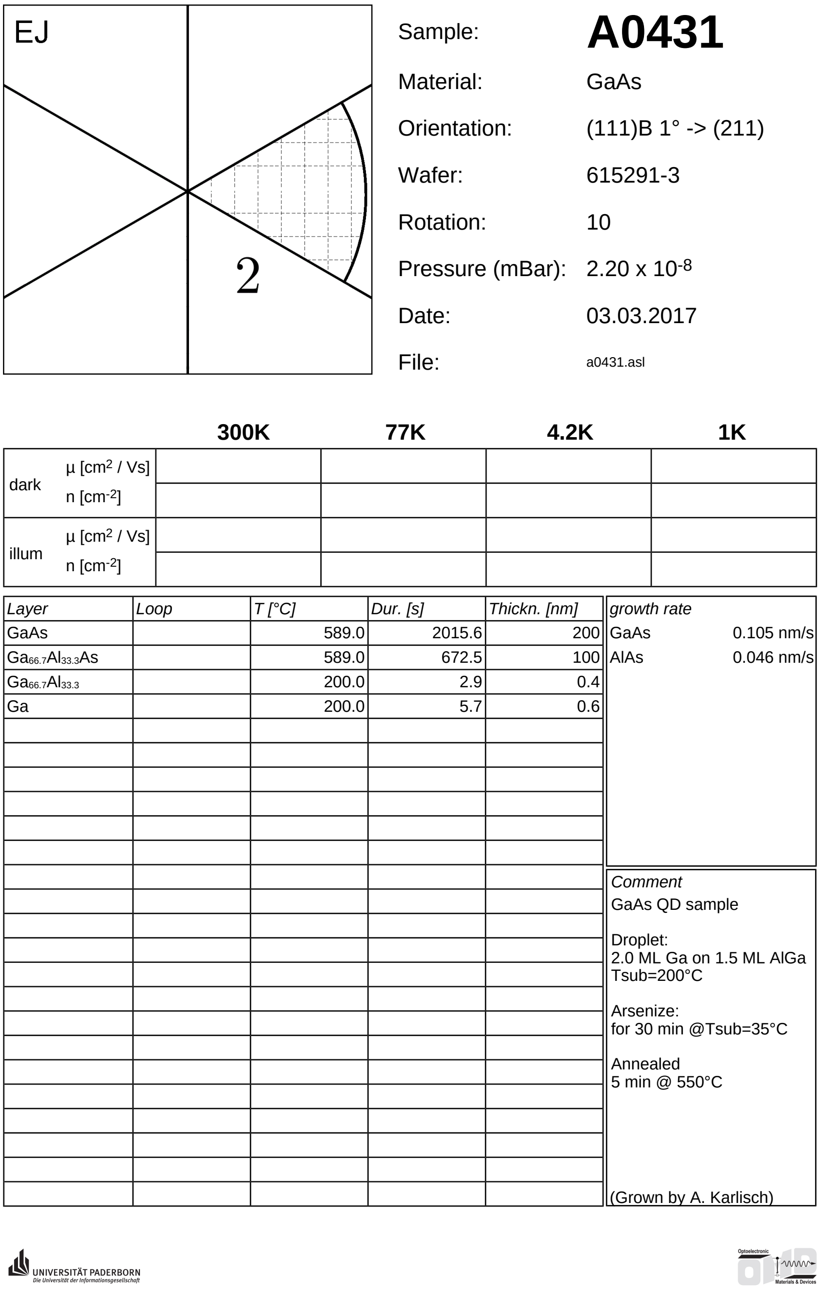

EJ

2

Sample:	**A0431**
Material:	GaAs
Orientation:	(111)B 1° -> (211)
Wafer:	615291-3
Rotation:	10
Pressure (mBar):	2.20 x 10^{-8}
Date:	03.03.2017
File:	a0431.asl

		300K	**77K**	**4.2K**	**1K**
dark	µ [cm^2 / Vs]				
	n [cm^{-2}]				
illum	µ [cm^2 / Vs]				
	n [cm^{-2}]				

Layer	*Loop*	*T [°C]*	*Dur. [s]*	*Thickn. [nm]*
GaAs		589.0	2015.6	200
$Ga_{66.7}Al_{33.3}As$		589.0	672.5	100
$Ga_{66.7}Al_{33.3}$		200.0	2.9	0.4
Ga		200.0	5.7	0.6

growth rate	
GaAs	0.105 nm/s
AlAs	0.046 nm/s

Comment

GaAs QD sample

Droplet:
2.0 ML Ga on 1.5 ML AlGa
Tsub=200°C

Arsenize:
for 30 min @Tsub=35°C

Annealed
5 min @ 550°C

(Grown by A. Karlisch)

Figure B.16: Growth report of sample A0431.

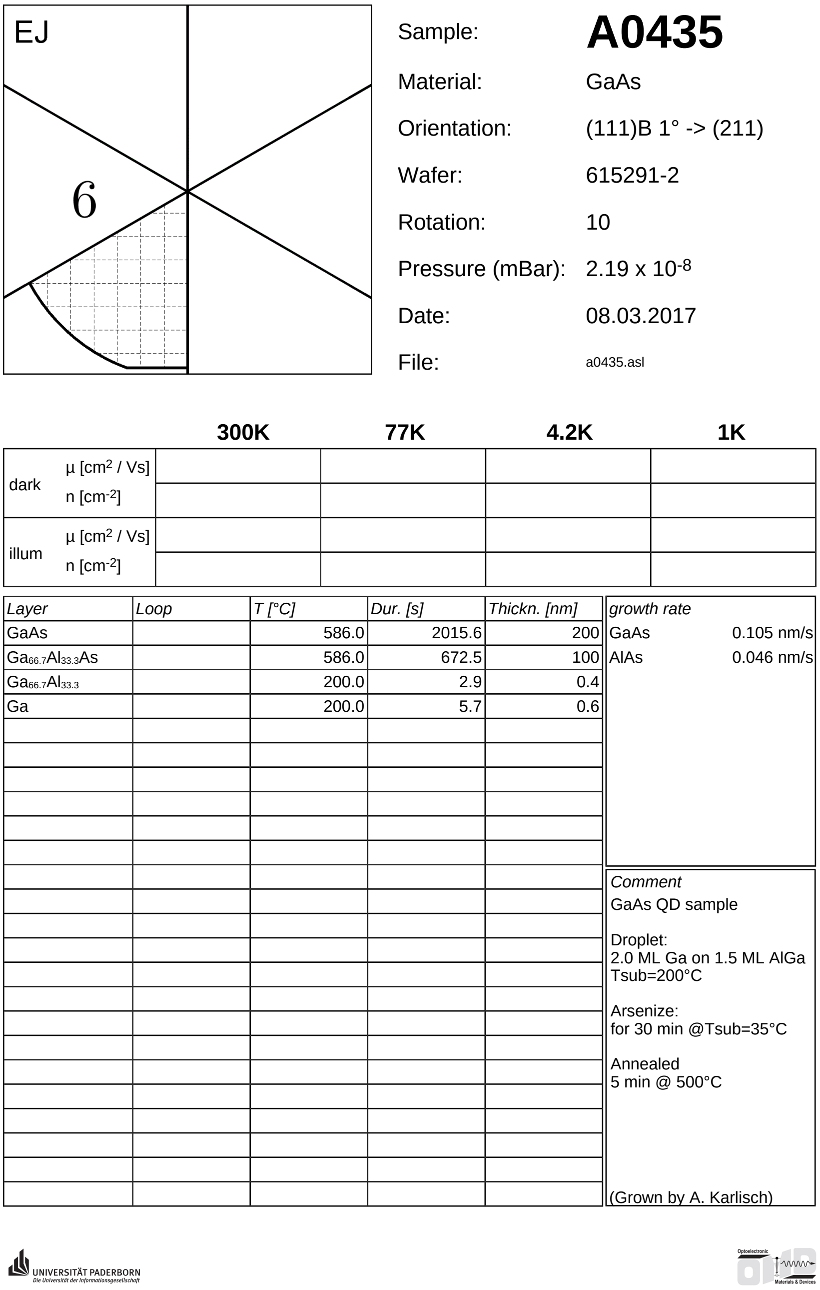

EJ

6

Sample: **A0435**

Material: GaAs

Orientation: (111)B 1° -> (211)

Wafer: 615291-2

Rotation: 10

Pressure (mBar): 2.19 x 10^{-8}

Date: 08.03.2017

File: a0435.asl

		300K	77K	4.2K	1K
dark	μ [cm^2 / Vs]				
	n [cm^{-2}]				
illum	μ [cm^2 / Vs]				
	n [cm^{-2}]				

Layer	*Loop*	*T [°C]*	*Dur. [s]*	*Thickn. [nm]*
GaAs		586.0	2015.6	200
Ga$_{66.7}$Al$_{33.3}$As		586.0	672.5	100
Ga$_{66.7}$Al$_{33.3}$		200.0	2.9	0.4
Ga		200.0	5.7	0.6

growth rate	
GaAs	0.105 nm/s
AlAs	0.046 nm/s

Comment

GaAs QD sample

Droplet:
2.0 ML Ga on 1.5 ML AlGa
Tsub=200°C

Arsenize:
for 30 min @Tsub=35°C

Annealed
5 min @ 500°C

(Grown by A. Karlisch)

UNIVERSITÄT PADERBORN
Die Universität der Informationsgesellschaft

Figure B.17: Growth report of sample A0435.

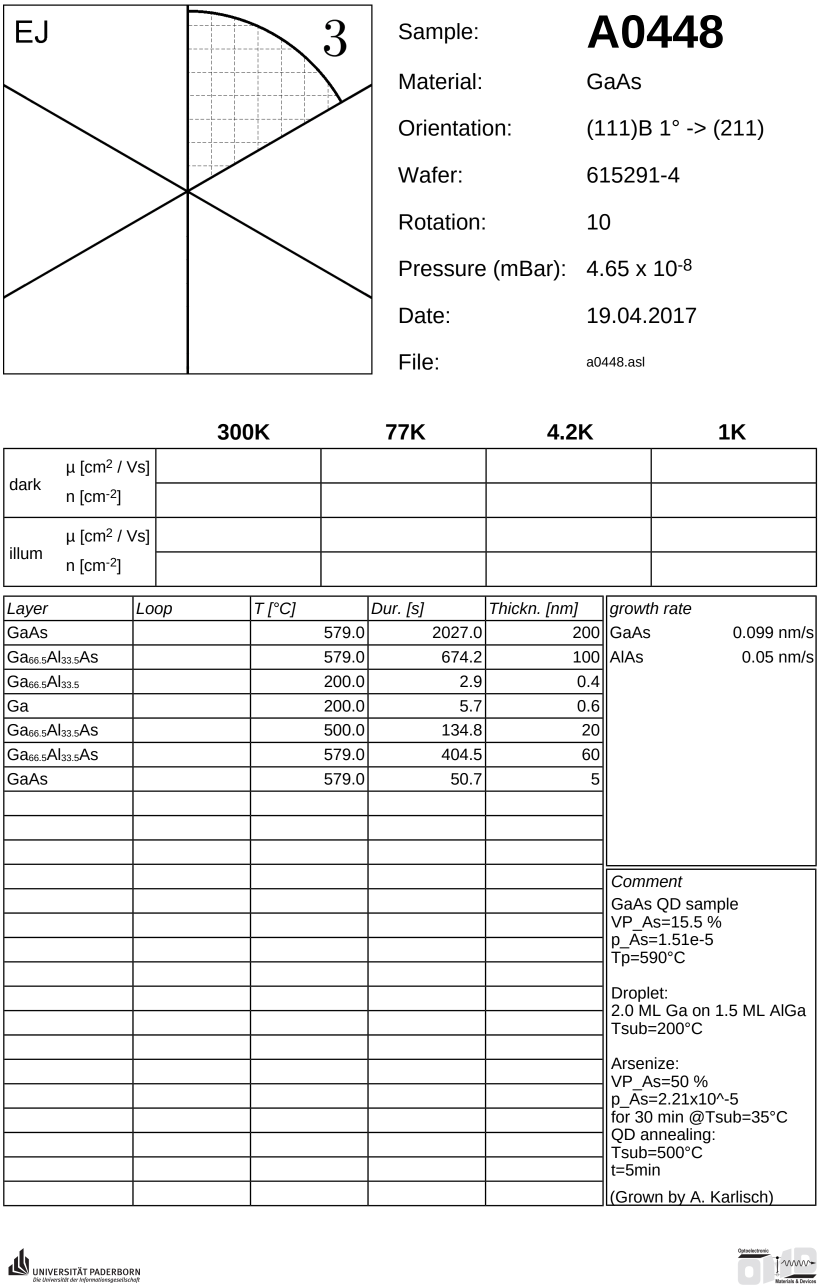

Sample: **A0448**
Material: GaAs
Orientation: (111)B 1° -> (211)
Wafer: 615291-4
Rotation: 10
Pressure (mBar): 4.65 x 10^{-8}
Date: 19.04.2017
File: a0448.asl

		300K	77K	4.2K	1K
dark	μ [cm^2 / Vs]				
	n [cm^{-2}]				
illum	μ [cm^2 / Vs]				
	n [cm^{-2}]				

Layer	*Loop*	*T [°C]*	*Dur. [s]*	*Thickn. [nm]*
GaAs		579.0	2027.0	200
Ga$_{66.5}$Al$_{33.5}$As		579.0	674.2	100
Ga$_{66.5}$Al$_{33.5}$		200.0	2.9	0.4
Ga		200.0	5.7	0.6
Ga$_{66.5}$Al$_{33.5}$As		500.0	134.8	20
Ga$_{66.5}$Al$_{33.5}$As		579.0	404.5	60
GaAs		579.0	50.7	5

growth rate	
GaAs	0.099 nm/s
AlAs	0.05 nm/s

Comment
GaAs QD sample
VP_As=15.5 %
p_As=1.51e-5
Tp=590°C

Droplet:
2.0 ML Ga on 1.5 ML AlGa
Tsub=200°C

Arsenize:
VP_As=50 %
p_As=2.21x10^-5
for 30 min @Tsub=35°C
QD annealing:
Tsub=500°C
t=5min
(Grown by A. Karlisch)

UNIVERSITÄT PADERBORN
Die Universität der Informationsgesellschaft

Optoelectronic Materials & Devices

Figure B.18: Growth report of sample A0448.

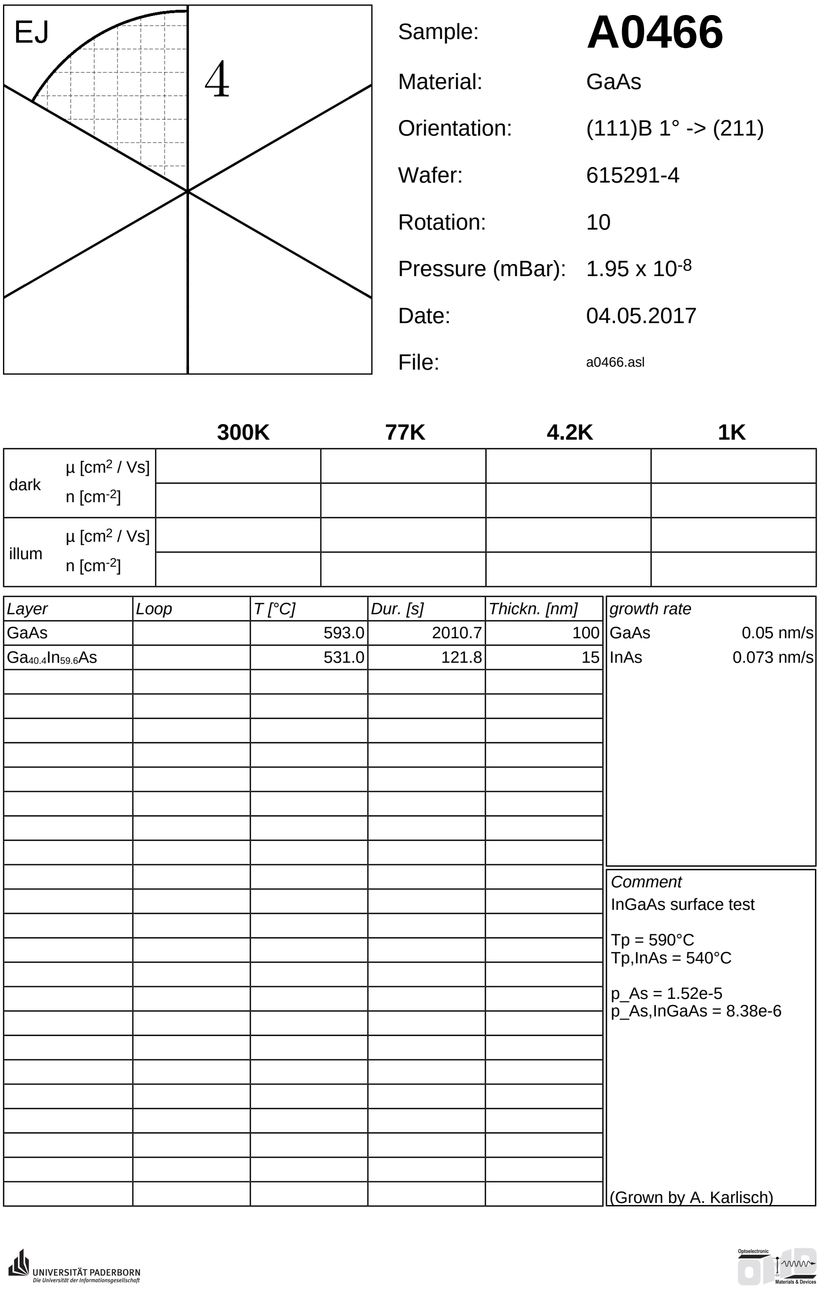

EJ

4

Sample: **A0466**

Material: GaAs

Orientation: (111)B 1° -> (211)

Wafer: 615291-4

Rotation: 10

Pressure (mBar): 1.95×10^{-8}

Date: 04.05.2017

File: a0466.asl

		300K	77K	4.2K	1K
dark	μ [cm^2 / Vs]				
	n [cm^{-2}]				
illum	μ [cm^2 / Vs]				
	n [cm^{-2}]				

Layer	*Loop*	*T [°C]*	*Dur. [s]*	*Thickn. [nm]*
GaAs		593.0	2010.7	100
$Ga_{40.4}In_{59.6}As$		531.0	121.8	15

growth rate	
GaAs	0.05 nm/s
InAs	0.073 nm/s

Comment

InGaAs surface test

Tp = 590°C
Tp,InAs = 540°C

p_As = 1.52e-5
p_As,InGaAs = 8.38e-6

(Grown by A. Karlisch)

UNIVERSITÄT PADERBORN
Die Universität der Informationsgesellschaft

Figure B.19: Growth report of sample A0466.

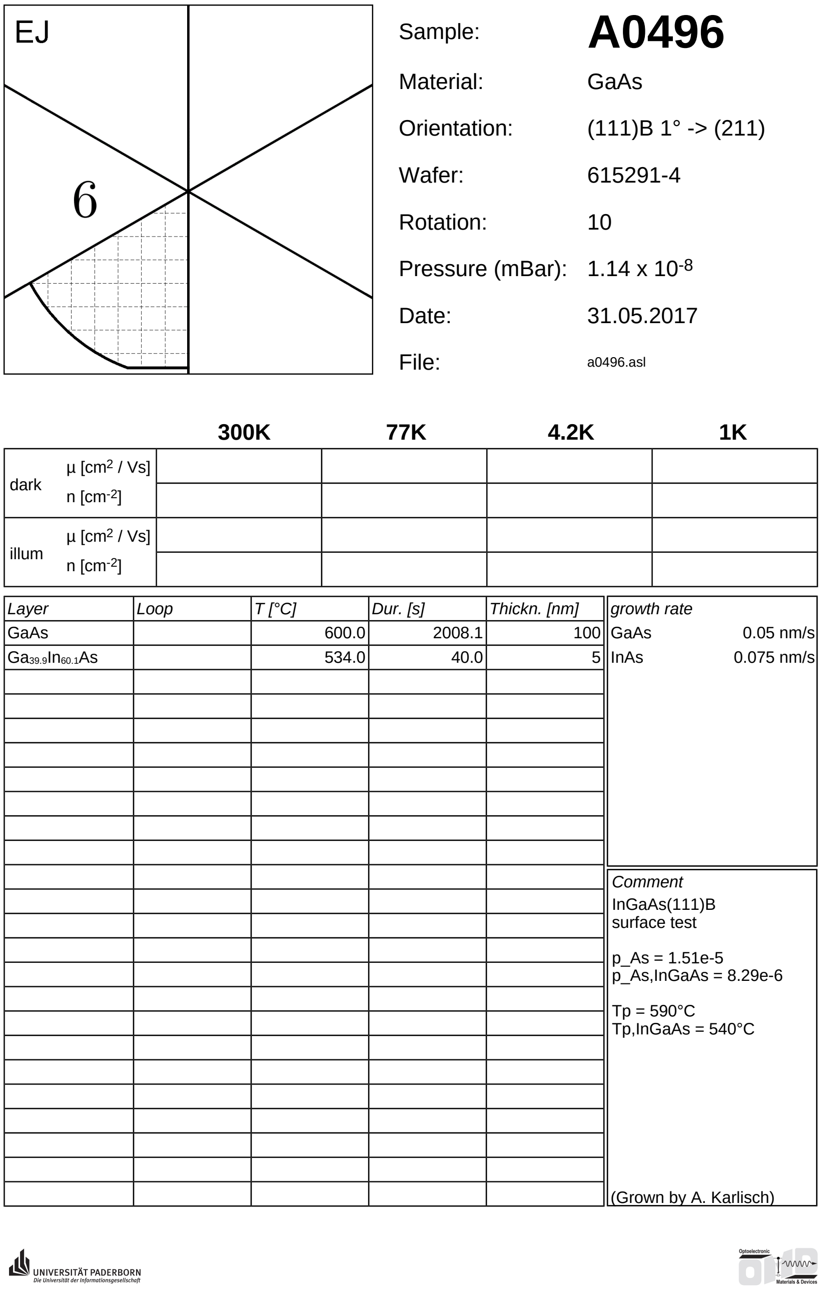

Sample: **A0496**
Material: GaAs
Orientation: (111)B 1° -> (211)
Wafer: 615291-4
Rotation: 10
Pressure (mBar): 1.14 x 10^{-8}
Date: 31.05.2017
File: a0496.asl

		300K	77K	4.2K	1K
dark	μ [cm^2 / Vs]				
	n [cm^{-2}]				
illum	μ [cm^2 / Vs]				
	n [cm^{-2}]				

Layer	*Loop*	*T [°C]*	*Dur. [s]*	*Thickn. [nm]*
GaAs		600.0	2008.1	100
$Ga_{39.9}In_{60.1}As$		534.0	40.0	5

growth rate	
GaAs	0.05 nm/s
InAs	0.075 nm/s

Comment
InGaAs(111)B
surface test

p_As = 1.51e-5
p_As,InGaAs = 8.29e-6

Tp = 590°C
Tp,InGaAs = 540°C

(Grown by A. Karlisch)

Figure B.20: Growth report of sample A0496.

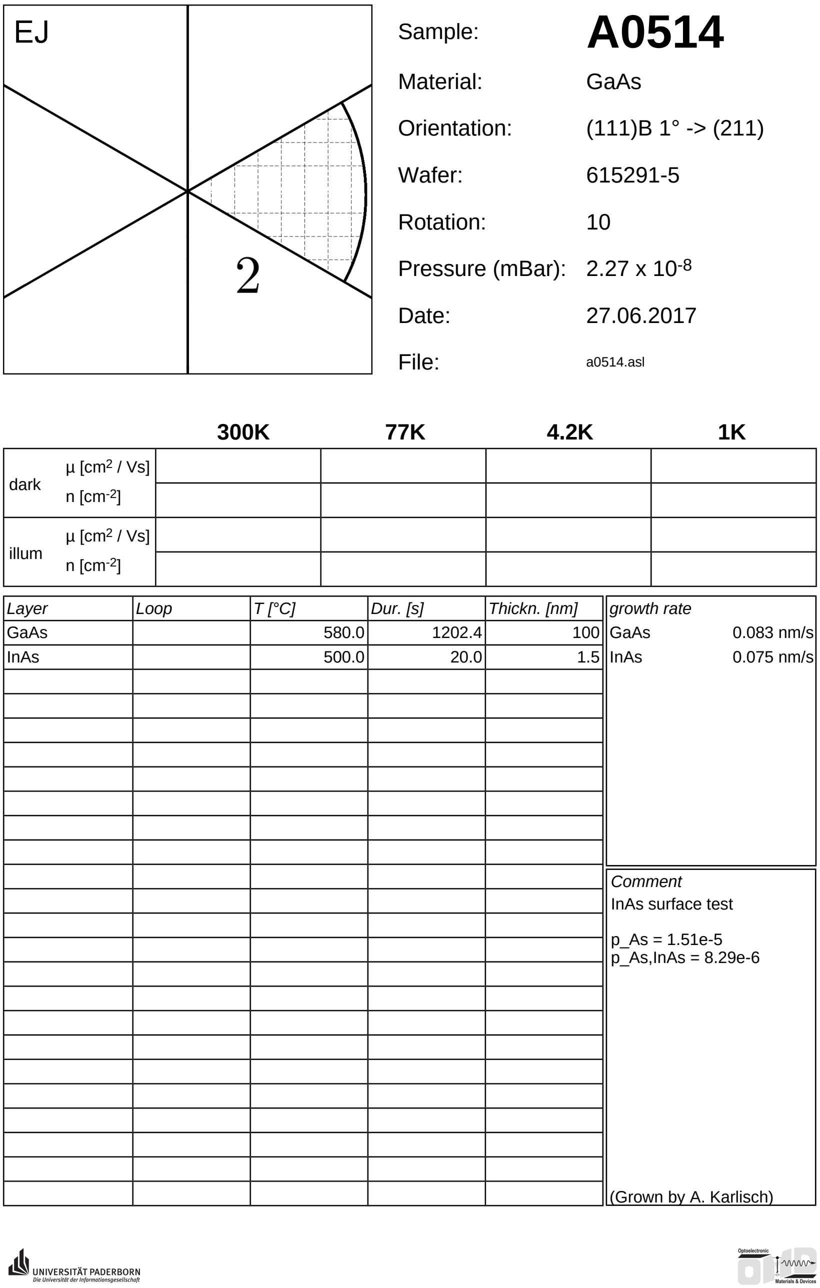

Sample: **A0514**
Material: GaAs
Orientation: (111)B 1° -> (211)
Wafer: 615291-5
Rotation: 10
Pressure (mBar): 2.27 x 10^{-8}
Date: 27.06.2017
File: a0514.asl

		300K	**77K**	**4.2K**	**1K**
dark	μ [cm^2 / Vs]				
	n [cm^{-2}]				
illum	μ [cm^2 / Vs]				
	n [cm^{-2}]				

Layer	*Loop*	*T [°C]*	*Dur. [s]*	*Thickn. [nm]*
GaAs		580.0	1202.4	100
InAs		500.0	20.0	1.5

growth rate	
GaAs	0.083 nm/s
InAs	0.075 nm/s

Comment
InAs surface test

p_As = 1.51e-5
p_As,InAs = 8.29e-6

(Grown by A. Karlisch)

UNIVERSITÄT PADERBORN
Die Universität der Informationsgesellschaft

Optoelectronic Materials & Devices

Figure B.21: Growth report of sample A0514.

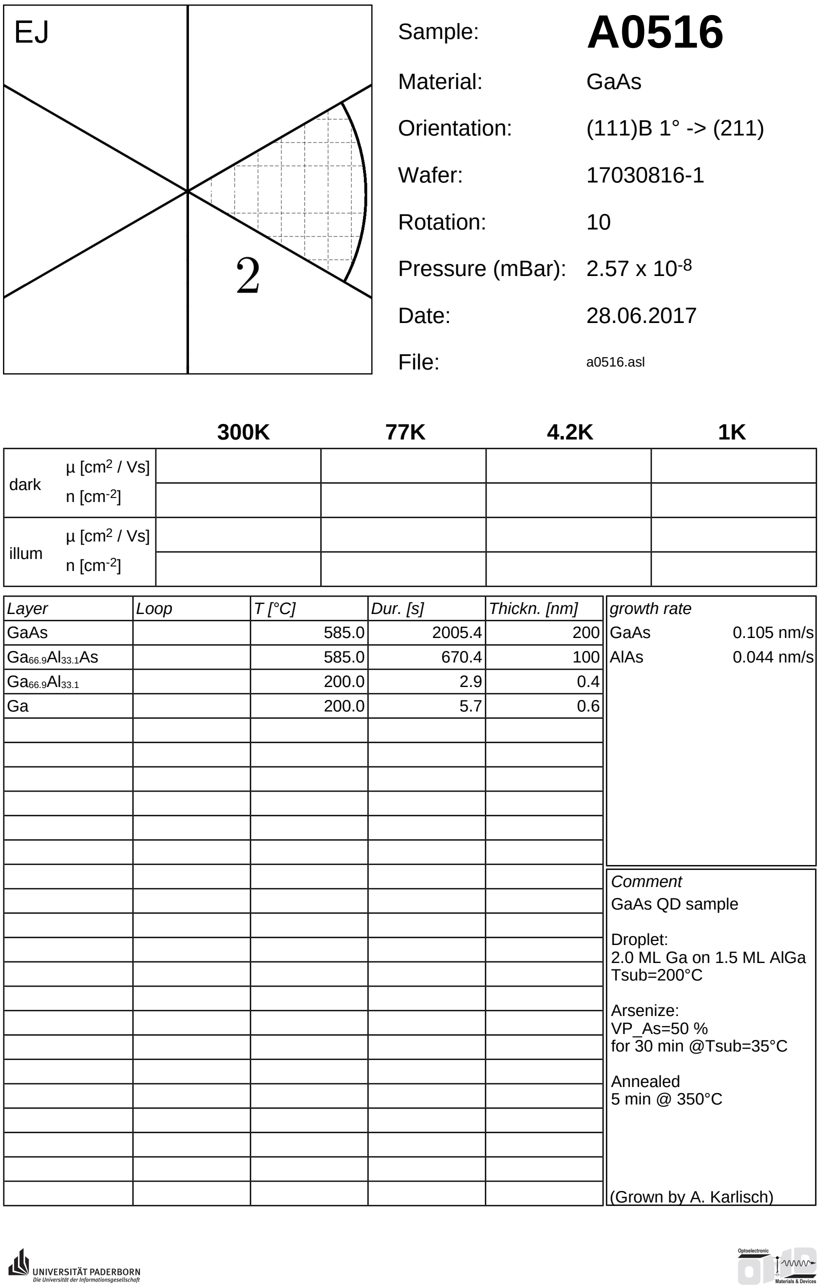

Sample: **A0516**
Material: GaAs
Orientation: (111)B 1° -> (211)
Wafer: 17030816-1
Rotation: 10
Pressure (mBar): 2.57 x 10^{-8}
Date: 28.06.2017
File: a0516.asl

		300K	77K	4.2K	1K
dark	μ [cm^2 / Vs]				
	n [cm^{-2}]				
illum	μ [cm^2 / Vs]				
	n [cm^{-2}]				

Layer	*Loop*	*T [°C]*	*Dur. [s]*	*Thickn. [nm]*
GaAs		585.0	2005.4	200
Ga$_{66.9}$Al$_{33.1}$As		585.0	670.4	100
Ga$_{66.9}$Al$_{33.1}$		200.0	2.9	0.4
Ga		200.0	5.7	0.6

growth rate	
GaAs	0.105 nm/s
AlAs	0.044 nm/s

Comment
GaAs QD sample

Droplet:
2.0 ML Ga on 1.5 ML AlGa
Tsub=200°C

Arsenize:
VP_As=50 %
for 30 min @Tsub=35°C

Annealed
5 min @ 350°C

(Grown by A. Karlisch)

UNIVERSITÄT PADERBORN
Die Universität der Informationsgesellschaft

Optoelectronic Materials & Devices

Figure B.22: Growth report of sample A0516.

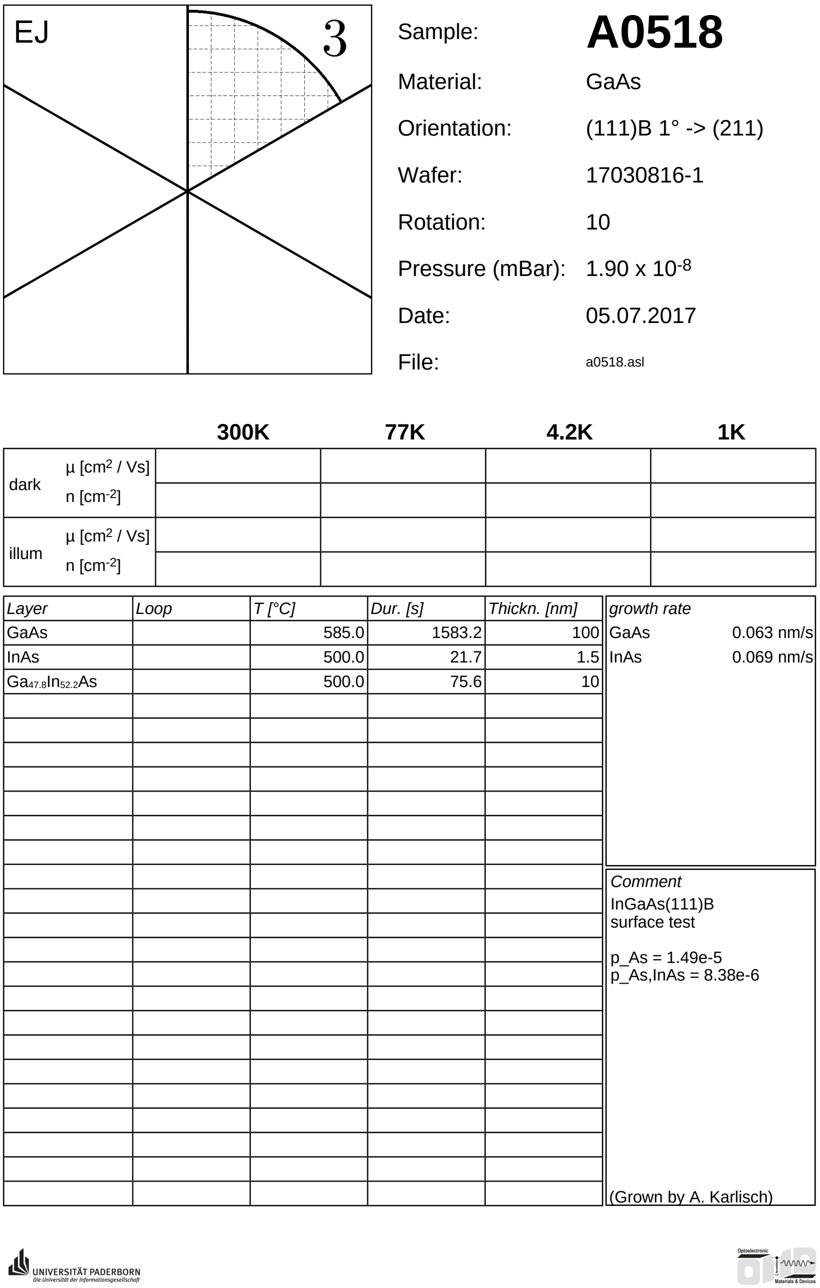

EJ

3

Sample: **A0518**

Material: GaAs

Orientation: (111)B 1° -> (211)

Wafer: 17030816-1

Rotation: 10

Pressure (mBar): 1.90 x 10^{-8}

Date: 05.07.2017

File: a0518.asl

		300K	**77K**	**4.2K**	**1K**
dark	μ [cm^2 / Vs]				
	n [cm^{-2}]				
illum	μ [cm^2 / Vs]				
	n [cm^{-2}]				

Layer	*Loop*	*T [°C]*	*Dur. [s]*	*Thickn. [nm]*
GaAs		585.0	1583.2	100
InAs		500.0	21.7	1.5
$\text{Ga}_{47.8}\text{In}_{52.2}\text{As}$		500.0	75.6	10

growth rate	
GaAs	0.063 nm/s
InAs	0.069 nm/s

Comment

InGaAs(111)B
surface test

p_As = 1.49e-5
p_As,InAs = 8.38e-6

(Grown by A. Karlisch)

Figure B.23: Growth report of sample A0518.

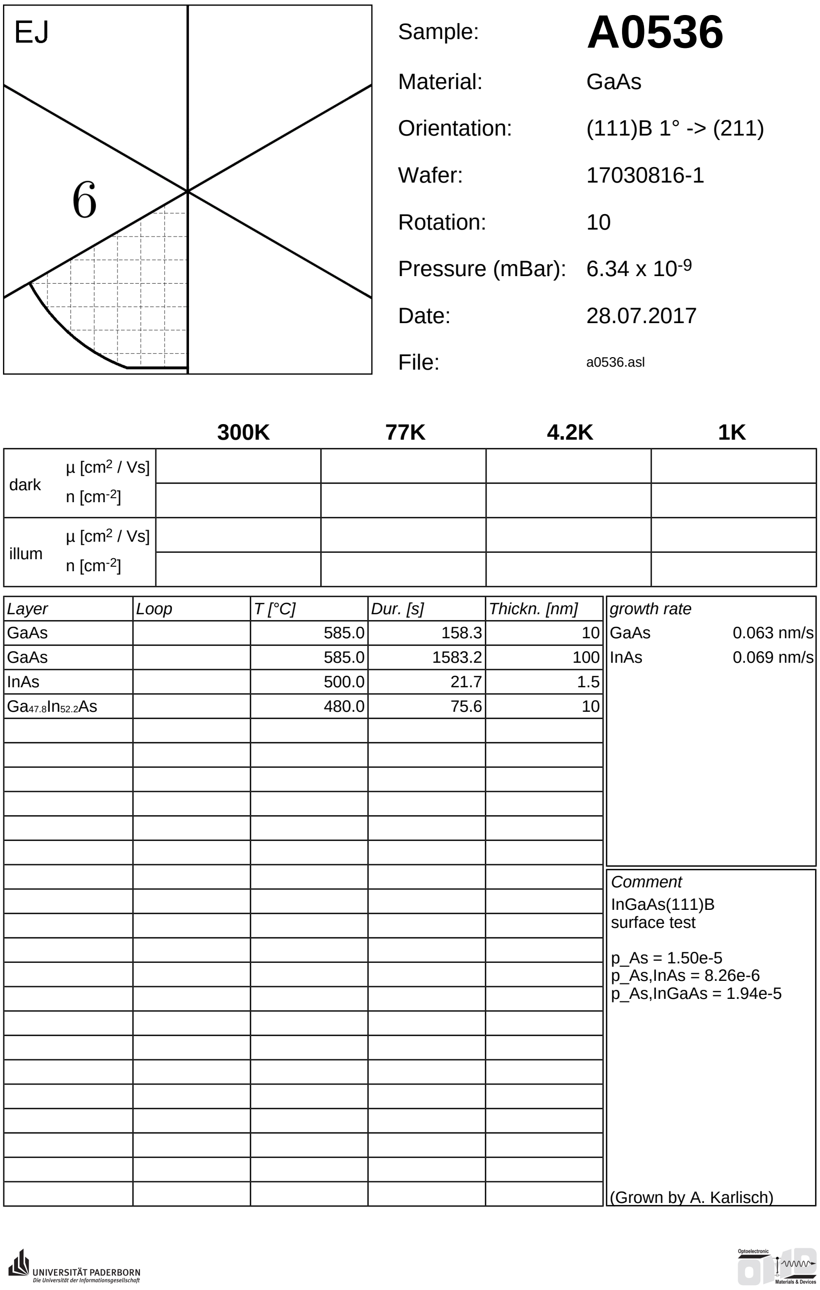

Sample: **A0536**
Material: GaAs
Orientation: (111)B 1° -> (211)
Wafer: 17030816-1
Rotation: 10
Pressure (mBar): 6.34×10^{-9}
Date: 28.07.2017
File: a0536.asl

		300K	**77K**	**4.2K**	**1K**
dark	μ [cm^2 / Vs]				
	n [cm^{-2}]				
illum	μ [cm^2 / Vs]				
	n [cm^{-2}]				

Layer	*Loop*	*T [°C]*	*Dur. [s]*	*Thickn. [nm]*
GaAs		585.0	158.3	10
GaAs		585.0	1583.2	100
InAs		500.0	21.7	1.5
$Ga_{47.8}In_{52.2}As$		480.0	75.6	10

growth rate	
GaAs	0.063 nm/s
InAs	0.069 nm/s

Comment
InGaAs(111)B
surface test

p_As = 1.50e-5
p_As,InAs = 8.26e-6
p_As,InGaAs = 1.94e-5

(Grown by A. Karlisch)

UNIVERSITÄT PADERBORN
Die Universität der Informationsgesellschaft

Optoelectronic Materials & Devices

Figure B.24: Growth report of sample A0536.

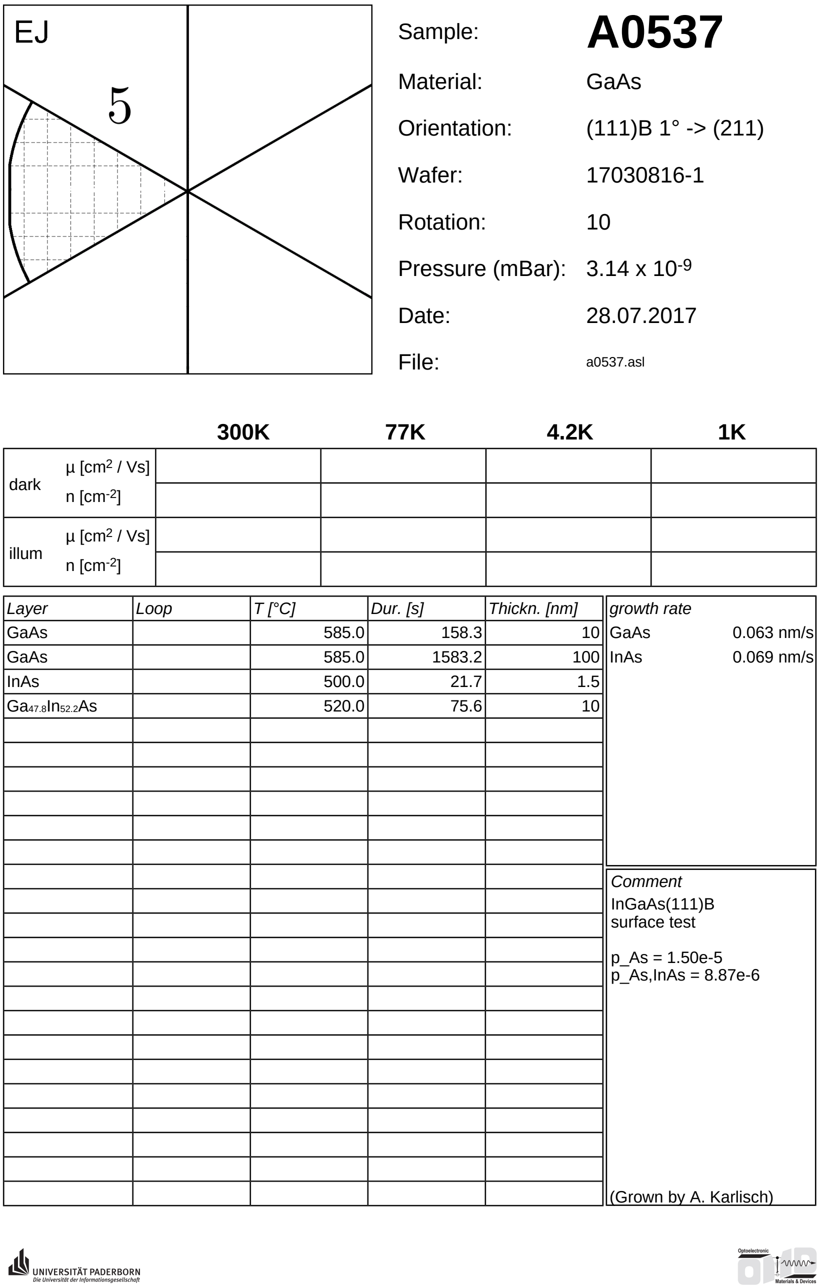

Sample: **A0537**
Material: GaAs
Orientation: (111)B 1° -> (211)
Wafer: 17030816-1
Rotation: 10
Pressure (mBar): 3.14 x 10^{-9}
Date: 28.07.2017
File: a0537.asl

		300K	**77K**	**4.2K**	**1K**
dark	μ [cm^2 / Vs]				
	n [cm^{-2}]				
illum	μ [cm^2 / Vs]				
	n [cm^{-2}]				

Layer	*Loop*	*T [°C]*	*Dur. [s]*	*Thickn. [nm]*
GaAs		585.0	158.3	10
GaAs		585.0	1583.2	100
InAs		500.0	21.7	1.5
$Ga_{47.8}In_{52.2}As$		520.0	75.6	10

growth rate	
GaAs	0.063 nm/s
InAs	0.069 nm/s

Comment
InGaAs(111)B
surface test

p_As = 1.50e-5
p_As,InAs = 8.87e-6

(Grown by A. Karlisch)

UNIVERSITÄT PADERBORN
Die Universität der Informationsgesellschaft

Optoelectronic Materials & Devices

Figure B.25: Growth report of sample A0537.

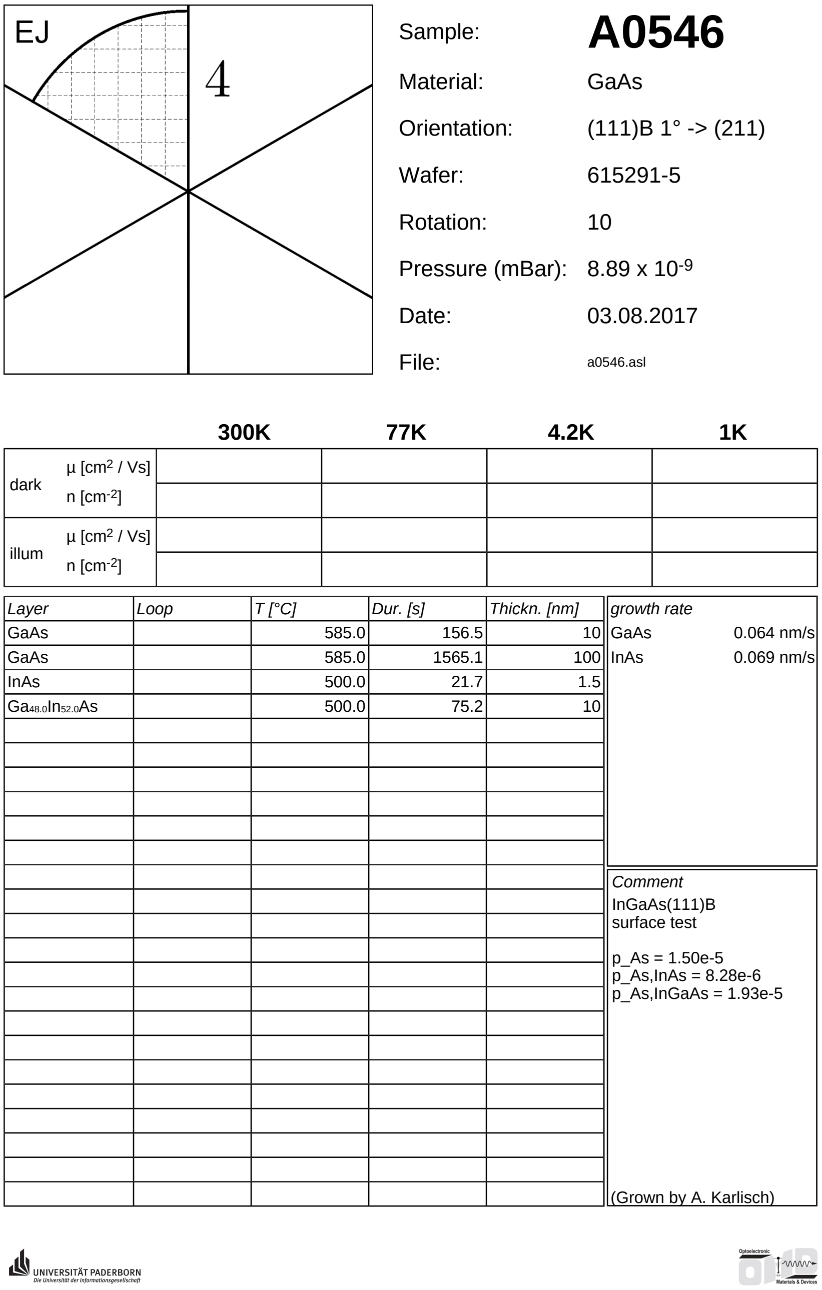

Sample: **A0546**
Material: GaAs
Orientation: (111)B 1° -> (211)
Wafer: 615291-5
Rotation: 10
Pressure (mBar): 8.89 x 10^{-9}
Date: 03.08.2017
File: a0546.asl

		300K	77K	4.2K	1K
dark	µ [cm^2 / Vs]				
	n [cm^{-2}]				
illum	µ [cm^2 / Vs]				
	n [cm^{-2}]				

Layer	*Loop*	*T [°C]*	*Dur. [s]*	*Thickn. [nm]*
GaAs		585.0	156.5	10
GaAs		585.0	1565.1	100
InAs		500.0	21.7	1.5
$Ga_{48.0}In_{52.0}As$		500.0	75.2	10

growth rate	
GaAs	0.064 nm/s
InAs	0.069 nm/s

Comment
InGaAs(111)B
surface test

p_As = 1.50e-5
p_As,InAs = 8.28e-6
p_As,InGaAs = 1.93e-5

(Grown by A. Karlisch)

UNIVERSITÄT PADERBORN
Die Universität der Informationsgesellschaft

Optoelectronic Materials & Devices

Figure B.26: Growth report of sample A0546.

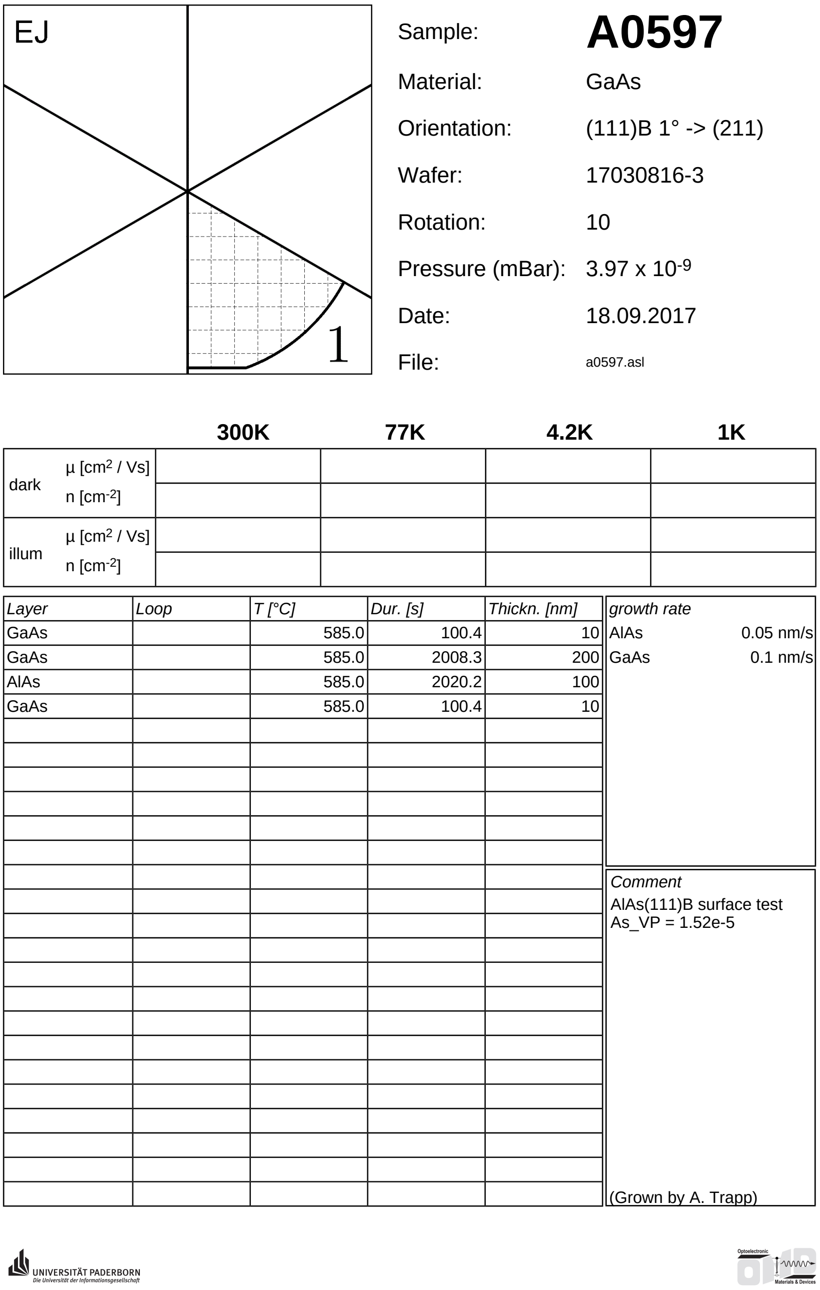

Sample: **A0597**
Material: GaAs
Orientation: (111)B 1° -> (211)
Wafer: 17030816-3
Rotation: 10
Pressure (mBar): 3.97 x 10^{-9}
Date: 18.09.2017
File: a0597.asl

		300K	77K	4.2K	1K
dark	μ [cm^2 / Vs]				
	n [cm^{-2}]				
illum	μ [cm^2 / Vs]				
	n [cm^{-2}]				

Layer	*Loop*	*T [°C]*	*Dur. [s]*	*Thickn. [nm]*
GaAs		585.0	100.4	10
GaAs		585.0	2008.3	200
AlAs		585.0	2020.2	100
GaAs		585.0	100.4	10

growth rate	
AlAs	0.05 nm/s
GaAs	0.1 nm/s

Comment
AlAs(111)B surface test
As_VP = 1.52e-5

(Grown by A. Trapp)

UNIVERSITÄT PADERBORN
Die Universität der Informationsgesellschaft

Optoelectronic Materials & Devices

Figure B.27: Growth report of sample A0597.

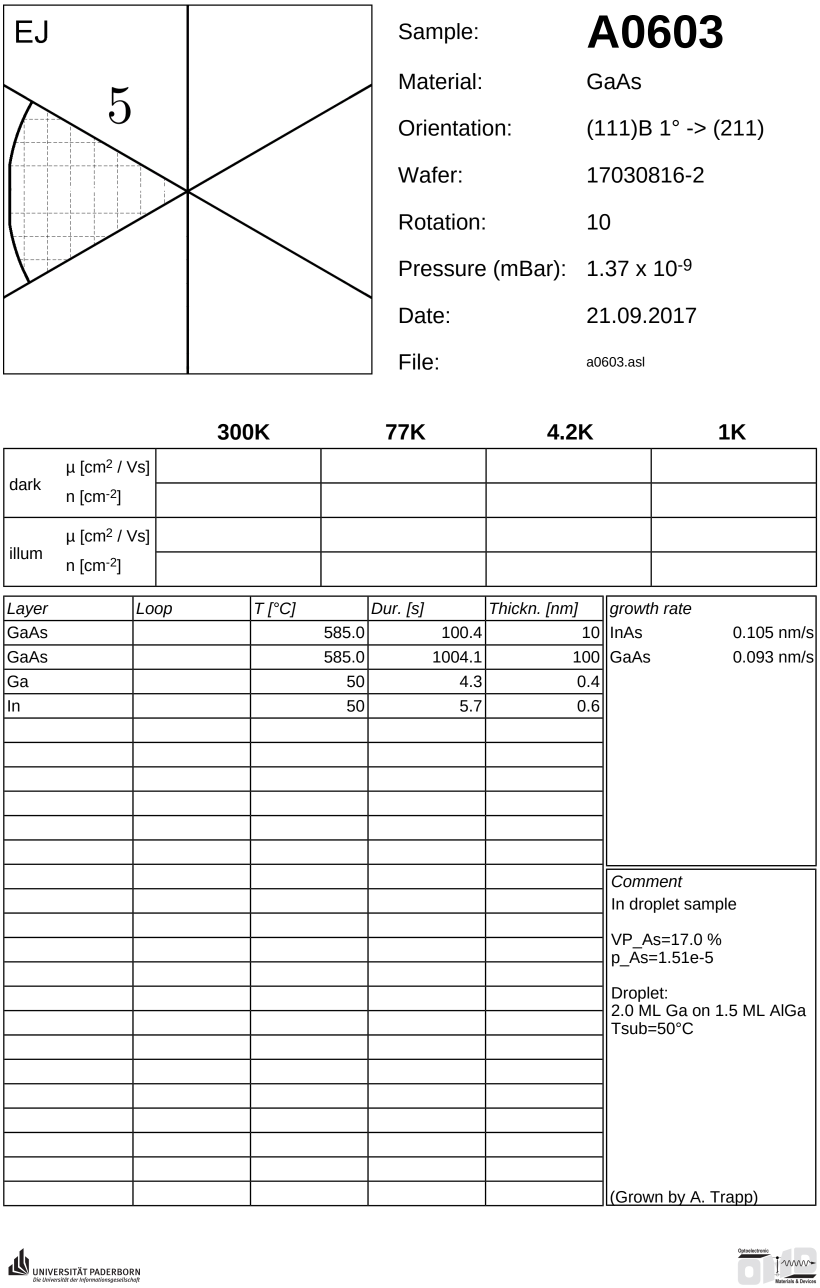

Sample: **A0603**
Material: GaAs
Orientation: (111)B 1° -> (211)
Wafer: 17030816-2
Rotation: 10
Pressure (mBar): 1.37 x 10^{-9}
Date: 21.09.2017
File: a0603.asl

		300K	77K	4.2K	1K
dark	μ [cm^2 / Vs]				
	n [cm^{-2}]				
illum	μ [cm^2 / Vs]				
	n [cm^{-2}]				

Layer	*Loop*	*T [°C]*	*Dur. [s]*	*Thickn. [nm]*
GaAs		585.0	100.4	10
GaAs		585.0	1004.1	100
Ga		50	4.3	0.4
In		50	5.7	0.6

growth rate	
InAs	0.105 nm/s
GaAs	0.093 nm/s

Comment
In droplet sample

VP_As=17.0 %
p_As=1.51e-5

Droplet:
2.0 ML Ga on 1.5 ML AlGa
Tsub=50°C

(Grown by A. Trapp)

UNIVERSITÄT PADERBORN
Die Universität der Informationsgesellschaft

Optoelectronic Materials & Devices

Figure B.28: Growth report of sample A0603.

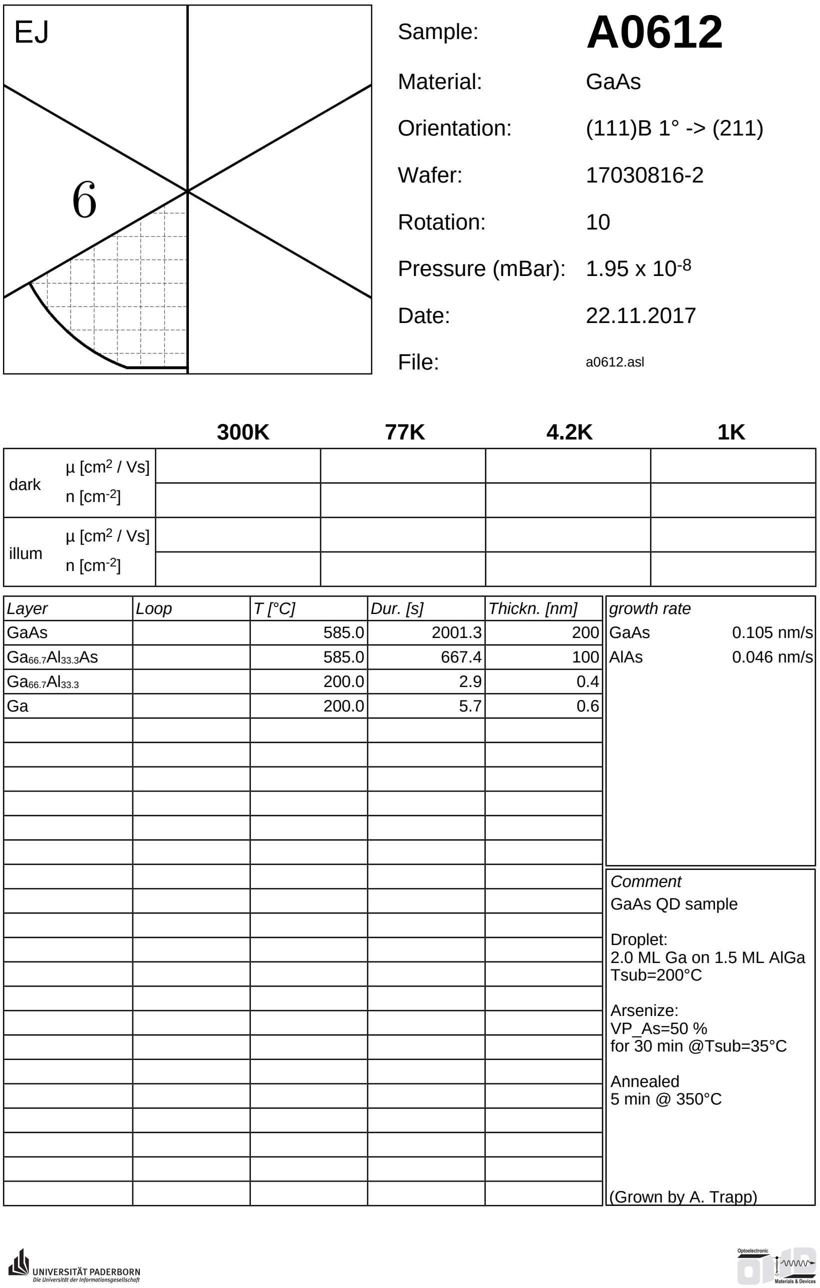

Sample: **A0612**
Material: GaAs
Orientation: (111)B 1° -> (211)
Wafer: 17030816-2
Rotation: 10
Pressure (mBar): 1.95 x 10^{-8}
Date: 22.11.2017
File: a0612.asl

		300K	77K	4.2K	1K
dark	μ [cm^2 / Vs]				
	n [cm^{-2}]				
illum	μ [cm^2 / Vs]				
	n [cm^{-2}]				

Layer	*Loop*	*T [°C]*	*Dur. [s]*	*Thickn. [nm]*
GaAs		585.0	2001.3	200
$Ga_{66.7}Al_{33.3}As$		585.0	667.4	100
$Ga_{66.7}Al_{33.3}$		200.0	2.9	0.4
Ga		200.0	5.7	0.6

growth rate	
GaAs	0.105 nm/s
AlAs	0.046 nm/s

Comment
GaAs QD sample

Droplet:
2.0 ML Ga on 1.5 ML AlGa
Tsub=200°C

Arsenize:
VP_As=50 %
for 30 min @Tsub=35°C

Annealed
5 min @ 350°C

(Grown by A. Trapp)

UNIVERSITÄT PADERBORN
Die Universität der Informationsgesellschaft

Optoelectronic Materials & Devices

Figure B.29: Growth report of sample A0612.

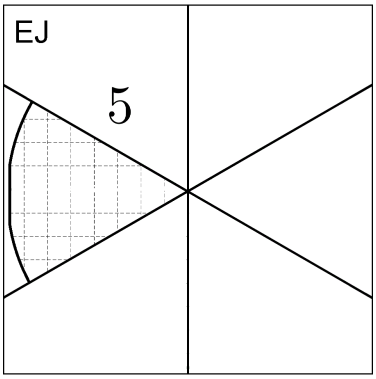

Sample: **A0617**
Material: GaAs
Orientation: (111)B 1° -> (211)
Wafer: 17030816-4
Rotation: 10
Pressure (mBar): 2.21 x 10^{-8}
Date: 30.11.2017
File: a0617.asl

		300K	77K	4.2K	1K
dark	μ [cm^2 / Vs]				
	n [cm^{-2}]				
illum	μ [cm^2 / Vs]				
	n [cm^{-2}]				

Layer	*Loop*	*T [°C]*	*Dur. [s]*	*Thickn. [nm]*
GaAs		585.0	103.6	10
GaAs		585.0	1035.5	100
Ga		50.0	4.3	0.4
In		50.0	5.7	0.6

growth rate	
GaAs	0.093 nm/s
InAs	0.105 nm/s

Comment

InAs QD sample
VP_As=12.5 %
p_As=1.59e-5
Tp=590°C

Droplet:
2.0 ML In on 1.5 ML Ga
Tsub=50°C

Arsenize:
VP_As=50 %
for 30 min @Tsub=35°C

(Grown by A. Trapp)

UNIVERSITÄT PADERBORN
Die Universität der Informationsgesellschaft

Optoelectronic Materials & Devices

Figure B.30: Growth report of sample A0617.

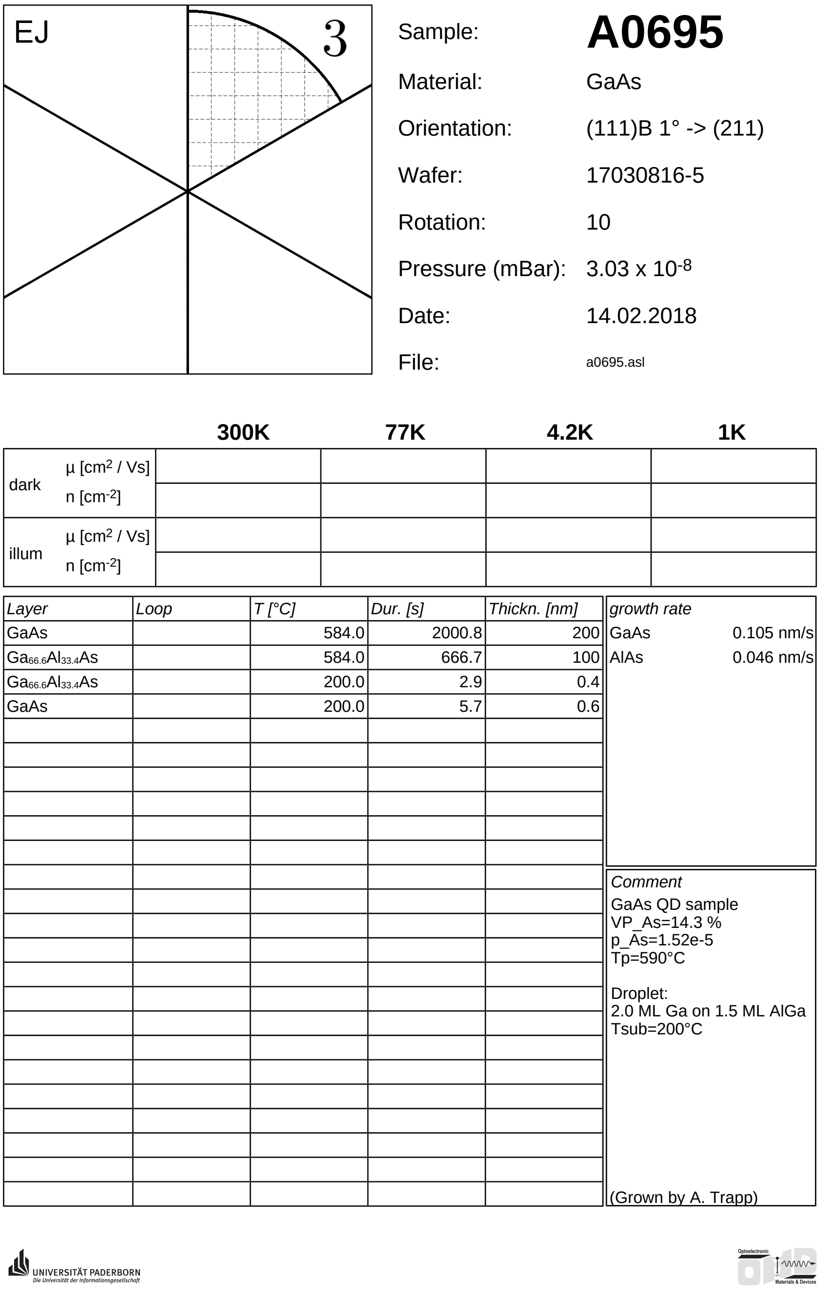

EJ 3

Sample: **A0695**
Material: GaAs
Orientation: (111)B 1° -> (211)
Wafer: 17030816-5
Rotation: 10
Pressure (mBar): 3.03 x 10^{-8}
Date: 14.02.2018
File: a0695.asl

		300K	77K	4.2K	1K
dark	μ [cm^2 / Vs]				
	n [cm^{-2}]				
illum	μ [cm^2 / Vs]				
	n [cm^{-2}]				

Layer	*Loop*	*T [°C]*	*Dur. [s]*	*Thickn. [nm]*
GaAs		584.0	2000.8	200
$Ga_{66.6}Al_{33.4}As$		584.0	666.7	100
$Ga_{66.6}Al_{33.4}As$		200.0	2.9	0.4
GaAs		200.0	5.7	0.6

growth rate	
GaAs	0.105 nm/s
AlAs	0.046 nm/s

Comment
GaAs QD sample
VP_As=14.3 %
p_As=1.52e-5
Tp=590°C

Droplet:
2.0 ML Ga on 1.5 ML AlGa
Tsub=200°C

(Grown by A. Trapp)

UNIVERSITÄT PADERBORN
Die Universität der Informationsgesellschaft

Optoelectronic Materials & Devices

Figure B.31: Growth report of sample A0695.

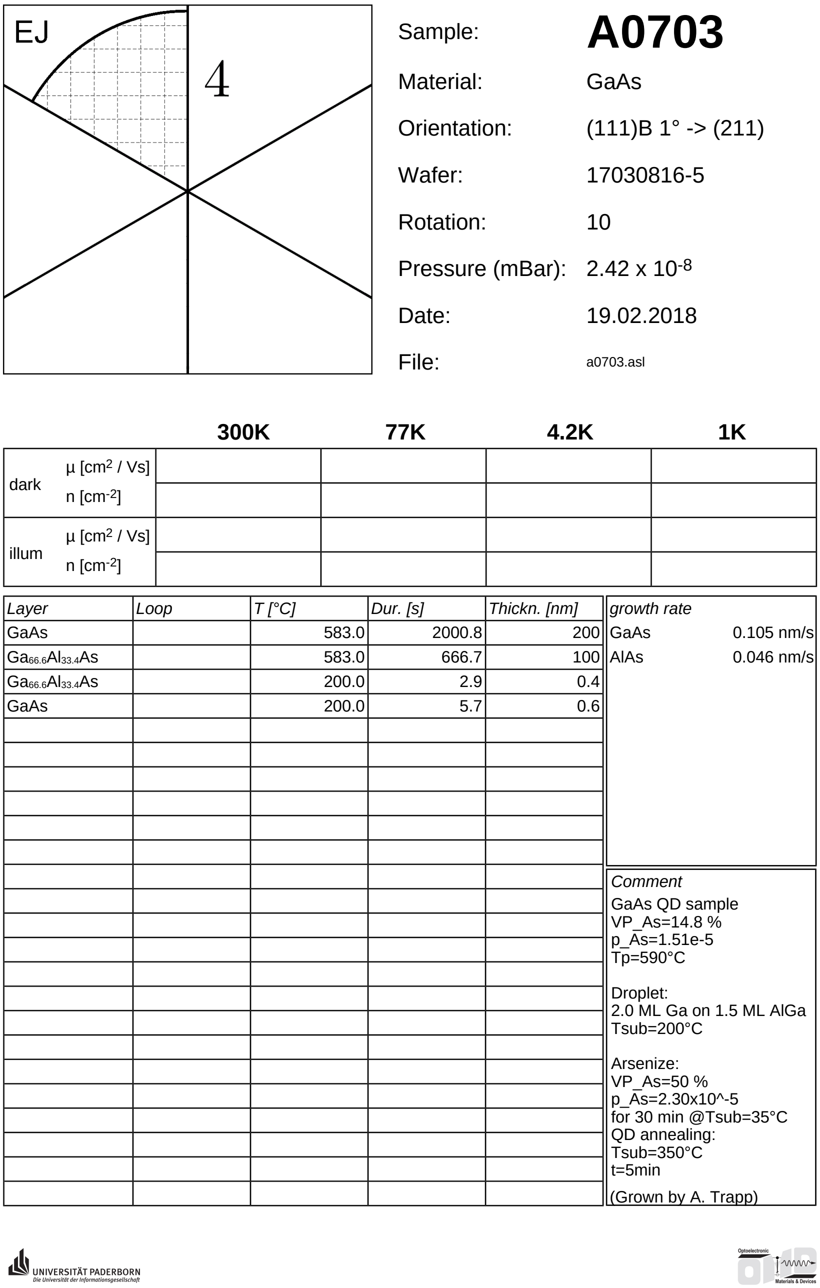

Sample:	**A0703**
Material:	GaAs
Orientation:	(111)B 1° -> (211)
Wafer:	17030816-5
Rotation:	10
Pressure (mBar):	2.42 x 10^{-8}
Date:	19.02.2018
File:	a0703.asl

		300K	**77K**	**4.2K**	**1K**
dark	µ [cm^2 / Vs]				
	n [cm^{-2}]				
illum	µ [cm^2 / Vs]				
	n [cm^{-2}]				

Layer	*Loop*	*T [°C]*	*Dur. [s]*	*Thickn. [nm]*
GaAs		583.0	2000.8	200
Ga$_{66.6}$Al$_{33.4}$As		583.0	666.7	100
Ga$_{66.6}$Al$_{33.4}$As		200.0	2.9	0.4
GaAs		200.0	5.7	0.6

growth rate	
GaAs	0.105 nm/s
AlAs	0.046 nm/s

Comment

GaAs QD sample
VP_As=14.8 %
p_As=1.51e-5
Tp=590°C

Droplet:
2.0 ML Ga on 1.5 ML AlGa
Tsub=200°C

Arsenize:
VP_As=50 %
p_As=2.30x10^-5
for 30 min @Tsub=35°C
QD annealing:
Tsub=350°C
t=5min

(Grown by A. Trapp)

UNIVERSITÄT PADERBORN
Die Universität der Informationsgesellschaft

Optoelectronic
Materials & Devices

Figure B.32: Growth report of sample A0703.

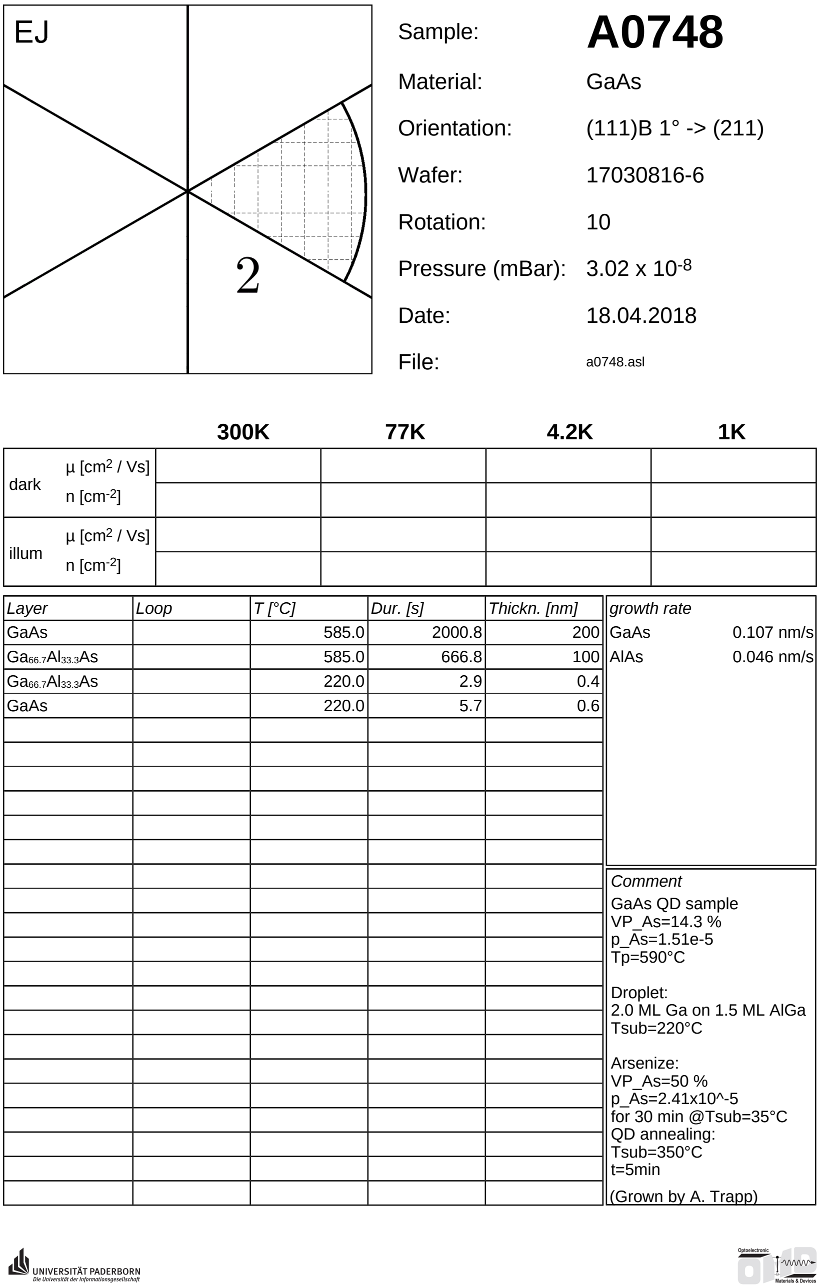

Sample: **A0748**
Material: GaAs
Orientation: (111)B 1° -> (211)
Wafer: 17030816-6
Rotation: 10
Pressure (mBar): 3.02 x 10^{-8}
Date: 18.04.2018
File: a0748.asl

		300K	77K	4.2K	1K
dark	μ [cm^2 / Vs]				
	n [cm^{-2}]				
illum	μ [cm^2 / Vs]				
	n [cm^{-2}]				

Layer	*Loop*	*T [°C]*	*Dur. [s]*	*Thickn. [nm]*
GaAs		585.0	2000.8	200
$Ga_{66.7}Al_{33.3}As$		585.0	666.8	100
$Ga_{66.7}Al_{33.3}As$		220.0	2.9	0.4
GaAs		220.0	5.7	0.6

growth rate	
GaAs	0.107 nm/s
AlAs	0.046 nm/s

Comment
GaAs QD sample
VP_As=14.3 %
p_As=1.51e-5
Tp=590°C

Droplet:
2.0 ML Ga on 1.5 ML AlGa
Tsub=220°C

Arsenize:
VP_As=50 %
p_As=2.41x10^-5
for 30 min @Tsub=35°C
QD annealing:
Tsub=350°C
t=5min
(Grown by A. Trapp)

UNIVERSITÄT PADERBORN
Die Universität der Informationsgesellschaft

Optoelectronic Materials & Devices

Figure B.33: Growth report of sample A0748.

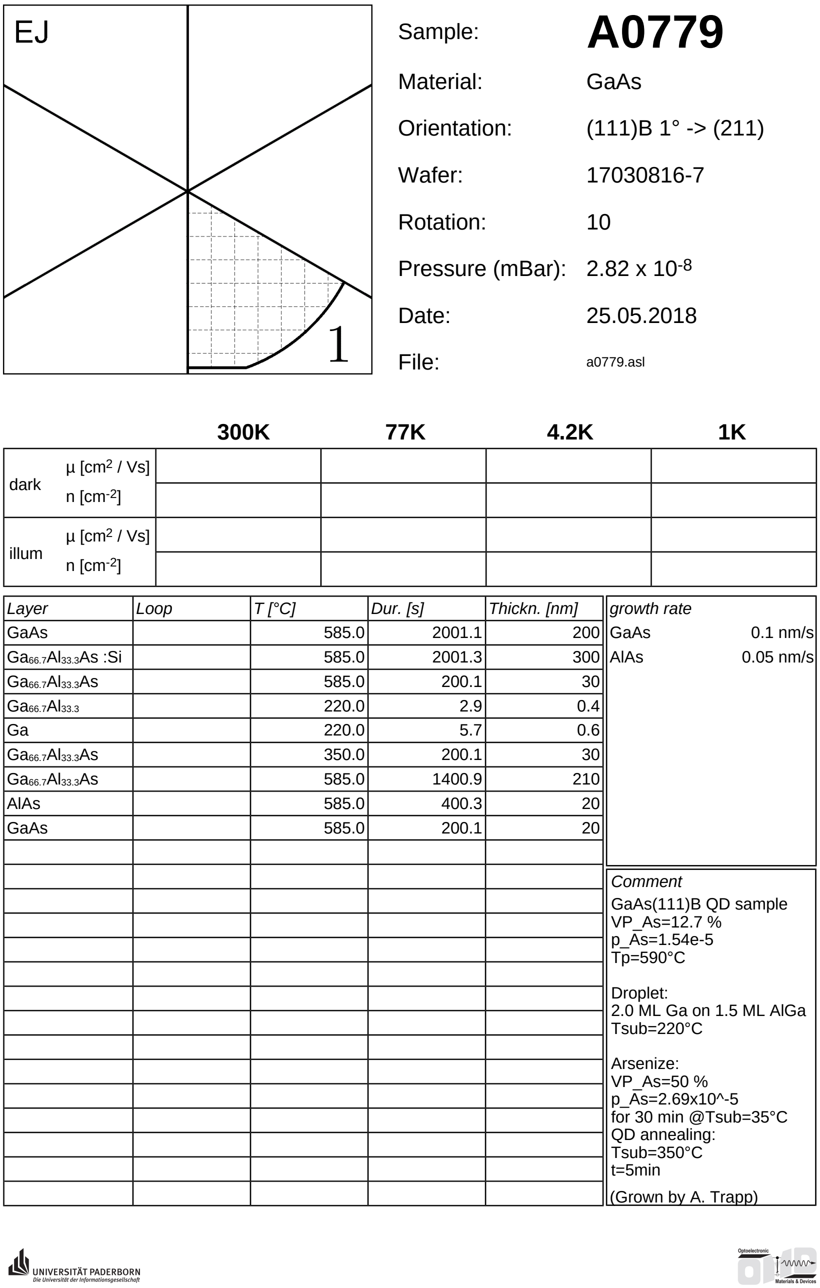

Sample: **A0779**
Material: GaAs
Orientation: (111)B 1° -> (211)
Wafer: 17030816-7
Rotation: 10
Pressure (mBar): 2.82 x 10^{-8}
Date: 25.05.2018
File: a0779.asl

		300K	**77K**	**4.2K**	**1K**
dark	μ [cm^2 / Vs]				
	n [cm^{-2}]				
illum	μ [cm^2 / Vs]				
	n [cm^{-2}]				

Layer	*Loop*	*T [°C]*	*Dur. [s]*	*Thickn. [nm]*
GaAs		585.0	2001.1	200
$Ga_{66.7}Al_{33.3}As$:Si		585.0	2001.3	300
$Ga_{66.7}Al_{33.3}As$		585.0	200.1	30
$Ga_{66.7}Al_{33.3}$		220.0	2.9	0.4
Ga		220.0	5.7	0.6
$Ga_{66.7}Al_{33.3}As$		350.0	200.1	30
$Ga_{66.7}Al_{33.3}As$		585.0	1400.9	210
AlAs		585.0	400.3	20
GaAs		585.0	200.1	20

growth rate	
GaAs	0.1 nm/s
AlAs	0.05 nm/s

Comment
GaAs(111)B QD sample
VP_As=12.7 %
p_As=1.54e-5
Tp=590°C

Droplet:
2.0 ML Ga on 1.5 ML AlGa
Tsub=220°C

Arsenize:
VP_As=50 %
p_As=2.69x10^-5
for 30 min @Tsub=35°C
QD annealing:
Tsub=350°C
t=5min
(Grown by A. Trapp)

UNIVERSITÄT PADERBORN
Die Universität der Informationsgesellschaft

Optoelectronic Materials & Devices

Figure B.34: Growth report of sample A0779.

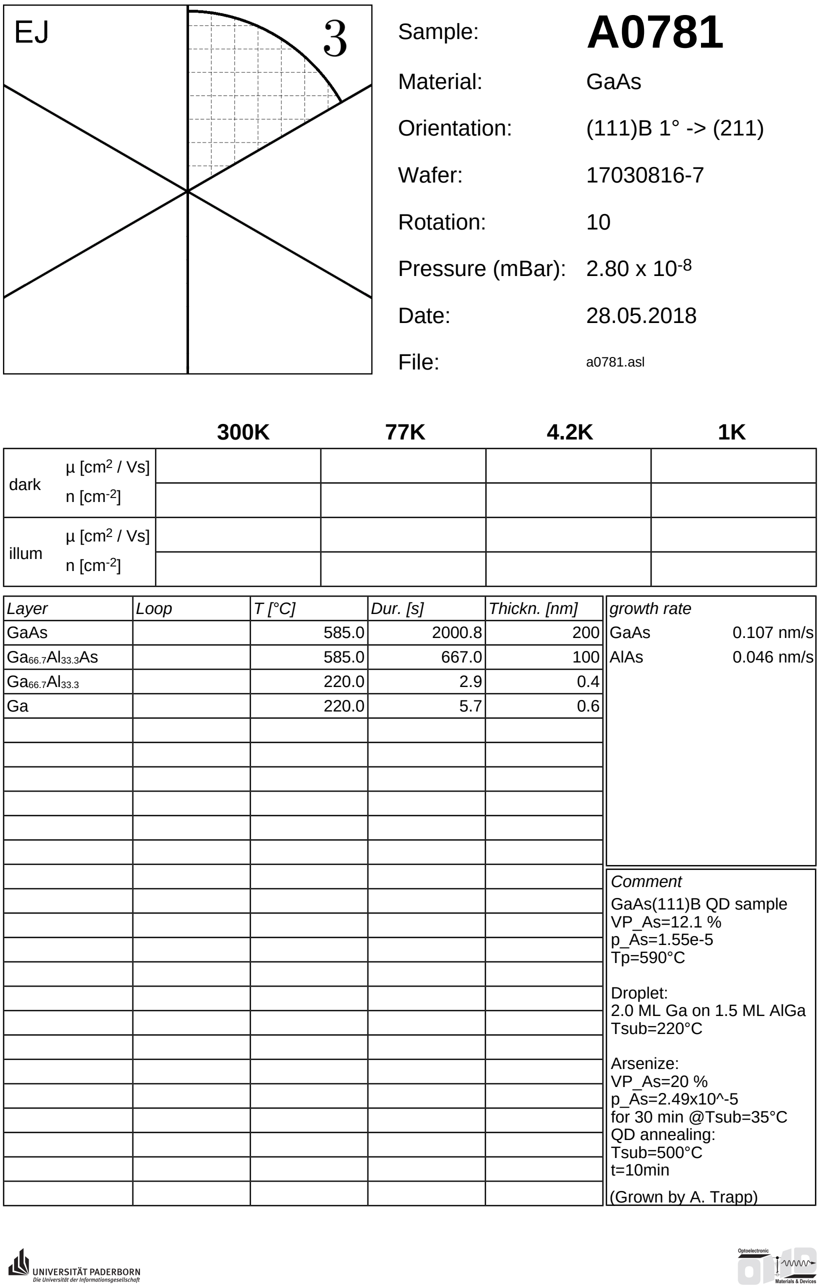

EJ

3

Sample: **A0781**

Material: GaAs

Orientation: (111)B 1° -> (211)

Wafer: 17030816-7

Rotation: 10

Pressure (mBar): 2.80 x 10^{-8}

Date: 28.05.2018

File: a0781.asl

		300K	**77K**	**4.2K**	**1K**
dark	μ [cm^2 / Vs]				
	n [cm^{-2}]				
illum	μ [cm^2 / Vs]				
	n [cm^{-2}]				

Layer	*Loop*	*T [°C]*	*Dur. [s]*	*Thickn. [nm]*
GaAs		585.0	2000.8	200
$Ga_{66.7}Al_{33.3}As$		585.0	667.0	100
$Ga_{66.7}Al_{33.3}$		220.0	2.9	0.4
Ga		220.0	5.7	0.6

growth rate	
GaAs	0.107 nm/s
AlAs	0.046 nm/s

Comment

GaAs(111)B QD sample
VP_As=12.1 %
p_As=1.55e-5
Tp=590°C

Droplet:
2.0 ML Ga on 1.5 ML AlGa
Tsub=220°C

Arsenize:
VP_As=20 %
p_As=2.49x10^-5
for 30 min @Tsub=35°C
QD annealing:
Tsub=500°C
t=10min
(Grown by A. Trapp)

UNIVERSITÄT PADERBORN
Die Universität der Informationsgesellschaft

Figure B.35: Growth report of sample A0781.

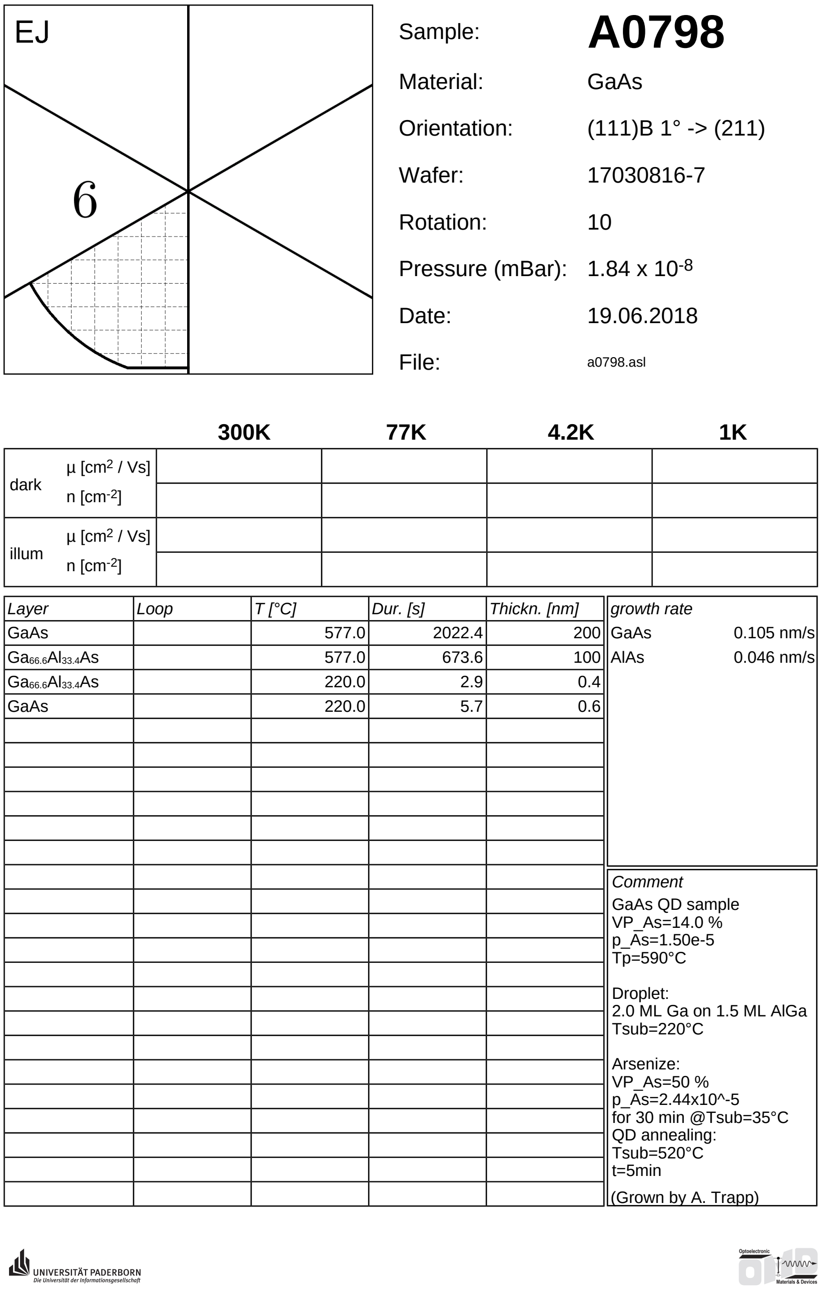

Sample: **A0798**
Material: GaAs
Orientation: (111)B 1° -> (211)
Wafer: 17030816-7
Rotation: 10
Pressure (mBar): 1.84 x 10^{-8}
Date: 19.06.2018
File: a0798.asl

		300K	77K	4.2K	1K
dark	µ [cm^2 / Vs]				
	n [cm^{-2}]				
illum	µ [cm^2 / Vs]				
	n [cm^{-2}]				

Layer	*Loop*	*T [°C]*	*Dur. [s]*	*Thickn. [nm]*
GaAs		577.0	2022.4	200
Ga$_{66.6}$Al$_{33.4}$As		577.0	673.6	100
Ga$_{66.6}$Al$_{33.4}$As		220.0	2.9	0.4
GaAs		220.0	5.7	0.6

growth rate	
GaAs	0.105 nm/s
AlAs	0.046 nm/s

Comment
GaAs QD sample
VP_As=14.0 %
p_As=1.50e-5
Tp=590°C

Droplet:
2.0 ML Ga on 1.5 ML AlGa
Tsub=220°C

Arsenize:
VP_As=50 %
p_As=2.44x10^-5
for 30 min @Tsub=35°C
QD annealing:
Tsub=520°C
t=5min
(Grown by A. Trapp)

UNIVERSITÄT PADERBORN
Die Universität der Informationsgesellschaft

Optoelectronic Materials & Devices

Figure B.36: Growth report of sample A0798.

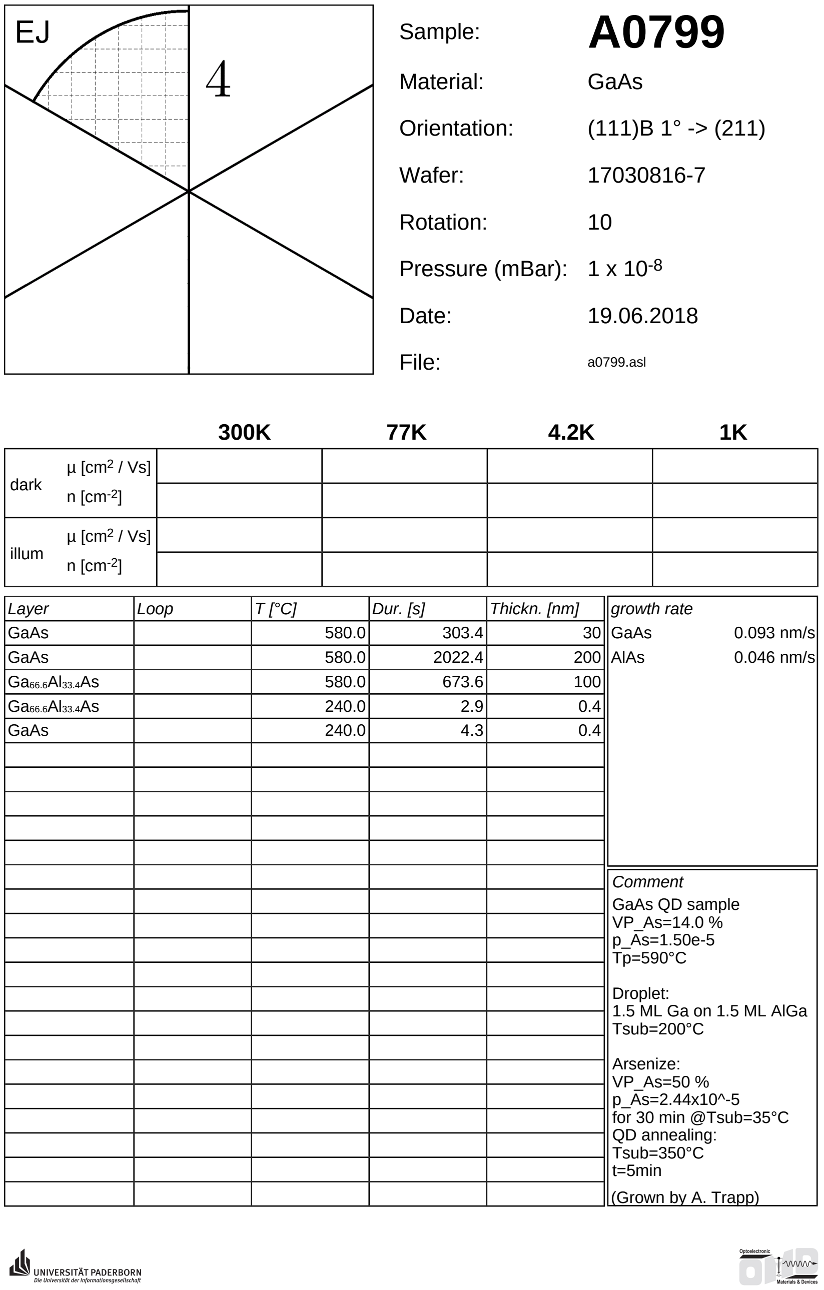

Sample: **A0799**

Material: GaAs

Orientation: (111)B 1° -> (211)

Wafer: 17030816-7

Rotation: 10

Pressure (mBar): 1 x 10^{-8}

Date: 19.06.2018

File: a0799.asl

		300K	**77K**	**4.2K**	**1K**
dark	μ [cm^2 / Vs]				
	n [cm^{-2}]				
illum	μ [cm^2 / Vs]				
	n [cm^{-2}]				

Layer	*Loop*	*T [°C]*	*Dur. [s]*	*Thickn. [nm]*
GaAs		580.0	303.4	30
GaAs		580.0	2022.4	200
$Ga_{66.6}Al_{33.4}As$		580.0	673.6	100
$Ga_{66.6}Al_{33.4}As$		240.0	2.9	0.4
GaAs		240.0	4.3	0.4

growth rate	
GaAs	0.093 nm/s
AlAs	0.046 nm/s

Comment

GaAs QD sample
VP_As=14.0 %
p_As=1.50e-5
Tp=590°C

Droplet:
1.5 ML Ga on 1.5 ML AlGa
Tsub=200°C

Arsenize:
VP_As=50 %
p_As=2.44x10^-5
for 30 min @Tsub=35°C
QD annealing:
Tsub=350°C
t=5min

(Grown by A. Trapp)

UNIVERSITÄT PADERBORN
Die Universität der Informationsgesellschaft

Optoelectronic Materials & Devices

Figure B.37: Growth report of sample A0799.

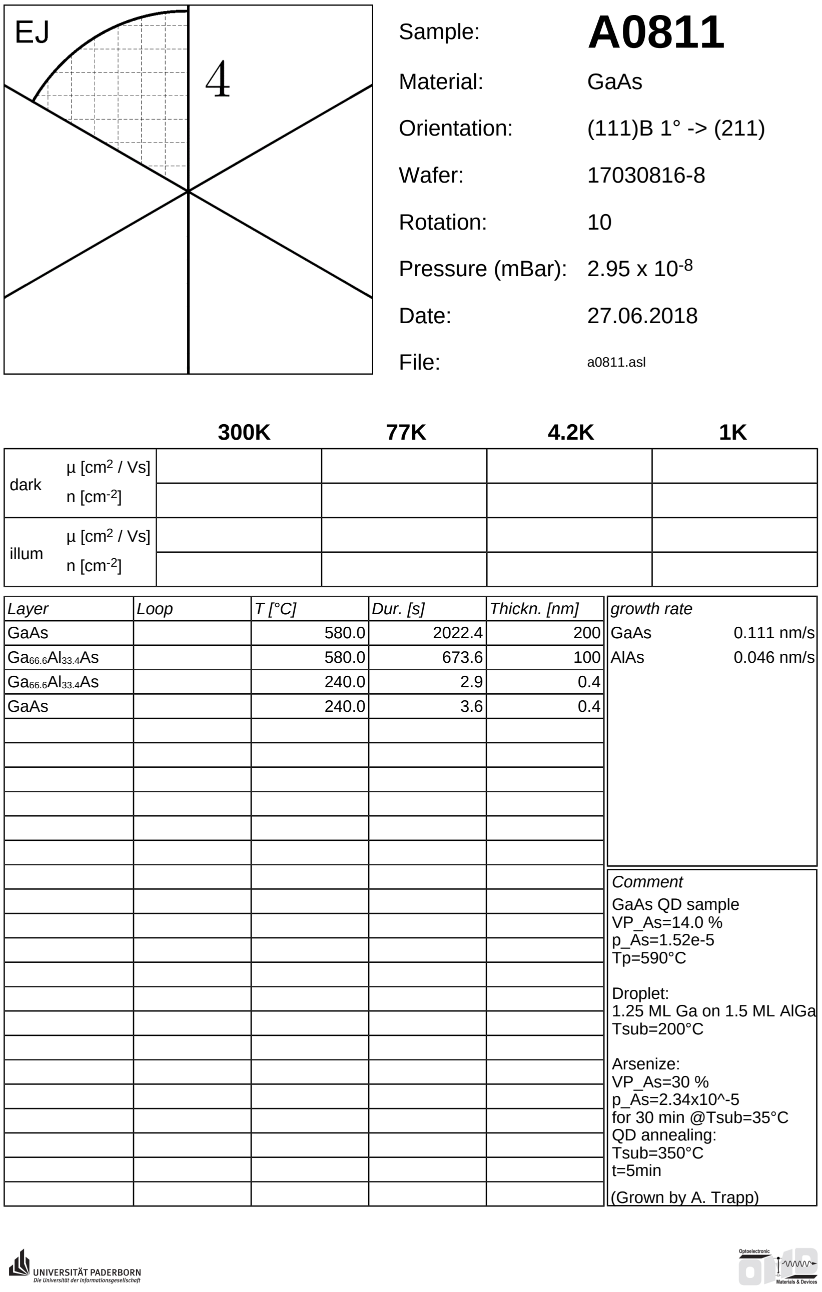

Sample:	**A0811**
Material:	GaAs
Orientation:	(111)B 1° -> (211)
Wafer:	17030816-8
Rotation:	10
Pressure (mBar):	2.95 x 10^{-8}
Date:	27.06.2018
File:	a0811.asl

		300K	**77K**	**4.2K**	**1K**
dark	µ [cm^2 / Vs]				
	n [cm^{-2}]				
illum	µ [cm^2 / Vs]				
	n [cm^{-2}]				

Layer	*Loop*	*T [°C]*	*Dur. [s]*	*Thickn. [nm]*
GaAs		580.0	2022.4	200
Ga$_{66.6}$Al$_{33.4}$As		580.0	673.6	100
Ga$_{66.6}$Al$_{33.4}$As		240.0	2.9	0.4
GaAs		240.0	3.6	0.4

growth rate	
GaAs	0.111 nm/s
AlAs	0.046 nm/s

Comment
GaAs QD sample
VP_As=14.0 %
p_As=1.52e-5
Tp=590°C

Droplet:
1.25 ML Ga on 1.5 ML AlGa
Tsub=200°C

Arsenize:
VP_As=30 %
p_As=2.34x10^-5
for 30 min @Tsub=35°C
QD annealing:
Tsub=350°C
t=5min
(Grown by A. Trapp)

UNIVERSITÄT PADERBORN
Die Universität der Informationsgesellschaft

Optoelectronic
Materials & Devices

Figure B.38: Growth report of sample A0811.

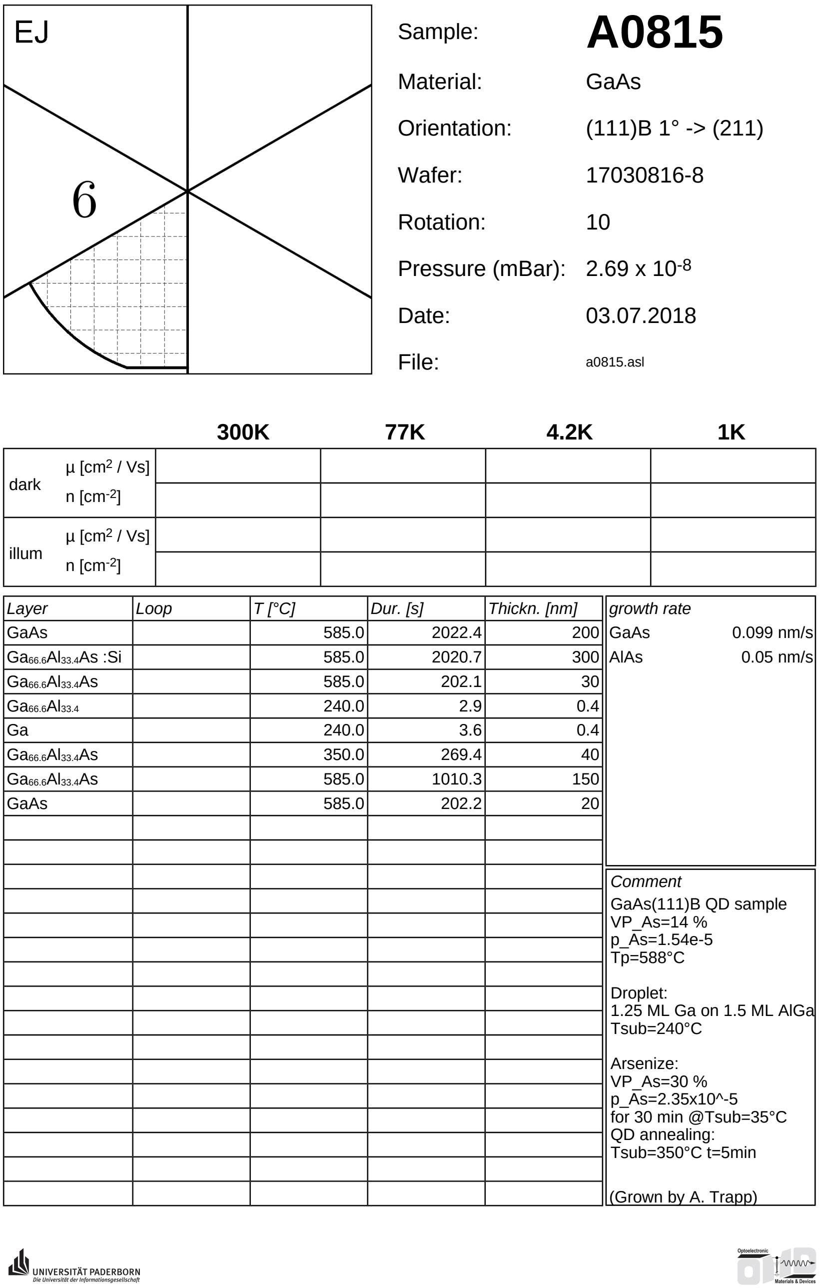

Sample: **A0815**
Material: GaAs
Orientation: (111)B 1° -> (211)
Wafer: 17030816-8
Rotation: 10
Pressure (mBar): 2.69 x 10^{-8}
Date: 03.07.2018
File: a0815.asl

		300K	77K	4.2K	1K
dark	μ [cm^2 / Vs]				
	n [cm^{-2}]				
illum	μ [cm^2 / Vs]				
	n [cm^{-2}]				

Layer	*Loop*	*T [°C]*	*Dur. [s]*	*Thickn. [nm]*
GaAs		585.0	2022.4	200
Ga$_{66.6}$Al$_{33.4}$As :Si		585.0	2020.7	300
Ga$_{66.6}$Al$_{33.4}$As		585.0	202.1	30
Ga$_{66.6}$Al$_{33.4}$		240.0	2.9	0.4
Ga		240.0	3.6	0.4
Ga$_{66.6}$Al$_{33.4}$As		350.0	269.4	40
Ga$_{66.6}$Al$_{33.4}$As		585.0	1010.3	150
GaAs		585.0	202.2	20

growth rate	
GaAs	0.099 nm/s
AlAs	0.05 nm/s

Comment
GaAs(111)B QD sample
VP_As=14 %
p_As=1.54e-5
Tp=588°C

Droplet:
1.25 ML Ga on 1.5 ML AlGa
Tsub=240°C

Arsenize:
VP_As=30 %
p_As=2.35x10^-5
for 30 min @Tsub=35°C
QD annealing:
Tsub=350°C t=5min

(Grown by A. Trapp)

UNIVERSITÄT PADERBORN
Die Universität der Informationsgesellschaft

Optoelectronic Materials & Devices

Figure B.39: Growth report of sample A0815.

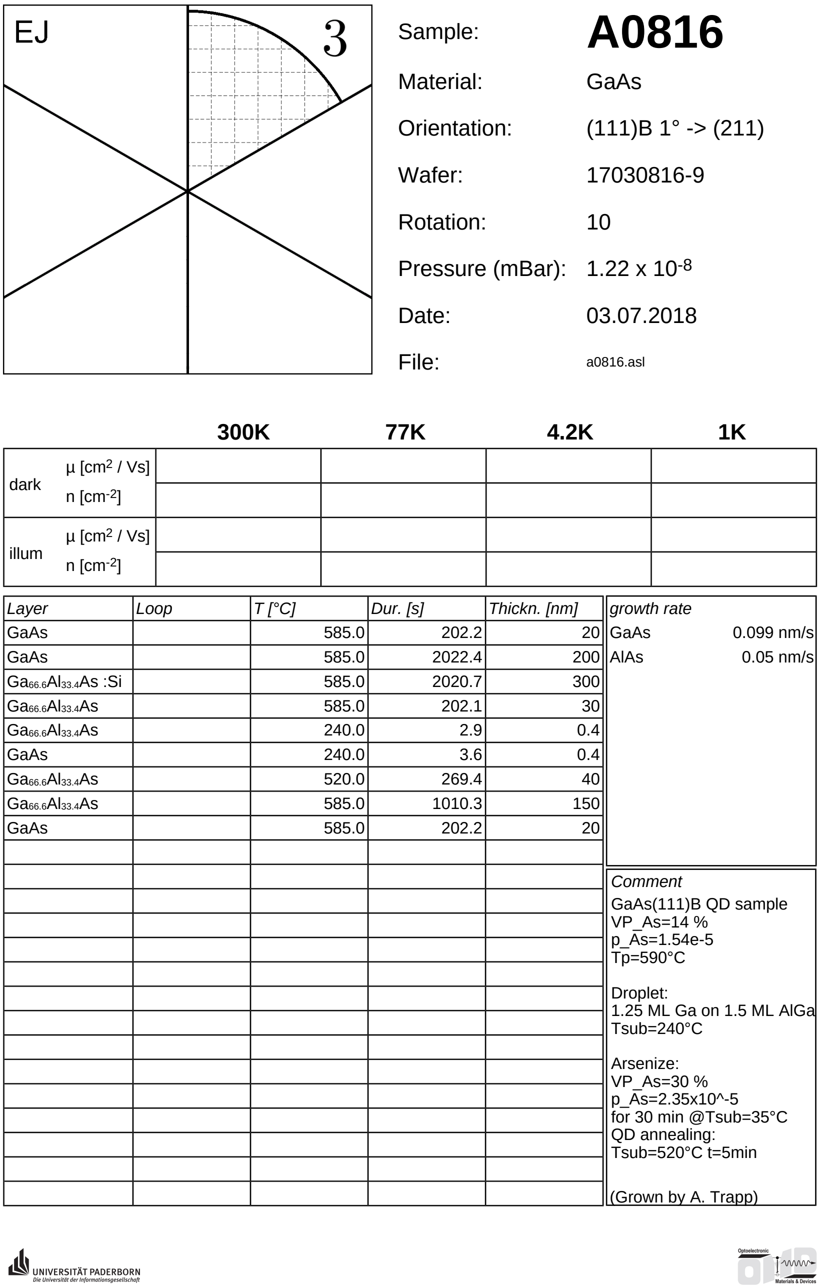

Sample: **A0816**
Material: GaAs
Orientation: (111)B 1° -> (211)
Wafer: 17030816-9
Rotation: 10
Pressure (mBar): 1.22 x 10^{-8}
Date: 03.07.2018
File: a0816.asl

		300K	77K	4.2K	1K
dark	μ [cm^{2} / Vs]				
	n [cm^{-2}]				
illum	μ [cm^{2} / Vs]				
	n [cm^{-2}]				

Layer	*Loop*	*T [°C]*	*Dur. [s]*	*Thickn. [nm]*
GaAs		585.0	202.2	20
GaAs		585.0	2022.4	200
$Ga_{66.6}Al_{33.4}As$:Si		585.0	2020.7	300
$Ga_{66.6}Al_{33.4}As$		585.0	202.1	30
$Ga_{66.6}Al_{33.4}As$		240.0	2.9	0.4
GaAs		240.0	3.6	0.4
$Ga_{66.6}Al_{33.4}As$		520.0	269.4	40
$Ga_{66.6}Al_{33.4}As$		585.0	1010.3	150
GaAs		585.0	202.2	20

growth rate	
GaAs	0.099 nm/s
AlAs	0.05 nm/s

Comment
GaAs(111)B QD sample
VP_As=14 %
p_As=1.54e-5
Tp=590°C

Droplet:
1.25 ML Ga on 1.5 ML AlGa
Tsub=240°C

Arsenize:
VP_As=30 %
p_As=2.35x10^-5
for 30 min @Tsub=35°C
QD annealing:
Tsub=520°C t=5min

(Grown by A. Trapp)

UNIVERSITÄT PADERBORN
Die Universität der Informationsgesellschaft

Optoelectronic Materials & Devices

Figure B.40: Growth report of sample A0816.

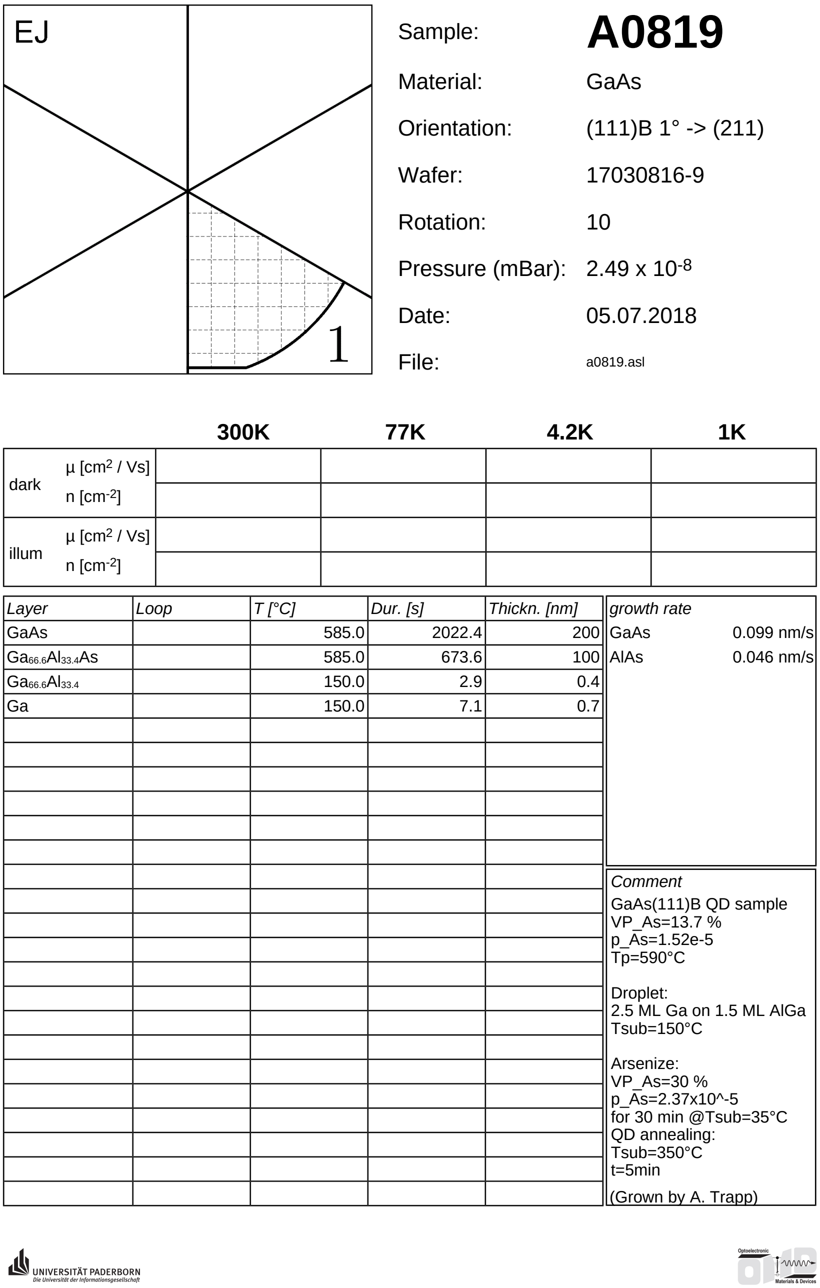

Sample: **A0819**
Material: GaAs
Orientation: (111)B 1° -> (211)
Wafer: 17030816-9
Rotation: 10
Pressure (mBar): 2.49×10^{-8}
Date: 05.07.2018
File: a0819.asl

		300K	**77K**	**4.2K**	**1K**
dark	μ [cm^2 / Vs]				
	n [cm^{-2}]				
illum	μ [cm^2 / Vs]				
	n [cm^{-2}]				

Layer	*Loop*	*T [°C]*	*Dur. [s]*	*Thickn. [nm]*
GaAs		585.0	2022.4	200
Ga$_{66.6}$Al$_{33.4}$As		585.0	673.6	100
Ga$_{66.6}$Al$_{33.4}$		150.0	2.9	0.4
Ga		150.0	7.1	0.7

growth rate	
GaAs	0.099 nm/s
AlAs	0.046 nm/s

Comment
GaAs(111)B QD sample
VP_As=13.7 %
p_As=1.52e-5
Tp=590°C

Droplet:
2.5 ML Ga on 1.5 ML AlGa
Tsub=150°C

Arsenize:
VP_As=30 %
p_As=2.37x10^-5
for 30 min @Tsub=35°C
QD annealing:
Tsub=350°C
t=5min
(Grown by A. Trapp)

UNIVERSITÄT PADERBORN
Die Universität der Informationsgesellschaft

Optoelectronic Materials & Devices

Figure B.41: Growth report of sample A0819.

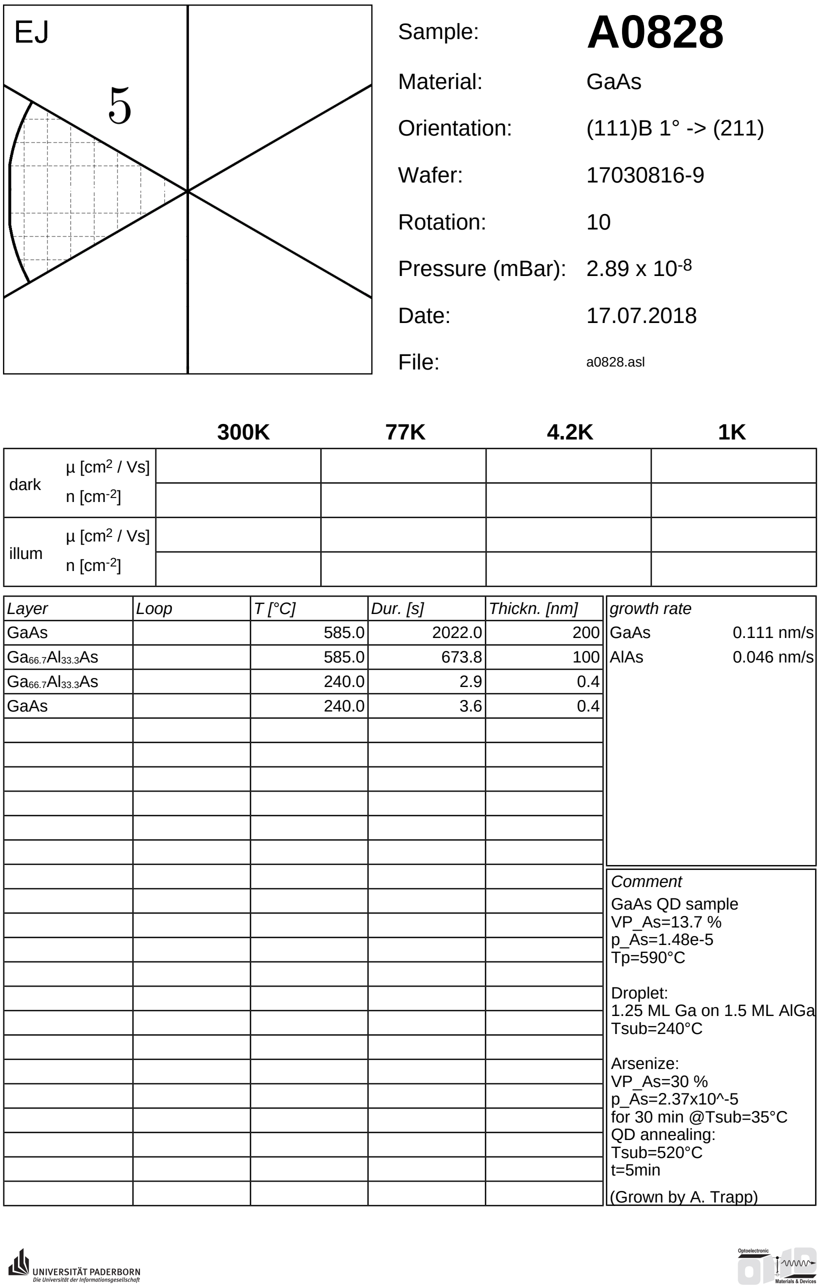

Sample: **A0828**
Material: GaAs
Orientation: (111)B 1° -> (211)
Wafer: 17030816-9
Rotation: 10
Pressure (mBar): 2.89 x 10^{-8}
Date: 17.07.2018
File: a0828.asl

		300K	77K	4.2K	1K
dark	μ [cm^2 / Vs]				
	n [cm^{-2}]				
illum	μ [cm^2 / Vs]				
	n [cm^{-2}]				

Layer	*Loop*	*T [°C]*	*Dur. [s]*	*Thickn. [nm]*
GaAs		585.0	2022.0	200
$Ga_{66.7}Al_{33.3}As$		585.0	673.8	100
$Ga_{66.7}Al_{33.3}As$		240.0	2.9	0.4
GaAs		240.0	3.6	0.4

growth rate	
GaAs	0.111 nm/s
AlAs	0.046 nm/s

Comment
GaAs QD sample
VP_As=13.7 %
p_As=1.48e-5
Tp=590°C

Droplet:
1.25 ML Ga on 1.5 ML AlGa
Tsub=240°C

Arsenize:
VP_As=30 %
p_As=2.37x10^-5
for 30 min @Tsub=35°C
QD annealing:
Tsub=520°C
t=5min
(Grown by A. Trapp)

Figure B.42: Growth report of sample A0828.

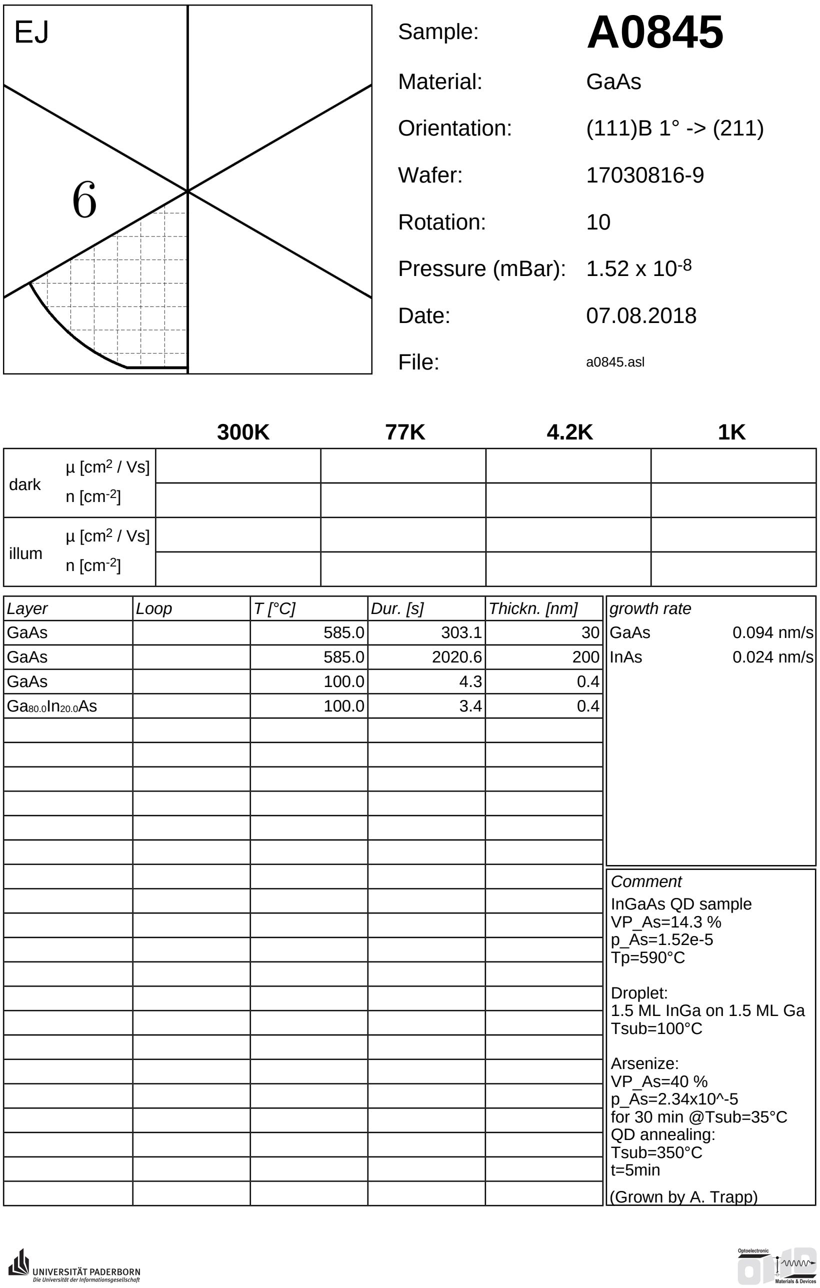

Sample:	**A0845**
Material:	GaAs
Orientation:	(111)B 1° -> (211)
Wafer:	17030816-9
Rotation:	10
Pressure (mBar):	1.52 x 10^{-8}
Date:	07.08.2018
File:	a0845.asl

		300K	**77K**	**4.2K**	**1K**
dark	μ [cm^2 / Vs]				
	n [cm^{-2}]				
illum	μ [cm^2 / Vs]				
	n [cm^{-2}]				

Layer	*Loop*	*T [°C]*	*Dur. [s]*	*Thickn. [nm]*
GaAs		585.0	303.1	30
GaAs		585.0	2020.6	200
GaAs		100.0	4.3	0.4
$Ga_{80.0}In_{20.0}As$		100.0	3.4	0.4

growth rate	
GaAs	0.094 nm/s
InAs	0.024 nm/s

Comment

InGaAs QD sample
VP_As=14.3 %
p_As=1.52e-5
Tp=590°C

Droplet:
1.5 ML InGa on 1.5 ML Ga
Tsub=100°C

Arsenize:
VP_As=40 %
p_As=2.34x10^-5
for 30 min @Tsub=35°C
QD annealing:
Tsub=350°C
t=5min
(Grown by A. Trapp)

UNIVERSITÄT PADERBORN
Die Universität der Informationsgesellschaft

Optoelectronic Materials & Devices

Figure B.43: Growth report of sample A0845.

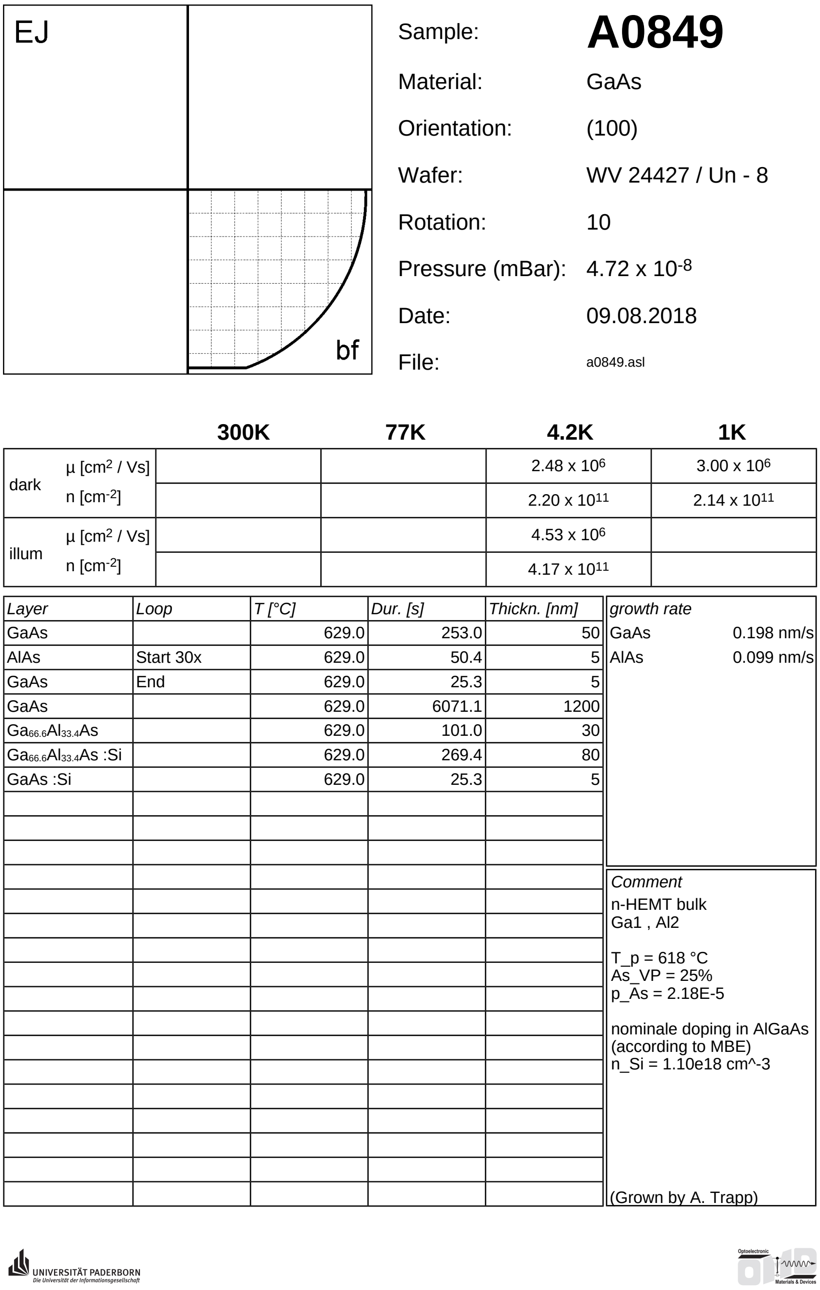

EJ

bf

Sample:	**A0849**
Material:	GaAs
Orientation:	(100)
Wafer:	WV 24427 / Un - 8
Rotation:	10
Pressure (mBar):	4.72×10^{-8}
Date:	09.08.2018
File:	a0849.asl

		300K	77K	4.2K	1K
dark	μ [cm^2 / Vs]			2.48×10^6	3.00×10^6
	n [cm^{-2}]			2.20×10^{11}	2.14×10^{11}
illum	μ [cm^2 / Vs]			4.53×10^6	
	n [cm^{-2}]			4.17×10^{11}	

Layer	*Loop*	*T [°C]*	*Dur. [s]*	*Thickn. [nm]*
GaAs		629.0	253.0	50
AlAs	Start 30x	629.0	50.4	5
GaAs	End	629.0	25.3	5
GaAs		629.0	6071.1	1200
$Ga_{66.6}Al_{33.4}As$		629.0	101.0	30
$Ga_{66.6}Al_{33.4}As$:Si		629.0	269.4	80
GaAs :Si		629.0	25.3	5

growth rate	
GaAs	0.198 nm/s
AlAs	0.099 nm/s

Comment

n-HEMT bulk
Ga1 , Al2

T_p = 618 °C
As_VP = 25%
p_As = 2.18E-5

nominale doping in AlGaAs
(according to MBE)
n_Si = 1.10e18 cm^-3

(Grown by A. Trapp)

UNIVERSITÄT PADERBORN
Die Universität der Informationsgesellschaft

Optoelectronic Materials & Devices

Figure B.44: Growth report of sample A0849.

List of Figures

List of Tables

Publications

During the creation of this thesis the following publications were created. Parts of the thesis are already published in some of them.

Scientific publications

1. A. Trapp and D. Reuter: 'Formation of self-assembled GaAs quantum dots via droplet epitaxy on misoriented GaAs(111)B substrates'. *Journal of Vacuum Science & Technology B, Nanotechnology and Microelectronics: Materials, Processing, Measurement, and Phenomena*, vol. **36**: 02D106 (2018).
2. T. Henksmeier, S. Shvarkov, A. Trapp, and D. Reuter: 'Molecular beam epitaxy growth and temperature-dependent electrical characterization of carbon-doped GaAs on GaAs(111)B'. *Journal of Crystal Growth*, vol. **512**: 164–168 (2019).

Submissions to international conferences

1. T. Riedl, V. Kunnathully, A. Karlisch, D. Reuter, N. Weber, C. Meier, R. Schierholz, and J. K. N. Lindner: 'Morphology, structure and enhanced PL of molecular beam epitaxial $In_{0.2}Ga_{0.8}As$ layers on nanopillar patterned GaAs'. *E-MRS Spring Meeting*. Strasbourg, 2017.

2. V. Kunnathully, T. Riedl, A. Karlisch, D. Reuter, and J. K. N. Lindner: ‘InAs heteroepitaxy on GaAs patterned by nanosphere lithography’. *E-MRS Fall Meeting.* Warsaw, 2017.
3. A. Trapp and D. Reuter: ‘Formation of self-assembled GaAs quantum dots via droplet epitaxy on misoriented GaAs(111)B substrates’. *33rd North American Molecular Beam Epitaxy Conference.* Galveston, 2017.
4. V. Kunnathully, T. Riedl, A. Trapp, D. Reuter, and J. K. N. Lindner: ‘Defect Formation in InAs Nanoislands Heteroepitaxially Grown on Nanopillar-Patterned GaAs(111)A’. *19th International Conference on Extended Defects in Semiconductors.* Thessaloniki, 2018.
5. T. Riedl, V. Kunnathully, A. Trapp, D. Reuter, and J. K. N. Lindner: ‘Strain Relaxation in InAs Nanoislands on top of GaAs(111)A Nanopillars’. *14th International Conference on Atomically Controlled Surfaces, Interfaces, Nanostructures.* Sendai, 2018.
6. V. Kunnathully, T. Riedl, A. Trapp, D. Reuter, and J. K. N. Lindner: ‘MBE Growth of InAs on Nanopillar-Patterned GaAs(111)A’. *14th International Conference on Atomically Controlled Surfaces, Interfaces, Nanostructures.* Sendai, 2018.
7. T. Henksmeier, S. Shvarkov, A. Trapp, and D. Reuter: ‘Molecular Beam Epitaxy Growth and Temperature-dependent Electrical Characterization of Carbon-Doped GaAs(111)B’. *International Conference on Molecular Beam Epitaxy.* Shanghai, 2018.

Submissions to national conferences

1. A. Karlisch, N. L. Sharma, S. Shvarkov, and D. Reuter: ‘Emission wavelength tuning of InAs quantum dot molecules by

rapid thermal annealing'. *DPG Spring Meeting 2016.* Regensburg, 2016.

2. A. Karlisch and D. Reuter: 'Formation of self-organized nanostructures by droplet epitaxy on AlGaAs(111)B'. *DPG Spring Meeting 2017.* Dresden, 2017.
3. A. Trapp, T. Henksmeier, and D. Reuter: 'Carbon doping of GaAs grown by molecular beam epitaxy on GaAs(100) and GaAs(111)B'. *DPG Spring Meeting 2018.* Berlin, 2018.
4. A. Trapp and D. Reuter: 'Formation of self-assembled GaAs quantum dots via droplet epitaxy on misoriented GaAs(111)B substrates'. *DGKK Workshop 2018.* Paderborn, 2018.
5. T. Riedl, V. Kunnathully, A. Trapp, T. Langer, D. Reuter, and J. K. N. Lindner: 'Relaxation of misfit in nanoscale InAs growths atop GaAs(111)A nanopillars'. *DGKK Workshop 2018.* Paderborn, 2018.
6. V. Kunnathully, A. Trapp, T. Riedl, T. Langer, D. Reuter, and J. K. N. Lindner: 'InAs heteroepitaxy on nano-pillar patterned GaAs(111)A'. *DGKK Workshop 2018.* Paderborn, 2018.

Acknowledgments

At this point I would like to sincerely thank everyone who supported me during this dissertation and who accompanied me on this way.

Foremost I thank **Prof. Dr. Dirk Reuter** for giving me the opportunity to work on this intriguing topic and making this dissertation possible at all. His passionate supervision, strong motivation and professional expertise made my work in his group very rewarding. Especially Prof. Reuter's open door policy allows informal exchange (and solution) of scientific and technical challenges in a short timeframe and keeps frustration, which is unavoidable for any scientific endeavor, low.

I also thank **Prof. Dr. Artur Zrenner** for making the scientific equipment and knowledge of his group available to be used for this dissertation. Important parts of this thesis would be missing without it. Additionally I am thankful for his work as my second reviewer.

I am thankful to **Dr. Thomas Riedl** and **Vinay Kunnathully** for our valuable discussions about crystallography and semiconductor epitaxy which promoted my understanding of both topics considerably. I also thank Dr. Riedl for his part in my doctoral committee.

I thank **Prof. Dr. Wolf Gero Schmidt** for his willingness to act as the chairman of my doctoral committee.

I would like to thank **Björn Jonas** for performing µPL experiments on my samples and helping me to interpret the resulting data. I want to also thank

Tobias Henksmeier and **Sebastian Krehs** for their help with processing and contacting for these measurements.

All members of the group for Optoelectronic Materials and Devices contributed to an enjoyable working environment and, occasionally, an enjoyable non-working environment and deserve thanks:

- I thank **apl. Prof. Dr. Donat J. As** and his vast experience in our field. He has an answer to nearly any physical question and, within short delay, a related publication and/or book to back it up. His insistence and participation on the coffee break added a scientific dimension to the social one and allowed a discussion of current challenges in a pleasant setting.
- I thank **Dr. Nand Lal Sharma** for introducing me to our MBE system and always providing me with valuable minutia and peculiarities of our system. The ground work he did during start-up of the MBE is the foundation of my experimental work with this system.
- I thank **Dr. Stepan Shvarkov** for teaching me the intricacies of photoluminescence spectroscopy and his relentless pursuit of finding errors in my understanding of semiconductor physics and expunging them.
- I thank my office-mate **Michael Deppe** for a pleasant and productive working atmosphere. The same acknowledgment goes to my other (ex-)colleagues **Dr. Tobias Wecker, Sarah Blumenthal, Viktoryia Zolatanosha, Timo Langer, Tobias Henksmeier, Akshay Kumar Verma, Siegfried Igges, Falco Meier, Fabian Tacken, Christian Kiessler, Tjorven Rebeccah Christin Grotemeyer-Bagnall, Jannick Alexander Saatz, Mario Littmann, Marlin Soliman, Martin Eppinger** and **Dennis Deutsch**.
- I thank **Bastian Aisenbrey** for his technical support for the MBE system, the whole clean room and whatever technical problem is presented

to him.

- I thank **Anja Blank** for her administrative support both within and without her job description and helping me to improve my grasp on the English language.

I also want to thank my physics teacher **Jörg Gastel** for preparing the most interesting lessons during my school education. I still fondly remember his creatively packaged exercises such as ‘Inspector Minkowski solves a relativistic murder’.

At last I thank my family for their support during my whole educational career: I thank **my parents** who subsidized and encouraged my physics education. My wife **Lisa** deserves thanks for her love, patience and unwavering support. I also want to thank my son **Justus** who arrived just in time to provide valuable motivation during the finishing touches of this thesis.